DEVELOPMENT OF WIND TURBINES TO OPERATE IN MODIFIED AXIAL FLOWS WHICH CONTAIN SWIRL VELOCITIES AND NON-UNIFORM DISTRIBUTIONS.

AUTHOR : GEORGE LEFTHERIOTIS.

A thesis submitted as a requirement for the degree of PhD in Engineering.

Submitted to the Department of Engineering, University of Warwick,
Coventry, U.K.

June 1992.

CONTENTS.

Dedicated to Angela.

ACKNOWLEDGMENTS.

I would like to thank my supervisor Mr. C. J. Carpenter for his help, guidance and encouragement.

Many thanks to Dr. C. Pollock and Mr. A. E. Corbett for their help with the generator test, Dr. J. Wallbank for his assistance with the blade casting, Mr. H. Hingle for helping me to produce the turbine moulds and Dr. C. T. Shaw, Dr. T. H. Thomas, Dr. C. E. Oram for the stimulating discussions we had.

I would also like to thank Marlec Engineering plc for providing us with the generator for the prototype turbine and Mr. A. Stobart, managing director of Recource Conservation plc for his cooperation in the counter-rotating turbine design.

Special thanks to Dimitris, Xanthi, Thanasis, Electra, Thanasis Kontos and George Tsakiris for their friendship.

Finally, I would like to thank the Commission of the European Communities, DG XII, for providing me with a grant (part of the Joule programme) in order to carry out this work.

AUTHOR'S DECLARATION.

Parts of Chapter 2 of this thesis (sections 2.1 and 2.2, excluding 2.2.3) were also included (with modifications) in my MSc thesis titled "Investigation of the vortex field generated by a slender delta wing and development of a procedure for the design of a wind turbine rotor to operate in this field", submitted to the University of Warwick, Dept. of Engineering, on May 1989.

Parts of Chapter 4 of this thesis were published in the following papers:

G. Leftheriotis and C. J. Carpenter, "Investigation of the delta wing-turbine system's suitability for large scale applications". Wind Engineering, Vol 15, No 1, 1991.

G. Leftheriotis and C. J. Carpenter, "Investigation of Reynolds number effects on the design of a delta wing vortex wind turbine". Wind Engineering, Vol 15, No 1, 1991.

G. Leftheriotis and C. J. Carpenter, "Development of a turbine to operate in the vortex field generated by a slender delta wing". Proceedings of the Amsterdam EWEC '91, Part 1.

SUMMARY.

In part A of this thesis, a procedure based on lifting line theory for the design of wind turbines operating in non-uniform, non-axial but axisymmetric flows is presented. This procedure was used for the design of conventional turbines which were compared with turbine designs produced by momentum theory. The overall trends of both theories were found to be similar, although the lifting line procedure was found to produce a more conservative estimate of the turbine performance. The above mentioned design procedure was also used for the turbine blade design of the wind power systems presented in parts B and C of the thesis.

Part B of the thesis deals with the development of the delta wing-turbine system: The system was scaled-up using the results of a previously developed design model, and its dimensions were compared with those of equivalent conventional turbines. It was found that the system compares well with conventional turbines up to rated power values equal to 100 kW. Its advantages were found to be the lower turbine diameter required for a given power output and the opportunity it provides for direct connection of the turbines to generators. The cost of this advantage is the relatively large delta wing required.

A system prototype with power output in the order of 1 kW was designed for testing. The prototype turbine blades were designed taking into account Reynolds number effects. In order to overcome the detrimental Re effects, use of a low Re aerofoil (GOE 795), reduction of the turbine number of blades to 10, increase of the blade chord, linear blade chord distribution and variable optimum angle of attack were found to be necessary, leading to a reduction of the turbine power coefficient drop to 4.7% below that of the original high Re design.

The prototype off design performance was predicted and it was found that increase of the blade chord at the hub region (for strength) and linearisation of the blade optimum twist angle (for ease of manufacture) did not affect the turbine performance significantly.

The generator to be used with the prototype turbine was bench-tested. Its model parameters and power losses were identified. For matching the generator with the turbine, an appropriate load for the generator was found. The prototype long-term performance was also estimated using the turbine performance characteristics, the generator test results and the Weibull distribution of wind occurrence probability. It was found that the generator is not ideally suited for the prototype turbine and that a generator of larger ratings would be more suitable.

Finally, the effects of yaw on the delta wing vortices were investigated experimentally. This was done in order to determine the feasibility of using the delta wing yaw to regulate the system power output. It was found that the above mentioned regulation technique can be used, provided that undue blade vibrations due to turbine-vortex misalignment and vortex bursting will not occur.

In part C, a procedure for the design of the counter-rotating turbine blades was developed. The above mentioned lifting line procedure as well as the existing knowledge of wind turbine wakes and counter-rotating rotor aerodynamics were used for the design of the counter-rotating turbine blades and the semi-empirical modelling of the two rotors' interaction.

The optimum axial distance between the two rotors was found to be equal to 1.4 times the rotors' radius. It was demonstrated that proper design of the turbine blades and appropriate axial positioning of the two rotors could increase the turbine performance by 27.4% above that of the original counter-rotating turbine design, called Trimble Mill.

It was also found that a considerable increase of the generator effective rotational speed (equal to 58%) can be achieved by the counter-rotating turbine, compared to that of a conventional turbine with the same number of blades, while the two turbines' power output was found to be at the same levels.

TERMINOLOGY.

A	Area swept by the turbine blades.
B	Turbine number of blades.
CF	Capacity factor. (See equation 5.2.8).
C_D	Drag coefficient. (See equation 2.1.4).
C_L	Lift coefficient. (See equation 2.1.4). Also generator load capacitance.
C_p	Power coefficient. (See equation 2.3.2).
C_q	Torque coefficient. (See equation 10.2.1).
c	Chord of turbine blade. Also length of the delta wing centreline and Weibull scale parameter.
D	Turbine diameter.
E	Waisting factor. (See equation 3.2.1).
E_A	Rms value of the emf produced by the generator. (See equation 5.2.1).
G	Dimensionless bound circulation. (See equation 2.2.8).
G_m	mth coefficient of the fourier expansion of G. (See equation 2.2.10).
b_m^a	Axial Lerbs factor. (See equations 2.2.13 and 2.2.14).
b_m^t	Tangential Lerbs factor. (See equations 2.2.13 and 2.2.14).
I	Rms value of generator current.
I_n^a	nth coefficient of the fourier expansion of i_a. (See equation 2.2.11).
I_n^t	nth coefficient of the fourier expansion of i_t. (See equation 2.2.11).
i_a	Axial induction factor for the flow on the lifting lines. (See equation 2.2.7).
i_a'	Axial induction factor for the flow on the biasctors. (See equation 2.2.19).
i_t	Tangential induction factor for the flow on the lifting lines. (See equation 2.2.7).
i_t'	Tangential induction factor for the flow on the biasctors. (See equation 2.2.19).
K_n	Slope of the $E_A(\omega)$ line. (See equation 5.2.1).
K_0	Parameter related to the helical vortex filament pitch. (See equation 2.2.1).
k	Weibull shape parameter. (See equation 5.2.4).
L	Lift per unit span. (See equation 2.1.4).
L_S	Generator synchronous inductance.
P	Power. Also generator number of poles.
P_R	Rated electrical power.
P_{av}	Average power. (See equation 5.2.6).
P_e	Electrical power.
P_{in}	Input power.
P_m	Mechanical power.
P_{misc}	Miscellaneous power losses. (See equation 5.1.6).
P_{out}	Output power.
P_{norm}	Normalised average power. (See equation 5.2.7).
Q	Torque.
R	Turbine radius.
R_A	Armature resistance.
R_L	Load resistance.
Re	Reynolds number.
R_h	Turbine hub radius.
r	Radial distance from the turbine axis of rotation.
r_0	Radius of a helical vortex filament.
s	Delta wing span.
T	Thrust per unit span.

U_1	Axial component of the counter-rotating turbine front rotor incoming velocity. (See equation 10.1.9).
U_{12}	Axial component of the counter-rotating turbine front to rear rotor interference velocity. (See equation 10.1.2).
U_2	Axial component of the counter-rotating turbine rear rotor incoming velocity. (See equation 10.1.3).
U_{21}	Axial component of the counter-rotating turbine rear to front rotor interference velocity. (See equation 10.1.8).
u	Axial component of the incoming flow velocity.
u_i	Axial induced velocity.
V	Rms value of the generator terminal voltage.
V_{IN}	Cut-in wind speed.
V_O	Cut-out wind speed.
V_R	Rated wind speed.
V_{t2}	Tangential component of the counter-rotating turbine front to rear rotor interference velocity.(See equation 10.1.9).
V_2	Tangential component of the counter-rotating turbine rear rotor incoming velocity. (See equation 10.1.3).
V_∞	Velocity of the undisturbed fluid.
v	Tangential component of the incoming flow velocity.
v_i	Tangential induced velocity.
W	Relative velocity of the wind with respect to a blade element.
w_i	Radial induced velocity.
x	Dimensionless radial distance from the turbine axis of rotation. (= r/R).
x_h	Dimensionless hub radius. (= R_h/R).
x_0	Dimensionless radius of a helicl vortex filament. (= r_0/R).
z	Axial distance between the counter-rotating turbine rotors.
α	Angle of attack.
α_{opt}	Optimum angle of attack.
β	Twist angle.
β_i	Aerodynamic angle. (See equation 2.3.8).
β_{i0}	Pitch angle of a helical vortex filament. (See equation 2.3.6).
Γ	Bound circulation. (See equation 2.1.5).
δ	Yaw angle. Also load angle (used in chapter 5, equation 5.1.3).
ζ	Dimensionless deistance between the counter-rotating turbine rotors. (= z/R).
η_g	Generator efficiency.
η_t	Transmission efficiency.
θ	Parameter related to a true helical surface. (See equation 2.2.3).
λ	Tip speed ratio. (= $\Omega R/V_\infty$).
ρ	Air density.
ϕ	Variable used for facilitating the induced velocity calculation. See equation 2.2.9.
ϕ_0	Same as above, for a helical vortex filament.
ψ	Azimuthal angle.
Ω,ω	Rotational speed.
ω_e	Electrical rotational speed. (See equation 5.1.1).

CHAPTER 1.

INTRODUCTION.

CHAPTER 1. INTRODUCTION.

The beginning of wind power application lies in ancient times as mankind has been harnessing this power source since the early antiquity. The birthplace of windmills is believed to be the eastern part of the Mediterranean basin and China [1]. In the seventeenth century BC, Hammurabi, king of Babylon, is thought to have conceived a plan for irrigating the Messopotamia plain with the aid of wind energy. The windmills used at that time were vertical axis machines, similar to those whose ruins were found in the Iranian plateau. In Egypt, during the third century BC, Hero of Alexandria in a study dealing with pneumatics designed a horizontal axis wind machine which provided compressed air to an organ [1]. In ancient China, only vertical axis windmills were used, with sails operating like swinging blades.

Windmills first appeared in Europe during the Middle Ages, in countries like Italy, Greece, France, Spain and Portugal. They were later introduced in Germany, Britain and Holland. The machines used in Europe were horizontal axis ones, with (usually) four blades. Their main use was to grind wheat (hence the name "windmill"), but they were also used for other purposes such as to extract oil from nuts and grains, to saw wood, to convert old rags into paper, to prepare coloured powder for use in dyes and others [1]. The sophistication of windmill design increased as time went by. Innovative breakthroughs such as the fan tail that allowed the rotor to turn itself towards the wind automatically and shuttered sails with slats arranged to open and close according to the wind strength providing self-regulation of the machine, improved windmill performance and eased the miller's job [2]. During the 19th century, another type of windmill appeared in the USA: The multibladed, slow running one used for water pumping in

farms known as the"American windmill". This machine was so popular in the USA that it became a regular feature of the rural landscape.

By the beginning of the 20th century, the first modern fast running wind turbines used for electricity production made their appearance. Small wind turbines (with rotor diameters around 2 to 3 m) appeared first, such as Jacobs, Windcharger and Electro. They were driving DC generators for charging batteries and providing electricity to radio sets and other home appliances in places which were not connected to the grid [3]. During the 20's, 30's and early 40's, a great deal of research was carried out in many countries (such as France, Germany, the USSR and the USA) for developing large scale wind turbines. The foundations of the modern wind turbine lay on that work [4]. Wind turbine design and performance prediction theories were developed following the advances in propeller design and aircraft wing analysis. Many design ideas and engineering breakthroughs were conceived during that period. Some of them are: Rigid propeller-like blades for improving aerodynamic efficiency, coning of the rotor blades for reducing stresses, pitch and yaw power regulation for more uniform operation under gusty conditions, inclination of the axis of rotation for reducing the bending moments exerted on the tower. The outcome of the above mentioned research was the design and construction of some remarkable wind turbines such as the 20m diameter Darrieus turbine erected in France in 1929, the 30m diameter Balaklava turbine (USSR) erected in 1931 with a rated output of 130 kW and the 53m diameter Smith-Putnam turbine erected in the USA in 1941. Its rated power was 1.25 MW and until 1975 it was the biggest turbine ever built. It was operational until 1945, when a blade failed. The machine was then abandoned as its repair and operation were unprofitable due to the low price of petrol [4]. The example of the Smith-Putnam machine is typical of the fate of all early wind turbines. Wind power was not considered to be cost-effective and reliable when

compared with other means of power generation (fossil fuel and nuclear power).

However during the 70's the wind power industry was reborn. The renewed interest in wind energy had several reasons: The oil crisis which caused petrol prices to soar has urged the governments of many countries to look for alternative sources of power. Also, as environmental issues started to prevail, more consideration was given to pollution-free sources of energy. Within that context, wind energy was seen as a clean energy source that could be implemented alongside the existing conventional sources as well as other renewables (solar, wave power, OTEC etc). Its role would be to supplement the existing power sources (not to replace them) and thus assist in saving valuable fossil fuel and reduce harmful emissions of pollutants. Wind power could also provide electricity to remote areas where connection to the grid is difficult and as it does not necessarily involve the use of advanced technology, it could be of great value to developing countries. Since the early 70's, governments of many countries have started funding wind energy research projects and subsidised companies who produced wind turbines and utilities that used them, in order to stimulate the market. A considerable number of companies included wind turbines in their range of products and new wind turbine manufacturers appeared.

Research in wind energy helped to improve wind turbine design and construction. During the last twenty years, many advances in the field of wind energy have taken place. Better knowledge of wind turbine aerodynamics, use of computers and new manufacturing techniques have made possible the design of more advanced turbines with near-optimum blade shapes. Lightweight materials such as plastics, composites and aluminium alloys were used for the blade construction leading to lighter and cheaper blades. Specially designed aerofoils, suitable to operate within the wind turbines' Reynolds number regime improved the turbines' efficiency. Computerised control and

monitoring of wind power plants enabled better overall performance to be obtained. Advances in power electronics made possible the use of synchronous generators and variable rpm operation of turbines replacing induction generators (that have lower efficiency) used in the traditional constant rpm mode. Variable rpm operation has the advantage of enabling the turbine to operate at its design point for a large range of wind speeds, although its cost-effectiveness is yet to be proved. Finally, the more expensive "hard" steel towers were replaced by "soft" concrete ones, further reducing the turbines' cost. During the 70's and 80's, the state of the art wind turbine was a 3-bladed stall regulated one operating at constant rpm. Nowadays, 2-bladed, pitch controlled, variable rpm ones tend to dominate. The turbines' rated electrical power has also moved from the kW to the MW range [5].

However, despite all the above mentioned improvements, wind power has not yet fulfilled its potential. Only a very small amount of the worldwide power demand is provided by wind turbines. This is due to the fact that wind power is still more expensive than other conventional energy sources (such as coal and gas). As mentioned in [6], although the price of wind turbines per kW of generated power has decreased from 1500 ECU/kW in 1982 to 800 ECU/kW in 1991 it cannot yet compete economically with other power sources. Therefore, further research is necessary for improving wind turbines' economics. This could be achieved in two ways: One is to develop new concepts of wind power generation, the other being to improve already existing designs.

The work to be presented in this thesis deals with both the above mentioned aspects. In part A of the thesis, a procedure is developed for the design of wind turbines to operate in modified axial flows, which contain swirl velocities and non-uniform distributions. This procedure is used in part B of the thesis, for the development

of a novel wind power machine. It is the delta wing-turbine system, that utilises a slender delta wing as a wind augmentor for increasing the wind power available to its two turbines, thus improving their performance. Part C of the thesis is about improving the blade design of an already operating counter-rotating wind turbine, formerly called Trimble mill. This wind power system has two coaxial, counter-rotating rotors, used for alleviating the need of gearboxes. It is hoped that the work to be presented will contribute towards making wind power a viable option.

PART A.

LIFTING LINE DESIGN OF TURBINE BLADES.

CHAPTER 2.

LIFTING LINE THEORY AND ITS APPLICATION TO WIND TURBINE DESIGN.

CHAPTER 2. LIFTING LINE THEORY AND ITS APPLICATION TO WIND TURBINE DESIGN.

2.0. INTRODUCTION.

In this chapter, a procedure for designing wind turbine blades is presented. This procedure is suitable for turbines operating in any kind of non-uniform, non-axial but axi-symmetric flow. It has been used for the design of the turbine blades of the delta wing-turbine system and also for designing the blades of the counter-rotating turbine rotors. With appropriate modifications, this procedure can be used for predicting the performance of a turbine, as will be explained in chapter 4.

2.1. PRINCIPLES OF THE DESIGN PROCEDURE.

The objective of a designer of a wind turbine is to estimate the optimum values of chord (c) and twist angle (β) of the turbine blades as functions of the radius (r) from the axis of rotation (see figure 2.1). For this purpose, two major theories have been developed. They are described in the following paragraphs.

2.1.1. Momentum theory.

The most widely used method for designing conventional wind turbines is based on momentum theory. This theory was founded by Betz [7] and Glauert [8]. Here only a brief account of this theory is given. A more detailed description of the theory is given by Lysen [9], Milne-Tomson [10] and Devries [11]. In momentum theory, the turbine is assumed to operate at a constant rotational speed (Ω). The incoming flow is

assumed to be axial and uniform far upstream of the turbine disc, with velocity V_∞. Downstream of the turbine and in its vicinity, the flow is not uniform and due to the pressure increase ahead of the turbine, the fluid velocity drops.

Two non-dimensional induction factors are introduced to express the turbine interference: a is the axial induction factor given from $V=V_\infty(1-a)$. a' is the tangential induction factor given from $\omega = \Omega(1-a')$. V and ω are the axial and rotational velocities (respectively) at an arbitrary point P of the turbine disc. The values of the local velocities at P are not constant in time, but oscillate as the blades of the rotating turbine approach and leave that point. The fluid becomes steady if an "actuator disc" is assumed with an infinite number of blades with infinitesimal chord, rather than a turbine with finite number of blades. With this assumption, the induction factors become independent of time and of the azimuthal position of point P on the rotor disc. They only depend on the radius r from the axis. For this reason, the fluid is divided into tubes (as shown in figure 2.2), each at a certain radius r on the rotor disc and with infinitesimal thickness dr. Each tube contains fluid streamlines and the tube expansion close to the rotor disc is a result of the air velocity reduction there. From the change of the fluid momentum and angular momentum as it interacts with the turbine and applying the fluid mass conservation law, expressions for the thrust (dT), power (dP) and torque (dQ) exerted on the turbine can be obtained for each one of the tubes. These expressions are exact only in the case of an "actuator disc", when steady flow is a reality. For a turbine with a finite number of blades, correction factors can be devised in order to improve the model accuracy. (More details about such correction factors will be given in chapter 3, where the lifting line and momentum theories are compared).

From a criterion for maximizing the turbine power, a relation between a and a' can be obtained. Using this relation and with proper combination of the expressions for dP, dT and dQ, with those obtained from blade element considerations

(assuming 2-dimensional flow for each blade element) the values of $c(r)$ and $\beta(r)$ for maximum power output of the turbine at a certain operating condition set by the tip speed ratio, ($\lambda = \Omega R/V_\infty$) can be obtained.

This theory is successful in the case of an axial uniform incoming flow, but for a swirling flow with both axial and tangential incoming velocities varying radially as in the case of the delta wing-turbine system and also of the rear counter-rotating turbine rotor, the use of momentum theory becomes problematic. Such flows become oversimplified, when attempting to make them compatible with the momentum theory requirements. For the delta wing-turbine system, the vortex flow is continuously fed from the delta wing leading-edges, and hence, mass conservation of the flow cannot be assumed. For the rear rotor of the counter-rotating turbine, the tangential component of the incoming wind velocity has to be neglected if momentum theory is to be used. Therefore, another approach is required for designing turbines to operate within such flows. This is described in the following section.

2.1.2. Lifting line theory.

This theory has been introduced by Prandtl [12], for the analysis of aeroplane wings. It has been extended for the design of propellers by Goldstein [13] and Theodorsen [14]. It has also been used for performance analysis of wind turbines (Politis [15], Afjeh [16]) and helicopter rotor blades (Miller [17]).

The main principles of the theory are:

a) Given that the aspect ratio of the turbine blade (or the aeroplane wing) is high, all the other characteristics of the blade, apart from its span (ie chord and thickness envelope) are neglected when the local flow on the blade is calculated. Therefore, each blade is substituted by a lifting line.

b) Potential vortices are superimposed on the lifting line, in order to create the circulation and hence the pressure difference (between the suction and pressure surfaces of the blade) responsible for the lift production. According to the Kutta-Joukovski condition, the lift per unit span produced on the blade is related to the circulation of the bound vortices (Γ) by:

$$L = \rho W \Gamma \tag{2.1.1}$$

where ρ is the fluid density and W is the local wind velocity in the vicinity of the blade.

c) At points along the span of the blade, the vortices turn through right angles and are shed in the fluid downstream of the blade, forming a semi-infinite vortex sheet. The trailing vorticity must always follow the direction of the local flow as it cannot sustain any load. A pressure difference between the two sides of the sheet, will force it to move towards the direction of equalising that difference. The vortex sheet for the case of an aeroplane wing is planar but for a turbine or a propeller, it forms a helix, due to the rotation of the blades (see figure 2.3). The strength of an element of the vortex sheet at a spanwise position r and with width dr is defined as:

$$\tilde{\Gamma} = \frac{d\Gamma}{dr} dr \tag{2.1.2}$$

where Γ is the circulation of the bound vortices at radius r. Usually, the strongest vortices occur at the blade tips, because at these regions the bound circulation slope is high, as the circulation drops rapidly to zero. These are the spanwise regions where trailing vortices appear in the case of aeroplane wings.

d) Both trailing and bound vorticity induce velocities on the flow, given by the Biot-Savart law:

$$d\vec{w}_i = \frac{\Gamma}{4\pi} \frac{d\vec{l} \times d\vec{S}}{S^3} \qquad (2.1.3)$$

dl represents an infinitesimal segment of a vortex filament and S is the distance between that segment and the point where dw_i is induced.

e) For a high aspect ratio blade, the radial induced velocity component remains negligible (apart from the blade tips) and 2-dimensional blade element formulae can be used to relate the lift and drag per unit span produced by the blade, to the local velocities and the blade geometrical characteristics:

$$L_t = \frac{1}{2} \rho W^2 C_L(\alpha) c(r)$$

$$D = \frac{1}{2} \rho W^2 C_D(\alpha) c(r) \qquad (2.1.4)$$

Combining the lift formula of (2.1.4) with equation (2.1.1), the following loading equation is obtained, that relates the bound circulation to the local flow geometry:

$$\Gamma = \frac{1}{2} W c(r) C_L(\alpha) \qquad (2.1.5)$$

f) Assuming a certain trailing vorticity pattern (as it will be explained later) and estimating the induced velocities along the blade, it is possible to solve equation (2.1.5) for Γ, with a given incoming flow distribution and blade configuration. This leads to performance analysis of turbines or propellers. On the other hand, design of optimum propellers is achieved by estimating the local flow for a certain circulation distribution and solving (2.1.5) for c(r). The $\beta(r)$ distribution can also be obtained from the local flow distribution when certain conditions are imposed.

It is evident that lifting line theory is more versatile than momentum theory

and having made less crude assumptions, it is also more realistic. Its main disadvantage is the complicated mathematics required for modelling the wake and for that reason it is used when momentum theory cannot produce accurate enough results (see [11]).

2.2. WAKE MODEL.

The trailing vorticity model chosen for the turbine design is that proposed by Lerbs in [18], for the analysis of non-optimum propellers. It is an expansion of the ideas of Goldstein [13] and Theodorsen [14], who solved the problem of optimum propellers. In the case of optimum propellers, a uniquely defined distribution of the bound circulation exists, that maximizes the thrust-to-torque ratio of the propeller. The bound circulation distribution of a non-optimum propeller can take any arbitrary value and therefore the propeller performance analysis is possible for operating conditions other than the optimum.

Since there are only minor differences between propellers and turbines, the theory of [18] will be presented for the case of a propeller first, and then it will be modified for the case of a turbine.

2.2.1. Description of the wake model.

Propellers are divided into three categories according to their loading: Lightly, moderately and heavily loaded ones. In the first, the aerodynamic loading of the propeller blades is low, and as a result, the induced velocities are small compared to the undisturbed wind velocity (V_∞). Therefore, they can be neglected in the calculation of the aerodynamic angle distribution along the blades β_i (r). (See figure 2.3). The expression for β_i (r) in that case becomes:

$$\beta_i(r) = \tan^{-1}(V_\infty / \Omega r)$$

For the lightly loaded propellers, the $\beta_i(r)$ does not depend on the induced velocities. Hence, the shape of the trailing vortex helices is known beforehand.

For moderately loaded propellers, the loading is high enough to produce induced velocities comparable to V_∞. As a result, $\beta_i(r)$ depends upon the induced velocities:

$$\beta_i(r) = \tan^{-1}\left(\frac{V_\infty + u_i}{\Omega r - v_i}\right)$$

In the above formula, u_i and v_i are the axial and tangential induced velocities respectively. However, the induced velocities are not high enough to produce an appreciable wake contraction. This is taken into account in the case of heavily loaded propellers, where the induced velocities are of similar magnitude as V_∞. (Used for the analysis of ship propellers when towing).

From our point of view, the moderately loaded propeller category is quite adequate, as for a turbine to be designed the induced velocities are expected to be high enough not to be negligible in the $\beta_i(r)$ calculation and on the other hand, the case where they become of similar magnitude with V_∞ is uninteresting to us, as the power produced by the turbine will become too small due to the vast reduction of the incoming flow velocity. For that reason, the wake model proposed by Lerbs was used. The basic assumptions of this model are:

a) The trailing vortex filaments shed from each blade element form helices with a pitch angle that coincides with the local relative velocity direction (ie the aerodynamic angle).

b) The wake contraction downstream of the propeller is neglected.

c) The vortex filaments retain their shape downstream of the propeller.

This last does not happen in reality, as the helices, once shed from the blades start to depart from their original shape, due to mutual induction of velocities on each other. They tend to group together around the strongest vortex filaments, as explained by Batchelor in [19] for the case of an aeroplane wing. If the axial incoming velocity is large, the vortex sheet goes away from the blades fast enough, so that wake deformation occurs several span lengths downstream from the blade and it does not affect the flow on the blade significantly, as from Biot-Savart law, (equation 2.1.3), $dw_i \sim S^{-2}$. In cases when the incoming velocity is small, such as wind turbines operating in low wind speeds [16], or hovering helicopter blades (where the incoming velocity is equal to u_i, [17]), deformation must be taken into account.

With these assumptions, the problem of a non-optimum moderately loaded propeller can be solved.

2.2.2. Deduction of equations for the induced velocities.

The mathematical formulation of the problem was presented by Lerbs in [18]. Here, the equations of [18] are reproduced with modifications and explanatory comments made where necessary.

Let us consider an infinite vortex filament of helical shape, at a distance r_0 from a cylindrical frame of reference and a point P with coordinates (r,ψ,z). (See figure 2.4). The vortex filament has a circulation $\bar{\Gamma}$ and induces velocities on P. In the following, the potential function of the vortex filament induced velocity field is estimated and expressions for the induced velocities are obtained. Then, these expressions are modified for the case of a semi-infinite vortex filament that simulates a part of the

trailing vortex sheet. Finally, by integrating over the entire blade span and also by taking into account the contributions of all the other trailing vortex sheets (springing from the other blades), the expressions for the induced flow of the entire wake are obtained.

The vortex filament of figure 2.4, with radius r_0 and pitch angle β_{i0} produces a 2-dimensional flow field. In order to express this property of the flow field, the concept of a "true helical surface" must be introduced. Let us assume a straight line which is normal to the z axis of figure 2.4, and which also intersects that axis. A true helical surface is generated by this line when the line rotates about the z axis with constant rotational speed and at the same tame translates along the z axis with constant velocity. The pitch of a true helical surface is defined as the length on the z axis covered during one revolution by the line generating the helical surface. The true helical surface that contains the vortex filament of figure 2.4 (ie that with radius r_0 and pitch angle β_{i0}) has a pitch equal to $2\pi K_0$. K_0 is defined as:

$$K_0 = r_0 \tan \beta_{i0} \tag{2.2.1}$$

As shown in figure 2.4,

$$\tan \beta_{i0} = dz/ds \qquad \text{and} \qquad d\psi = ds/r_0$$

Hence:

$$K_0 = r_0 \tan \beta_{i0} = r_0\, dz/ds \Rightarrow K_0 = dz/d\psi \tag{2.2.2}$$

Therefore, K_0 has the same value for all true helical surfaces with the same pitch.

Since the vortex filament of figure 2.4 is an infinite one, all points with radius r lying on a true helical surface with pitch equal to that of the helical surface that contains the filament (ie $2\pi K_0$) will experience the same flow. In order to distinguish between different helical surfaces (all having the same pitch), the following variable is introduced:

$$\theta = \psi - z/K_0 \tag{2.2.3}$$

The value of θ is constant on any true helical surface with pitch $2\pi K_0$. Indeed, a change

in θ is expressed as:

$$d\theta = \frac{\partial \theta}{\partial \psi} d\psi + \frac{\partial \theta}{\partial z} dz \Rightarrow d\theta = d\psi - \frac{dz}{K_0}$$

Substituting the value of K_0 (from equation 2.2.2.) into the above expression, we get:

$$d\theta = 0 \Rightarrow \theta = \text{constant}$$

However, different values of θ represent different helical surfaces. For example, helical surfaces with different θ intersect the plane $z = 0$ at different azimuthal positions as can be seen from equation 2.2.3. Therefore, the flow field of figure 2.4 depends only on r and θ.

For the case $\beta_{i0} = 90°$ (or $\theta=\psi$), it is easy to see that of the velocity components (in cylindrical coordinates), the axial and tangential are even functions of θ, while the radial is odd. Also, the flow field on a plane z=constant is periodic relative to θ, with period 2π. Assuming that these properties of θ are retained for every value of β_{i0} and z, it is possible to analyze the velocity field as a fourier series with respect to θ and with period 2π. The velocity potential must also be periodic and with the same period. Multiples of z and ψ can also occur in the velocity potential. To satisfy these conditions, we write for the potential ϕ:

$$\phi = G_0 + G_1\psi + G_2 z + G_3 f_0(r) + \sum_{n=1}^{\infty} f_n(r) \sin(n\theta)$$

From this series, we get the velocity components:

$$u_i = \frac{\partial \phi}{\partial z} = G_2 - \frac{1}{K_0} \sum_{n=1}^{\infty} n f_n(r) \cos(n\theta) \quad \text{(axial component)}$$

$$v_i = \frac{1}{r} \frac{\partial \phi}{\partial \psi} = \frac{1}{r} \left[G_1 + \sum_{n=1}^{\infty} n f_n(r) \cos(n\theta) \right] \quad \text{(tangential component)}$$

$$w_i = \frac{\partial \phi}{\partial r} = G_3 f_0'(r) + \sum_{n=1}^{\infty} f_n'(r) \sin(n\theta) \quad \text{(radial component)}$$

These expressions satisfy the above conditions, since u_i, v_i and w_i depend only on r and θ and furthermore, u_i and v_i are even functions of θ, while w_i is odd. The boundary conditions are:

$$u_i = v_i = w_i = 0 \text{ as } r \to \infty$$

$$\text{and } u_i = \frac{\bar{\Gamma}}{2\pi} \frac{1}{K_0} \text{ (from Biot - Savart law),}$$

$$v_i = \text{finite}, \quad w_i = 0 \text{ as } r = 0.$$

Stoke's law on a circle with radius r and with z constant gives:

$$\int_0^{2\pi} v_i \, r \, d\psi = \begin{cases} 0 \; ; \; r < r_0 \\ \bar{\Gamma} \; ; \; r > r_0 \end{cases}$$

The requirement that the flow divergence is zero anywhere in the field, applied on a circle with radius r and z constant gives:

$$r \int_0^{2\pi} w_i \, d\psi = 0$$

Thus constants G_0, G_1, G_2 and G_3 are found to be:

$$G_0 = \frac{\bar{\Gamma}}{2}, \; G_1 = \frac{\bar{\Gamma}}{2\pi}, \; G_2 = G_3 = 0 \quad \text{for} \quad r > r_0$$

$$G_0 = \frac{\bar{\Gamma}}{2}, \; G_1 = 0, \; G_2 = \frac{\bar{\Gamma}}{2\pi} \frac{1}{K_0}, \; G_3 = 0 \quad \text{for} \quad r < r_0$$

with G_0 arbitrarily chosen for convenience. It is evident that the flow is divided into two parts, the internal for $r<r_0$ and the external for $r>r_0$. The functions $f_n(r)$ are determined from Laplace's equation:

$$\nabla^2 \phi = 0 \Rightarrow \frac{\partial^2 \phi}{\partial r^2} + \frac{1}{r} \frac{\partial \phi}{\partial r} + \frac{1}{r^2} \frac{\partial^2 \phi}{\partial \psi^2} + \frac{\partial^2 \phi}{\partial z^2} = 0$$

Substituting the value of ϕ in the above, we get:

$$\frac{d^2 f_n}{d r^2} + \frac{1}{r} \frac{d f_n}{d r} - n^2 \left(\frac{1}{r^2} + \frac{1}{K_0^2} \right) f_n = 0$$

Substituting $t = nr/K_0$, we get the Bessel's modified equation:

$$\frac{d^2 f_n}{d t^2} + \frac{1}{t}\frac{d f_n}{d t} - \left(\frac{n^2}{t^2} + 1\right) f_n = 0$$

The general solution is:

$$f_n(r) = a_n I_n\left(\frac{n}{K_0} r\right) + b_n K_n\left(\frac{n}{K_0} r\right)$$

with n an integer and $I_n(x)$ the modified Bessel function of the first kind and order n, given by:

$$I_n(x) = (i)^n J_n(ix) \qquad \text{with}$$

$$J_n(ix) = \sum_{r=0}^{\infty} (-1)^r \frac{(ix/2)^{n+2r}}{r!\,\Gamma(n + r + 1)}$$

The Gamma function $\Gamma(n)$ is defined as the integral:

$$\Gamma(n) = \int_0^{\infty} x^{n-1} e^{-x}\, dx$$

In the case n is an integer,

$$I_n(x) = I_{-n}(x) \qquad \text{and then } K_n(x) \text{ is defined as:}$$

$$K_n(x) = \lim_{p \to n} \frac{\pi}{2}\left[\frac{I_{-p}(x) - I_p(x)}{\sin(px)}\right]$$

The limiting values of I_n and K_n are:

$$I_n(x) = \text{finite}\ , \quad K_n(x) \to \infty \quad \text{as } x \to 0$$

$$I_n(x) \to \infty\ , \quad K_n(x) \to 0 \quad \text{as } x \to \infty$$

Therefore, in order to avoid singularities, $b_n = 0$ in the internal field and $a_n = 0$ in the external. The values of a_n and b_n are obtained from the condition that the potential and velocity field is continuous during the transition from the internal to the external field. That is at:

$$r = r_0, \quad \phi_i(r_0) = \phi_e(r_0) \qquad \text{and} \qquad \left.\frac{\partial \phi_i}{\partial r}\right|_{r_0} = \left.\frac{\partial \phi_e}{\partial r}\right|_{r_0}$$

with ϕ_i and ϕ_e the potential for the internal and external field respectively.

The values of a_n and b_n are found to be:

$$a_n = \frac{r_0}{K_0}\frac{\Gamma}{\pi} K_n'\left(\frac{n}{K_0} r_0\right),$$

$$b_n = \frac{r_0}{K_0}\frac{\Gamma}{\pi} I_n'\left(\frac{n}{K_0} r_0\right)$$

with I_n' and K_n' the derivatives of I_n and K_n respectively, for the argument (nr_0/K_0). Having estimated the values of f_n and a_n, b_n, the potential function for the internal and external field becomes:

$$\phi_i = \frac{\Gamma}{2} + \frac{\Gamma}{2\pi}\left[\frac{z}{K_0} + 2\frac{r_0}{K_0}\sum_{n=1}^{\infty} I_n K_n' \sin\left\{ n\left(\psi - \frac{z}{K_0}\right)\right\}\right]$$

$$\phi_e = \frac{\Gamma}{2\pi}\left[\psi + \frac{2r_0}{K_0}\sum_{n=1}^{\infty} K_n I_n' \sin\left\{ n\left(\psi - \frac{z}{K_0}\right)\right\}\right]$$

Assuming B symmetrically spaced blades, the contributions of the helices on the other blades, with the same radius r_0, differ only in ψ with $\psi_p = (\psi - 2\pi)(p-1)/B$, $p = 1, \ldots, B$.

Summing the contribution of all B filaments, we get:

$$\phi_i = B\frac{\Gamma}{2} + B\frac{\Gamma}{2\pi}\left[\frac{z}{K_0} + \frac{2r_0}{K_0}\sum_{n=1}^{\infty}\sum_{p=1}^{B} I_n K_n' \sin\left\{ n\left(\theta - 2\pi\frac{p-1}{B}\right)\right\}\right]$$

$$\phi_e = \frac{\Gamma}{2\pi}\left[\sum_{p=1}^{B}\left(\psi - 2\pi\frac{p-1}{B}\right) + \frac{2r_0}{K_0}\sum_{n=1}^{\infty}\sum_{p=1}^{B} K_n I_n' \sin\left\{ n\left(\theta - 2\pi\frac{p-1}{B}\right)\right\}\right]$$

After laborious trigonometric manipulations on the double sums, the above expressions

can be reduced to:

$$\phi_i = B\frac{\bar{\Gamma}}{2} + B\frac{\bar{\Gamma}}{2\pi}\left[\frac{z}{K_0} + 2\frac{r_0}{K_0}\sum_{n=1}^{\infty} I_{Bn}\, K_{Bn}' \sin\left\{ nB\left(\psi - \frac{z}{K_0}\right)\right\}\right]$$

$$\phi_e = \frac{\bar{\Gamma}}{2\pi}\left[B\psi - 2\pi\sum_{p=1}^{B}\frac{p-1}{B} + 2B\frac{r_0}{K_0}\sum_{n=1}^{\infty} K_{Bn}\, I_{Bn}' \sin\left\{ nB\left(\psi - \frac{z}{K_0}\right)\right\}\right]$$

Here, Γ_{Bn} and K'_{Bn} are functions of (nBr_0/K_0).

Hence, only the multiples of B contribute to the potential function. For example, if B=3, only I_3, I_6, I_9, etc contribute to $\phi_{i\,e}$.

So far, the equations for the velocity potential have been obtained for the case of B infinite vortex filaments with radius r_0 and pitch angle β_{r0}, symmetrically spaced with respect to ψ. In the case of a propeller, the filaments simulating the trailing vorticity are semi-infinite. The fundamental difference between the flow produced by infinite and semi-infinite vortex filaments is that the former produce a 2-dimensional field, while the latter produce a 3-dimensional one. By Biot-Savart law considerations, it can be proved (see [18]), that with respect to the axial and tangential velocities, the front half of the helices induces the same amount of induced velocities as the rear half on the lifting lines and on the bisectors between them o_n_l_y. With respect to the radial component, the two halves induce velocities of the same magnitude and opposite signs. Therefore, by virtue of the above observation, the axial and tangential induced velocity components can be obtained on the lifting lines merely by dividing the velocities from the infinite filaments by 2. No information can be obtained for the radial component. However, as it has been assumed that the flow on the lifting lines is 2-dimensional, (derivation of the loading equation 2.1.5), knowledge of w_i is not necessary.

Taking the appropriate derivatives for ϕ_i and ϕ_e and dividing them by 2 we get for the flow on the lifting line with z=0, ψ=0:

The internal field is:

$$\bar{u}_{ii} = \frac{1}{2}\frac{\partial \phi_i}{\partial z} = \frac{B\bar{\Gamma}}{4\pi}\frac{1}{K_0}\left[1 - 2B\frac{r_0}{K_0}\sum_{n=1}^{\infty} n\, I_{Bn}\left(\frac{nBr}{K_0}\right) K_{Bn}'\left(\frac{nBr_0}{K_0}\right)\right]$$

$$\bar{v}_{ii} = \frac{1}{2r}\frac{\partial \phi_i}{\partial \psi} = \frac{1}{r}\frac{B^2\bar{\Gamma}\, r_0}{2\pi K_0}\sum_{n=1}^{\infty} n\, I_{Bn}\left(\frac{nBr}{K_0}\right) K_{Bn}'\left(\frac{nBr_0}{K_0}\right)$$

The external field is: (2.2.4)

$$\bar{u}_{ie} = -\frac{B^2\bar{\Gamma}}{2\pi}\frac{r_0}{K_0}\sum_{n=1}^{\infty} n\, K_{Bn}\left(\frac{nBr}{K_0}\right) I_{Bn}'\left(\frac{nBr_0}{K_0}\right)$$

$$\bar{v}_{ie} = \frac{1}{r}\frac{B\bar{\Gamma}}{4\pi}\left[1 + 2B\frac{r_0}{K_0}\sum_{n=1}^{\infty} n\, K_{Bn}\left(\frac{nBr}{K_0}\right) I_{Bn}'\left(\frac{nBr_0}{K_0}\right)\right]$$

For the numerical solution of the problem, the Bessel functions and their derivatives are replaced by Nicholson's asymptotic expansions [20]. They are:

$$I_n(ny) = \left(\frac{1}{2\pi n\sqrt{1+y^2}}\right)^{0.5} e^{nY}$$

$$K_n(ny) = \left(\frac{\pi}{2n\sqrt{1+y^2}}\right)^{0.5} e^{-nY}$$

$$Y = \sqrt{1+y^2} - \frac{1}{2}\ln\left(\frac{\sqrt{1+y^2}+1}{\sqrt{1+y^2}-1}\right)$$

In our case, n=Bn, $y=r/K_0$ for I, K and $y=r_0/K_0$ for I', K'. With these approximations, the sums in the expressions for the induced velocity components can be calculated and give the following results:

$$\bar{u}_{ii} = \frac{1}{K_0}\frac{B\bar{\Gamma}}{4\pi}(1 + B_2) \quad , \quad \bar{u}_{ie} = -\frac{1}{K_0}\frac{B\bar{\Gamma}}{4\pi}B_1$$

$$\bar{v}_{ii} = -\frac{1}{r}\frac{B\bar{\Gamma}}{4\pi}B_2 \quad , \quad \bar{v}_{ie} = \frac{1}{r}\frac{B\bar{\Gamma}}{4\pi}(1 + B_1) \qquad (2.2.5)$$

with

$$B_{1,2} = \left(\frac{1 + y_0^2}{1 + y^2}\right)^{0.25}\left[\frac{1}{e^{BA_{1,2}} - 1} \mp \frac{1}{2B}\frac{y_0^2}{(1 + y_0^2)^{1.5}}\ln\left(1 + \frac{1}{e^{BA_{1,2}} - 1}\right)\right]$$

$$A_{1,2} = \pm\left(\sqrt{1 + y^2} - \sqrt{1 + y_0^2}\right) \mp \frac{1}{2}\ln\left\{\frac{\left(\sqrt{1 + y_0^2} - 1\right)\left(\sqrt{1 + y^2} + 1\right)}{\left(\sqrt{1 + y_0^2} + 1\right)\left(\sqrt{1 + y^2} - 1\right)}\right\} \qquad (2.2.6)$$

$$y_0 = \frac{r_0}{K_0} = \frac{1}{\tan\beta_{i0}} \quad , \quad y = \frac{r}{K_0} = \frac{x}{x_0\tan\beta_{i0}} \quad , \quad x = \frac{r}{R} \quad , \quad x_0 = \frac{r_0}{R}$$

and R the propeller radius.

According to the exact location within the field, (internal or external), one of the factors B_1, B_2 becomes indeterminate. Each time, one must calculate only that part of $B_{1,2}$ that corresponds to the appropriate part of the field.

The above expressions for the induced velocities (equations 2.2.5) become infinite when $r \to r_0$. To avoid that difficulty, two induction factors are introduced:

$$i_a = \frac{\bar{u}_i}{\bar{\Gamma}/\{4\pi\,(r - r_0)\}} \quad , \quad i_t = \frac{\bar{v}_i}{\bar{\Gamma}/\{4\pi\,(r - r_0)\}}$$

Therein, $\Gamma/\{4\pi(r-r_0)\}$ is the velocity induced at r by a straight semi-infinite vortex filament situated at r_0. As both numerator and denominator in the above expressions for $i_{a,t}$ tend to infinity at the same rate when $r \to r_0$, the values of $i_{a,t}$ remain finite.

Substituting equations 2.2.5 in the expressions for $i_{a,t}$ we get:

$$i_{ai} = \frac{Bx}{x_0 \tan\beta_{i0}} \left(\frac{x_0}{x} - 1\right)(1 + B_2)$$

$$i_{ae} = -\frac{Bx}{x_0 \tan\beta_{i0}} \left(\frac{x_0}{x} - 1\right)B_1$$

$$i_{ti} = B\left(\frac{x_0}{x} - 1\right)B_2 \qquad (2.2.7)$$

$$i_{te} = -B\left(\frac{x_0}{x} - 1\right)(1 + B_1)$$

The limiting values for $i_{a,t}$ are:

$$i_a \to \cos^2\beta_{i0}, \quad i_t \to \sin\beta_{i0} \quad \text{for} \quad x \to x_0 \quad (\text{or } r \to r_0).$$

The induction factors depend on the number of blades B, the ratio x_0/x and the pitch angle β_{i0} of the helix at r_0. The values of $i_{a,t}$ are plotted in figure 2.5 for B=3. It is evident that i_t increases with β_{i0} increasing (with B and x_0/x being constant). The behaviour of i_a is the opposite. It decreases with β_{i0} increasing. This can be explained qualitatively if the helical vortices are replaced with straight ones. Then, as shown in figure 2.6, when β_{i0} = 90°, the induced velocity becomes tangential, while when β_{i0} = 0°, it becomes axial.

So far, formulae have been derived for the axial and tangential velocity components induced at a point P of the lifting line with z=0, ψ=0, by the B semi-infinite helical vortex filaments with radius r_0 and pitch angle β_{i0}. To find the total values of u_i, v_i, one must sum the contributions of all the trailing vortex filaments from R_h to R. (R_h is the hub radius). This can be achieved by integrating equations 2.2.5 from R_h to R, with respect to r_0 and using equations 2.2.7. For the tangential velocity, we get:

$$\frac{v_i}{V_\infty} = \frac{1}{2}\int_{x_h}^{1} \frac{dG}{dx_0} \frac{1}{x - x_0} i_t \, dx_0$$

with x = r/R and G the non-dimensional bound circulation:

$$G = \frac{\Gamma}{2\pi R V_\infty} \qquad (2.2.8)$$

The formula for v_i / V_∞ is similar to that for the downwash of a finite aeroplane wing. The only difference is that in our case the curvature of the trailing vortex filaments has been allowed for by introducing $i_{a,t}$. For a finite wing, $i_a = 0$, $i_t = 1$. (See figure 2.3).

The above integral can be calculated by slightly modifying the theory used by Glauert in [8]. For this purpose, a new variable, ϕ (not to be confused with the symbol used for the potential function) is introduced:

$$x = \tfrac{1}{2}(1+x_h) - \tfrac{1}{2}(1-x_h)\cos\phi \qquad (2.2.9)$$

When $x = x_h$, $\phi = 0$, when $x = 1$, $\phi = \pi$.

At the tip and hub of the blade, the pressure difference between the pressure and suction sides of the blade aerofoil is equalised. Hence, the circulation becomes zero at the tip and hub. Since this change of G is continuous, it can be analysed in a fourier sine series with respect to ϕ:

$$G(\phi) = \sum_{m=1}^{\infty} G_m \sin(m\phi) \qquad (2.2.10)$$

The induction factors depend on both x and x_0. They can be expressed as a cosine fourier series:

$$i_{a,t}(\phi, \phi_0) = \sum_{n=0}^{\infty} L_n^{a,t}(\phi) \cos(n\phi_0) \qquad (2.2.11)$$

In the above formula, ϕ_0 is given by (2.2.9), with x replaced by x_0.

With use of (2.2.10) and (2.2.11), it can be shown that:

$$\frac{v_i}{V_\infty} = \frac{1}{1 - x_h} \sum_{m=1}^{\infty} m\, G_m\, h^t_m(\phi)$$

with

$$h^t_m(\phi) = \int_0^\pi \frac{i_t(\phi\,,\,\phi_0)\,\cos(m\phi_0)}{\cos\phi_0 - \cos\phi}\, d\phi_0$$

$$= \frac{1}{2} \sum_{n=0}^{\infty} I^t_n(\phi) \left[\int_0^\pi \frac{\cos(m+n)\phi_0}{\cos\phi_0 - \cos\phi}\, d\phi_0 + \int_0^\pi \frac{\cos(m-n)\phi_0}{\cos\phi_0 - \cos\phi}\, d\phi_0 \right]$$

It is evident from the above formulae, that the integral representing the induced velocities can be reduced to the sum of two integrals of the same type as those known from Glauert [8]:

$$\int_0^\pi \frac{\cos\mu\phi_0}{\cos\phi_0 - \cos\phi}\, d\phi_0 = \pi\, \frac{\sin\mu\phi}{\sin\phi}$$

Using the above formula, we get for the integrals within $h^t_m(\phi)$:

$$\text{if } m > n \;:\; \frac{\pi}{\sin\phi} \sin(m\phi) \sum_{n=0}^{m} I^t_n(\phi)\, \cos(n\phi)$$

$$\text{if } m < n \;:\; \frac{\pi}{\sin\phi} \cos(m\phi) \sum_{n=m+1}^{\infty} I^t_n(\phi)\, \sin(n\phi)$$

The same apply for u_i / V_∞ and finally we get:

$$\frac{u_i}{V_\infty} = \frac{1}{1 - x_h} \sum_{m=1}^{\infty} m\, G_m\, h^a_m(\phi) \qquad (2.2.12)$$

$$\frac{v_i}{V_\infty} = \frac{1}{1 - x_h} \sum_{m=1}^{\infty} m\, G_m\, h^t_m(\phi)$$

with

$$h^{a,t}_m(\phi) = \frac{\pi}{\sin\phi}\left[\sin(m\phi)\sum_{n=0}^{m} I^{a,t}_n(\phi)\cos(n\phi) + \cos(m\phi)\sum_{n=m+1}^{\infty} I^{a,t}_n(\phi)\sin(n\phi)\right] \quad (2.2.13)$$

At the end points, $\phi = 0°$ and $\phi = 180°$, $h^{a,t}_m(\phi)$ become indefinite. From L'Hospital's law, we get:

$$h^{a,t}_m(0) = \pi\left[m\sum_{n=0}^{m} I^{a,t}_n(0) + \sum_{n=m+1}^{\infty} n\, I^{a,t}_n(0)\right]$$

$$h^{a,t}_m(180°) = -\pi\cos(m\,180°)\left[m\sum_{n=0}^{m} I^{a,t}_n\cos(n\,180°) + \sum_{n=m+1}^{\infty} n\, I^{a,t}_n\cos(n\,180°)\right] \quad (2.2.14)$$

Lerbs concluded in [18], that equations 2.2.10 to 2.2.14 provide a system for analysing propellers with an arbitrary bound circulation distribution. By these equations, calculation of the induced velocities produced by any distribution of G (satisfying the boundary conditions) and wake geometry (ie β_{i0} distribution) is possible. However, in order to satisfy the condition that the vortex sheets and the streamlines in the wake coincide as they leave the lifting lines (ie the aerodynamic angle β_i coincides with the pitch angle β_{i0} when $r = r_0$), successive approximations are necessary as the induction factors (and hence the induced velocities) depend upon the direction of the sheets. The bound circulation also depends on the induced velocities (in case G is unknown) and since G, u_i, and v_i are inter-related in a non-linear way, the design problem can only be solved iteratively.

2.2.3. Modifications for estimating the induced velocities on the bisectors.

For the design of the delta wing system turbine, knowledge of the flow on the lifting lines is quite adequate. However, for designing the counter-rotating turbine, the

induced velocities on the bisectors between lifting lines must also be known. For that reason, the equations of [18], (also presented above), have been modified.

The points lying on the bisector between the lifting lines with $\psi_0 = 0$ and $\psi_1 = 2\pi/B$ have coordinates: (r, z = 0, $\psi = (\psi_0+\psi_1)/2 = \pi/B$). In order to estimate the velocities induced by B vortex filaments with radius r_0 and pitch angle β_{i0} on that bisector, the appropriate derivatives of the velocity potential must be taken. Since the velocity potential functions are exactly the same as before, the same procedure is followed, as that for obtaining equations 2.2.4. However, in this case, $\psi=\pi/B$ and the term sin[$nB(\psi - z/K_0)$] appearing at the velocity potential expressions becomes after derivation equal to $\cos(n\pi)$ which is equal to $(-1)^n$. Hence the induced velocities on the bisector with $\psi = \pi/B$ are for the internal field:

$$\bar{u}_{ii} = \frac{1}{2}\frac{\partial \phi_i}{\partial z} = \frac{B\bar{\Gamma}}{4\pi}\frac{1}{K_0}\left[\, 1 - 2B\,\frac{r_0}{K_0}\sum_{n=1}^{\infty}(-1)^n\, n\, I_{Bn}\left(\frac{nBr}{K_0}\right) K_{Bn}'\left(\frac{nBr_0}{K_0}\right)\right]$$

$$\bar{v}_{ii} = \frac{1}{2r}\frac{\partial \phi_i}{\partial \psi} = \frac{1}{r}\,\frac{B^2\,\bar{\Gamma}\,r_0}{2\pi\,K_0}\sum_{n=1}^{\infty}(-1)^n\, n\, I_{Bn}\left(\frac{nBr}{K_0}\right) K_{Bn}'\left(\frac{nBr_0}{K_0}\right) \qquad (2.2.15)$$

For the external field:

$$\bar{u}_{ie} = -\,\frac{B^2\,\bar{\Gamma}}{2\pi}\,\frac{r_0}{K_0}\sum_{n=1}^{\infty}(-1)^n\, n\, K_{Bn}\left(\frac{nBr}{K_0}\right) I_{Bn}'\left(\frac{nBr_0}{K_0}\right)$$

$$\bar{v}_{ie} = \frac{1}{r}\,\frac{B\bar{\Gamma}}{4\pi}\left[1 + 2B\,\frac{r_0}{K_0}\sum_{n=1}^{\infty}(-1)^n\, n\, K_{Bn}\left(\frac{nBr}{K_0}\right) I_{Bn}'\left(\frac{nBr_0}{K_0}\right)\right]$$

Equations 2.2.4 and 2.2.15 differ only by the $(-1)^n$ factor, as explained above. The sums in the above equations can be calculated by laborious manipulations. This was already done for the flow on the lifting lines (equation 2.2.5) and the laborious work can be avoided. Comparing equations 2.2.4. and 2.2.5 we get for the sums appearing in (2.2.4):

$$\sum_{n=1}^{\infty} n\, I_{Bn}\, K_{Bn}' = \frac{K_0}{2Br_0} B_2$$

$$\sum_{n=1}^{\infty} n\, K_{Bn}\, I_{Bn}' = \frac{K_0}{2Br_0} B_1 \qquad (2.2.16)$$

The following relations are obvious:

$$\sum_{n=1}^{\infty} n\, I_{Bn}\, K_{Bn}' = \sum_{n=1,3,5} n\, I_{Bn}\, K_{Bn}' + \sum_{n=2,4,6} n\, I_{Bn}\, K_{Bn}'$$

$$\sum_{n=1}^{\infty} (-1)^n n\, I_{Bn}\, K_{Bn}' = -\sum_{n=1,3,5} n\, I_{Bn}\, K_{Bn}' + \sum_{n=2,4,6} n\, I_{Bn}\, K_{Bn}'$$

Combining the above, we get:

$$\sum_{n=1}^{\infty} (-1)^n n\, I_{Bn}\, K_{Bn}' = 2\sum_{n=2,4,6} n\, I_{Bn}\, K_{Bn}' - \sum_{n=1}^{\infty} n\, I_{Bn}\, K_{Bn}'$$

Changing n to l = n/2, at the first sum of the right hand side we get:

$$\sum_{n=1}^{\infty} (-1)^n n\, I_{Bn}\, K_{Bn}' = 2\sum_{l=1}^{\infty} 2l\, I_{B2l}\, K_{B2l}' - \sum_{n=1}^{\infty} n\, I_{Bn}\, K_{Bn}'$$

However, the Bessel functions of order B(2l) and (2B)l are exactly the same, hence we can write (substituting l by n):

$$\sum_{n=1}^{\infty} (-1)^n n\, I_{Bn}\, K_{Bn}' = 4\sum_{n=1}^{\infty} n\, I_{(2B)n}\, K_{(2B)n}' - \sum_{n=1}^{\infty} n\, I_{Bn}\, K_{Bn}' \qquad (2.2.17)$$

Thus, the sums of (2.2.17) can be calculated. For example, $\Sigma\, n\, K_{(2B)n}\, I'_{(2B)n}$ is equal to $(K_0 B_1')/(4Br_0)$. This was obtained using (2.2.16). The value of B_1' can be calculated from equations 2.2.6 changing B to 2B wherever it appears.

Finally, the values of the induced velocities can be calculated substituting equations 2.2.17 into equations 2.2.15:

$$\bar{u}_{ii}' = \frac{1}{K_0}\frac{B\bar{\Gamma}}{4\pi}(1 - B_2 + 2B_2')$$

$$\bar{v}_{ii}' = \frac{1}{r}\frac{B\bar{\Gamma}}{4\pi}(B_2 - 2B_2')$$

$$\bar{u}_{ie}' = -\frac{1}{K_0}\frac{B\bar{\Gamma}}{4\pi}(2B_1' - B_1) \qquad (2.2.18)$$

$$\bar{v}_{ie}' = \frac{1}{r}\frac{B\bar{\Gamma}}{4\pi}(1 + 2B_1' - B_1)$$

The induction factors for the bisectors can be calculated from (2.2.18) in the same way as for the lifting lines. They are:

$$i_{ai}' = \frac{Bx}{x_0 \tan\beta_{i0}}\left(\frac{x_0}{x} - 1\right)(1 - B_2 + B_2')$$

$$i_{ii}' = -B\left(\frac{x_0}{x} - 1\right)(B_2 - 2B_2')$$

$$i_{ae}' = -\frac{Bx}{x_0 \tan\beta_{i0}}\left(\frac{x_0}{x} - 1\right)(2B_1' - B_1) \qquad (2.2.19)$$

$$i_{te}' = -B\left(\frac{x_0}{x} - 1\right)(1 + 2B_1' - B_1)$$

The limiting values of the induction factors for the bisectors are:

$$i_a' \to 0 \text{ and } i_t' \to 0 \text{ for } x \to x_0$$

The rest of the procedure for calculating the flow on the bisectors is exactly the same as that for the lifting lines, apart from the fact that in this case, the solutions for u_i and v_i do not have to be successively approximated, since the bound circulation is prescribed (it is that of the lifting lines).

2.2.4. Modifications for a wind turbine.

The transformation of equations 2.2.10 to 2.2.14 to fit the case of a turbine

is straightforward. Figure 2.3 shows that the induced velocities in the case of a wind turbine are opposite in sign to those of a propeller. The same applies to the bound and trailing vortex sheet circulation. The physical meaning of these differences is that in the case of a turbine, the pressure side of the blade aerofoil faces the incoming flow, while for a propeller, it is the suction side of the aerofoil that faces the incoming flow. In the vicinity of the turbine blade, an increase in pressure occurs just ahead of it. The induced velocity u_i is opposite in direction to V_∞, so that the total axial velocity will be reduced to correspond to the pressure increase. (The local velocity components are shown in figure 2.8). The tangential induced velocity v_i has opposite direction to Ωr (tangential velocity of the turbine at r). This happens because a torque is exerted on the turbine by the wind. Equal torque, with opposite sign is exerted by the turbine on the air, making it rotate in the opposite direction downstream of the turbine. Since the air rotates with a relative velocity $-\Omega r$ for a frame of reference fixed on the turbine blade, the resultant tangential velocity for a blade element will be $-\Omega r - v_i$. The relative local velocity for a turbine is:

$$W = \{ (V_\infty - u_i)^2 + (\Omega r + v_i)^2 \}^{0.5} \qquad (2.2.20)$$

For a propeller, the axial velocity is enhanced due to the pressure drop just ahead of the propeller blades. Therefore, u_i is in the same direction as V_∞. The propeller experiences a decelerating torque by the wind and hence, v_i is in the same direction as Ωr. The resultant tangential velocity for a propeller is $-\Omega r + v_i$. The relative local velocity for a propeller is:

$$W = \{ (V_\infty + u_i)^2 + (\Omega r - v_i)^2 \}^{0.5} \qquad (2.2.21)$$

For transforming the equations for u_i and v_i to fit the case of a turbine, all that must be done is to change their signs. This can be achieved by leaving equations 2.2.12

unchanged and using equation 2.2.20 in the calculation of the bound circulation distribution instead of (2.2.21).

One step further is to fit this model to the case of a non-uniform, non-axial axi-symmetric flow. In such a flow the incoming wind velocity (to the turbine) has two components that vary radially: An axial one u(r) and a tangential one v(r). The situation on a blade element of a turbine operating in such a flow is shown in figure 2.8. Assuming that the turbine rotates in the same direction as the wind, (as is the case for both the delta wing system turbine and the rear rotor of the counter-rotating turbine), the relative tangential velocity is: $-\Omega r + v - v_i$. The relative local velocity is:

$$W = \{ (u - u_i)^2 + (\Omega r - v + v_i)^2 \}^{0.5} \qquad (2.2.22)$$

Hence, for the case of a turbine operating within a non-uniform, non-axial axi-symmetric flow, the bound circulation is calculated from (2.1.5) using (2.2.22) for the relative velocity distribution.

With this modification the wake model is complete and together with an appropriate loading equation based on equation 2.1.5, the turbine blade design problem can be solved. The procedure followed for this purpose is presented in the next section.

2.3. TURBINE BLADE DESIGN PROCEDURE.

Unlike the case of a propeller or a turbine designed using momentum theory, on the lifting line level there is not a clear optimisation criterion for a wind turbine design. This was reported in reference [15]. In the case of a propeller, the quantity to be optimised is the thrust-to-torque ratio (T/Q). A relation between axial and tangential velocities can be achieved considering the far wake characteristics (see for example

references [13] and [14]), which leads to an optimum bound circulation distribution. For a wind turbine however, it is the power that has to be maximised and this cannot determine the circulation or induced velocity distributions uniquely. The only optimisation possible is adjustment of the blade twist angle, at each blade element, so that the angle of attack will be equal to its optimum value throughout the blade. This condition gives the optimum lift-to-drag ratio for a given aerofoil and optimises the torque produced by the turbine in the sense that stall is avoided. Hence, the twist angle distribution is an unknown, as it changes with the local relative velocity changing. The above properties of β can be expressed by the formula (see also figure 2.8):

$$\beta(r) = \beta_i(r) - \alpha_{opt} \tag{2.3.1}$$

The equations obtained so far, are the loading equation (2.1.5), equations for the induced velocities, (2.2.12) and also (2.3.1). The blade chord cannot be related to the rest of the variables and hence, the number of unknown variables is more than the number of equations. This problem can be overcome, if the turbine is designed for a prescribed chord distribution. Various chord distributions must be tested, for various operating conditions. For each of them, the circulation and induced velocities can be estimated, as well as the twist angle distribution. For each case, the power coefficient is calculated from:

$$C_p = \frac{\text{Power produced by the turbine}}{\text{Power of the undisturbed flow}} \tag{2.3.2}$$

Both numerator and denominator of the above expression are calculated for the same area which is the area swept by the turbine blades. Comparisons between different

turbines are possible, since C_p is a measure of the turbine efficiency.

The loading equation for the dimensionless bound circulation is (substituting equ.2.2.8 into equ. 2.1.5):

$$G = \frac{1}{4\pi}\left(\frac{W}{V_\infty}\right) C_L(\alpha_{opt}) \frac{c(r)}{R} \qquad (2.3.3)$$

with $C_L(\alpha_{opt})$ the value of C_L for the optimum value of the angle of attack. C_L is the same along the blade, by virtue of (2.3.1). (W/V_∞) comes from dividing both terms of (2.2.22) by V_∞:

$$\frac{W}{V_\infty} = \left[\left(\frac{u}{V_\infty} - \frac{u_i}{V_\infty}\right)^2 + \left(\frac{\Omega r}{V_\infty} + \frac{v_i}{V_\infty} - \frac{v}{V_\infty}\right)^2 \right]^{0.5}$$

Substituting $\lambda = (\Omega R)/V_\infty$:

$$\frac{W}{V_\infty} = \left[\left(\frac{u}{V_\infty} - \frac{u_i}{V_\infty}\right)^2 + \left(\lambda x + \frac{v_i}{V_\infty} - \frac{v}{V_\infty}\right)^2 \right]^{0.5} \qquad (2.3.4)$$

It is evident from equations 2.3.3 and 2.2.12 that G and u_i, v_i are inter-related in a non-linear way. The problem can only be solved iteratively. The iteration steps are:

a) Definition of known parameters.

The known parameters are: Number of blades B, blade hub and tip radii R_h, R, tip speed ratio λ, aerofoil characteristics (ie α_{opt}, $C_L(\alpha_{opt})$, $C_D(\alpha_{opt})$), chord distribution c(r) and the initial values of the induced velocities which are taken as zero for the first iteration cycle.

b) Calculation of G.

The bound circulation G is calculated at an adequate number of radial stations along the blade using equation 2.3.3. From equation 2.2.9, the radii are defined as r = xR, as the

parameter to be equally spaced along the blade is ϕ.

c) Analysis of G in a fourier series.

The bound circulation G is analysed in a fourier series calculating the M first terms of the sum in equation 2.2.10:

$$G(\phi) = \sum_{m=1}^{M} G_m \sin(m\phi) \qquad (2.3.5)$$

d) Calculation of induction factors.

The induced velocities on a station ϕ on the blade are calculated summing the contributions of an adequate number of trailing vortex filaments with positions on the blade defined by ϕ_0. Therefore, for each ϕ and ϕ_0 the values of $i_{a,t}(\phi,\phi_0)$ are calculated from equations 2.2.7 using equations 2.2.6. First the aerodynamic angle β_{i0} (ie the value of β_i at ϕ_0) is calculated. It coincides with the pitch angle of the helical vortex filament at ϕ_0 and is given by:

$$\beta_{i0}(\phi_0) = \tan^{-1}\left(\frac{\frac{u}{V_\infty}(\phi_0) - \frac{u_i}{V_\infty}(\phi_0)}{\lambda x + \frac{v_i}{V_\infty}(\phi_0) - \frac{v}{V_\infty}(\phi_0)}\right) \qquad (2.3.6)$$

(The deduction of the above equation is obvious from figure 2.8). Then, according to the values of ϕ and ϕ_0 one of the terms of equation 2.2.6 is calculated depending on whether the flow is internal or external and from equation 2.2.7, the values of $i_{a,t}$ are obtained.

e) Analysis of induction factors in a fourier series.

The induction factors are analysed in a fourier series summing N+1 terms (from 0 to N) of equation 2.2.11:

$$i_{a,t}(\phi\ ,\ \phi_0) = \sum_{n=0}^{N} I_n^{a,t}(\phi) \cos(n\phi_0) \qquad (2.3.7)$$

f) Calculation of Lerbs factors.

The Lerbs factors $h^{a,1}_{m}(\phi)$ are calculated for each ϕ and m (from 1 to M) using equations 2.2.13 and 2.2.14. Note that since a finite number of $I^{a,1}_{n}$ coefficients is calculated, the second sum in the above equations (from m+1 to ∞) is limited to the terms m+1 to M in the case $n > m$. It becomes zero if $n \leq m$.

g) Calculation of new values for the induced velocities, aerodynamic angle and G.

The new values of u_i/V_∞, v_i/V_∞, β_i and G are also calculated for each ϕ. u_i/V_∞ and v_i/V_∞ from equations 2.2.12, β_i from equation 2.3.6, substituting ϕ_0 with ϕ:

$$\beta_i(\phi) = \tan^{-1}\left(\frac{\frac{u}{V_\infty}(\phi) - \frac{u_i}{V_\infty}(\phi)}{\lambda x + \frac{v_i}{V_\infty}(\phi) - \frac{v}{V_\infty}(\phi)}\right) \qquad (2.3.8)$$

G is calculated from equation 2.3.3 using the new values of u_i/V_∞, v_i/V_∞ this time for the calculation of W.

h) Convergence test.

The old and new values of G are compared for each ϕ and if they are close enough, the procedure goes on to the next step. Otherwise, the values of u_i/V_∞, v_i/V_∞, β_i and G are updated and the iteration starts again from step (c), until convergence is achieved.

i) Calculation of twist angle.

The twist angle is calculated for each ϕ from equation 2.3.1

j) Calculation of power coefficient.

The power coefficient (C_p) is calculated using equation 2.3.2. For estimating the power produced by the turbine, the elemental power of each blade element is integrated along the blade, multiplied by the number of blades. Also, according to the application, other quantities important in wind turbine aerodynamics can be calculated, such as rotor thrust, torque coefficient, forces on the blades, Reynolds number, etc.

After these calculations, the procedure is completed. With this iterative algorithm the bound circulation, induced velocities, twist angle distribution and power coefficient can be estimated for a turbine with a given number of blades and chord distribution, for a given operating condition set by the tip speed ratio. In order to find the most promising configuration, a parametric study must be carried out for assessing the impact of each parameter on the turbine's efficiency. Comparison of results can lead to the most suitable turbine for each application, as will be seen in the next chapter, where conventional turbines (operating in an axial, uniform incoming flow) are designed by this method and compared with similar designs produced by momentum theory.

FIGURES FOR CHAPTER 2.

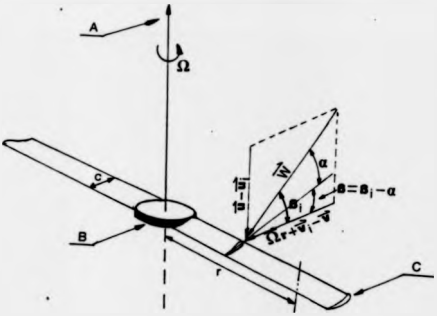

Figure 2.1. Turbine characteristics. A: Axis of rotation. B: Hub disc. C: Tip.

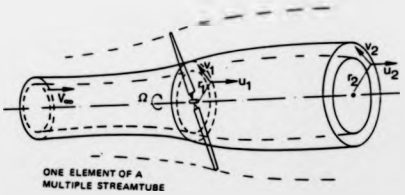

Figure 2.2. Stream tubes used in momentum theory. (From [11]).

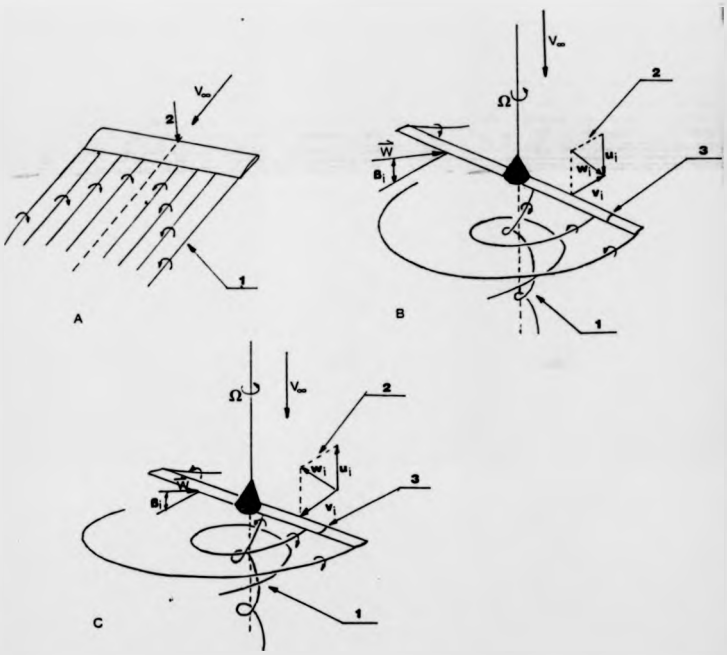

Figure 2.3. Trailing vorticity systems.

A: Aeroplane wing. B: Propeller.C: Turbine.
In all of the above:
1. Trailing vorticity. 2. Induced velocities. 3. Blade elements

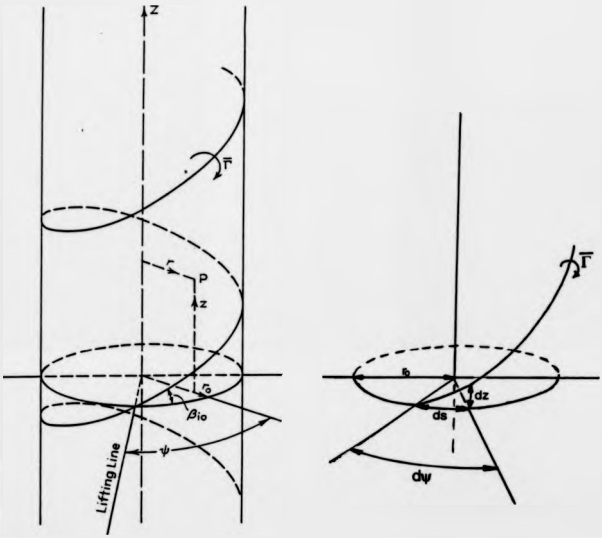

Figure 2.4. Geometry of an infinite helical vortex filament. (From [18]).

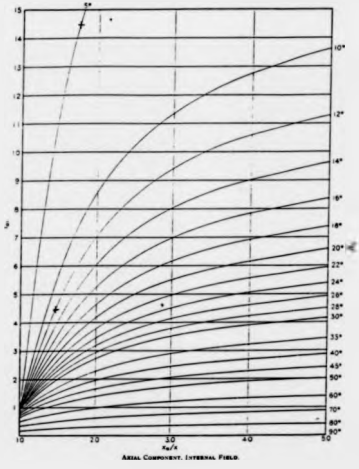

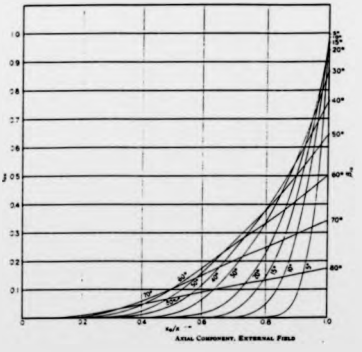

Figure 2.5 a.

Values of i_a factor (for internal and external field) as function on x_0 / x and $\beta_{.6}$ for a 3-bladed propeller. (Taken from [18]).

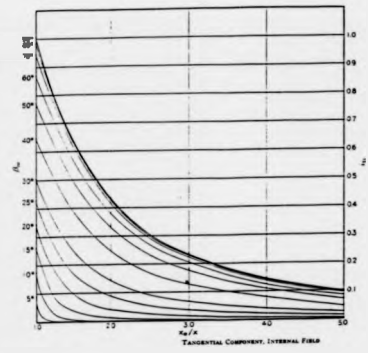

Figure 2.5 b.

Values of i_t factor (for internal and external field) as function on x_0 / x and β_{i0} for a 3-bladed propeller. (Taken from [18]).

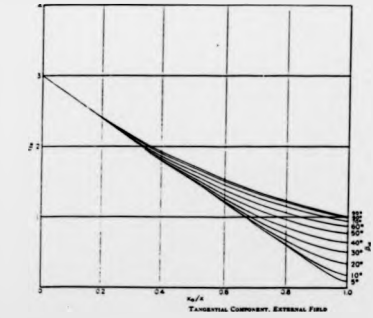

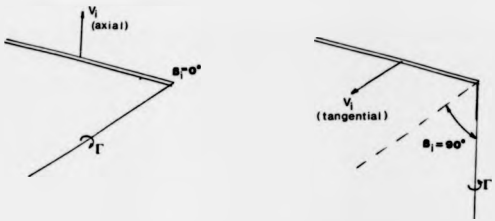

Figure 2.6. Direction of induced velocity.

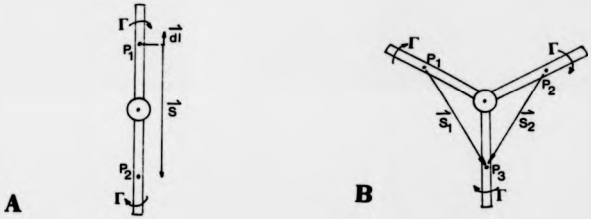

Figure 2.7. Contributions to induced velocity from lifting lines.

A: Two blades. The velocity induced at P_2 from P_1 is zero as $dl \times S = 0$. (Biot-Savart law).

B: Three blades. The velocities V_1 and V_2 induced at P_3 from P_1 and P_2 are of opposite sign and same magnitude. Hence, V_1 and V_2 cancel-out.

The same applies for any number of symmetrically spaced blades.

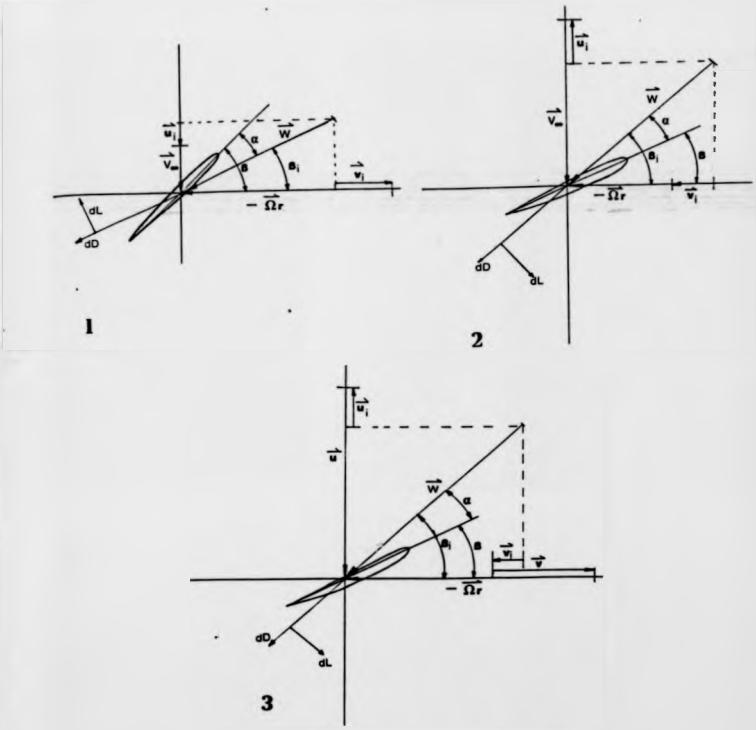

Figure 2.8. Local velocity vectors and forces on blade elements.

1. Propeller. 2. Conventional turbine. 3. Turbine operating in a non-uniform, non-axial, axisymmetric flow.

CHAPTER 3.

LIFTING LINE DESIGN OF CONVENTIONAL WIND TURBINES. COMPARISON WITH MOMENTUM THEORY.

CHAPTER 3. LIFTING LINE DESIGN OF CONVENTIONAL WIND TURBINES. COMPARISON WITH MOMENTUM THEORY.

3.0. INTRODUCTION.

In this chapter, the lifting line blade design procedure has been used for designing conventional wind turbines (ie turbines operating in a purely axial incoming flow). This was done in order to compare the present design method with the more widely used momentum theory and also for investigating the effects of various parameters involved in wind turbine design, on the turbine performance.

3.1. DESCRIPTION OF THE PROCEDURE.

The procedure for designing turbine blades operating in a general axisymmetric incoming flow has been analysed in chapter 2. The design work presented here is based on that procedure.

3.1.1. Calculation method.

For the turbine blade design, the iterative algorithm presented in chapter 2 was used. The only modification done concerns the incoming flow velocity distribution. A purely axial incoming flow was assumed, hence, in equation 2.2.22 (which gives the relative velocity at each blade element), the tangential incoming flow component is taken to be zero. ($v = 0$). However, the axial incoming flow at the turbine rotor disc was not assumed to be uniform. The turbine hub (centre-body) effect was also taken into account

and as it will be seen later, this causes the incoming flow to vary radially. Apart from these modifications, the rest of the algorithm was not changed.

3.1.2. Numerical techniques used.

A computer program (written in fortran) was developed for designing the turbine blades. This program is similar to that used for the design of the delta wing-vortex turbine system blades. The numerical techniques and results of the vortex turbine design are described in [21]. Some modifications to the procedure used in [21] were found to be necessary. These are related to the analysis of the bound circulation (G) and induction factors ($i_{a,t}$) in fourier series and also to the updating of the induced velocities' values during each iteration step.

In [21], the fourier coefficients required for the analysis of G and $i_{a,t}$ (see equations 2.3.5 and 2.3.7) were calculated by numerical integration:

$$G_m = \frac{2}{\pi} \int_0^{\pi} G(\phi) \sin(m\phi)\, d\phi$$

$$I_n^{a,t}(\phi) = \frac{2}{\pi} \int_0^{\pi} i_{a,t}(\phi, \phi_0) \cos(n\phi_0)\, d\phi_0, \quad n = 1, 2, \ldots, N$$

and

$$I_0^{a,t}(\phi) = \frac{1}{\pi} \int_0^{\pi} i_{a,t}(\phi, \phi_0)\, d\phi_0$$

Here, for each quantity, a system of linear equations was solved instead, thus estimating G_m and $I^{a,t}_n$. This was done as follows: The values of $G(\phi)$ and $i_{a,t}(\phi)$ were calculated at an adequate number of stations along the turbine blade, equal to the number of fourier coefficients required. (M for G, N+1 for $i_{a,t}$). Then, systems of linear equations were constructed writing equation 2.3.5 M times for the calculation of G_m and equation 2.3.7

N+1 times for $I^{a,t}_{n}$. The unknown variables in these systems are the fourier coefficients which can be estimated by solving the systems. For that purpose, the NAG library subroutine F04ATF was used. This routine can solve linear systems using Crout's factorisation method [22]: Given a system of linear equations Ax = b (with A and all other capital symbols in this section representing matrices and x, b, and other lower case symbols representing vectors), the routine first decomposes A using Crout's factorisation with partial pivoting PA = LU, with P a permutation matrix, L the lower triangular and U the upper triangular matrices. An approximation to x is found by forward and backward substitution, ie Ly = Pb and Ux = y. The residual vector r = b-Ax is then calculated and a correction d is found by the solution of LUd = r. Then, x is replaced by (x + d) and the process is repeated until full machine accuracy is obtained. This method is more time consuming but it was necessary as it was found that unlike the case of the vortex flow, the numerical integration method produced poor results.

As was reported in [21], the lifting line design procedure is divergent if blade chord distributions with maximum chord-to-radius ratio larger than 0.15 are used. ($c_{max}/R > 0.15$). This is caused by undue oscilations in the values of β_i (aerodynamic angle) between iteration steps. For ensuring convergence for $c_{max}/R > 0.15$, a relaxation technique was used: Each time the induced velocities' values were updated, (before the start of the next iteration step), instead of substituting the old induced velocities' values with the new ones, only a percentage of the new values was added to the old according to the following formula:

$$u_i = u_{i,old} + F\,(u_{i,new} - u_{i,old})$$
$$v_i = v_{i,old} + F\,(v_{i,new} - v_{i,old}) \qquad (3.1.1)$$

F in the above formula is the "relaxation factor', which determines the percentage of new values to be added to the old ones. For example, if F = 1.0, then, $u_i = u_{i,new}$ and $v_i = v_{i,new}$

as was the case in [21]. With this modification, convergence is possible for any chord distribution. However, the larger c_{max}/R, the lower the F required for convergence and hence, with c_{max}/R increasing, more iterations (and thus more time) is needed.

For assessing the turbine's efficiency, the value of C_p for each turbine design was calculated. C_p is given by equation 2.3.2. In our case, the flow far upstream of the turbine is uniform, with velocity V_∞. Hence the undisturbed flow power for an area equal to that swept of the turbine is:

$$P = \tfrac{1}{2} \rho (V_\infty)^3 \pi R^2$$

The turbine power is:

$$P_T = \int_{R_h}^{R} B \Omega \, dQ$$

with $dQ = r\, dF$, the torque exerted on a blade element with radius r.

The driving force on a blade element is (see also figure 2.8):

$$dF = dL \sin\beta_i - dD \cos\beta_i = \tfrac{1}{2} \rho W^2 c(r) (C_L \sin\beta_i - C_D \cos\beta_i) dr$$

Hence:

$$dQ = \tfrac{1}{2} \rho W^2 c(r) G_i r\, dr$$

with $G_i = C_L \sin\beta_i - C_D \cos\beta_i$ and finally:

$$P_T = \tfrac{1}{2} \rho B \Omega \int_{R_h}^{R} W^2 c(r) G_i r\, dr$$

Hence, C_p becomes:

$$C_p = \frac{B\lambda}{\pi R^2} \int_{R_h}^{R} \left(\frac{W}{V_\infty}\right)^2 \left(\frac{c}{R}\right) G_i r\, dr \qquad (3.1.2)$$

with:

$$G_i = C_L \sin\beta_i - C_D \cos\beta_i \text{ and } \lambda = \frac{\Omega R}{V_\infty}$$

For calculating C_p numerically, Simpson's integration method has been used. Equation

3.1.2 is not suitable for the numerical integration as the quantity which is equally spaced along the blade is ϕ and not r (or x). Therefore, the integral of (3.1.2) must be transformed. This is done as follows:

$$r = x\,R \Rightarrow r\,dr = R^2\,x\,dx.$$

Also, from (2.2.9) we get:

$$r\,dr = \tfrac{1}{4}\,R^2\,[\,(1 - x_h^2) - (1 - x_h)^2\cos\phi\,]\,\sin\phi\,d\phi.$$

Thus:

$$C_p = \frac{B\lambda}{4\pi}\int_0^{\pi}\left(\frac{W}{V_\infty}(\phi)\right)^2\frac{c}{R}(\phi)\;G_1\;G_2\;d\phi$$

with:

$$G_1 = C_L\sin\beta_i - C_D\cos\beta_i \qquad (3.1.3)$$

$$G_2 = \left\{(1 - x_h^2) - (1 - x_h)^2\cos\phi\right\}\sin\phi$$

Trial runs of the program were carried out in order to assess the accuracy of the numerical techniques used. The design results for conventional turbines were found to be more sensitive to changes of the number of fourier coefficients, initial induced velocities and of the convergence criterion than these for the vortex turbine. 51 fourier coefficients were found to be adequate for the analysis of G (30 were used in [21]) and 53 for the analysis of $i_{a\,i}$ (30 were used in[21]). The convergence criterion was:

$$|G_{new} - G_{old}| \le 10^{-4}\,|G_{new}|. \qquad \text{(In [21], } 10^{-3} \text{ was used).}$$

This was necessary so that runs starting with different initial induced velocity values would give differences in the C_p values less than 1%.

Quicker convergence was achieved using (u_i/V_∞) initial = 0.4 and (v_i/V_∞) initial = 0.0 throughout the blade for the first iteration cycle.

The relaxation factor was found to range from 0.2 to 0.5, ie 20% to 50% of the induced velocities' new values was added to the old ones.

3.1.3. Hub size and interference.

The turbine hub size was chosen to be $R_h = 0.2R$. This is the largest hub size that doesn't affect adversely the power produced by a turbine, as reported in [23] where an investigation of centre-body effects on turbine performance was carried out. The hub interference was taken into account by altering the uniform incoming flow velocity distribution. Far upstream of the turbine, the undisturbed wind velocity is equal to V_∞. On the turbine rotor disc however, it is changed due to the centre-body interference. The formula:

$$\frac{u(x)}{V_\infty} = 1 + 0.2 \left(\frac{x_h}{x}\right)^{2.2} \qquad (3.1.4)$$

expresses the hub interference and was derived experimentally in [23] by investigating the flow around hemispherical centre-bodies. Equation 3.1.4 gives less suction than does the "ideal" case, ie that of potential theory for a sphere [24], where the change of incoming velocity due to the hub is:

$$\frac{u(x)}{V_\infty} = 1 + 0.5 \left(\frac{x_h}{x}\right)^{3} \qquad (3.1.5)$$

However, the difference in C_p for turbines designed using equation 3.1.5 for the incoming flow as compared to similar turbines for which equation 3.1.4 was used, was found to be in the range of 1% to 2%. The small difference in C_p is caused by the small hub size that doesn't create a large disturbance to the flow.

3.1.4. Choice of aerofoil section.

The aerofoil section chosen to be used is NACA 4415. This section is often used in wind turbine applications. Its construction is easy,since it is 15% thick, and it is a well documented aerofoil with many references reporting wind tunnel tests of it. Indeed, results of four different tests for this section were found and compared with each other. These results are presented in references [25], [26], [27] and [28]. Comparison of results revealed that those of [25] didn't agree with those of [26], [27] and [28]. In the tests presented in [25], the values of C_D and stall angle were found to be larger than those of the other references. These differences were probably due to different levels of turbulence between the tests. The larger separation resistance and higher drag of [25] reveals the presence of a turbulent boundary layer which may have been caused either by high free-stream turbulence or by bad aerofoil surface finish (or both). The results of [25] were not used since they didn't agree with the rest. Reference [26] contains tests of NACA 4415 at very high Reynolds numbers. (The smallest being $3x10^6$). The lowest value of Re for which tests of NACA 4415 were carried out is $7x10^5$ and was found in [27] and [28]. The values of α_{opt}, $C_L(\alpha_{opt})$ and $C_D(\alpha_{opt})$ are:

Reference [27]	Reference [28]
$Re = 7x10^5$	$Re = 7x10^5$
$\alpha_{opt} = 5°$	$\alpha_{opt} = 5°$
$C_L(\alpha_{opt}) = 0.89$	$C_L(\alpha_{opt}) = 0.91$
$C_D(\alpha_{opt}) = 0.0100$	$C_D(\alpha_{opt}) = 0.0105$

An average was taken of the two sets of results and the aerofoil data used are:

$$Re = 7x10^5$$

$$\alpha_{opt} = 5^\circ$$

$$C_L(\alpha_{opt}) = 0.90$$

$$C_D(\alpha_{opt}) = 0.01025$$

The wind turbines designed here were chosen to be of medium size. with rotor diameters equal to 5m. For such turbine dimensions, the blade chord Re is expected to be supercritical. Indeed, the Re values of all turbines designed were found to range from 10^5 to $8x10^5$, for V_∞ = 10 m/sec. These values of Re are high enough for Re effects to be ignored, and the aerofoil data for a single Re value (presented above) were used. The difference in C_p of turbines designed using the aerofoil data for $Re = 7x10^5$ compared with those designed using data for $Re = 3x10^6$ (taken from [26]) was found to be less than or equal to 2%. This shows that the effect of Re on the turbine C_p is not a great one for supercritical chord Re values and hence the use of aerofoil data for a single Re value is justified.

3.2. PRESENTATION OF RESULTS.

In this section, the results obtained from the design procedure described above are presented and discussed.

The nondimensional chord distribution of all the blades designed is given by:

$$\frac{c}{R} = C_0 \frac{\sin\phi}{x^E} \qquad (3.2.1)$$

The above formula was chosen as it produces blade shapes which are compatible with the

boundary conditions of the problem: In equation 2.3.5 the blade bound circulation (G) is analysed in a fourier sine series. For doing that, it was assumed that G drops to zero at the tip and hub of the blade. From equation 2.3.3 it is evident that G can become zero only if the chord distribution becomes zero too. The alternative way for satisfying the boundary conditions is to assume that the blade angle of attack at the tip and hub is equal to its zero lift value. However, this cannot be done in our case, as the angle of attack was assumed to be equal to α_{opt} throughout the blade (equation 2.3.1) for optimising C_L / C_D. Equation 3.2.1 produces blades that satisfy the above requirement. The exponent E in that formula has a profound effect on the blade shape. With it increasing, the blade becomes increasingly "waisted" as can be seen in figure 3.14. "Waisting" is preferred in describing the blade shape to "taper", as the blade taper ratio which is usually defined as root chord:tip chord (see [30]) does not apply in our case. The taper ratio will also be used, but redefined as:

$$\text{Taper ratio} = \frac{\text{Maximum blade chord}}{\text{Blade chord at } r = 0.8R} \qquad (3.2.2)$$

Thereafter, the exponent E in (3.2.1) will be called "waisting factor". As can be seen from figure 3.14, increasing E increases the blade taper.

Two families of blades were designed, one having $c_{max}/R = 0.1$ and another with $c_{max}/R = 0.2$. For each value of E, an appropriate C_0 was found, so that the value of c_{max} / R would be one of the two mentioned above. For the first family (with $c_{max}/R=0.1$), 3, 6 and 10-bladed turbines were designed with varying degree of blade waisting (E ranging from 1.0 to 2.5). For the second family, (with $c_{max}/R=0.2$), only 3 and 6-bladed turbines were designed since the 10-bladed ones would operate at too low tip speed ratios. For each turbine, a value of λ was found (λ_{opt}) for which C_p was maximised. It took several runs of the program to spot the maximum of C_p. The program

needed a considerable time to converge (15 to 20 mins) and in order to reduce the number of runs, the step for λ was chosen to be 0.25, and hence the accuracy whith which λ_{opt} was calculated was $\pm$ 0.125. This was satisfactory, since the slope of C_p close to its maximum was found to be small.

In tables 1 and 2 the design results are shown for each family of turbines. In each box of these tables the values of $C_{p\,max}$ and λ_{opt} are shown.

In figures 3.1 to 3.12 the distributions of G, u_i / V_∞, v_i / V_∞ and β along the blade are shown. Fig. 3.1-3.4 are for B=3, c_{max}/R=0.1, fig. 3.5-3.8 are for B=10, c_{max}/R=0.1 and fig. 3.9-3.12 for B=3, c_{max}/R=0.2. In each of these plots, five curves are shown for different values of E. Each curve is for the value of λ for which $C_{p\,max}$ is obtained (λ_{opt}). Using the information provided by these tables and figures the influence of all relevant parameters can be assessed. The parameters are:

- Number of blades (B)
- Blade waisting (Value of E)
- Maximum chord (c_{max} / R)

3.2.1. Effect of number of blades.

It can be seen from tables 1 and 2 that with E and c_{max} / R remaining the same, increasing B causes $C_{p\,max}$ to increase and λ_{opt} to decrease. Increase of B means approaching the "actuator disc" situation, for which the Betz limit applies. Comparing figures 3.1 and 3.5, it can be seen that with E being the same, the circulation shape is similar for different values of B. However, the values of G for the same radial position decrease with B increasing. Hence, the blade loading decreases with increasing number of blades.

TABLE 1		$x_h = 0.2$, Aerofoil = NACA 4415, $Re = 7 \times 10^5$, $V_\infty = 10$ m/sec. $\frac{C}{R} = C_D \frac{\sin\phi}{x^2}$, $c_{max}/R = 0.10$								
		C_D : 0.045 E : 1.0	0.032 1.3	0.025 1.5	0.022 1.6	0.020 1.7	0.017 1.8	0.015 1.9	0.013 2.0	0.0065 2.5
B = 3	$C_{p,max}$	0.4082	0.4484	0.4646	0.4701	0.4724	0.4744	0.4722	0.4687	0.4184
	λ_{opt}	6.5	8.0	8.75	9.25	9.5	10.0	10.25	10.75	12.25
B = 6	$C_{p,max}$	0.4751	0.5063	0.5196	0.5228	0.5214	-		0.5103	0.4491
	λ_{opt}	5.0	5.75	6.5	6.75	7.0	-	-	7.75	8.75
B = 10	$C_{p,max}$	0.5181	0.5421	0.5510	0.5516	0.5469	-	-	0.5289	0.4579
	λ_{opt}	4.0	4.75	5.0	5.25	5.25	-	-	6.0	6.75

TABLE 2		$x_h = 0.2$, Aerofoil = NACA 4415, $Re = 7 \times 10^5$, $V_\infty = 10$ m/sec. $\frac{C}{R} = C_D \frac{\sin\phi}{x^2}$, $c_{max}/R = 0.20$								
		C_D : 0.09 E : 1.0	0.064 1.3	0.05 1.5	0.044 1.6	0.004 1.7	0.032 1.8	0.030 1.9	0.026 2.0	0.013 2.5
B = 3	$C_{p,max}$	0.3587	0.4030	0.4282	-	0.4410	0.4467	0.4434	0.4451	0.3988
	λ_{opt}	4.25	5.0	5.75	-	6.25	6.75	7.0	7.25	8.5
B = 6	$C_{p,max}$	0.4289	0.4673	0.4863	0.4916	0.4906	-	-	0.4849	-
	λ_{opt}	3.25	3.75	4.25	4.5	4.5	-	-	5.25	-

The reduction of G with increasing B is caused by the decrease of λ_{opt} (see tables 1 and 2) and the subsequent reduction of the relative velocity W. Comparing figures 3.2 and 3.6 (plots for the same E), it can be seen that u_i / V_∞ increases towards the hub and

decreases towards the tip with B increasing. The reduction of u_i / V_∞ close to the tips brings about the increase of $C_{p\,max}$ with B. However, the shape of u_i / V_∞ is roughly the same for turbines with the same blade shape and different number of blades. From figures 3.3 and 3.7 it can be seen that v_i / V_∞ increases rapidly with B increasing. The general shape of v_i / V_∞ remains similar for different B but the distribution maximum moves closer to the hub with B increasing.

From figures 3.4 and 3.8 it can be seen that the twist angle distribution along the blade behaves as follows: The values of β for a given radial station increase with B increasing due to the reduction of λ_{opt} and W, but its shape remains essentially the same.

Conclusions:

i. With B increasing, $C_{p,max}$ increases and λ_{opt} decreases.

ii. With B increasing, no major changes are observed to the shape of G, u_i/V_∞, v_i/V_∞ and β distributions along the blade.

3.2.2. Effect of blade waisting.

Varying the waisting factor (E), has great effects on the turbine results. It can be seen from tables 1 and 2 that with E increasing, λ_{opt} is also increasing, due to the reduction of the turbine solidity. $C_{p\,max}$ increases with E increasing, until a maximum is obtained. With further increase of E, $C_{p,max}$ drops. The maximum of $C_{p\,max}$ was found to depend on the number of blades: For B = 3, E_{opt} = 1.8, for B = 6 and 10, E_{opt} = 1.6. The value of E_{opt} doesn't depend on c_{max} / R, as can be seen from tables 1 and 2.

The above mentioned effects can be explained by analysing the influence E has on G and the local flow around the blades. From figures 3.1, 3.5 and 3.9,

(comparing plots of different E at each figure), it can be seen that for E = 1.0, G(x) is almost symmetrical about x=0.6. With E increasing, the G(x) maximum moves towards the root. Also, due to the rotor solidity reduction with increasing E, G(x) (for the same x) is decreasing for x larger than 0.5. This change of G(x) has significant effects on the induced velocities. It can be seen from figures 3.2, 3.6 and 3.10 for u_i / V_∞ and 3.3, 3.7, 3.11 for v_i / V_∞, that both quantities follow the change of G(x). They increase close to the hub and decrease close to the tip with E increasing. At the tip, the reduction of induced velocities is quite dramatic. For $c_{max} / R = 0.1$, B = 3, we get:

E=1.0, u_i / V_∞ (x=1.0) ≈ 0.5
E=2.0, u_i / V_∞ (x=1.0) ≈ 0.25
} Reduction of 2.0 times.

E=1.0, v_i / V_∞ (x=1.0) ≈ 0.038
E=2.0, v_i / V_∞ (x=1.0) ≈ 0.018
} Reduction of 2.1 times.

Thus, the tip vortex is significantly reduced in strength with increasing E. The relative wind velocity increases with E increasing, since λ_{opt} increases (ie Ωr increases) and u_i decreases. (See equation 2.2.21). Since $C_p \sim W^2$ (see equation 3.1.3), increase of E causes $C_{p\,max}$ to increase. However, C_p is also dependent on c ($C_p \sim c$), and there is a limit to how beneficial the increase of W can be, since a large reduction of the blade chord close to the tip (without increase of the number of blades) has adverse effects. The value of E for which the two conflicting trends balance is E_{opt}. The dependence of E_{opt} on the number of blades can be explained as follows: The few-bladed turbines operate at larger λ_{opt} than similar multi-bladed turbines and thus W is larger. Hence, for few-bladed turbines, C_p starts being reduced by the blade chord reduction (with increasing E) at larger values of E. That is why larger values of E_{opt} are observed for B=3 compared to B=6 and 10. Finally, from figures 3.4, 3.8 and 3.12 it can be seen that with E increasing, $\beta(x)$ decreases throughout the blade. This is again due to the increase of λ_{opt}. The

decrease of $\beta(x)$ is more pronounced in the hub region.

Conclusions:

i. Increasing blade waisting (E), causes λ_{opt} to increase due to the reduction of the turbine solidity.

ii. Increasing E causes the blade loading to become more pronounced close to the hub region. (This is advantageous from the structural point of view).

iii. The reduction of chord with E increasing counter-balances the increase of relative wind velocity and an optimum value of E can be found (depending on B), for which $C_{p,max}$ gets its highest value.

3.2.3. Effect of maximum chord.

Increase of the maximum blade chord (c_{max} / R) means increase of the turbine solidity. This reduces $C_{p\,max}$ and λ_{opt} as can be seen comparing tables 1 and 2. This reduction of $C_{p\,max}$ is caused by the increase of the induced velocities throughout the blade (compare figures 3.2 and 3.10 and also 3.3 and 3.11), and the decrease of λ_{opt} that reduces W. The bound circulation also increases throughout the blade (see figures 3.1 and 3.9) as well as the twist angle (compare figures 3.4 and 3.12). The shape of G, u_i/V_∞, v_i/V_∞ and β along the blade does not change significantly with c_{max} / R.

Conclusion:

Increase of c_{max} / R increases the turbine loading and the strength of the tip vortex while it reduces both $C_{p\,max}$ and λ_{opt}.

3.2.4. Other remarks on the turbine design results.

In figures 3.13 and 3.14, the chord shapes of blades for various values of E and with $c_{max} / R = 0.1$ and 0.2 respectively are shown. It can be seen that some of the blades are strongly and non-linearily tapered, especially those for which $C_{p\,max}$ is optimised (ie E=1.8 for B=3 and E=1.6 for B=6, 10). Also, from figures 3.4, 3.8 and 3.12 it is evident how strongly the blades must be twisted in order to match the local flow. The strong taper and twist of the blades makes their construction difficult and the blade design usually has to be compromised towards easier to make and less expensive blades.

From tables 1 and 2 it can be seen that of turbines with the same solidity, those with more and narrower blades produce more $C_{p,max}$ at larger λ_{opt}. (Compare turbines with B = 6 from table 1 to those with B = 3 from table 2).

3.3. COMPARISON WITH MOMENTUM THEORY.

In this part, the turbine design method based on lifting line theory is compared with momentum theory. Both qualitative and quantitative comparisons were made.

3.3.1. Momentum theory and tip loss corrections.

In chapter 2, the basic principles of momentum theory were presented. It was also mentioned that in order to refine the design model and alleviate the limitations of the "actuator disc" assumption, corrections are necessary. These corrections are called "tip loss corrections" and their derivation and use is explained in the following.

Due to the "actuator disc" assumption, momentum theory cannot predict the reduction of circulation at the blade tip and hub caused by the crossflow from the pressure to the suction sides of the blade. That leads to underestimation of the induced velocities and overestimation of C_p. To rectify this situation, theoretically based corrections have been developed. The most commonly used tip loss corrections are those devised by Prandtl. A correction factor F is used in order to describe the loss of circulation at the blade tips. It is given by:

$$F = \frac{B\Gamma}{\Gamma_{\infty}} \tag{3.3.1}$$

with Γ the circulation of each blade and Γ_{∞} the circulation of the "actuator disc", as explained in [23]. There are two formulae for F. One is:

$$F = \frac{2}{\pi} \arccos(e^{x})$$
$$\text{with } x = -\frac{1}{2} B \frac{R - r}{r \sin\beta_i} \tag{3.3.2}$$

It is derived (as explained in [30]) replacing the helical vortex system shed from the blades, with a simpler one consisting of a distribution of equidistant, semi-infinite planar vortex sheets springing from the blades. The vortex filaments within these sheets are normal to the turbine axis of rotation. Conformal mapping can be used for calculating the reduction in potential difference between two plates approaching the blade tips. This is then coupled to the reduction of circulation around the tips.

The other formula is:

$$F = \frac{2}{\pi} \arccos(e^{x})$$
$$\text{with } x = -\frac{1}{2} B \left(1 - \frac{r}{R}\right) \sqrt{1 + \lambda^2} \tag{3.3.3}$$

This is defined (as explained in [31]) assuming that the trailing vorticity lies on the surface of a circular cylinder with radius R, and estimating its effect.

There are also different opinions on how to implement these corrections. Two different methods are available, one called "simple" and another "exact". (See reference [15]). In the former, ("simple"), the force and torque relations derived from momentum considerations are multiplied by F and thus the reduction of forces on the blade tips is brought about. In the latter, ("exact"), the induced velocity factors a and a' as well as the local axial and rotational velocity components (see chapter 2) appearing in the momentum, force and torque relations are multiplied by F, so that the change in circulation comes through the change in the local flow.

Having that situation in mind, it is reasonable to argue that the lifting line predictions should be more accurate, since the effect of the tip vortices on the turbine performance is an intrinsic feature of the theory.

3.3.2. Qualitative comparison.

The trends observed in the turbine design using lifting line theory are also present when momentum theory is used. Highly tapered and twisted blades are the momentum theory optimum designs as explained in [31] and [9]. Figure 3.15 (taken from [33]) shows the design of three optimum blades using momentum theory. (Note that in figure 3.15 C_L is taken to be constant, so that the cC_L ordinate represents chord). The shapes look similar to those of figures 3.13 and 3.14. With the tip speed ratio (called "x" in figure 3.15) increasing, the blade waisting and taper ratio (as defined in equation 3.2.2) increase:

For $\lambda = 6$, taper ratio = 2.7, for $\lambda = 8$, taper ratio = 3.7,

and for $\lambda = 10$, taper ratio = 4.5.

The above results are for a μ_m ($= C_D / C_L$) value of 0.0025. In figure 3.16, similar results

are shown (ie chord and twist angle distributions for optimum turbines designed by momentum theory) taken from reference [34]. The twist angle distributions of figure 3.16 are similar to those shown in figures 3.4, 3.8 and 3.12. Note the reduction of twist angle values throughout the blade with λ increasing, which can also be observed in the lifting line design results. (In that case, $\beta(x)$ decreases with E increasing, which is equivalent to increasing λ, as can be seen in tables 1 and 2).

Figure 3.17 (taken from [9]) shows plots of $C_{p\,max}$ of optimum turbines designed by momentum theory, versus the design point λ and for various values of B and C_L/C_D. Different points of each curve of that figure represent different turbine designs, with the same number of blades and lift-to-drag ratio. Each turbine is designed to operate at a given tip speed ratio, and hence the dependence of the C_p of an optimum turbine on the design point is revealed. From figure 3.17, it is evident that with increasing number of blades, the $C_{p,max}$ produced by a turbine increases. This trend can also be observed in tables 1 and 2. It can also be seen from figure 3.17, that for given values of B and C_L/C_D, there exists a tip speed ratio (λ_{opt}), for which $C_{p\,max}$ gets its optimum value, and that with further increase of λ, $C_{p\,max}$ decreases. This trend can also be observed in tables 1 and 2, with E increasing. (As explained above, increase of E causes λ to increase).

It can therefore be concluded that the results of both theories agree qualitatively, since the same trends are observed.

3.3.3. Quantitative comparison.

For getting a more detailed estimation of the degree to which the two theories agree, three blade shapes were compared, designed for the same operating conditions:

- The first was designed by momentum theory without tip loss corrections, using a method presented in [9].
- The second was designed by momentum theory with tip loss corrections (ie use of equation 3.3.3 and the "simple" method). That was done in [23].
- The third was designed using the lifting line design procedure.

All turbines were 3-bladed ones operating at $\lambda_{design} = 5.0$. The NACA 4415 aerofoil was used in all three designs. For the momentum theory blade design, the input parameters are λ, B and $C_L(\alpha_{opt})$ and the outputs are the c(r) and β(r) distributions, ie the optimum blade shape. The lifting line design procedure requires prior knowledge of the chord distribution. In order to find the optimum blade shape predicted by the lifting line design procedure using equation 3.2.1 for the blade chord, various turbines were examined, with various blade shapes, at a single operating condition (ie $\lambda_{design} = 5.0$) and the configuration producing the maximum C_p was sought. It was found to be that appearing in table 2, for E=1.3. This turbine produced the highest C_p of all that were tested, since (as can be seen in table 2) its λ_{opt} is equal to λ_{design}. Blades with larger values of E were found to produce less C_p at λ=5, as their λ_{opt} values are larger than λ_{design}. Therefore, in the lifting line design procedure, and for a given blade family, the optimum turbine to operate at a given tip speed ratio is that for which $\lambda_{opt} = \lambda_{design}$. However, it cannot be claimed that the above mentioned chord distribution is the absolute optimum, since there are infinite different chord distributions, other than those given by equation 3.2.1, that have not been tested. It is hoped that if this is true and another better chord distribution exists, it will only exhibit trivial differences from the one used here.

In figure 3.18, the chord distributions of the three designs are shown. It can be seen that only trivial differences appear up to x = 0.6. However, the differences become more pronounced approaching the tip. Momentum theory without tip loss

corrections gives larger blade chords close to the tip. Implementation of tip loss corrections increases the blade taper which is still less than that required by the lifting line method. Also, use of tip loss corrections with momentum theory produces blades with tip chords equal to zero, like those required by lifting line theory. The blade chords produced by the two latter procedures agree quite well. The lifting line design method probably predicts larger induced velocities at the tip region and smaller chord values are required.

Figure 3.19 shows the twist angle distributions predicted by the three methods. The predictions agree quite well from x = 0.4 to x = 0.9. Differences occur only at the tip and hub regions. Momentum theory with no tip loss corrections gives the lowest twist angles close to the hub, because the hub influence has not been taken into account. The largest twist is required at the hub region by the lifting line blade. This is due to the fact that only the lifting line blade chord drops to zero at the hub region. At the tip region, both momentum theory methods give similar results for β. The lifting line method predicts a drop of β at the tip region below the momentum theory values. This is caused by the large increase of u_i/V_∞ at the tip region. (See figure 3.10, for E=1.3). The increase of u_i/V_∞ at the tip region (and the subsequent drop of β) can be supported by the findings of references [31] and [35]. In [31], the performance of a blade designed without tip loss corrections, with λ_{design} = 5, B = 3 and using the NACA 4415 aerofoil, was analysed using momentum theory with tip loss corrections. Figures 3.20 a and b (extracted from [31]) show that the blade angle of attack drops close to the tip, due to the vast increase of the axial induced velocity at that region. It is evident that if the blade were set at smaller angles of attack at the tip region (like those required by the lifting line method), the angle of attack would be closer to its optimum value. Note that figure 3.20 b resembles figure 3.10, for E=1.3. Also, in [35] the results of wind tunnel tests of a wind

turbine model are presented. One of the conclusions of these experiments was that the values of induced velocities close to the blade tips were much larger than those predicted by momentum theory with tip loss corrections. This also supports the lifting line design method findings.

Finally, the turbine C_p predicted by the three procedures is:

- Momentum theory without tip loss corrections: C_p=0.545. (Result from [32]).
- Momentum theory with tip loss corrections: C_p = 0.431. (Result from [23]).
- Lifting line design method: C_p = 0.403.

It is evident that as the tip vortex effects become more important in the calculations an increasingly conservative estimation of C_p results.

3.4. CONCLUSIONS.

The most important conclusions from this study are:

1. The turbines designed by the lifting line method to operate in a purely axial flow have highly tapered, waisted and twisted blades.
2. An increase of the number of blades increases the maximum power produced by the turbine, reduces the optimum value of tip speed ratio and does not affect significantly the shape of the G, u_i / V_∞, v_i / V_∞ and β distributions along the blade.
3. An increase in blade waisting (and thus taper), increases λ_{opt} due to the turbine solidity reduction. It also causes the blade loading to become more pronounced close to the hub, while it reduces the induced velocities close to the tip region limiting the adverse effects of the tip vortex. The reduction of chord with increasing blade waisting counterbalances the beneficial

increase of relative velocity and a blade chord distribution can be found (depending on the number of turbine blades) that optimises the turbine power.

4. An increase on the maximum chord value (ie of the blade width but not of the taper) increases the turbine loading and the strength of the tip vortex, while it reduces both the maximum C_p produced by the turbine and λ_{opt}.
5. Qualitative comparison between the present design method and momentum theory (both being used for designing conventional turbines) reveals that the results of both theories agree, since similar trends can be observed.
6. Quantitative comparison of the two methods reveals that when tip loss corrections are implemented within momentum theory, good agreement with predictions of the lifting line design method is observed. However, the lifting line method suggests a requirement for blades with smaller chord values at the tip region for the same operating conditions, and hence it predicts a stronger tip vortex. The lifting line method gives a more conservative estimate of the maximum power produced by the turbine designed.

FIGURES FOR CHAPTER 3

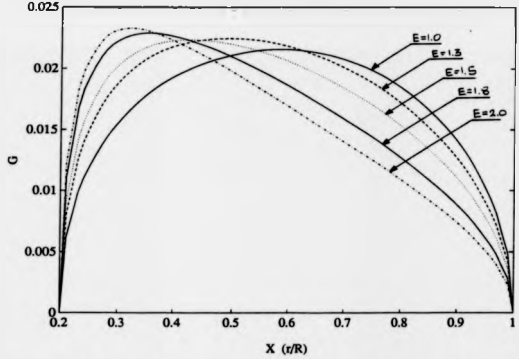

Figure 3.1. Bound circulation distribution along the blade. (B = 3, c_{max} / R = 0.1).

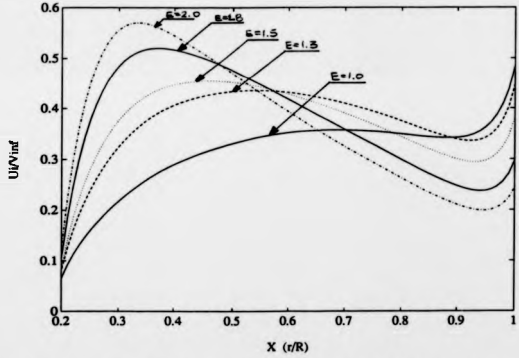

Figure 3.2. Axial induced velocity distribution along the blade. (B = 3, c_{max} / R = 0.1).

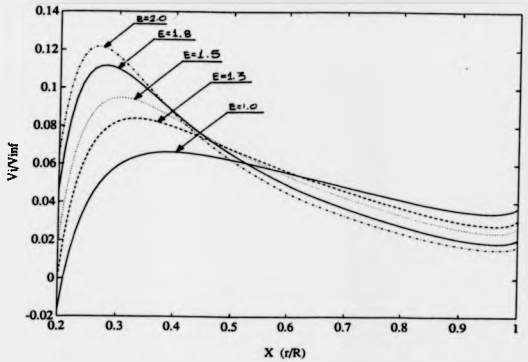

Figure 3.3. Tangential induced velocity distribution along the blade. ($B = 3$, $c_{max} / R = 0.1$).

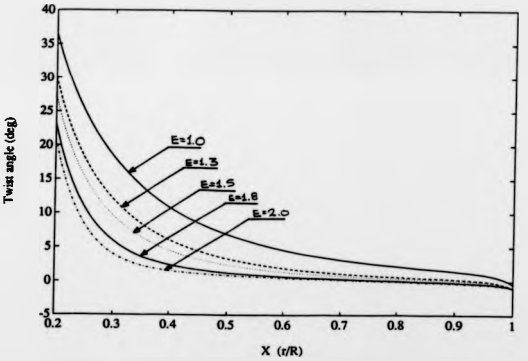

Figure 3.4. Twist angle distribution along the blade. ($B = 3$, $c_{max} / R = 0.1$).

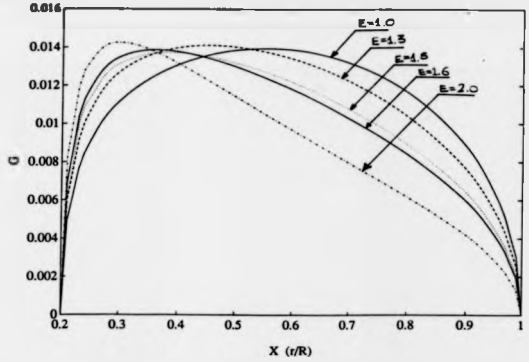

Figure 3.5. Circulation distribution along the blade. (B = 10, c_{max} / R = 0.1).

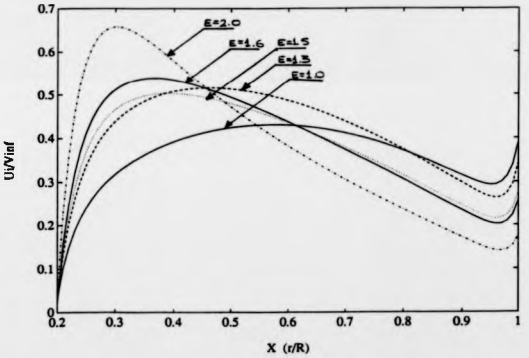

Figure 3.6. Axial induced velocity distribution along the blade. (B = 10, c_{max} / R = 0.1).

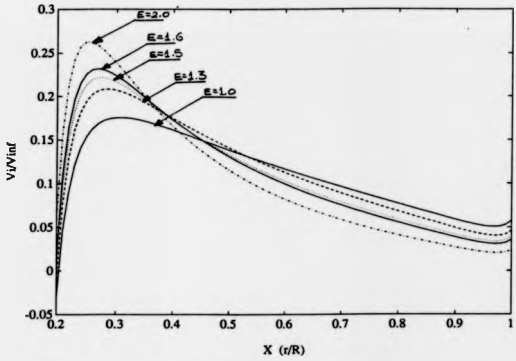

Figure 3.7. Tangential induced velocity distribution along the blade. ($B = 10$, $c_{max} / R = 0.1$).

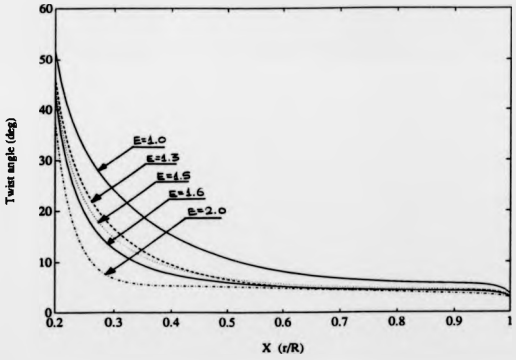

Figure 3.8. Twist angle distribution along the blade. ($B = 10$, $c_{max} / R = 0.1$).

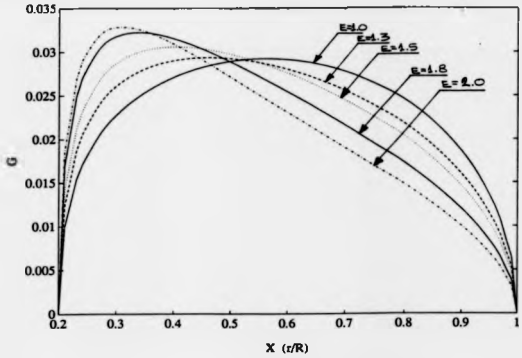

Figure 3.9. Circulation distribution along the blade. (B = 3, c_{max} / R = 0.2).

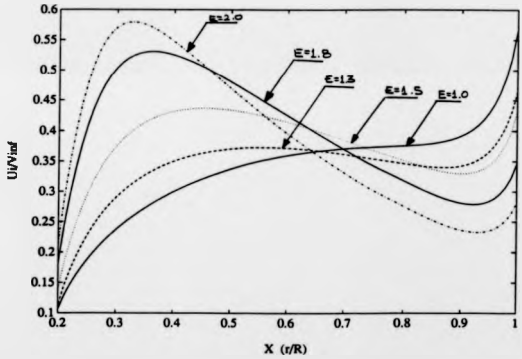

Figure 3.10. Axial induced velocity distribution along the blade. (B = 3, c_{max} / R = 0.2).

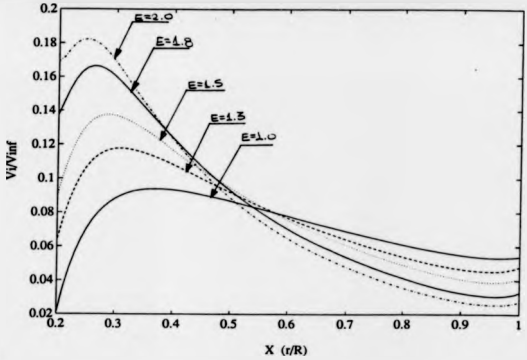

Figure 3.11. Tangential induced velocity distribution along the blade.
($B = 3$, $c_{max} / R = 0.2$).

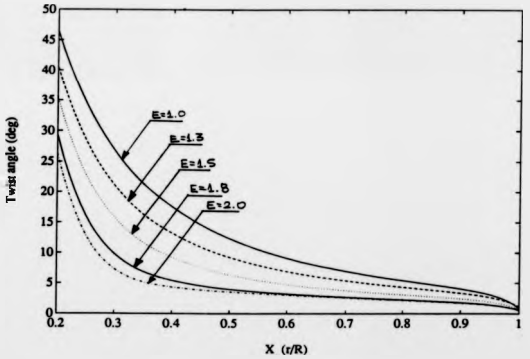

Figure 3.12. Twist angle distribution along the blade. ($B = 3$, $c_{max} / R = 0.2$).

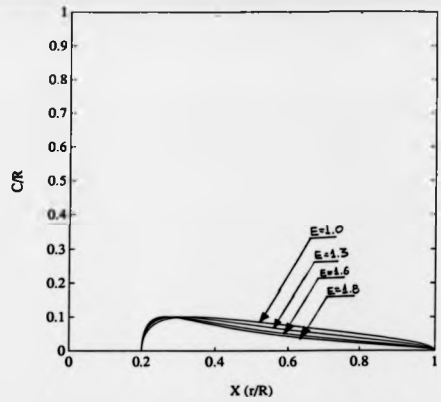

Figure 3.13. Dimensionless chord distribution for various values of E. (c_{max} / R = 0.1).

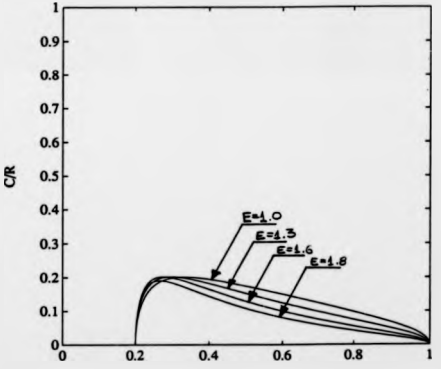

Figure 3.14. Dimensionless chord distribution for various values of E. (c_{max} / R = 0.2).

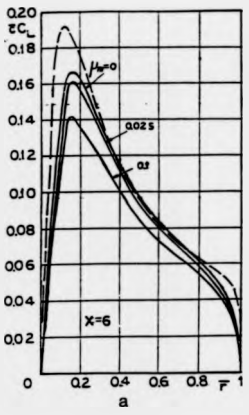

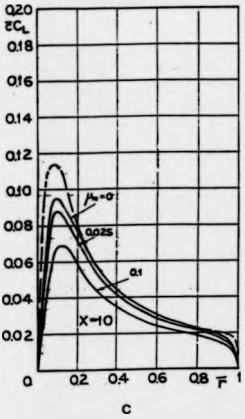

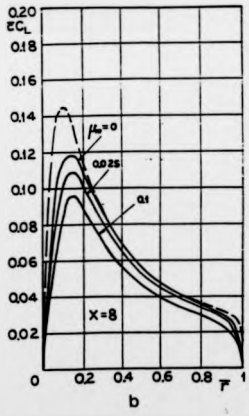

Figure 3.15.

Blade chord-lift distributions for optimum performance 3-bladed wind turbines. (taken from [33]).

In these figures, x stands for tip speed ratio.

Hence;

3.15 a: $\lambda = 6$.

3.15 b: $\lambda = 8$.

3.15 c: $\lambda = 10$.

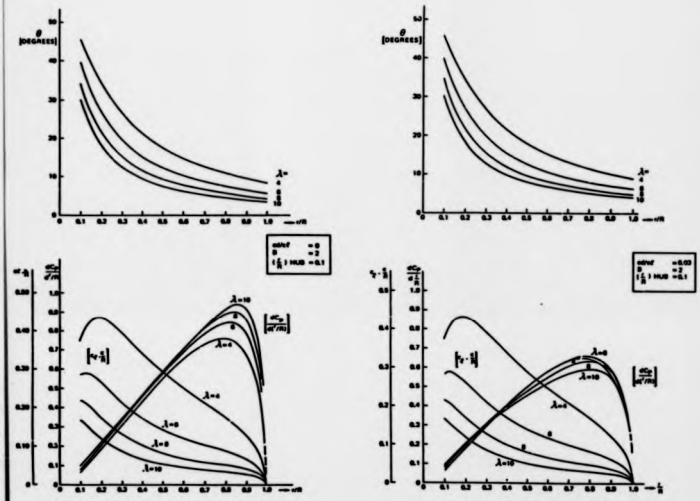

Figure 3.16. Twist angle and blade chord-lift distributions of optimum wind turbines. (Taken from [34]).

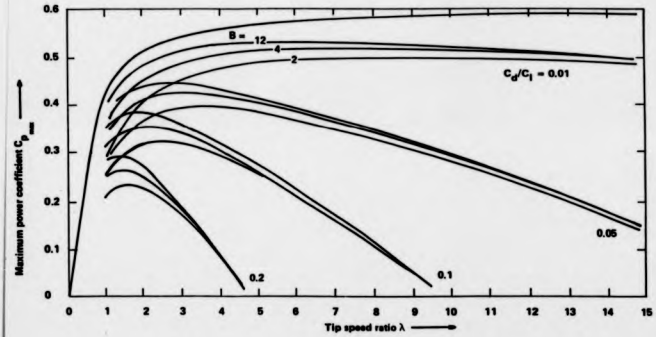

Figure 3.17. Influence of blade number B and drag-to lift ratio on the maximum attainable power coefficient for each tip speed ratio. (taken from [9]).

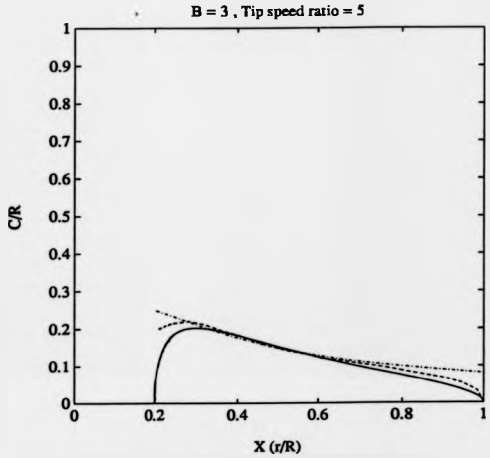

Figure 3.18. Comparison between lifting line and momentum theory based blade design methods for a turbine with B=3, λ_{design} = 5, aerofoil : NACA 4415.

Blade chord distribution

" —" : Lifting line design.
"---" : Momentum theory with tip loss corrections.
"----" : Momentum theory without tip loss corrections.

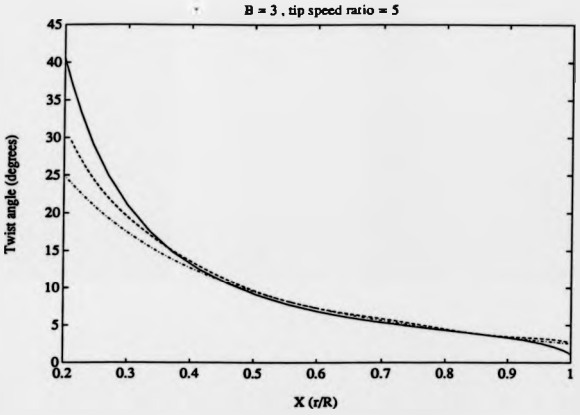

Figure 3.19. Comparison between lifting line and momentum theory based blade design methods for a turbine with B=3, λ_{design} = 5, aerofoil : NACA 4415.

Twist angle distribution

" —" : Lifting line design.
"---" : Momentum theory with tip loss corrections.
"----" : Momentum theory without tip loss corrections.

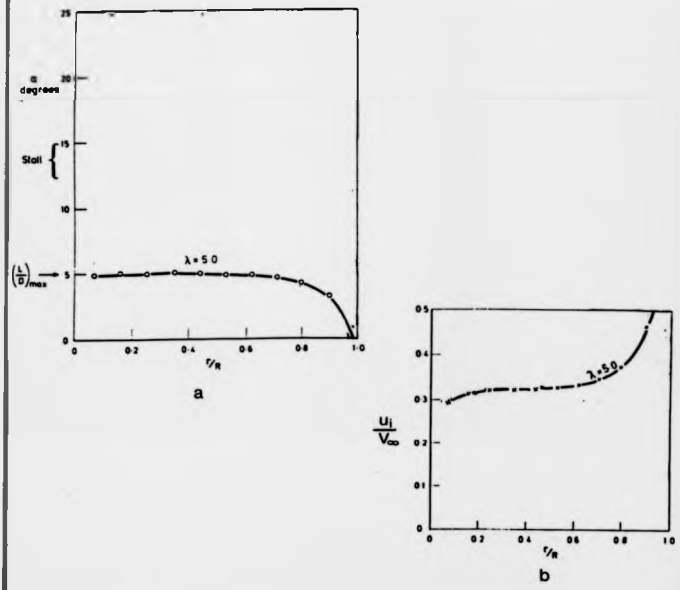

Figure 3.20. Angle of attack (3.20 a) and axial induced velocity distribution (3.20 b) of a turbine blade designed by momentum theory without tip loss corrections, as predicted by momentum theory with tip loss corrections. (Taken from [31]).
Both plots are for optimum tip speed ratio.

PART B.

DELTA WING-TURBINE SYSTEM.

CHAPTER 4.

DESIGN AND PERFORMANCE ANALYSIS OF THE VORTEX TURBINE.

CHAPTER 4. DESIGN AND PERFORMANCE ANALYSIS OF THE VORTEX TURBINE.

4.0. INTRODUCTION.

In this chapter the delta wing-turbine system is compared with conventional turbines of various sizes, and the vortex turbine is redesigned to operate in the low Reynolds number regime. The turbine performance at off-design conditions is also predicted.

4.1. DESCRIPTION OF THE DELTA WING-TURBINE SYSTEM.

It is well known that a slender delta wing with sharp leading edges produces at incidence a pair of vortices over its upper (suction) surface. The presence of these vortices results in the production of additional lift from the wing, called vortex lift. Hence, delta wings have been used as lifting surfaces for supersonic aircraft such as Concorde in order to provide extra lift in the take-off and landing stages of the flight. The main geometric characteristics of a delta wing are its sweepback angle (ϕ), and the configuration of its upper surface. This may be flat, or it may have chordwise or spanwise camber. The wing must also have sharp leading edges in order to produce the vortices. The angle of attack (α) at which the wing is set relative to the airflow is also essential. These characteristics of the wing are shown in figure 4.1.

The mechanism of vortex production has to do with the lift exerted on the wing at non-zero incidence. The air flowing around a delta wing set at an angle of attack α generates a pressure difference between the upper and lower surfaces of the wing

which is responsible for the lift production. Due to this pressure difference, the air close to the leading edges of the delta wing flows from the lower to the upper surface in much the same way as at the tips of an unswept wing of finite span. If the delta wing edges are sharp enough, separation of the boundary layer occurs. This effect generates an airflow which when separated from the leading edge moves over the upper surface and towards the centreline. The air masses close to the wing surface and near the leading edges are sucked by the fast moving air above them and follow the flow in a way that forms the vortices. (See figure 4.2). The flow, fed continuously from the leading edges on moving downstream, takes the form of two vortices (one for each leading edge), conical in shape and almost symmetric about the vortex cone centreline. (See figure 4.2). The two vortices are the mirror image of each other and thus the flow is symmetric about a plane normal to the wing surface, passing through the wing centreline.

Another important feature of the vortex flow is that the wind velocity within the vortices is found to be larger than that of the undisturbed flow far upstream of the delta wing. Hence the flow is "concentrated" from a larger area (outside the vortices) into a smaller one (in the vortices). A turbine operating within one of the vortices can take advantage of the increase in wind velocity (and thus wind power). Hence, the delta wing can be used as a "wind power augmentor". A delta wing with two turbines on it (one operating within each vortex) will be called a "delta wing-turbine system" hereafter. The idea of using a delta wing as a wind augmentor is not a new one. Several studies have been carried out in the past for developing this concept as well as surveys of the delta wing flow (related to aircraft wing development) and are presented in the following section.

4.2. REVIEW OF PREVIOUS WORK ON THE SUBJECT.

Experimental tests of delta wing models for measuring the wind velocities within the vortices have been carried out in the past. (See references [36], [37] and [38]). The flow surveys of these references are rather limited in scope and usually complimentary to more detailed measurements of the aerodynamic forces exerted on the delta wings. The first extensive flow survey can be found in reference [39]. It was carried out by Sforza who was the first to put forward the idea of using a delta wing as a wind power augmentor. Also, in [40], (by the same author), a prototype of the delta wing-turbine system has been reported to be under construction for testing the concept. Greff (see [41]) designed a similar prototype but of much larger size and performed a cost analysis of the system. The work of Greff appeared to be the last on the subject at that time. In both references [40] and [41], wind turbines were designed to operate within the delta wing vortices. However, given the flow complexity, a simple (and thus inadequate) design method has been used based on blade element considerations. It was recognised, (see [42]) that proper design of the vortex turbine blades would significantly improve the performance of the system.

During the present author's studies for the MSc degree at the University of Warwick (Jan. 1988-June 1989), an attempt was made in order to develop further the delta wing-turbine system (see reference [43]). A series of wind tunnel tests of delta wing models was carried out in order to measure the wind velocity distribution within the vortices. The velocity components of the flow (for a cylindrical frame of reference with its "z" axis coinciding with the vortex centreline) were measured in more detail than in the previous investigations, and contour plots of all velocity components in the vortices were obtained. From that investigation it was found that of the wings tested, the

best results were produced by a 79° sweptback wing, set at an angle of attack of 25°, and this was chosen to be used as an augmentor for the delta wing-turbine system. The power in the vortices produced by that wing was found to be 3.2 times as large as that of the undisturbed flow, for the same area. Of the wind velocity components, the axial was found to be the dominant one, (about 0.6 of the total velocity), the tangential was less than the axial (about 0.3 of the total) and the radial was found to be the smallest (about 0.1 of the total). The contour plots for all three components are shown in figure 4.3. It is evident from that figure that all components exhibit significant radial variations while the tangential and radial ones vary considerably with azimuth. More details about these experiments can be found in the author's MSc thesis, [43], and also in [44].

Using the information obtained by the wind tunnel tests, the vortex turbine was designed using a lifting line design procedure, whose principles have been analysed in chapter 2. The incoming flow to the turbine was taken to be the azimuthal average of the axial and tangential velocity distributions. (See figure 4.4). The radial component was neglected as it was not expected to have any significant effects. The turbine was assumed to be situated at 0.8c downstream of the wing apex (c is the wing centreline length), with its axis coinciding with the vortex centreline for obtaining the maximum flow axisymmetry, and with its diameter (D) being equal to c/6.4. Also, the turbine was assumed to rotate in the same direction as the vortex flow and with a rotational speed larger than that of the flow. The best design produced by that procedure was a 15-bladed turbine with strongly tapered, twisted and narrow blades. It was found to operate at λ=8. The aerofoil used for the turbine blades was NACA 4412.

For the case of the vortex turbine, C_p can be defined in two ways. The standard definition is:

$$C_{p,turbine} = \frac{\text{Turbine power}}{3.2\left(\frac{1}{2}\rho V_{\infty}^{3} \pi R^{2}\right)} \qquad (4.2.1)$$

The above equation is derived from (2.3.2). The power of the undisturbed flow upstream of the wing is multiplied by 3.2 which is the power increase in the vortices. Thus, the power of the flow attacking the turbine is obtained. The other definition is:

$$C_{p,system} = \frac{\text{Turbine power}}{\frac{1}{2}\rho V_{\infty}^{3} \pi R^{2}} \qquad (4.2.2)$$

The latter definition of C_p includes in the C_p value the power increase caused by the delta wing vortices. For the above mentioned turbine, $C_{p\,turbine} = 0.439$, while $C_{p,system} \approx 1.406$. In the case of the delta wing-turbine system, (unlike the conventional turbines designed in chapter 3), a multi-bladed turbine operating at a high tip speed ratio can be used, due to the wind velocity increase within the vortices. More details about the vortex turbine design can be found in [43] and also in [21].

The work to be presented in the rest of this chapter is a direct continuation of the above mentioned design work.

4.3. INVESTIGATION OF THE DELTA WING-TURBINE SYSTEM'S SUITABILITY FOR LARGE SCALE APPLICATIONS.

In the following work, the delta wing-turbine system is scaled-up and compared with already operational conventional wind turbines for assessing the system's suitability for large scale applications, as might be used for input to the National Grid. The comparison is done using the following important parameters: The relative sizes of the delta wing and the reference turbines; the ratio of rated power to turbine swept area; the ratio of the system's rotor swept area to the conventional turbine swept area; and the

delta wing area compared with the surface area of the reference turbine tower.

4.3.1. Presentation of the scaling-up method.

Four reference conventional turbines were used. They are:

- 1. Polenko WPS8 (15 kW)
- 2. Aiolos 55 (55 kW)
- 3. Aiolos 100 (100 kW)
- 4. WEG MS-3 (300 kW)

The characteristics of these turbines are shown in tables 1, 2, 3 and 4 respectively, together with the system scaling-up results for comparison.

It is evident that the rated electrical power (P_e) of the system and the conventional turbine with which it is being compared must be the same. With the power output given, the dimensions of the delta wing and the turbines can be calculated on the basis of the design results presented in the previous section and comparisons can follow. The rated electrical power of the system is given by:

$$P_e = \rho V_R^3 C_{p\,system} \eta_t \eta_g \pi R^2 \qquad (4.3.1)$$

In the above formula, P_e is equal to twice the power produced by one turbine (see equation 4.2.2) since the system was assumed to have two turbines, one for each vortex. Also, η_t and η_g are the gearbox (transmission) and generator efficiencies respectively. Use of gearboxes was assumed because, although the vortex turbine tip speed ratio is high enough to obtain direct coupling to a generator for small turbine diameters (lower than 2m), for large turbine diameters which result from the system scaling-up, the turbine rotational speed decreases and direct connection to a generator is not any more possible. In equation 4.3.1, the following parameters must be determined:

a) $C_{p\ system}$. As will be seen later, the delta wing will be a large structure, and its apex may be at a height grater than 20m. Therefore, wind shear effects are considerable. The fact that along the wing's leading edges the undisturbed wind velocity varies due to wind shear effects is expected to influence the vortices. Wind shear effects on the delta wing vortices were experimentally investigated in [45] by testing a delta wing model (with sweepback angle equal to 79°) in a wind tunnel. The result from that study was that although proximity of the delta wing to the ground (without a wind shear present) increased the wind velocity within the vortices, when a wind shear was added the beneficial ground plane effect was counterbalanced by the wind shear effect, leaving the wind velocity within the vortices nearly the same as that shown in figure 4.3. Therefore, the turbine C_p is not expected to change considerably when a wind shear is present. The value of 1.406 was used for the power coefficient, derived from the design work of [43].

b) η_t and η_g. Typical values of $\eta_t = 0.8$ and $\eta_g = 0.8$ were chosen. Hence, 64% of the mechanical power produced by the turbine is converted to electrical. This is a fair assumption, since most conventional turbines have overall efficiencies of 25% to 30%, ie $C_p \eta_t \eta_g = 0.25$ to 0.30 and with $C_p = 0.4$, this implies that $\eta_t \eta_g = 0.625$ to 0.750.

c) V_R. Determining a reasonable value for the rated windspeed (V_R) is very important, since $P_e \sim V_R^3$. The wind regime at which the delta wing-turbine system operates must be related to that of the reference turbine, for a fair comparison. The system's turbines are expected to operate at a lower rated windspeed than that of the conventional turbine with which they are being compared because the former are closer to the ground. Since the delta wing is tilted in pitch however, it "catches" fast-moving air from higher altitudes and directs it downwards, towards the turbines. Wind shear effects were taken into account when determining the rated windspeed for the system. This was done as follows: The V_R value for the reference turbine (ie the undisturbed windspeed at

the turbine's hub height) was assumed to be the undisturbed wind velocity at the delta wing apex height. (It will be shown later that the delta wing apex and the reference turbine hub heights are similar). The one-seventh power law (see reference [46]) was used for calculating the undisturbed wind velocity at the wing's trailing edge:

$$\frac{V(z_1)}{V(z_2)} = \left(\frac{z_1}{z_2}\right)^{1/7} \qquad (4.3.2)$$

The wing trailing edge was taken to be 3m above the ground for all the delta wing-turbine systems examined. Finally, V_R was assumed to be the average of V_{apex} (= V_R ref. turbine) and $V_{tr.\ edge}$:

$$V_R = \frac{V_{apex} + V_{tr.\ edge}}{2} \qquad (4.3.3)$$

With all parameters in equation 4.3.1. determined, the scaling-up calculations follow. Firstly, the value of R was calculated from equation 4.3.1:

$$R = \left[\frac{P_e}{\pi\, \rho\, V_R^3\, C_p\, \eta_t\, \eta_g}\right]^{1/2} \qquad (4.3.4)$$

The delta wing centreline length was given by: c = 6.4 D. The wing span (s) and apex height (h) were calculated from $s = 2\,c\,\cot(79°)$ and $h = c\,\sin(25°) + 3m$ respectively. (79° is the sweepback angle and 25° is the angle of attack). The turbine rotational speed (Ω) is given by:

$$\Omega = \frac{2\lambda V_R}{D}\,\frac{60}{2\pi} \text{ (in rpm)} \qquad (4.3.5)$$

4.3.2. Presentation of scaling-up results.

In tables 1 to 4, the system's scaling-up results are shown for four different cases: Case 1 with P_e = 15kW. Case 2 with P_e = 55kW. Case 3 with P_e = 100kW and

case 4 with P_e = 300kW. In each case the system V_R is different, calculated from (4.3.3) in order to match the flow the reference turbine is experiencing. From tables 1, 2, 3 and 4 it is evident that with P_e increasing, the system's turbine radius increases. Comparison

TABLE 1 CASE 1
P_e = 15 kW

	Delta wing-turbine system	Reference turbine: Polenko WPS8
V_R	10.5 m/s	12 m/s
R	1.9 m	4.25 m
D	3.8 m	8.5 m
c	24.32 m	-
s	9.45 m	-
h	13.28 m	16 m
Ω	430.22 rpm	Not known
B	15	3
$\frac{P_e}{2\pi R^2}$ = 661.3 W/m^2	$\frac{P_e}{\pi R_{ref}^2}$ = 264.3 W/m^2	$\frac{\pi R_{ref}^2}{2\pi R^2}$ = 2.5
Delta wing Area = 114.9 m^2	Tower Area = 104.9 m^2	

TABLE 2 CASE 2
P_e = 55 kW

	Delta wing-turbine system	Reference turbine: AIOLOS 55
V_R	12 m/s	14 m/s
R	3.1 m	7.75 m
D	6.2 m	15.5 m
c	39.7 m	-
s	15.4 m	-
h	19.78 m	24 m
Ω	295.7 rpm	56 rpm
B	15	3
$\frac{P_e}{2\pi R^2}$ =910.9 W/m^2	$\frac{P_e}{\pi R_{ref}^2}$ = 291.5 W/m^2	$\frac{\pi R_{ref}^2}{2\pi R^2}$ = 3.13
Delta wing Area : 305.7 m^2	Tower Area : 278.7 m^2	

between tables 1 and 5 reveals that the system's turbine radius decreases for the same P_e and with V_R increasing. For each case, the ratio [rated power]:[turbine swept area] was calculated as an indication of the system's performance and it was compared with that of the reference turbines. For the system, $P_e/2\pi R^2$ was calculated, since two turbines are used. It was found that $P_e/2\pi R^2$ increases with V_R increasing (since $P_e \sim V_R^3$). For the reference turbines, $P_e/\pi R_{ref}^2$ was calculated. It was also found to increase with V_R increasing for the turbines of cases 1, 2 and 3. Comparing cases 1 and 4 reveals that the WEG MS-3 turbine has a higher $P_e/\pi R_{ref}^2$ than the Polenko turbine. This is due to the technology improvement in turbine design and construction that has taken place in the recent years. Polenko WPS8 is a rather old turbine, while WEG MS-3 is a recent state-of-the-art turbine with better blade quality and generator-transmission efficiencies than the former.

TABLE 3 CASE 3
P_e = 100 kW

	Delta wing-turbine system	Reference turbine: AIOLOS 100
V_R	12.9 m/s	15 m/s
R	3.7 m	9.5 m
D	7.4 m	19 m
c	47.36 m	
s	18.41 m	
h	23.0 m	30.0 m
Ω	266.35 rpm	52 rpm
B	15	3
$\frac{P_e}{2\pi R^2}$ = 1162.6 W/m²	$\frac{P_e}{\pi R_{ref}^2}$ = 352.7 W/m²	$\frac{\pi R_{ref}^2}{2\pi R^2}$ = 3.3
Delta wing Area : 435.9 m²	Tower Area : 437.9 m²	

Comparison of the delta wing system and the reference turbines reveals that the system requires less turbine swept area than the conventional turbines (for the same power output). As a comparative indicator, the ratio $\pi R_{ref}^2/2\pi R^2$ was calculated for

all cases. The ratio is always larger than 1.0 and its highest value is that for case 3. Its lowest value is 1.36 for case 4 showing once more the improved performance of the WEG MS-3 turbine. Another very important parameter is the overall size of the system.

TABLE 4 CASE 4
P_e = 300 kW

	Delta wing-turbine system	Reference turbine : WEG MS-3
V_R	9.5 m/s	11 m/s
R	10.0 m	16.5 m
D	20.0 m	33.0 m
c	128.0 m	-
s	49.8 m	-
h	57.1 m	25 m
Ω	72.6 rpm	48 rpm
B	15	2
$\frac{P_e}{2\pi R^2}$ = 477.5 W/m^2	$\frac{P_e}{\pi R_{ref}^2}$ = 350.8 W/m^2	$\frac{\pi R_{ref}^2}{2\pi R^2}$ = 1.36
Delta wing Area : 3187 m^2	Tower Area : 350.0 m^2	

If the system is physically larger than the equivalent conventional turbine, it is not expected to be cost-effective, as more material will be needed for its construction. To determine this, the overall dimensions of the system were compared with those of the reference turbines. Figures 4.5, 4.6 and 4.7 show sketches of the systems and equivalent turbines for cases 1, 3 and 4 respectively. Figures 4.5 and 4.6 show that the systems compare favourably with the reference turbines. Their turbines are smaller and closer to the ground which makes installation and maintenance easier. The delta wing center of mass is lower, which is an advantage. However, large delta wings are needed. Their centreline lengths are: 24.3m for case 1 and 47.4m for case 3. The vertical height (h) of the delta wing apex is 13.3m and 23.0m for cases 1 and 3 respectively. These heights are smaller than the tower heights of the equivalent reference turbines, as shown in figures 1

and 2. Also, the delta wing spans for cases 1, 2 and 3 are about the same as the equivalent reference turbines' rotor diameters. As an indication of the material required for construction, the delta wing area was compared with the reference turbine tower surface area. For cases 1, 2 and 3 the two areas are about the same. Therefore, it can be concluded that the delta wing system is of comparable size with a conventional turbine producing the same power up to 100kW.

However, comparison between the system and the WEG MS-3 turbine (see figure 4.7 and table 4) is in favour of the latter. This is due to the enormous size of the delta wing required. Although the delta wing turbines are smaller in diameter than the WEG MS-3 rotor, the delta wing centreline is 128m long and the wing apex height is about 57m above the ground, while the WEG MS-3 turbine tower height is only 25m. The increase of the delta wing relative size compared to the reference turbine for case 4 is caused by the decrease in the [tower height]:[rotor diameter] ratio with P_e increasing for the conventional turbines. As shown below:

Polenko WPS8: h/D = 1.88

Aiolos 100: h/D = 1.57

WEG MS-3: h/D = 0.76

Unlike conventional turbines, the ratio of [delta wing centreline]:[rotor diameter] remains constant (c/D=6.4) and this causes the increase in the delta wing relative size.

4.3.3. Changes in the system's design for increasing the turbine rotational speed.

As can be seen from tables 1, 2, 3 and 4, for all cases the system turbines operate at a rotational speed lower than 500 rpm which is considered as the lowest value of a generator's rotational speed for it to operate efficiently. (See also reference [47]).

Therefore gearboxes are necessary. However, the rotational speed of the system turbines is much higher than that of the equivalent reference turbines. For example, for case 2, we get: Ω/Ω_{ref}=5.4. This means that lower step-up ratio gearboxes will be necessary for the system turbines. This should reduce the gearbox weight and improve its efficiency [48]. However, it will also be noticed from tables 1, 2, 3 and 4 that the system's turbines operate at rotational speeds which are close to the 500 rpm threshold (especially that of case 1). Alterations to the system's design were attempted for increasing Ω and making direct coupling of the turbines to generators possible. One alteration is to mount the system on a tower. This would increase V_R and since a lower turbine radius would be needed for the same power output, Ω should increase. Mounting the system on a tower was considered practical only for the 15kW case where the smallest delta wing is required. In table 5, the characteristics of a system mounted on a 16m high tower,

TABLE 5 CASE 5

P_o = 15 kW. System on top of a 16m high tower.

	Delta wing-turbine system	Reference turbine : Polenko WPS8
V_R	12 m/s	12 m/s
R	1.6 m	4.25 m
D	3.2 m	8.5 m
c	20.5 m	-
s	8.0 m	-
h	24.86 m	16 m
Ω	572.9 rpm	Not known
B	15	3
$\frac{P_o}{2\pi R^3}$ = 932.5 W/m^2	$\frac{P_o}{\pi R_{ref}^2}$ = 264.3 W/m^2	$\frac{\pi R_{ref}^2}{2\pi R^3}$ = 3.5

producing 15kW of power are shown. The delta wing dimensions are about 16% smaller than that of case 1. The turbine's rotational speed is 572.9 rpm and for that case direct connection to a generator is possible. Furthermore, there would appear to be no reason

why the system should not be mounted inverted, with the apex lower than the trailing edge and turbines suspended beneath the delta wing. As well as facilitating easier access for maintenance, the turbines would be substantially sheltered from rain.

TABLE 6

AEROFOIL : NACA 4412

$\alpha_{opt} = 4°$, $C_L(\alpha_{opt}) = 0.85$, $C_D(\alpha_{opt}) = 0.007$.

Rotational speed for various turbine configurations

No. of blades (B) → / Turbine radius (R) ↓	B = 2 $C_{p,max} = 1.011$ $\lambda = 18.0$ With direct coupling performance decrement to 10%	B = 5 $C_{p,max} = 1.201$ $\lambda = 13.0$ With direct coupling performance decrement to 8.5%	B = 10 $C_{p,max} = 1.332$ $\lambda = 9.5$ With direct coupling performance improve to 13.5%	B = 15 $C_{p,max} = 1.406$ $\lambda = 8.0$ $C_{p,max}\eta_t = 1.125$
CASE 1 R = 1.9 m V_a = 10.7 m/s D = 3.8 m	968 rpm	699.1 rpm	510.9 rpm	430.2 rpm
CASE 2 R = 3.1 m V_a = 12 m/s D = 6.2 m	665 rpm	480.5 rpm	351.2 rpm	295.7 rpm
CASE 3 R = 3.7 m V_a = 12.9 m/s D = 7.4 m	599.3 rpm	432.8 rpm	316 3 rpm	266.4 rpm
CASE 4 R = 10 m V_a = 9.3 m/s D = 20 m	163.3 rpm	117.9 rpm	86 2 rpm	72.6 rpm
Tip Mach Number	0.50	0.36	0.27	0.23

Another way of increasing Ω is to reduce the number of turbine blades. As explained in [21] and also in chapter 3, a reduction of the number of turbine blades reduces the turbine aerodynamic efficiency. However, if due to the increase in Ω, direct coupling to a generator is possible, $\eta_t = 1.0$ and the system overall efficiency ($C_p\eta_t\eta_g$) may increase. In table 6, the rotational speed of the system turbines for cases 1, 2, 3 and 4 were calculated when 2-bladed, 5-bladed and 10-bladed turbines were used. For this calculation, the turbine radius was taken to be the same as that of the original design (ie the 15-bladed turbine version) for all cases and the power output was allowed to vary. For case 1, it can be seen from table 6 that Ω is larger than 500 rpm and hence direct coupling is possible for all turbine versions mentioned above. However, only the use of a 5-bladed or a 10-bladed version improves the system's performance compared to the

system with the 15-bladed turbines. Use of a 10-bladed turbine seems quite attractive, since $C_p\eta_t\eta_g$ increases by 15% compared to the original design. For case 2, it is possible to achieve direct coupling using the 2-bladed turbine. Use of 5-bladed turbines gives a value of Ω of 480.5 rpm which is just below the 500 rpm minimum at which direct coupling can be considered. For case 3, only 2-bladed turbines can produce a high enough Ω, while for case 4, gearboxes are necessary. It can therefore be concluded that direct coupling of the system's turbines to generators can be advantageously be achieved by reducing the number of turbine blades for systems with turbine diameters up to 3.7m.

4.3.4 Conclusions.

The most important conclusions drawn from this study are:

1. Compared with equivalent conventional turbines, the delta wing-turbine system requires lower total turbine swept area for the same power output. The two turbines operate closer to the ground which reduces erection and maintenance costs. They also operate at higher rpm and hence can be more efficient.
2. The delta wing required may be a large structure. This could be a disadvantage if the material needed for its construction is more than that of the equivalent conventional turbine. The relative delta wing size compared to the size of the reference turbine tower, increases with increasing power output as a result of the tower height to turbine diameter ratio dropping with increasing power output for conventional turbines.
3. Comparison between the delta wing-turbine system and the conventional turbines favours the former for lower power outputs (15 kW to 100 kW)

and the latter for higher power outputs (300 kW and above).

4. Alterations in the system's design can eliminate the need for gearboxes. Mounting the system on a tower is an attractive solution for the case of 15kW of rated electrical power, with the possibility of inverting the system to facilitate better turbine access and to provide some rain protection to the turbines. Reduction of the turbines' number of blades can also make direct coupling to generators possible, producing a net performance improvement in smaller systems.
5. Advantages and disadvantages of the system compared to equivalent conventional turbines:

Advantages:

- Smaller rotor area for a given rated power.
- Rotors operate at larger rotational speeds. This enables use of lighter weight and more efficient gearboxes, or if alterations in the system's design are implemented, gearboxes can be eliminated (for power outputs approximately up to 100kW).
- Rotors are closer to the ground. This reduces erection and maintenance costs.

Disadvantages:

- The only disadvantage is the large delta wing needed. However, for smaller power turbines, (15-100 kW), the overall sizes of equivalent machines are comparable.

4.4. DESIGN OF VORTEX TURBINE TO OPERATE IN THE LOW REYNOLDS NUMBER REGIME.

The decision was made to design and build a delta wing-turbine system prototype for proving the concept and assessing the accuracy of the turbine design method. The vortex turbine of the prototype was chosen to have a diameter of 1.2m. Reynolds number effects become signficant for turbines of small sizes, and the prototype vortex turbine was redesigned taking into account Re effects. The modifications necessary to the original turbine design are described in the following.

4.4.1. Reynolds number effects.

The delta wing-turbine system was originally designed for large scale applications assuming that Reynolds number effects were negligible. This assumption is true for the delta wing, since vortex generation is Re-independent as long as the leading edges are sharp enough to produce a totally separated flow. The only effect Re may have on the vortices is limited to their viscous core and the occurrence of vortex breakdown which is not of interest from our point of view.

The vortex turbine on the other hand, is greatly affected by Re: The C_p produced by a turbine is a non-dimensional quantity and it is desirable for it to be scale independent. However, in reference [49], C_p was found to vary considerably with turbine diameter, especially for small scale rotors (less than 2m in diameter), reflecting the effects of varying Reynolds number based on chord length (chord Re) on the aerofoil characteristics. These effects are caused by the boundary layer behaviour of aerofoils at low values of Re (typically below 10^5).

As explained in references [50], [51], [52] and [53], the boundary layer of

an aerofoil upper (suction) surface starts by being laminar (assuming a smooth aerofoil surface and low free stream turbulence). Depending on Re, it may or may not trip to turbulent. For low values of Re, the boundary layer is still laminar beyond the minimum pressure point and if the pressure gradients are mild enough, the flow can be completely laminar throughout the aerofoil. As the angle of attack increases, the adverse pressure gradients become steeper and laminar separation of the boundary layer is inevitable. At very low Re, (below $3x10^4$), this separation can cover the entire rear of the aerofoil thus causing a severe reduction of $dC_L/d\alpha$ and an increase of C_D. For higher Re values however, the separated laminar boundary layer undergoes transition to turbulence as the free shear layer generated by separation is more transition susceptible. The subsequent turbulent entrainment of high-speed fluid causes the flow to reattach to the surface, forming a separation bubble, which is the most important characteristic of low Re boundary layers on aerofoils. Downstream of the reattachment point, the newly formed turbulent boundary layer is capable of negotiating quite severe adverse pressure gradients without separation. This allows for some pressure recovery downstream of the reattachment point and hence to an improvement in the C_L/C_D ratio of the aerofoil. For very large Re values (beyond 10^6), transition to turbulence can occur before the minimum pressure point and the separation bubble can be avoided. As was pointed out by Charmichael [52], the bubble length (ie the distance from separation to reattachment) can be expressed as a Reynolds number of about $5x10^4$. This is consistent with the general observation that the critical Re value of an aerofoil is about $7x10^4$. Below this value, the aerofoil is physically too short for the bubble to form and its $(C_L/C_D)_{opt}$ is very poor. Beyond the critical Re value, acceptable values of $(C_L/C_D)_{opt}$ can be obtained and they increase rapidly with Re increasing. This can be explained as follows: For a supercritical aerofoil of chord Re equal to $7x10^4$, the separation bubble covers a large

portion of the aerofoil upper surface and changes the pressure distribution by effectively altering the shape over which the outer potential flow is developed. Hence, the sharp suction peak predicted by potential flow theory is not realised and a suction plateau of a reduced level extends over the region occupied by the bubble. With Re increasing, the relative bubble length (with respect to the aerofoil chord) decreases allowing for increasingly more suction to be obtained which in turn improves the aerofoil performance. Re effects become negligible for Re > $2x10^5$. The Reynolds number regime below 10^5 is usually called "low Re regime".

Wind turbines of small diameters (below 2m) with high aspect ratio blades can have subcritical blade chord Re values resulting in reduced efficiency. Indeed, the chord Re values of the vortex turbine when scaled-down to the prototype size (ie D = 1.2m) and for a value of V_∞ = 10 m/s were found to range from $5x10^4$ at the hub to $4x10^4$ at the tip. For these values of Re and for the aerofoil chosen (NACA 4412), $(C_L/C_D)_{opt}$ was found to be about 23, (see reference [25]), while for the original design for which Re was taken to be equal to $3x10^6$, the NACA 4412 $(C_L/C_D)_{opt}$ was about 100. The C_p prediction for the prototype vortex turbine (using the lifting line design procedure of [43] with $(C_L/C_D)_{opt}$ = 23) was found to be 20% less than that of the original design (with $(C_L/C_D)_{opt}$ = 100). Therefore, modifications to the original design were necessary for improving the prototype turbine's efficiency.

4.4.2. Modifications in the blade design procedure.

The lifting line blade design procedure used for the high Re vortex turbine design in [43] was also used here, with some modifications. The derivation of equations as well as the steps of the iteration have been presented in chapter 2.

For the analysis of the bound circulation (G) and induction factors ($i_{a,t}$) in

the fourier series the numerical integration method has been used, since for the case of the vortex flow, it was found to produce satisfactory results. The following formulae have been used for the fourier coefficients G_m and $I^{a,i}_n$:

$$G_m = \frac{2}{\pi}\int_0^{\pi} G(\phi)\,\sin(m\phi)\,d\phi$$

$$I^{a,i}_n(\phi) = \frac{2}{\pi}\int_0^{\pi} i_{a,i}(\phi\,,\,\phi_0)\,\cos(n\phi_0)\,d\phi_0\,,\quad n = 1\,,\,2\,,\,\ldots\,,\,N \qquad (4.4.1)$$

and

$$I^{a,i}_0(\phi) = \frac{1}{\pi}\int_0^{\pi} i_{a,i}(\phi\,,\,\phi_0)\,\,d\phi_0$$

The integrals in the above equations were numerically calculated using the Simpson's method. 30 coefficients were found to be necessary for the analysis of both G and $i_{a,i}$. For estimating each coefficient, 61 points along the blade were used in the numerical integration method.

The incoming flow velocity distributions were taken to be those shown in figures 4.4. (Axial and tangential components).

The relaxation technique described in chapter 3 (equation 3.1.1) was found to be necessary for achieving convergence for values of c_{max}/R larger than 0.15.

Finally, for incorporating Re effects in the design procedure, the following modification was applied: After convergence was achieved and before C_p was calculated, the values of chord Re along the blade were estimated using the local flow results and the blade chord distribution. For each blade station, $C_D(\alpha_{opt})$ was calculated from data as a function of Re:

$$C_D(\alpha_{opt}, Re) = \begin{cases} C_{D1}, & Re \le 7x10^4 \\ C_{D2}, & 7x10^4 < Re < 9x10^4 \\ C_{D3}, & Re \ge 9x10^4 \end{cases} \qquad (4.4.2)$$

with C_{D1}, C_{D2} , C_{D3} depending on the aerofoil section used each time.

Most of the turbines designed had a chord distribution given from equation 3.2.1 which produces waisted and tapered blades. However, some blades with linear taper distribution (and no waisting) were also tried. The diameter of all turbines was taken as 1.2m and the V_∞ value was chosen to be 10 m/s.

4.4.3. Changes in the turbine blade design.

There are two ways of improving the performance of the prototype turbine at its low Reynolds numbers. One is to improve the aerofoil section performance by using a more suitable low Re aerofoil. The other is to improve the $(C_L/C_D)_{opt}$ ratio by increasing the chord Re towards supercritical values , and by adjusting the value of α_{opt} along the blade according to the local chord Re. The attempts made in all directions are presented below. All low Re turbines designed were compared with the original high Re turbine design which will be called "reference turbine" hereafter and whose turbine power coefficient is $C_{p,ref} = 0.439$.

1. Change of aerofoil section.

Information about low Re aerofoils was obtained from references [54] and [55]. Five sections which seemed the most promising were selected and tested. For each

aerofoil, the maximum performance of a 10-bladed turbine with $C_0 = 0.03$ and $E = 1.5$ in equation 3.2.1 was estimated (using the above mentioned design procedure) and the C_p results were compared with $C_{p,ref}$. The characteristics of each aerofoil together with the investigation results are shown in table 7. From this table it is evident that the larger the aerofoil $C_L(\alpha_{opt})$ the lower is the λ at which $C_{p\,max}$ is achieved. This happens because with $C_L(\alpha_{opt})$ increasing the induced drag also increases. The values of induced

TABLE 7

$B = 10$, $C_0 = 0.03$, $E = 1.5$, $R = 0.6$ m , $V_\infty = 10$ m/s. Data referred to $Re = 6x10^4$.

Aerofoil :	NACA 0012	FX M2	GOE 795	E 193	SOKOLOV
α_{opt} :	6°	3°	6°	11°	10°
$C_L(\alpha_{opt})$:	0.625	0.725	0.80	1.08	1.12
$(C_L/C_D)_{opt}$:	25.0	32.5	40.0	39.0	52.0
ΔC_p *	-17.1%	-14.8%	-9.0%	-10.7%	-12.7%
λ **	7.6	7.25	7.0	6.0	5.25

* $\Delta C_p = (C_p - C_{p,ref})/C_{p,ref} \times 100$.

** this is the tip speed ratio at which $C_{p,max}$ is achieved.

velocities (u_i, v_i) for the same λ and different $C_L(\alpha_{opt})$ values change in proportion with $C_L(\alpha_{opt})$. The best C_p result is achieved for the GOE 795 section. The aerofoils with lower $C_L(\alpha_{opt})$ (ie NACA 0012 and FX M2), although they operate at higher λ and subsequently have higher chord Re, do not produce more C_p since their $(C_L/C_D)_{opt}$ values are poor even at relatively high Re. On the other hand, the high lift aerofoils (ie SOKOLOV and E 193) produce less C_p than GOE 795 even though they have higher $(C_L/C_D)_{opt}$ ratios. This can be explained by comparing the SOKOLOV and GOE 795 sections. In table 8, the values of Re and $(C_L/C_D)_{opt}$ for the two aerofoils are shown for

TABLE 8

$B = 10$, $C_0 = 0.03$, $E = 1.5$, $R = 0.6$ m , $V_\infty = 10$ m/s.

	Aerofoil : GOE 795 $\lambda_{opt} = 7$		Aerofoil : SOKOLOV $\lambda_{opt} = 5.75$	
r/R	Re (at λ_{opt})	$(C_L/C_D)_{opt}$ (at λ_{opt})	Re (at λ_{opt})	$(C_L/C_D)_{opt}$ (at λ_{opt})
0.4	100,000	55	80,000	56
0.9	50,000	35	40,000	10

two radial stations along the blade for the value of λ for which each turbine achieves $C_{p,max}$. It is clear that the turbine with the SOKOLOV section operates at lower λ (due to the high $C_L(\alpha_{opt})$ value) than that with the GOE 795 section. At a lower λ however, Re is also lower and hence $(C_L/C_D)_{opt}$ remains lower or equal to that of GOE 795, resulting in the production of less C_p. The aerofoil chosen to be used for the prototype turbine design is GOE 795 which has a moderate $C_L(\alpha_{opt})$ that keeps the induced drag at low levels. At the same time, it has sufficiently high $(C_L/C_D)_{opt}$ to produce the largest C_p from all the turbines presented in table 7. However, its C_p value is still 9% less than $C_{p\,ref}$.

2. Increasing Re.

Although the GOE 795 section has a better performance than the NACA 4412 aerofoil (which was used for the reference turbine) at low Reynolds numbers, the values of chord Re for a 15-bladed turbine with $C_0 = 0.015$, $E = 1.5$ (ie the reference turbine blade parameters), with $D = 1.2$m, $V_\infty = 10$ m/s and using GOE 795 are still subcritical. As shown in table 9, column 1, the C_p produced by by such a turbine is 12.5% less than $C_{p\,ref}$. The C_p can improve if the chord Re becomes supercritical. This can be achieved in two ways.

a) Increasing the blade chord length.

A turbine with blades of chord length to radius ratio three times larger than

TABLE 9

R = 0.6 m , V_∞ = 10 m/s. Aerofoil : GOE 795

	1	2	3	4	5	6	7	8
	B = 15 C_0 = 0.015 E = 1.5	B = 10 C_0 = 0.030 E = 1.5	B = 9 C_0 = 0.030 E = 1.5	B = 8 C_0 = 0.030 E = 1.5	B = 8 C_0 = 0.062 E = 1.0	B = 5 C_0 = 0.045 E = 1.5	B = 10 Linear chord contraction. α_{tip} = 6°	B = 10 Linear chord distribution. Variable α_{tip}
ΔC_p *	-12.5%	-9.0%	-10.4%	-12.0%	-22.5%	-19.6%	-6.3%	-4.7%
λ **	8.0	7.0	7.25	7.5	5.25	7.5	6.75	6.75

*$\Delta C_p = (C_p - C_{p,ref})/C_{p,ref} \times 100$

** this is the tip speed ratio at which $C_{p,max}$ is achieved.

that of the reference turbine was tested. The number of blades was reduced to 5, so that the turbine solidity would be the same as that of the reference turbine. That was necessary in order to keep the turbine tip speed ratio at the same high levels (between 6 and 8) and thus make direct coupling of the turbine to a generator possible. As shown in table 9, column 6, although the chord Re is supercritical thoughout the blade, the C_p value was found to be considerably lower than $C_{p\,ref}$ (-19.6%). The C_p was reduced as a result of the reduction in number of blades. For better results, more blades were needed of smaller chord, and three more turbines were tested: A 10-bladed, a 9-bladed and an 8-bladed one. Their chord-to-radius ratio was double that of the reference turbine. The waisting distribution was kept the same as that of the reference turbine (ie E=1.5). It was found (see table 9, columns 2, 3 and 4) that the 10-bladed turbine produced the best results. The chord Re was found to be supercritical for the inboard 80% of the blade (for optimum conditions). The turbine was found to operate at λ = 7 and to produce a C_p 9% less than $C_{p\,ref}$. The other two turbines operate at marginally larger λ (λ increases with B decreasing) and produce less C_p (this being an effect of the reduction in the number of blades).

b) Reduction in taper.

Another way to increase Re close to the tip is the reduction of taper. An 8-bladed turbine was tested with $c/R = 0.062 \sin\phi/x$. It had the same maximum chord as the 10-bladed turbine, but the chord was considerably larger at the tip region. (See figure 4.8). The vast increase in the tip vortex strength (ie the u_i and v_i values close to the tip) down-graded the turbine's efficiency, causing it to operate at lower λ (=5.25) and produce 22.5% less C_p than $C_{p,ref}$. (See table 9, column 5). Several other turbines were also tested, having values of E between 1.0 and 1.5. They all had considerably larger chord at the tip region compared to the 10-bladed turbine and as a result, they produced less C_p. A 10-bladed turbine with linear chord distribution (ie no waisting) was also tried. Its chord configuration is shown in figure 4.8. It can be seen that the linear taper blade and the blade with $C_0 = 0.03$, E = 1.5, have almost the same chord from $x = 0.9$ to $x = 1.0$. That should keep the tip vortex strength at the same levels for both turbines. However, the linear taper blade has larger chord from $x = 0.4$ to $x = 0.9$. That should increase the local Re values in that region. As can be seen in table 9, column 7, the linear taper turbine operates at $\lambda = 6.75$ and produces a C_p 6.3% less than $C_{p,ref}$. This improvement in the turbine performance is a result of the increase of Re in the region $0.4 \le x \le 0.9$. It can be therefore concluded that a turbine with linear chord distribution is more suitable at the low Re regime.

3. Increase of $(C_L/C_D)_{opt}$ by adjusting α_{opt} according to Re.

For the GOE 795 aerofoil, the value of α_{opt} depends on Re at the low Reynolds number regime. With Re increasing, the boundary layer on the suction side of the aerofoil remains attached for increasingly large angles of attack, and as C_L increases more rapidly than C_D, α_{opt} (and $(C_L/C_D)_{opt}$) increases. The turbines presented in table 9, columns 1 to 7, were designed assuming that $\alpha_{opt} = 6°$. This value of α_{opt} is achieved

when Re = $6x10^4$. However, the values of Re vary along the blade from 10^5 at x=0.2 to $4x10^4$ at x=0.9. As a further improvement in the turbine blade design, α_{opt} was allowed to vary linearly from 7° at the blade hub, to 5° at the tip, so that the largest part of the blade would operate at optimum angle of attack. A turbine with linear chord distribution (like the one in table 9, column 7) and with the above modification implemented was tested. As shown in column 8 of table 9, a further improvement of C_p was achieved: C_p was found to be 4.7% less than $C_{p\,ref}$ at λ=6.75.

The turbine chosen to be used for the delta wing-turbine system prototype is that with the linear chord distribution and variable α_{opt}. Its characteristics are shown in table 10. It produces 4.7% less C_p than the reference turbine, but this is the smallest possible reduction in the turbine efficiency due to scale effects.

TABLE 10

B = 10 , D = 1.2 m , V_∞ = 10 m/s , $C_{p\,max}$ = 0.419 , λ = 6.75.

$$c/R = \begin{cases} 1.7\,x - 0.255\,, & 0.15 \le x \le 0.23 \\ -0.169\,x + 0.175\,, & 0.23 < x < 0.98 \\ -0.5\,x + 0.5\,, & 0.98 \le x \le 1.00 \end{cases}$$

x	c/R	β (twist angle) in degrees
0.150	0.000	83.04
0.196	0.079	52.24
0.325	0.120	24.93
0.509	0.090	9.64
0.706	0.056	5.04
0.876	0.028	4.51
0.979	0.010	2.53
1.000	0.000	1.90

4.4.4. Conclusions.

The main conclusions drawn from this study are:

1. The power coefficient produced by a turbine depends on the turbine's dimensions, especially for turbines of small diameter whose chord

Reynolds numbers are below 10^5.

2. A high Re turbine designed to operate in the flow produced by a 79° sweptback delta wing set at an angle of attack of 25° exhibits a drop of 20% of its power coefficient when it is scaled down to a diameter of 1.2 m.
3. Use of low Re aerofoils improves the low Re vortex turbine performance. Of the sections tested, the GOE 795 produced the best results.
4. Different principles apply for the optimisation of delta wing vortex turbines operating at the high Re regime as opposed to those operating at the low Re regime. For the former, reduction of blade chord length and increase of number of blades improves their performance. Only construction feasibility considerations set the limit to how small the blade chord can become. For the latter however, the fact that the chord Re must be supercritical restricts the reduction of the blade chord length. Turbines with blades of larger chord-to radius ratio and fewer blades than the former are more suitable.
5. A turbine with linear blade chord distribution was found to perform better than other similar turbines with different chord distributions, as higher values of chord Re (and hence C_L/C_D) were obtained in the region between $x = 0.4$ and $x = 0.9$, for that turbine. Adjustment of the α_{opt} values along the blade according to the local Re, further improves the turbine performance.
6. A 10-bladed turbine having blades with linear chord distribution and with α_{opt} varying linearly from 7° at the blade hub to 5° at the tip, was chosen to be used for a delta wing-turbine system prototype. The aerofoil chosen is GOE 795. The turbine operates at $\lambda = 6.75$ and produces a C_p 4.7% lower than that of the high Re, 15-bladed turbine.

4.5. PERFORMANCE ANALYSIS OF THE PROTOTYPE TURBINE.

The blade design procedure can predict the prototype turbine performance at optimum operating conditions only. For estimating the turbine performance at non-optimum conditions (ie values of λ other than λ_{opt}), a performance analysis procedure was developed, based on lifting line theory. It is presented here.

4.5.1. Description of the procedure.

The turbine performance analysis procedure used here was first proposed by Politis, [15], for predicting the performance of conventional turbines. It was modified to fit the case of the prototype turbine. This procedure is also based on the theory developed by Lerbs, [18], and the wake model presented in chapter 2 is used. Unlike the turbine design case, the geometrical characteristics of the turbine (ie chord c and twist angle β distributions along the blade) are known before hand when the turbine performance is sought. Hence, the condition imposed by equation 2.3.1 does not hold and the angle of attack can take any value along the blade, according to the local flow at each blade element. Therefore, C_L in the loading equation 2.3.3 is no longer a constant, but a variable, and equation 2.3.3 becomes:

$$G = \frac{1}{4\pi} \frac{W}{V_\infty} \frac{c}{R} \left[\frac{dC_L}{d\alpha} (\beta_i - \beta) + C_{L0} \right] \qquad (4.5.1)$$

In the above equation, C_L was assumed to vary linearily with α ($= \beta_i - \beta$). C_{L0} is the lift coefficient value for zero angle of attack, which is larger than zero for cambered aerofoils, and $dC_L/d\alpha$ is the slope of the lift coefficient. The linearisation of C_L is

essential in obtaining a convergent iterative procedure for solving the problem as will be seen later. Substituting equations 2.2.12 into 2.3.8, we get:

$$\tan\beta_i = \frac{u/V_\infty - \frac{1}{1-x_h}\sum_{m=1}^{M} m\, G_m\, h_m^a}{\lambda x - v/V_\infty + \frac{1}{1-x_h}\sum_{m=1}^{M} m\, G_m\, h_m^t} \qquad (4.5.2)$$

Equations 4.5.1 and 4.5.2 provide a system for solving the problem. The unknown variables are the distributions of β_i and G along the blade for each operating condition. Since these are inter-related in a non-linear way, the problem can only be solved iteratively, by successive approximations. The iteration scheme used here, is different from that presented in chapter 2 and was proposed by Politis in [15]. The iteration steps are:

STEP 1.

An initial distribution of the aerodynamic angle β_i along the blade is assumed. The β_i values are calculated at an adequate number of stations along the blade (ie on M points). Substituting that in equation 4.5.2 a system of M linear equations can be obtained which can be solved for the M coefficients (G_m) resulting from the analysis of G in a sine fourier series. (See equation 2.3.5).

STEP 2.

After the G_m values are calculated, substitution of the resulting value of G in equation 4.5.1 (and by use of equation 2.3.5) yields a β_i distribution which is in general different from the initial. If step 1 is repeated using the new β_i distribution, an overoscillating iterative sequence results which is divergent. Damping of the β_i change between iterations is needed and it is obtained as follows: Equation 4.5.1 is solved for β (ie twist angle) instead of β_i and a "new" β distribution is obtained. It is evident that the new β distribution has no physical meaning, as it is not possible to change the blade twist angle

to suit the local flow. It is merely used as a guide as to how β_i should change. It can also be noted that an analytical expression of C_L as a function of β is necessary in equation 4.5.1 in order to obtain the new values of β. The linear relation used is true for almost all aerofoils before stall.

STEP 3.

The distributions of β_{new} and β are compared, and if they are not close enough, the values of β_i are updated using the following correction factor:

$$\Delta\beta = \mu\left(\frac{\beta - \beta_{new}}{|\beta| + |\beta_{new}| + Q}\right) \qquad (4.5.3)$$

with μ a damping constant and Q a positive constant that prevents the denominator from becoming zero when $\beta = \beta_{new} = 0$. The new β_i distribution is then calculated by:

$$\beta_{i,new} = \beta_i (1 + \Delta\beta) \qquad (4.5.4)$$

In that way, β_i is directed towards values that bring β_{new} closer to β. If for example $\beta_{new} > \beta$, then $\Delta\beta < 0$ and $\beta_{i,new}$ decreases. The iteration is then repeated until convergence is achieved.

STEP 4.

After convergence is achieved, all other calculations follow. The power coefficient of the turbine is calculated using equation 3.1.3. For the vortex turbine, equation 3.1.3 leads to estimation of $C_{p,system}$. (See equation 4.2.2). For obtaining $C_{p,turbine}$, $C_{p,system}$ must be divided by 3.2 (ie the power concentration in the vortex). Other useful quantities that are calculated are the driving force and thrust distributions along the blade.(dF_D and dT respectively). They are given from:

$$\begin{aligned} dF_D &= \tfrac{1}{2}\rho W^2 c (C_L \sin\beta_i - C_D \cos\beta_i) dr \\ dT &= \tfrac{1}{2}\rho W^2 c (C_L \cos\beta_i + C_D \sin\beta_i) dr \end{aligned} \qquad (4.5.5)$$

4.5.2. Numerical techniques used.

A computer program written in fortran was developed for performing the above mentioned calculations. The numerical techniques applied are described here.

For solving the system of linear equations resulting from (4.5.2), the values of $h^{a,t}_m$ must be calculated. This is done as follows: The values of the induction factors $i_{a,t}$ are calculated first, by use of equations 2.2.7. Then, they are analysed in fourier series using equation 2.2.11. The fourier coefficients $I^{a,t}_n$ are calculated by solving a system of linear equations as described in chapter 3, part 3.1.1. With the values of $I^{a,t}_n$ known, the Lerbs factors $h^{a,t}_m$ can be calculated from equations 2.2.13 and 2.2.14. The linear system of equations resulting from (4.5.2) is solved using the technique described in chapter 3, part 3.1.1. The number of fourier coefficients used for the analysis of G and $i_{a,t}$ (M and N+1 respectively) affects the accuracy of the results. The more the fourier coefficients, the better the accuracy. However, the values of M and N determine the number of linear equations to be solved, and as the time required by the linear system solving routine is proportional to M^3 (or N^3), more fourier coefficients means a more time-consuming program. A good compromise was found to be the choice of 31 fourier coefficients for both G and $i_{a,t}$ (ie M = 31 and N = 30). The difference in C_p when 41 coefficients were used was found to be less than 1%, while the time required for an iteration was about 10 seconds (with 31 coefficients).

For estimating C_p, the integral of equation 3.1.3 was calculated numerically using Simpson's method. For facilitating the numerical integration, an odd number of fourier coefficients (and hence points along the blade) was used.

The aerofoil used is GOE 795. Its $C_L(\alpha)$ characteristics for different

values of Re (taken from reference [54]) are shown in figure 4.9. It is evident that changing Re does not have a large effect on $C_L(\alpha)$. For simplicity, Re effects on C_L were ignored. For linearising the $C_L(\alpha)$ curve, the set of lines shown in figure 4.9 was used (for all values of Re). Each time, after the angle of attack of a blade element was calculated, the appropriate line was selected and $C_L(\alpha)$ was estimated. The performance analysis procedure used here cannot predict the turbine behaviour when the blade is stalled, as the vortex wake assumed is not retained when stall occurs. However, estimates of the turbine performance can be obtained when only a small part of the blade (less than 20%) is stalled. This can be achieved assuming that the aerofoil lift curve continues to have a positive slope beyond stall and using the broken line shown in figure 4.9 for calculating C_L for α values beyond 10°. Attempts to use negative slope lines for estimating C_L beyond stall were unsuccessful as divergent iterative sequences resulted. The inaccuracy introduced by the use of positive $dC_L/d\alpha$ is not expected to be significant, as stall occurs at the inboard part of the blade which does not contribute much to the torque produced by the turbine.

The effects of Re on C_D are significant as shown in figure 4.10. The curves shown in figure 4.10 are approximations of experimental data (taken from [54]), by a least square method, using orthogonal Chebyshev polynomials. For angles of attack larger than 9°, no experimental data were available and when calculation of the drag coefficient for $\alpha > 9°$ was required, the C_D values were extrapolated by straight lines derived from the last two points of each curve (ie those with $\alpha = 8.5°$ and 9°). After the angle of attack and the Re value at each blade element was calculated, $C_D(\alpha, Re)$ was estimated as follows: For given values of α and Re, (say α_0 and Re_0) the C_D values were calculated for the two curves of figure 4.10 whose Reynolds number values were the closest to Re_0 (say $C_D(\alpha_0, Re_1)$ and $C_D(\alpha_0, Re_2)$). The value of $C_D(\alpha_0, Re_0)$ was then

calculated by linear interpolation between $C_D(\alpha_0,Re_1)$ and $C_D(\alpha_0,Re_2)$. For values of Re lower than 40000 and larger than 100000, extrapolation was performed. Thus, the large influence of Re on C_D was taken into account.

The convergence criterion used was:

$$|\beta_{new}(r) - \beta(r)| \leq 10^{-3} |\beta(r)|$$

The relative error was thus limited to 0.1%.

The damping constant μ values (see equation 4.5.3) were found to be in the range between 0.1 and 0.01, with an average number of iterations required for convergence between 80 and 800 respectively. The convergence speed was found to be related to the bound circulation values. The larger G was, the more iterations were needed. The constant Q in equation 4.5.3 was given a value equal to 0.001.

4.5.3. Results presentation.

The main objectives of the vortex turbine performance analysis are: Assessment of the effect various modifications of the initial blade design (which is shown in table 10) may have on the turbine power output, and investigation of Re effects on the turbine performance. In the following section, the results of both investigations are presented.

a). Effect of blade modifications.

The modifications on the blade shape are: Increase of the blade chord at the hub region for structural reasons (the blade chord was assumed to be zero at the hub when the blade was designed) and linearisation of the twist angle distribution for ease of manufacture. The modified blade characteristics are shown in figures 4.11 and 4.12. In

figure 4.11, the dimensionless chord distribution of the blade is shown. It follows the design chord distribution from x = 0.23 to x = 1.0. Below x = 0.23, the blade chord increases linearily, departing from the design characteristics and gets its maximum value at the hub (x = 0.15). However, since the blade chord at the hub was not taken to be zero, a different boundary condition for the hub had to be found, so that the bound circulation would become zero at that point. As can be seen from equation 4.5.1, the only way for G to become zero if $c/R \neq 0$ is to arrange the flow in such a way, so that the resulting angle of attack is equal to its zero lift value $\alpha(C_L=0)$. It is equal to -1.904° for the GOE 795 section, as can be seen from figure 4.9. This condition creates large axial induced velocities at the hub region as will be seen later. In figure 4.12, the blade twist angle distribution is shown. Instead of the non-linear twist distribution required by the blade design, three straight lines were used for approximating $\beta(x)$. At the hub region, (x =0.15 to x = 0.23) the blade was chosen to have constant twist, departing from the design requirements. For the rest of the blade, two straight lines were found to approximate well the design twist distribution, as shown in figure 4.12.

For assessing the effects these modifications have, the performance of a turbine with modified blades was estimated. The undisturbed wind velocity far upstream of the delta wing was taken to be V_∞ = 10 m/s, while the incoming flow components in the vortices are shown in figure 4.4. The turbine blade diameter was chosen to be 1.2 m and the areofoil used is GOE 795.

In table 11, the distributions of Reynolds number and twist angle along the blade for three different values of the tip speed ratio are shown. It is evident from that table, that with λ increasing, Re increases and α decreases throughout the blade. The Re increase is caused by the increase in the local relative velocity (W). Also, with λ increasing, the rotational component of the relative flow velocity increases (since λ =

TABLE 11

	λ = 6.00		λ = 6.75		λ = 9.00	
x	Re	α (deg)	Re	α (deg.)	Re	α (deg.)
0.190	56872	-1.904	66212	-1.904	93499	-1.904
0.187	96787	10.772	98589	8.340	111361	3.355
0.291	85390	11.308	91530	7.481	116651	1.876
0.444	87480	9.991	98550	6.490	134809	1.751
0.619	86851	8.044	99037	5.491	136778	1.793
0.788	69337	7.311	78951	5.278	108283	2.037
0.919	39845	7.362	45296	5.732	61817	2.807
1.000	0	--	0	--	0	--

$\Omega R/V_\infty$) and thus α decreases. (See also figure 2.8). From the above table, it can also be seen that for all values of λ, the angle of attack gets its zero lift value at the hub, as required by the boundary condition there. $C_{p,max}$ was obtained at λ = 6.75. For λ = 6, stall starts to appear at the inboard part of the blade. (As can be seen in figure 4.9, the stall angle for GOE 795 is: $\alpha_{stall} = 10°$). With λ reducing further than 6, stall was found to spread towards the outer part of the blade. For λ = 6.75, it can be seen from table 11 that the values of Re are supercritical for the inboard 80% of the blade approximately. The angle of attack gets values close to its maximum (ie 7° to 5° according to Re). The values of α decrease from x = 0.19 to x = 0.80 as was expected since the blade was designed with a variable α_{opt}. At the hub region, the α values depart from the design values due to the different boudary condition, chord and twist angle distribution. For λ= 9, Re is supercritical almost throughout the blade, while the angle of attack values decrease further.

The distributions of G, u_i/V_∞, v_i/V_∞, dT/dr and dF_D/dr are shown in figures 4.13, 4.14, 4.15, 4.16 and 4.17 respectively for three different values of λ, namely 6, 6.75 and 9. The value of G at each blade element depends upon the relative wind velocity (W) which increases towards the tip, the chord (c) that decreases towards the tip, and the values of C_L that depend on α. The combination of these three parameters can lead to local maxima and minima, as shown in figure 4.13, which become more

pronounced with λ increasing. It is also evident that G decreases throughout the blade with λ increasing. This is caused by the decrease of α (and hence C_L) with λ increasing. The loading drops more rapidly at the hub region than at the tip region with λ increasing and this results in an increase of the relative loading towards the tip. For example, the ratio G(0.8R)/G(0.2R) is 0.5 for λ = 6 and 0.7 for λ = 9. The axial induced velocity gets large values close to the hub (see figure 4.14). This is a requirement of the boundary condition there. The strong tip vortex causes u_i/V_∞ to increase towards the tip. Significant changes in the shape and magnitude of u_i/V_∞ can be observed with changing λ. The tangential induced velocity (figure 4.15) increases from x = 0.15 to x = 0.17 and then drops until a local minimum at x =0.96. Then a small increase occurs caused by the tip vortex. With λ increasing, v_i/V_∞ decreases throughout the blade.

In figures 4.16 and 4.17 the distributions of thrust and driving force per unit span are shown. The thrust has a maximum at about x = 0.75 to 0.8 and then drops rapidly with increasing x, which is an advantage from the structural point of view, since the strength of the blade beyond 0.8R is low. It is also evident that with λ increasing, dT/dr becomes more pronounced towards the tip. The driving force distribution has the opposite behaviour. It has a maximum at about x = 0.18 and then drops throughout the blade. The driving force values remain significant up to x = 0.8. Hence, the blade can produce considerable torque at the region x = 0.5 to 0.8.

The $C_{p,max}$ produced by the turbine (at λ = 6.75) was found to be equal to 0.418, (or $C_{p,system}$= 1.338) which is just 0.24% less than that of the original turbine (see table 10). It can therefore be concluded that the modifications in the blade shape did not affect significantly the turbine performance. The fact that the original and modified blades differ the most at the hub region which contributes little to the turbine torque is probably the reason why no considerable loss of power resulted from the blade

modifications. The turbine with the modified blades was chosen to be built for the system prototype.

Re effects on the turbine performance.

For investigating the Reynolds number effects on the turbine performance, the power coefficient of the turbine was predicted for various values of the undisturbed wind velocity, thus changing Re. The results are shown in figure 4.18. In that figure, $C_{p,system}$ is plotted versus λ for various values of V_∞ ranging from 3 m/s to 13 m/s. It is evident from figure 4.18 that $C_{p\,max}$ is achieved for all values of V_∞ at $\lambda = 6.75$, and hence differences in Re do not result in a different λ_{opt}. This was expected, as C_L was assumed to be Re independent and therefore the bound circulation, dimensionless induced velocities and angle of attack values remain the same for a given λ with V_∞ changing. Hence the angle of attack distributions shown in table 11, as well as the distributions in figures 4.13, 4.14 and 4.15 are representative of the turbine behaviour at all values of V_∞. It should also be mentioned that evaluation of the turbine performance below $\lambda = 5$ was not possible as stall was spread to a considerable part of the blade (more than 20%). Unlike the bound circulation and induced velocities distributions, the Re, C_D and the driving force and thrust values are affected by the V_∞ change: For $\lambda = 6.75$, Re remains subcritical throughout the blade for $V_\infty = 3$ m/s (Re is above 25000 at the inboard 70% of the blade for that wind speed) and up to $V_\infty = 7$ m/s. (Re is above 65000 for the inboard 70% of the blade for $V_\infty = 7$ m/s). It gets supercritical values for a substantial part of the blade (ie the inboard 70%) for $V_\infty = 8$ m/s, and increases further with increasing V_∞. At 13 m/s, it is supercritical for the inboard 90% of the blade with its peak value (about 131000) appearing at $x = 0.53$. With Re increasing, the C_L/C_D ratio improves throughout the blade and for all values of λ resulting in an improvement of $C_{p,max}$ equal to 16.6% between 3 m/s and 13 m/s as can be seen from figure 4.18. The

shape of the $C_p(\lambda)$ curves changes with V_∞ changing due to the non-linear change of C_D.

It can therefore be concluded that Re effects were found to affect considerably the performance of the delta wing system prototype turbine.

4.5.4. Conclusions.

The most important conclusions from this study are:

1. Increase of the blade chord towards the turbine hub and linearisation of the blade twist angle distribution were not found to affect significantly the performance of the delta wing system prototype turbine, as a reduction of 0.24% in $C_{p\,max}$ resulted from those modifications. The turbine with the modified blades was chosen to be constructed for the prototype.
2. Reynolds number effects were found to affect the turbine performance considerably as variations in the undisturbed wind velocity resulted in significant changes of the turbine power. Increase of V_∞ from 3 m/s to 13 m/s causes the turbine $C_{p,max}$ to increase by 16.6%. However, the value of λ_{opt} was not found to change significantly with V_∞, although slight changes in the $C_p(\lambda)$ curve were observed.

FIGURES FOR CHAPTER 4.

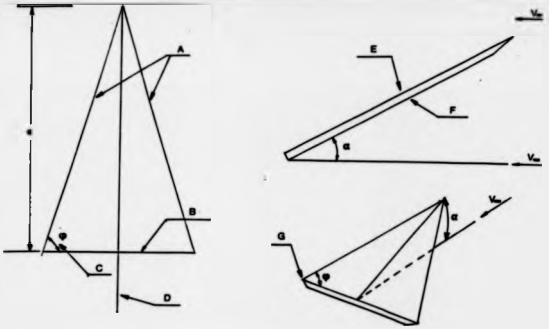

Figure 4.1. Geometrical characteristics of a delta wing.
A: Leading edges. B: Trailing edge
C: Sweepback angle. D: Centreline
E: Upper surface. F: Lower surface
G: Sharp leading edges.

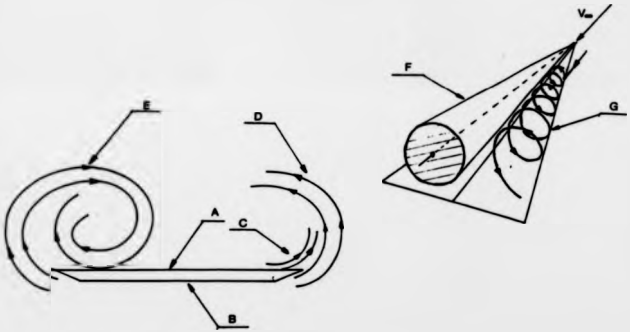

Figure 4.2.Formation of leading edge vortices.
A: Low pressure side. B: High pressure side.
C: Flow sucked by the fast moving air masses.
D: Flow shed from the leading edge. E: fully formed vortex. F: Vortex cone. G: A streamline.

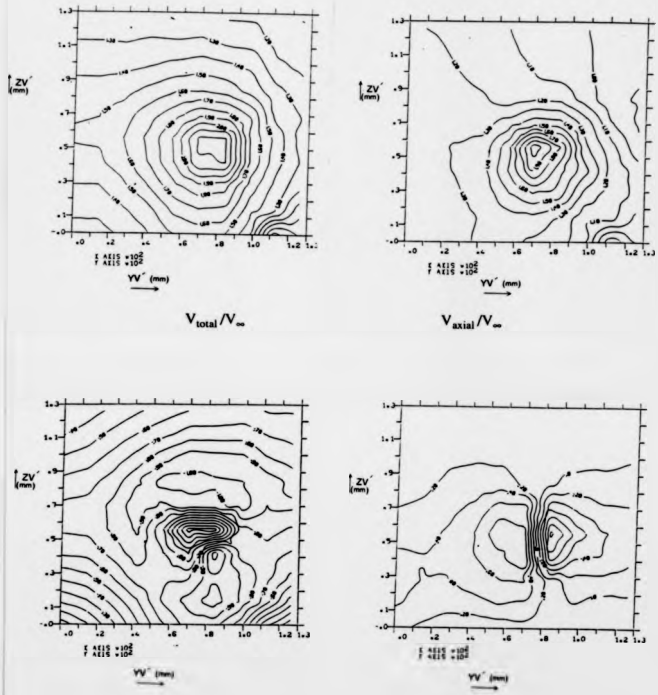

Figure 4.3. Velocity contours in the vortex created by a 79° sweptback delta wing set at an angle of attack of 25°. (Taken from [43]).

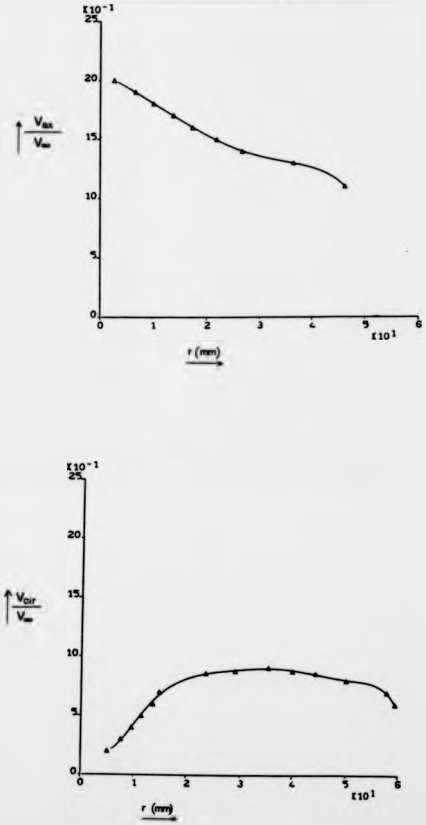

Figure 4.4. Incoming flow components to the vortex turbine. (taken from [43]).

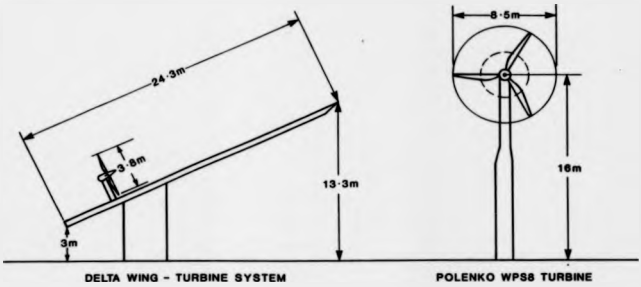

Figure 4.5. Relative sizes of delta wing-turbine system and the equivalent conventional turbine. Case 1. P_o = 15 kW.

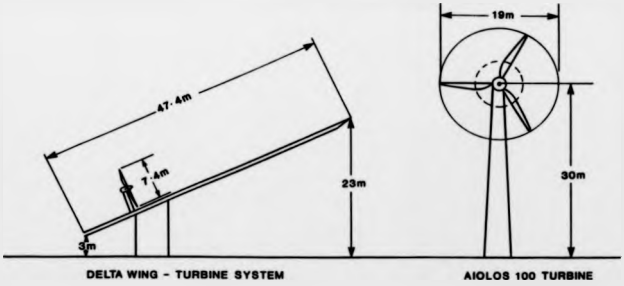

Figure 4.6. Relative sizes of delta wing-turbine system and the equivalent conventional turbine. Case 3. P_o = 100 kW.

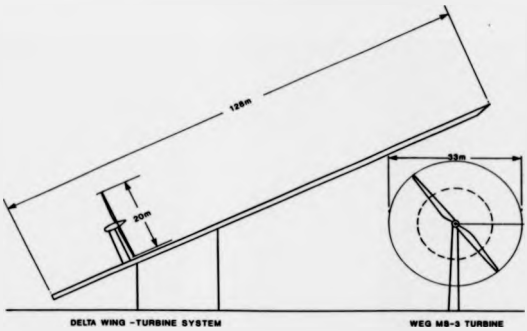

Figure 4.7. Relative sizes of delta wing-turbine system and the equivalent conventional turbine. Case 4. P_e = 300 kW.

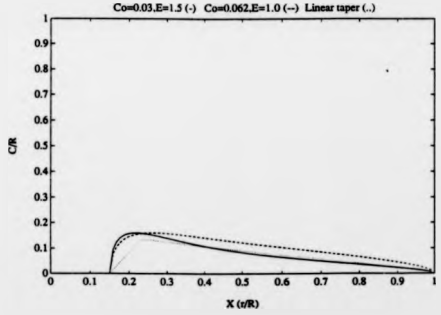

Figure 4.8. Dimensionless chord versus dimensionless radius for three different blade configurations.

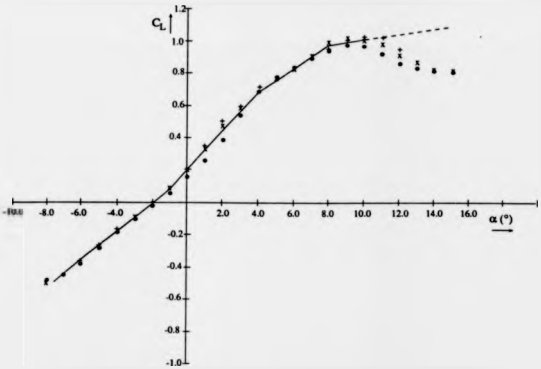

Figure 4.9. $C_L(\alpha)$ lines used in the turbine performance analysis program. Aerofoil: GOE 795. Values of Re: '+' : 40000, '*' : 60000, '+' : 80000. (Experimental data taken from [54]).

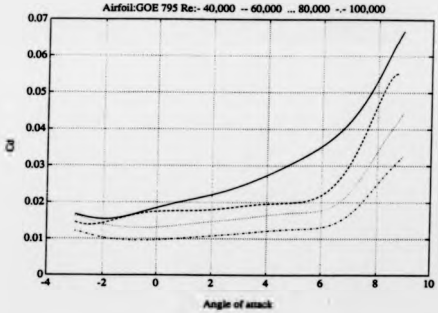

Figure 4.10. $C_D(\alpha)$ plots for various values of Re. (Experimental data taken from [54]).

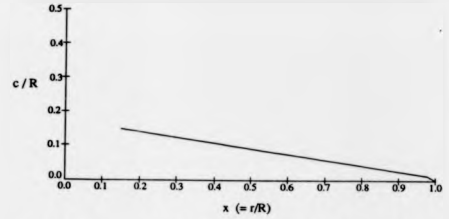

Figure 4.11. Dimensionless chord distribution of the modified blade.

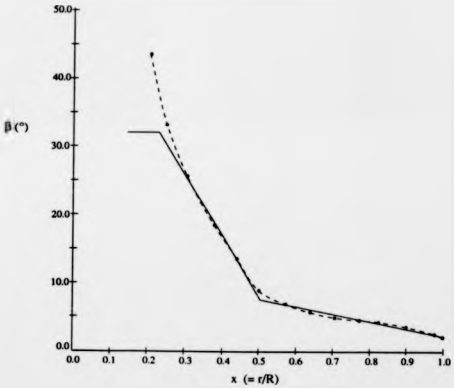

Figure 4.12. Twist angle distribution of the modified blade.
(Three straight lines approximate the original distribution).

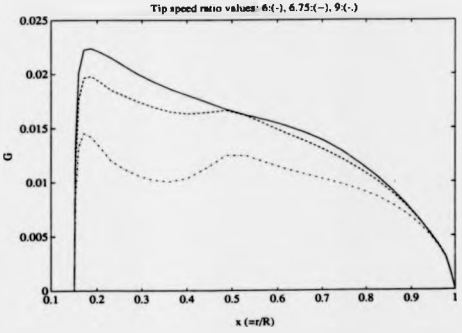

Figure 4.13. Turbine performance results. G(x) plots for various values of λ.

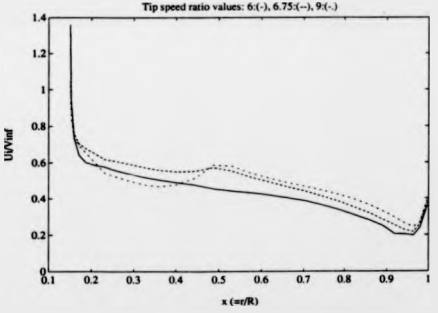

Figure 4.14. Turbine performance results. u_i / V_∞ plots for various values of λ.

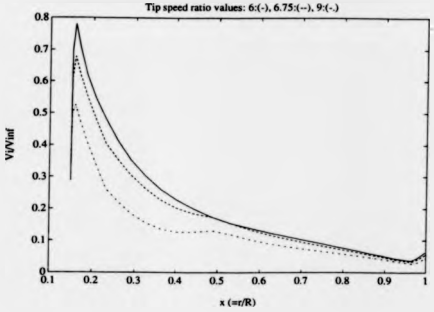

Figure 4.15. Turbine performance results. v_i/V_∞ plots for various values of λ.

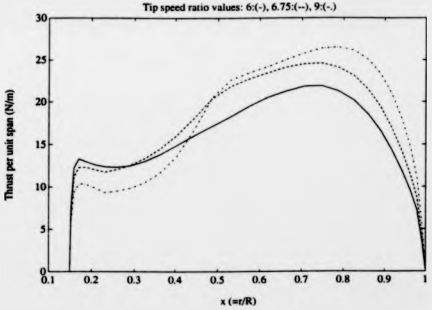

Figure 4.16. Thrust per unit span distribution along the modified blade.
R = 0.6 m, V_∞ = 10 m/s.

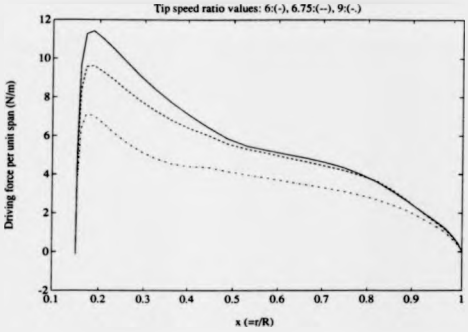

Figure 4.17. Driving force per unit span distribution along the modified blade.
R = 0.6 m, V_∞ = 10 m/s.

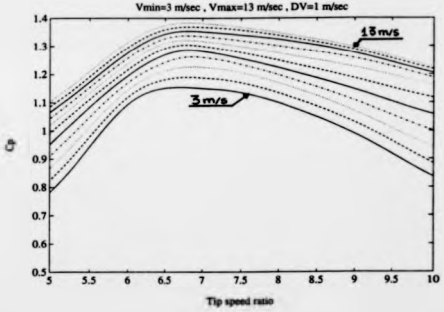

Figure 4.18. Vortex turbine performance prediction.
$C_{p,system}(\lambda)$ plots for various values of V_∞.

CHAPTER 5.

TESTING OF THE SYSTEM PROTOTYPE GENERATOR AND PREDICTION OF THE PROTOTYPE LONG-TERM PERFORMANCE.

CHAPTER 5. TESTING OF THE SYSTEM PROTOTYPE GENERATOR AND PREDICTION OF THE PROTOTYPE LONG-TERM PERFORMANCE.

5.0. INTRODUCTION.

In the first part of this chapter, the bench test of the electric generator to be used together with the delta wing-turbine system prototype is presented. The objectives of this test are:

a) Estimation of the generator model parameters, ie the relation between the emf (E_A) produced by the generator and rotational speed, as well as estimation of the armature resistance (R_A) and the generator synchronous reactance (L_S).

b) Estimation of the generator power losses. With the power losses known, it will be possible to calculate the the mechanical power produced by the prototype turbine when its test will take place. Effectively, the second part of the generator test is a calibration of the machine.

The generator test data are used in the second part of this chapter, together with the turbine performance predictions for estimating the long-term prototype performance. An appropriate model of the generator and load is developed for evaluating the electrical power produced at various wind speeds and the Weibull distribution of wind occurrence probability is used for obtaining the prototype long-term performance characteristics at various wind regimes.

5.1. GENERATOR TEST.

The generator used is a synchronous one. Its theory is presented in brief here, before an account of the test instrumentation, procedure and results is given. The information about electric machines' theory presented here was obtained from references [3], [56] and [57].

5.1.1. Theory of synchronous generators.

A synchronous generator is an electric machine that can convert mechanical power into alternating electrical power. A typical machine of this type has two parts. One is moving (called rotor) and the other is stationary (called stator). The stator contains wound coils and when an AC current flows through them a rotating magnetic field is produced. (See reference [56] for more details). This procedure can also be reversed: A rotating magnetic field can excite the stator windings which produce an alternating current. The rotating magnetic field is provided either by a permanent magnet (as in our case) which characterises the permanent magnet machines, or by an electromagnet, ie a set of coils fed by a DC power source. The rotational speed of the AC current (called electrical speed, ω_e) is directly proportional to the mechanical rotational speed (ω) of the rotor. That is the reason why such a machine is called "synchronous". ω_e depends on the number of poles the rotor magnet has. Let us assume that a magnet with P poles is used. As the rotor poles approach and leave one of the stator coils, the magnetic flux through the coil alternates. During a full mechanical cycle (ie a full revolution of the rotor) it is evident that the magnetic flux through the stator coils is reversed P times and hence P/2 cycles are "sensed" by the coil. Therefore:

$$\omega_e = (P/2)\,\omega \qquad (5.1.1)$$

A synchronous generator can be single or multi-phase, depending on the layout of its stator coils (also called the armature). A single phase synchronous generator can be modelled as shown in figure 5.1. (For a multi-phase one, figure 5.1 is the per phase equivalent). There are three model parameters for such a generator: The emf (E_A) produced by its armature, the armature resistance (R_A) and the synchronous reactance (L_S). *(Note that in the following, all symbols of currents or voltages represent the rms values of these quantities).* The maximum of the magnetic flux through the stator coils cannot change, since a permanent magnet is assumed and the emf produced by the generator depends only on ω:

$$E_A = K\,\omega \qquad \text{or} \qquad E_A = K_e\,\omega_e \qquad (5.1.2)$$

When a current is flowing through the stator windings, a secondary magnetic field is crated by the stator which distorts the original magnetic field (ie that of the rotor) in the air gap between stator and rotor. This effect is called armature reaction. The magnetic field distortion causes the armature current to lag E_A. The synchronous inductance (L_S) simulates this effect. Finally, the armature resistance depends on the diameter and length of the wire used for the stator coils as well as the wire material and the generator operating temperature.

The phasor diagram of a permanent magnet synchronous generator is shown in figure 5.2. The generator is assumed to be connected to a lagging load. The angle between the generator terminal voltage (V) and I is ϕ, while δ is the angle between E_A and V, called "load angle". As can be seen from figure 5.2, δ is given by:

$$\cos\delta = \frac{V + IR_A\cos\phi + I\omega_e L_S \sin\phi}{E_A} \qquad (5.1.3)$$

In order to determine the model parameters of a synchronous generator, the following tests must be carried out:

a) The open circuit test. The generator terminal voltage (V) is measured for different rotational speeds with the generator terminals open. In that case, (see figure 5.1), $V = E_A$ and the open circuit characteristic (ie equation 5.1.2) can be obtained.

b) The short circuit test. This test is carried out for estimating L_S. With the generator terminals shorted, the current (I) is measured for different rotational speeds. In that case, the load impedance is zero, and as can be seen from figure 5.1, I is given by:

$$I = \frac{E_A}{\sqrt{R_A^2 + \omega_e^2 L_S^2}} \qquad (5.1.4)$$

By use of equations 5.1.4 and 5.1.2, L_S can be calculated from:

$$L_S = \frac{1}{\omega_e}\sqrt{\left(\frac{K_\phi \omega_e}{I}\right)^2 - R_A^2} \qquad (5.1.5)$$

c) Estimation of R_A. The armature resistance can be found by applying a DC voltage through the stator coils while the generator is not operational, and measuring the resulting current. The generator must be at a temperature similar to that of usual operating conditions.

The power flow through a generator is shown in figure 5.3. There are several types of losses in an electric generator. These are:

Electrical or copper losses. These occur in the armature and field (ie rotor) windings of a generator. They are given by: $P_A = I^2 R_A$ (for the armature winding) and $P_F = I^2 R_F$ (for the field winding). For a permanent magnet generator, P_F is zero.

Core losses. These are hysteresis and eddy current losses in the metal of a generator.

Mechanical losses. (Windage-friction). These are associated with mechanical effects Windage losses are caused by friction between the machine moving parts and the air

inside the generator casing. Friction losses are caused by friction in the generator bearings.

Stray losses. Stray losses cannot be placed in any of the above categories. No matter how well losses are accounted for, some always escape inclusion.

The following equation expresses the power flow through a permanent magnet generator:

$$P_{in} = P_{out} + I^2R_A + P_{misc} \qquad (5.1.6)$$

In the above relation, P_{in} is the input power provided by the prime mover, P_{out} is the power output which for the case of a single phase synchronous generator is $IV\cos\phi$ as can be seen from figure 5.2. I^2R_A represents the electrical losses and P_{misc} includes "miscellaneous" losses, ie mechanical, core and stray losses lumped together. For calibrating the generator, P_{misc} has to be estimated for various values of I and ω.

5.1.2. Description of the generator and test instrumentation.

a) Generator. The generator used is a permanent magnet, single phase, synchronous AC machine of disc geometry. Such a machine is also called an "axial flux' generator, as the direction of the magnetic flux is parallel to the shaft. A sketch of a typical axial flux machine is shown in figure 5.4, taken from reference [58] where an account of recent developments in axial flux generators is given. The generator in the present work was developed at the University of Warwick. It is now being produced by Marlec Engineering Co. Ltd, for use with the Rutland Furlmatic 1800 wind turbine manufactured by the same company. It was granted to us by the director of the above mentioned company. The rotor magnet has 12 poles and comprises two halves that can be separated (see figure 5.4). When the two halves are close together, they are held in place by magnetic forces. The stator has a set of twelve coils connected in series with

140 loops each. They are made of copper wire and they do not have iron cores for enhancing the magnetic flux through them. They are however embedded in epoxy resin and thus the stator is quite solid and strong. The stator is positioned between the two rotor halves and two cable leads provide the electrical power to the load. The stator's rated current is 2A (manufacturer's data). The generator is designed to provide about 220 W of electrical power at a rotational speed of 600 rpm when connected to an appropriate load. Its cold armature resistance is 25.7 Ω at 20° C. The generator can be connected directly to the prototype turbine, without having to use a gearbox.

b) Description of the test rig, motor and torque transducer. The test rig to which the generator was attached comprises a DC motor connected to a torque transducer. The DC motor was used for driving the generator. Both its stator and rotor are electromagnets. Its rotational speed can vary from 0 to 3000 rpm depending on the power fed to the field and armature windings. The motor was wired-up as a separately excited one during the tests. For exciting the armature winding, a variac and a three phase rectifier unit was used. For the field winding (which had lower power requirements), an off-the-shelf variac with a built-in rectifier was used. The motor rotational speed could be increased either by increasing the armature current or by decreasing the field current. The motor was linked to the generator via a torque transducer for measuring the torque. The transducer is a TG-2/B Vibro-meter slipringless one. Its operating principle as explained in [59] is as follows: The centre of the transducer shaft is reduced in diameter (as can be seen in figure 5.5) and this portion is the measuring section. Two flanges fixed on either side of this section hold an inductive coil system and its cores. The coils are fixed on the larger diameter part of the shaft, while their cores are fixed on the smaller diameter part. When a torque (either static or dynamic) is applied, the smaller diameter part of the shaft is twisted. Hence, the relative

position between the coils and their cores changes and likewise does the coil inductance. There are four coils connected in a four arm inductive bridge arrangement. At no load, the bridge is balanced. When a torque is applied, the bridge imbalance voltage can be used for measuring the torque. The bridge is supplied with power via a rotary transmitter. Another rotary transmitter is used for picking-up the output signal. Hence, no sliprings are necessary. The torque transducer characteristics are:

- Minimum torque: 1.9 Nm.
- Maximum torque: 38.0 Nm.
- Accuracy: 0.25-0.5% of fsd (full scale display).
- Maximum speed: 22000 rpm.

Together with the transducer, a Vibro-meter 8-MCA-1/AO multi-channel carrier frequency system is used for providing the bridge input signal and picking-up the output. The 8-MCA-1/AO system consists of a power supply/oscillator unit and a carrier frequency amplifier. As shown in the block diagram of figure 5.6, the oscillator provides the signal for the torque transducer bridge excitation. The bridge imbalance signal is picked-up by the amplifier. It then passes through a band-pass filter, a demodulator, an amplifier and two low-pass filters, and is finally directed towards the output terminals. The output from the torque meter and amplifier was read on a DC voltmeter. The output voltage was in the range of -2.5V to +2.5V, with the torque range varying according to the different sensitivity settings of the "range" rotary switch of the amplifier. The range selected for the test was "25", the second most sensitive, that divided the output signal by 5. The most sensitive setting (that didn't attenuate the signal) failed to produce repeatable results and suffered from too much noise so it was not used. The amplifier needed at least half an hour to heat-up before the tests could start. Before each run, the bridge was

position between the coils and their cores changes and likewise does the coil inductance. There are four coils connected in a four arm inductive bridge arrangement. At no load, the bridge is balanced. When a torque is applied, the bridge imbalance voltage can be used for measuring the torque. The bridge is supplied with power via a rotary transmitter. Another rotary transmitter is used for picking-up the output signal. Hence, no sliprings are necessary. The torque transducer characteristics are:

- Minimum torque: 1.9 Nm.
- Maximum torque: 38.0 Nm.
- Accuracy: 0.25-0.5% of fsd (full scale display).
- Maximum speed: 22000 rpm.

Together with the transducer, a Vibro-meter 8-MCA-1/AO multi-channel carrier frequency system is used for providing the bridge input signal and picking-up the output. The 8-MCA-1/AO system consists of a power supply/oscillator unit and a carrier frequency amplifier. As shown in the block diagram of figure 5.6, the oscillator provides the signal for the torque transducer bridge excitation. The bridge imbalance signal is picked-up by the amplifier. It then passes through a band-pass filter, a demodulator, an amplifier and two low-pass filters, and is finally directed towards the output terminals. The output from the torque meter and amplifier was read on a DC voltmeter. The output voltage was in the range of -2.5V to +2.5V, with the torque range varying according to the different sensitivity settings of the "range" rotary switch of the amplifier. The range selected for the test was "25", the second most sensitive, that divided the output signal by 5. The most sensitive setting (that didn't attenuate the signal) failed to produce repeatable results and suffered from too much noise so it was not used. The amplifier needed at least half an hour to heat-up before the tests could start. Before each run, the bridge was

balanced at no load by adjustment of a resistive and a capacitive potentiometer.

The torque transducer and amplifier were calibrated statically: One end of the transducer shaft was clamped on the test rig frame, the other being connected to a pulley. Weights were hung from the pulley and for each weight the amplifier output voltage was recorded. There were two measuring units on the amplifier and they were both calibrated. Units 1 and 2 were on the right and left hand side of the amplifier respectively. The torque direction was clockwise looking from the motor towards the torque meter and was chosen to coincide with the wind turbine direction of rotation during the prototype tests. The calibration curves of both units are shown in figure 5.7. It is evident that the linearity of the transducer is excellent. Unit 2 was chosen to be used, as a least square line could be fitted through the measurement points with less scatter than unit 1. (See figure 5.7). The least square line fitted for unit 2, shown in figure 5.7 is:

$$F = AV_{out} \qquad \text{(in Kg)}$$

with :

$$A = 10.1 \text{ Kg/V}$$

The torque could then be calculated in Nm multiplying F with C L:

$$Q = F C L$$

with C a conversion factor, C=9.81 N/Kg and L the pulley torque arm, L=0.07m. Repeatability of the voltage readings was checked and it was found that that the difference in voltage between any two repeated readings for the same torque was ±0.01V at the most. This is consistent with the manufacturer's data: The torque meter accuracy is ±0.5% of fsd. In our case, fsd is 2.5V and hence the instrument accuracy is ±0.0125V. The DC voltmeter sensitivity was 0.005V, which corresponds to a torque of 0.03Nm, ie 63 times the transducer minimum torque.

c) Other instruments used. A Feedback EW604 electromagnetic watt

meter was used for measuring the generator power output. Its power range lies between 250 mW and 10 kW. Its accuracy is better than 2.0% of fsd. Three variable resistors were used as loads for the generator, each for a different current range. They consisted of wound coils. Their length could vary using a runner that disconnected the desirable percentage of resistor length. These resistors were not purely ohmic loads however, due to their coil-like shape (as it will be seen later). Their characteristics are:

- Resistor 1 : 0-1024 Ω, I_{max} = 1.0 A
- Resistor 2 : 0-614 Ω, I_{max} = 1.7 A
- Resistor 3 : 0-164 Ω, I_{max} = 3.2 A

A tachometer was used for picking-up the rotational speed when attached to the motor shaft. For reading the generator terminal voltage and current, a digital AC voltmeter and an avometer (respectively) were used. A sketch of the experimental set-up is shown in figure 5.8.

5.1.3. Generator model parameters estimation.

The results of the tests for evaluating the generator model parameters are presented in the following section.

a) Open circuit test. The open circuit characteristics of the generator are shown in figure 5.9. It is evident that E_A increases linearly with ω increasing and equation 5.1.2 holds. The slope K was calculated from the above figure:

$$K = 0.294 V/rpm$$

Since ω (in rpm) = (60/2π) ω (in rad/sec),

$$K = 2.81 \text{ V sec}$$

and since $\omega_e = (P/2)\,\omega = 6\,\omega$,

$K_e = 0.468$ V sec.

b) Short circuit test. The short circuit test was then carried out. The current flowing through the shorted generator windings was measured for different values of ω. For each value of ω, the current was found to decrease with time, as the stator windings were heating-up. Enough time was allowed for the current to stabilize before readings were taken. After each measurement of I, the generator was brought to a halt and a DC voltage was applied to its terminals for measuring R_A. In figure 5.10 the variation of the short circuit current (I) with ω is shown. The current does not increase linearly with ω increasing, due to the changing R_A as explained in [4]. From equation 5.1.4, it can be seen that if the synchronous impedance ($Z_S = [R_A^2 + \omega_e^2 L_S^2]^{1/2}$) had been constant, then I(ω) would have been linear. However, Z_S increases since R_A increases with temperature. With I and R_A known, L_S can be calculated from equation 5.1.5. L_S was estimated for 11 values of ω ranging from 135 rpm to 285 rpm. No readings were taken beyond 285 rpm, as the generator was heating excessively. The following table contains the calculated L_S values.

TABLE 1

ω (rpm)	L_S (H)
135	0.0465
149	0.0498
161	0.0475
179	0.0459
199	0.0489
204	0.0454 (min)
216	0.0498 (max)
228	0.0458
237	0.0480
244	0.0483
285	0.0470
$\bar{L}_S = 0.0475$ H (+4.8% -4.5%)	

The L_S values do not seem to follow any particular trend. They are scattered about the average value (shown at the foot of table 1). This value is comparable with that estimated

for a similar generator in [61]. The generator examined in [61] is a permanent magnet synchronous one of larger size and ratings than the one used here, and its L_S value was found to be 0.027 H, which is of the same order of magnitude as the L_S calculated here. The scatter in the L_S values was caused by the scatter in I and R_A.

c) Estimation of armature resistance. R_A was estimated using the technique described in section 5.1.1. However, the generator's operating conditions are expected to vary widely during the system prototype test, and use of a single value of R_A was not considered realistic. In order to monitor the R_A change, a thermo-couple needs to be installed close to the stator windings, so that the stator temperature is known. However, at the time the generator test was carried out, a thermo-couple was not available and the best alternative was to monitor the variation of R_A with I, assuming that the ambient temperature would be the same (about 22° C), so that the generator windings would always settle at the same temperature for a certain operating condition. The above assumption was thought to be reasonable, as the test was carried out indoors. The variation of R_A with I is shown in figure 5.11. The R_A increase with I increasing is not linear, due to the non-linear increase of the generator temperature. For currents up to 1.0 A, the generator was mildly warm, while for larger currents it heated-up rapidly. A 5th order polynomial was found to approximate the $R_A(I)$ curve best. It is shown in figure 5.11.

5.1.4. Generator calibration.

The procedure and results of the tests for determining the generator power losses are presented here.

a) Experimental procedure. Tests were carried out for a wide range of

rotational speeds (from 200 rpm to 1500 rpm) and currents (from 0.3 A to 2.2 A). The ω range was determined by the tip speed ratio range required for the system prototype test. For an undisturbed wind speed of 10 m/s, $\lambda(C_{P,max}) = 6.75$ (see chapter 3) and $\omega(C_{p,max})$ =1000 rpm. For ω = 200 rpm, λ = 1.35 and for ω = 1500 rpm, λ = 10.1. The λ range [1.35 - 10.1] is enough for sampling the turbine $C_p(\lambda)$ curve. The minimum value of I (=0.3 A) was determined by the lower limit of the torque meter measurement. Below I = 0.3 A, the torque readings were not repeatable. The maximum current (I = 2.2 A) was 1.1 times the generator rated current and the generator heated-up excessively when operating for a considerable time at higher currents, so it was not considered safe to continue the tests for I values larger than 2.2A. Readings were taken for 10 values of I, namely 0.3A, 0.5A, 0.8A, 1.0A, 1.2A, 1.4A, 1.6A, 1.8A, 2.0A and 2.2A.

For each I value, about 22 values of ω were sampled. During each run, ω was allowed to vary while I was kept constant. This was done in order to keep the generator temperature (and hence R_A and the copper power losses) constant. In order to keep the current constant for each value of ω, the generator load was changed by adjustment of the variable resistors. The quantities measured were (see also figure 5.8): The rotational speed (ω), the input torque (Q), the generator terminal voltage (V) and current (I) and the power produced by the generator (P_{out}). Immediately after each run, R_A was measured using a DC power source.

The generator was allowed to operate at a medium rotational speed (about 700 rpm) for a quarter of an hour, at the desirable current value, before readings were taken. This was done in order to allow the generator and load and also the bearings to heat-up. It was found that the input torque was somewhat larger with cold bearings, as the lubricant in them had a higher viscosity. Once the bearings were warm, no noticeable change in the input torque was observed even if they further heated-up. During the

prototype tests, the bearings can be heated-up by inverting the generator's operation. The generator can operate as a motor when an AC current is provided to its armature.

With the information obtained from the test, it was possible to estimate $P_{misc}(I,\omega)$ from equation 5.1.6:

$$P_{misc}(I,\omega) = Q\omega - P_{out} - I^2R_A \qquad (5.1.7)$$

In the above equation, $Q\omega$ is the input power, P_{out} is the output power read on the watt meter and I^2R_A is the copper loss.

During the early stages of the tests a problem was encountered: The voltage readings from the torque meter amplifier output were fluctuating considerably with time. These fluctuations could be as high as ±20% of the measured average. The fluctuations did not start immediately after the motor was turned on, but after about 5 minutes of operation. Various tests were carried out in order to isolate the source of the problem. It is believed that they are real torque fluctuations associated with the generator and load and not noise caused by the torque measuring equipment. Since only an estimate of the average steady state torque was necessary, the problem was solved by passing the amplifier output signal through a low-pass filter before it was read on the voltmeter. The filter arrangement is shown in figure 5.12. Its elements are a resistor (R_F = 10 MΩ) and a capacitor (C_F = 1 μF). The filter was found to dampen the voltage ripples sufficiently. However, a significant voltage drop occured on the filter resistor. The filter output voltage was almost half of the input voltage. The filter was calibrated versus the amplifier output and the calibration results are shown in figure 5.13. Due to that voltage drop, the overall torque sensitivity was halved and since the voltmeter sensitivity was 0.005 V, (ie 0.01 V of the amplifier output voltage) the torque sensitivity was reduced to 0.06 Nm which is equal to 1/32 of the lowest measurable torque. With that problem solved, torque measurements were possible.

b) Presentation of results. For all values of I, the measured torque was found to be nearly constant for values of ω larger than 500 rpm. Below 500 rpm, the torque increased slightly with ω increasing. Between 700 rpm and 800 rpm, another phenomenon was observed: The test rig was resonating and the noise produced by it as well as the shaft vibrations (which were kept at low levels at all other rotational speeds) were increased. Also, within the resonance regime, the input torque levels were slightly lower. The resonance intensity depended on the generator current and with it increasing the noise and vibrations increased. During the open circuit test however, (when I = 0), no resonance was observed. It is therefore safe to conclude that it was the generator that was resonating. It must therefore be noted that before the prototype test is carried out, the turbine blades' resonant frequencies must be evaluated. If they are found to be near the generator resonance band, certain operating conditions must be avoided during the prototype test otherwise serious damage of the turbine may result.

Fluctuations of the torque readings were observed even after the filter was installed. They were found to be within the torque transducer accuracy levels (ie ±0.5% of fsd). However, for low values of I, the torque was also low and the relative errors were considerable. The maximum relative errors in torque together with the average torque level for each value of I are shown in table 2. It is evident that the torque values measured are quite low compared to the torque meter ratings. For I = 0.3A, the average torque level was less than the lowest measurable torque of the transducer. Even for I = 2.2A, for which the maximum torque was measured, the torque level was still 5.5 times less than the transducer maximum measurable torque. For better results, a more sensitive torque transducer is necessary, which however was not available.

TABLE 2

I (A)	Maximum relative error in torque readings	Average torque level (N m)
0.3	9.0%	1.57
0.5	6.6%	2.00
0.8	5.0%	2.84
1.0	4.0%	3.58
1.2	3.0%	4.28
1.4	2.8%	5.01
1.6	2.6%	5.43
1.8	2.3%	6.08
2.0	2.1%	6.65
2.2	2.0%	6.94

With use of equation 5.1.7, a chart of $P_{misc}(I,\omega)$ was made, shown in figure 5.14. The scatter which is more pronounced for the lower values of I (0.3A to 1.4A) is due to the torque fluctuations. For larger currents, (above 1.4A) the scatter is reduced. The behaviour of $P_{misc}(I,\omega)$ is as expected. For the same ω and with I increasing, it increases due to increasing core losses. For the same I and with ω increasing, it also increases due to increasing mechanical losses. For all values of I above 0.5A, the slope of the P_{misc} curves is reduced within the ω range [700 rpm-850 rpm] due to the lower torque values caused by the generator resonance. The value of P_{misc} is almost doubled (for all ω) between the lowest and largest values of I, while the output power increases more than 7 times. The curves shown in figure 5.14 were interpolated through the experimental data for eliminating scatter. Those curves rather than the experimental data were used in all the calculations that follow. The repeatability of the measurements was tested by checking the torque levels after each run was completed and no significant differences were observed. It was felt that there wasn't any need to test the repetability of the electrical quantities measurements, because they seemed to be quite consistent. A full set of readings for I = 1.0A was repeated and the results of both runs are shown in figure 5.15. The experimental points seem to lie in the same band.

In figure 5.16, $P_{out}(I,\omega)$ measured on the wattmeter is shown. It can be seen that the generator power output for the same I increases linearily with ω increasing. For the same ω, with I increasing P_{out} increases except for the regime with $I > 1.0A$ and $\omega < 600$ rpm where the trend is reversed. The accuracy of the wattmeter readings is much better than that of the torque meter, and the scatter is insignificant. The graphs of figures 5.14 and 5.16 were used for calculating the generator efficiency (η_g) which is shown in figure 5.17 plotted versus I for constant ω values. The efficiency was chosen to be plotted that way, so that only one parameter would be changing (ie the generator load). If η_g was plotted versus ω for constant values of I, both the generator load and the rotational speed would be changing. The generator efficiency increases with ω increasing for the same I, but at a reducing rate. The value of I at which the maximum of efficiency is achieved for each ω increases with ω increasing.

The maximum value of η_g is obtained at $\omega \approx 1500$ rpm, with $I \approx 1.4A$ and is about 70%. This value of efficiency is rather low for a typical generator, but this was expected as the generator armature resistance is considerable. Also, the stator windings do not have iron cores for enhancing the magnetic flux through them. Of the power loss for that case, about 1/3 is due to electrical losses (I^2R_A) and the other 2/3 are due to mechanical, core and other losses (P_{misc}).

Using the charts of figures 5.14 and 5.16, the ratios P_{misc}/P_{out} and I^2R_A/P_{out} were calculated for various values of I and ω. They are shown in tables 3 and 4. It can be seen from those tables that for low values of I (ie $I = 0.3A$), P_{misc} is by far the most important power loss component throughout the ω range examined. For intermediate values of I (ie $I = 1.0A$), P_{misc} and the electrical losses are of the same order of magnitude for low ω, but with ω increasing, P_{misc} dominates. For large values of I (ie $I = 2.0A$), I^2R_A is larger for low ω. With ω increasing, P_{misc} and the electrical losses are

TABLE 3

$\frac{P_{mec}}{P_{out}}$

ω (rpm) \ I (A)	0.3	1.0	2.0
500	0.658	0.356	0.456
1000	0.901	0.375	0.361
1500	0.917	0.424	0.357

TABLE 4

$\frac{I^2 R_A}{P_{out}}$

ω (rpm) \ I (A)	0.3	1.0	2.0
500	0.185	0.256	0.833
1000	0.031	0.117	0.303
1500	0.021	0.077	0.185

comparable. In figure 5.18, plots of V(ω) are shown for three values of I, (0.5A, 1.0A and 2.0A). It can be seen that the terminal voltage increases linearly with ω increasing. Also, for the same ω, V drops with I increasing. The slope of all three lines shown in figure 5.18 is similar. Using the graphs of figures 5.16 and 5.18, the angle ϕ between the terminal voltage (V) and the current (I) phasors can be estimated as follows: The generator's apparent power is VI while the real power is $P_{out} = VI\cos\phi$. Hence:

$$\phi = \cos^{-1}(P_{out}/VI)$$

In figure 5.19, ϕ(ω) is shown for three values of I (0.5A, 1.0A and 2.0A). It is evident that the resistors used are not purely ohmic loads and ϕ gets considerable values. The behaviour of ϕ changes with I:

- For I = 0.5A, ϕ drops with increasing ω.
- For I = 1.0A, ϕ is nearly constant.
- For I = 2.0A, ϕ increases with increasing ω.

This can be explained as follows: Angle ϕ depends on the relative magnitude of the resistive and reactive components of the load impedance. During the tests, when ω increased, the load was changed for keeping I constant. Both load resistance and reactance increase with ω increasing, the former due to the increase of the resistor active length, the latter due to the same effect that increases the coil self-inductance, and also due to the ω increase. Hence, for I = 0.5A, the load resistance increases more rapidly than its reactance with ω increasing. For I = 1.0A, both load resistance and reactance

increase by the same rate and thus ϕ is kept nearly constant. For I = 2.0A, the load reactance increases more rapidly than the resistance, causing ϕ to increase with ω increasing.

The load angle δ (see figure 5.2) was also calculated using equation 5.1.3. For doing so, the results of the open circuit test (ie the K_e value), the short circuit test (ie the L_S value) and the generator calibration (ie figures 5.11, 5.18 and 5.19) were used. δ was calculated for I = 2.0A and for various values of ω. The results are shown in the following table:

TABLE 5

ω (rpm)	δ (°)	$\omega_e L_S$ (Ω)
500	1.89	14.8
600	4.66	17.8
700	6.05	20.8
1000	8.01	29.7
1500	9.26	44.5
$R_A(I = 2.0A) = 31.64\ \Omega$		

It is evident that with increasing ω the angle δ also increases. This is due to the increase of the synchronous reactance ($\omega_e L_S$). The values of δ are relatively low, because of the large R_A. In a typical synchronous machine, the synchronous reactance is about 10 times as large as the armature resistance as explained in [61] and the load angle is about 15° to 20°. For the generator tested however, (as well as for other similar machines described in [60]), R_A and $\omega_e L_S$ are of the same order of magnitude, and hence δ gets low values (see also figure 5.2). For lower currents, δ is even lower. For I = 0.5A for example, the synchronous reactance voltage ($I\omega_e L_S$) is about 10 times lower than the terminal voltage and δ is almost zero at ω = 500 rpm and a mere 3.65° at ω = 1500 rpm.

With knowledge of $P_{misc}(I,\omega)$, the power produced by the vortex turbine during the prototype experiment can be estimated using equation 5.1.6. During the

experiment, for each pair of operating conditions (ie ω and I), P_{out} will be measured on a wattmeter, P_{misc} will be calculated using the calibration chart of figure 5.14 and for estimating the electrical losses a thermo-couple placed near the stator windings will be used for estimating R_A. The power output and losses will be then added to give P_{in} which in this case is the mechanical power of the turbine.

5.1.5. Conclusions.

The most important conclusions from this study are:

1. The generator model parameters have been estimated. They can be used together with the turbine power output predictions for estimating the prototype long term performance.
2. The generator power losses have been identified and measured. Thus the generator was calibrated in order to be used as a power absorber by the prototype turbine.
3. The generator maximum efficiency was found to be 70%. It was obtained at I = 1.4A and ω = 1500 rpm.

5.2. PROTOTYPE LONG-TERM PERFORMANCE ESTIMATION.

In this section, the generator test results are used together with the turbine performance predictions for estimating the long-term performance of the delta wing-turbine system prototype. The generator and load chosen for it were modelled by use of an appropriate electrical circuit and the annual power yield of the prototype was predicted using wind statistics. A brief account of the relevant theory is given first.

5.2.1. Theory.

a) Generator load matching. The power produced by a generator depends on the application it is chosen for. In our case, the generator was chosen to heat-up a resistor. This is the simplest possible load that can be used and hence the generator-load modelling is also simplified. Use of wind power for heating purposes has a wide range of applications, especially for small scale machines, such as space or water heating. A heating resistor is not sensitive to the AC signal frequency variations and hence the generator can operate at variable rpm in order to optimise the turbine power output. For that to be achieved, the turbine must operate at optimum tip speed ratio at all windspeeds below the rated. As can be seen from equation 4.2.1, the mechanical power (P_m) produced by the prototype turbine is proportional to V_∞^3. The P_m maximum for a given windspeed is achieved at $\lambda_{opt} = 6.75$, when C_p is maximised. Since $\lambda_{opt} = \omega R/V_\infty$, it is evident that the maximum turbine power will be proportional to ω^3. ($P_{m\,max} \sim \omega^3$). Hence, a load must be found that will make the generator power requirement proportional to ω^3. In figure 5.20, the generator-load model is shown when a single resistor (R_L) is used as load. The power consumed on the resistor is $P_e = I^2 R_L$. Also, $I = E_A/Z$, with Z the total circuit impedance. Using equation 5.1.2, we get:

$$P_e = \frac{K_e^2\,\omega_e^2\,R_L}{(R_L + R_A)^2 + \omega_e^2\,L_S^2} \qquad (5.2.1)$$

It is evident that if $R_L + R_A >> \omega_e L_S$, $P_e \sim \omega_e^2$, while if $R_L + R_A << \omega_e L_S$, P_e = constant. Therefore, a single resistor is not a wise load choice, since $P_e \sim \omega_e^2$ at the most. For a better load matching, several resistors can be used together with relays and a controller that can switch on the appropriate percentage of the total resistance for matching the

turbine output. Such a system is described in [61]. However, this method has several shortcomings as reported in [3], especially concerning the system stability when the windspeed changes. Another idea presented in [62] is the use of an autotransformer inserted between the generator and the resistor. The autotransformer can vary the resistor voltage and hence its power in a smooth fashion. However, the price of an autotransformer is comparable to that of a generator and it was not considered a practical solution. The load matching method used is presented in [3]. Instead of a single resistor, a resistor connected in series with a capacitor (C_L) is used as a load. Thus, a series resonant circuit results, shown in figure 5.21. The electrical power in that case is given by:

$$P_e = \frac{K_e^2 \omega_e^2 R_L}{(R_L + R_A)^2 + \left(\omega_e L_S - \frac{1}{\omega_e C_L}\right)^2} \qquad (5.2.2)$$

The current flowing through the circuit of figure 5.21 is:

$$I = \frac{E_A}{Z} = \frac{K_e \omega_e}{\sqrt{(R_L + R_A)^2 + \left(\omega_e L_S - \frac{1}{\omega_e C_L}\right)^2}} \qquad (5.2.3)$$

At a certain value of ω_e, called resonant rotational speed $\omega_{e,res}$, $\omega_{e,res} L_S = 1/(\omega_{e,res} C_L)$ and the load becomes purely resistive. The various possibilities for the P_e variation with ω_e are shown in table 6. It evident that for the resonant load system, P_e varies widely with ω_e. A set of C_L, R_L can be found for obtaining $P_e \sim \omega_e^3$ in the rotational speed regime of interest. This load opimization is a passive one and does not require wind or frequency sensors or controllers. It will therefore be the least expensive.

b) Wind statistics. For estimating the prototype long-term performance a wind speed occurence probability distribution is required. Two such distributions are the most common in wind statistics. They are the Weibull and Raleygh distributions. The

TABLE 6

CASE 1 $\omega_e << \omega_{e,res}$	CASE 2 $\omega_e = \omega_{e,res}$	CASE 3 $\omega_e >> \omega_{e,res}$
$P_e \sim \dfrac{K_e^2 \omega_e^2 R_L}{(R_A + R_L)^2 + \dfrac{1}{\omega_e^2 C_L}}$	$P_e = \dfrac{K_e^2 \omega_e^2 R_L}{(R_A + R_L)^2}$	$P_e \sim \dfrac{K_e^2 \omega_e^2 R_L}{(R_A + R_L)^2 + \omega_e^2 L_S^2}$
a) $R_{ext} << \dfrac{1}{\omega_e^2 C_L} \Rightarrow P_e \sim \omega_e^4$ b) $R_{ext} >> \dfrac{1}{\omega_e^2 C_L} \Rightarrow P_e \sim \omega_e^2$	$P_e \sim \omega_e^2$	a) $R_{ext} << \omega_e^2 L_S^2 \Rightarrow P_e \sim \omega_e^0$ b) $R_{ext} >> \omega_e^2 L_S^2 \Rightarrow P_e \sim \omega_e^2$

later is a special case of the former. The Weibull distribution was chosen to be used for this analysis, as it is a more general one and can fit wind data quite effectively since it is a two parameter function. The probability density (f) of the Weibull distribution is given by:

$$f(V) = \frac{k}{c}\left(\frac{V}{c}\right)^{k-1} \exp\left[-\left(\frac{V}{c}\right)^{k}\right] \quad (k > 0,\ V > 0,\ c > 1) \qquad (5.2.4)$$

k is called the shape factor, while c is the scale factor. The former is dimensionless while the latter has dimensions of velocity. In figure 5.22, f(V) is shown for c =1 and various values of k. The effect of the shape factor is evident. With k increasing, the f(V) curve has a narrower peak, which means that the most probable windspeeds are gathered in an increasingly narrow region. Hence, k is associated with the distribution standard deviation. Also, with k increasing, the most probable speed approaches the windspeed which is equal to c. For most wind regimes, k gets a value of about 2. However, with the average windspeed increasing, k tends to increase marginally. The effect of the scale factor is to move the peak of f(V) on the x axis. With c increasing, the most probable speed value increases, but the probability for that windspeed decreases so that the area beneath the f(V) curve remains equal to unity. The plots of figure 5.22 can be scaled-up by multiplying the x-ordinates by c and dividing the y-ordinates by the same amount. It

is also evident from figure 5.22, that the Weibull distribution is not symmetric about the most probable windspeed. The average windspeed is slightly larger than the most probable one. As can be seen in figure 5.23, for k within the region from 1.5 to 3.0, c is equal to 1.12 times the average windspeed:

$$c = 1.12 \langle V \rangle \qquad (5.2.5)$$

For a set of wind data from a given site, several methods exist in order to estimate c and k and thus fit a Weibull distribution to the data. (See references [7] and [8]). This will not concern us however, since there isn't a particular site of interest. In this study, k and c will be regarded as parameters and their effects on the prototype performance will be assessed.

The variation of the electrical power produced by a wind turbine with V_∞ is shown in figure 5.24. There are three very important windspeed values associated with this curve:

- V_{IN} (Cut-in speed).
- V_R (Rated speed).
- V_O (Cut-out speed).

V_{IN} is the windspeed at which the machine just starts to produce electrical power. The turbine starts rotating at a slightly lower windspeed, but the power produced is consumed in overcoming the generator and transmission losses.

V_R is the rated windspeed for which the turbine has been designed. At that windspeed it produces rated power (P_R).

V_O is the cut-out speed, above which the turbine is shut down, in order to prevent structural damage.

These three values of V_∞ divide the $P_e(V_\infty)$ curve into two regions. Between V_{IN} and V_R, the turbine produces power less than P_R and it is in that region that special effort is

made to maximise the electrical power output. Between V_R and V_O, an appropriate power regulating mechanism, which is present in all wind power plants, reduces either the aerodynamic efficiency of the turbine (pitch or stall control) or the wind attacking the turbine (yaw control), so that the power produced will be as close to P_R as possible. A large amount of wind power is wasted in that region. This happens because operation of the turbine at optimum conditions in that region would increase its rotational speed to unacceptable values. In some cases, the limit to how large V_R can become is imposed by the generator whose ratings should not be exceeded. The former P_e region is called partial power range. The latter is called constant power range.

For a given wind regime, there is a value of V_R that optimises the turbine long-term performance. This can be explained as follows: An increase of the turbine's V_R increases P_R ($\sim V_R^3$), but if the new V_R value is less frequent than the old one, the turbine will operate less time at V_R. This may reduce the long-term performance of the turbine. The balance between the two conflicting trends can be found calculating the turbine average electrical power P_{av}, using the Weibull distribution:

$$P_{av} = \int_{V_{IN}}^{V_O} P_e(V)\, f(V)\, dV \quad , \qquad \text{or:} \qquad (5.2.6)$$

$$\therefore \quad P_{av} = \int_{V_{IN}}^{V_R} P_e(V)\, f(V)\, dV + P_R \int_{V_R}^{V_O} f(V)\, dV = P_1 + P_2$$

P_1 is the power of the partial power range, while P_2 is that of the constant power range. It is desirable to make P_{av} independent of the turbine's particular design and the wind regime characteristics. For that purpose, P_{av} is normalised as follows:

$$P_{norm} = \frac{P_{av}}{\frac{1}{2}\rho C_p \eta_R A c^3} \qquad (5.2.7)$$

The denominator in the above expression is the rated power of a turbine with

aerodynamic efficiency C_p, generator and transmission efficiency η_R (ie the efficiency at V_R), of area A at a rated windspeed equal to c^3. c^3 is used since c is related to the average windspeed of a site. P_{norm} is therefore independent of the turbine performance and dimensions and of the wind regime mean windspeed. It depends on the relative values of V_{IN}, V_R and V_O, the ratio V_R/c (ie the relative positions of $P_e(V)$ and $f(V)$), k and the shape of the $P_e(V)$ curve in the partial power range. Another important parameter is the capacity factor (CF), which is defined as:

$$CF = P_{av} / P_R \qquad (5.2.8)$$

CF expresses the amount of time (say within a year) that the turbine produces power equal to P_R. It is a very useful indication of how the turbine power is distributed in time: A low CF value means that the turbine will operate most of the time in the partial power range and it will produce power less than P_R. This situation may be unacceptable in some cases such as pumping water, where a minimum amount of power has to be provided in order to overcome a certain head. However, when a wind turbine is used as a fuel saver, providing electricity to a grid, capacity factor is not as important as P_{av} optimisation, and low values of CF can be tolerated. With knowledge of $P_{norm}(V_R/c)$ and $CF(V_R/c)$ decisions for the installation of a wind turbine at a given site are possible.

5.2.2. Description of the numerical techniques used.

For the estimation of the prototype long-term performance, a computer program was developed written in fortran. The numerical techniques used are described here.

a) Generator load matching. The power input to the generator is the mechanical power produced by the turbine. For the generator load optimisation,

knowledge of the turbine power at various values of $V_{\sim}$ and λ is necessary. The $C_p(\lambda,V_{\sim})$ plots shown in figure 4.18, which are the results of the turbine performance analysis, were used. The data of figure 4.18 were tabulated and an appropriate two-parameter interpolation routine was used. This routine was taken from the NAG fortran library. It is the E01ACF routine which interpolates at a given point (A,B), in our case $(\lambda,V_{\sim})$, from a table of function values defined on a rectangular grid, by fitting bi-cubic spline functions. For constructing the $C_p(\lambda,V_{\sim})$ table, the values of C_p for λ less than 5 were extrapolated, and hence the results in the λ region from 0 to 5 are not reliable. However, that doesn't affect the final results' accuracy, since the load optimisation was such that the turbine was operating at near optimum conditions throughout the partial power range.

For optimising the generator load, the values of R_L and C_L for the resonant circuit must be found. This was done using the following iterative procedure:

Step 1. Initial values of R_L and C_L were chosen. Also, the generator model parameters (established by the generator test) were used. The turbine optimum mechanical power was estimated at two values of $V_{\sim}$, namely $V_1 = V_R$ and $V_2 = (V_R+V_{IN})/1.7$. The value of 1.7 as chosen because it provided the best match between the generator power requirement and the turbine optimum power. The turbine power for those windspeeds was P_{m1} and P_{m2} respectively. Also, ω and ω_e were calculated for each $V_{\sim}$ value.

Step 2. The generator armature resistance (R_A) was calculated using the 5-th degree polynomial that approximates its dependence on I. (See figure 5.11). However, as can be seen from equation 5.2.3, I also depends on R_A and for calculating R_A and I, another iteration was used (nested within the outer iteration): An initial value of R_A was assumed and I was found from equation 5.2.3. Then, $R_{A,new}$ was calculated for the new value of I. If $R_{A,old}$ and $R_{A,new}$ were not close enough, the procedure was repeated, until

convergence was achieved. This procedure was repeated every time an estimate of R_A and I was needed.

Step 3. With I and R_A known, equation 5.1.6. was used for estimating the required electrical power (P_{e1}) at V_1, so that the wind turbine would operate at optimum conditions. In equation 5.1.6, P_{in} was taken to be equal to P_{m1}, while $P_{misc}(I,\omega)$ was estimated using the same technique as that for the $C_p(\lambda,V_\infty)$ calculation (ie tabulation of the $P_{misc}(I,\omega)$ values and interpolation using the E01ACF routine).

Step 4. Equation 5.2.2. was solved for R_L with P_e equal to P_{e1}, yielding:

$$R_L = \frac{\sqrt{B_1^2 - 4A_1C_1} - B_1}{2A_1}$$

With:

$$A_1 = P_{e1} \qquad (5.2.9)$$

$$B_1 = 2P_{e1}R_A - K_e^2\omega_e^2$$

$$C_1 = \left[R_A^2 + \left(\omega_e L_S - \frac{1}{\omega_e C_L}\right)^2\right]P_{e1}$$

Thus, the new value of R_L was estimated. For speeding-up the iteration, the $R_{L,new}$ value was used for calculating P_{e2} (using the same technique as that for the calculation of P_{e1}, described above), and equation 5.2.2 was solved for $1/C_L$ this time, with $P_e = P_{e2}$, yielding:

$$C_L = \frac{2A_2}{\sqrt{B_2^2 - 4A_2C_2} - B_2}$$

With: (5.2.10)

$$A_2 = \frac{P_{e2}}{\omega_e}, \quad B_2 = -2P_{e2}L_S$$

$$C_2 = P_{e2}R_L\left[(R_L + R_A)^2 + (\omega_e L_S)^2 - (K_e\omega_e)^2\right]$$

In both equations 5.2.9 and 5.2.10, the solution branches omitted produced negative

results, with no physical meaning.

Step 5. The new and old values of C_L were compared, and if they were not close enough, the procedure was repeated until convergence was achieved. The convergence criterion was: $| C_{L,new} - C_{L,old} | \leq 10^{-10} C_{L,new}$.

Once R_L and C_L were estimated and a satisfactory load match was achieved, equations 5.1.6 and 5.2.2 were used for obtaining the $P_g(V_\infty)$ curve. This was done as follows: The equation $P_{in} - P_{out} - I^2R_A - P_{misc} = 0$ was solved for 201 values of V_∞ within the (V_{IN}, V_R) region, using the bisection method. For each value of V_∞, an appropriate value of ω was found so that the generator power demand would meet the turbine power supply. $I(V_\infty)$ and $\eta_g(V_\infty)$ were also calculated, for obtaining more details of the generator performance.

b) Prototype long-term performance estimation. This was done as follows: Appropriate values of k, c, V_{IN}, V_R and V_O were chosen and equations 5.2.4, 5.2.6, 5.2.7 and 5.2.8 were used for estimating P_{norm} and CF. The integrals of equation 5.2.6 were calculated numerically, using Simpson's method with 201 points. With all other parameters remaining the same, different values of V_R were tried and thus the $P_{norm}(V_R/c)$ and $CF(V_R/c)$ curves were obtained. Finally, the effects of k and c were examined by repeating the above for different values of the two parameters.

5.2.3. Presentation of results.

a) Generator load optimisation. As explained in the previous section, for the load optimisation, choice of appropriate values for V_R and V_{IN} was necessary. Various values of V_R were tried and it was found that the maximum possible rated windspeed was 9 m/s. Above that value, the generator current at V_R was exceeding its

ratings by a considerable amount. (this will be explained in more detail later). For V_{IN}, a value of 3 m/s was chosen, since prediction of C_p below that value was not possible, due to the turbine performance routine limitations. For V_{IN} = 3 m/s and V_R = 9 m/s, the values of the resonant circuit elements were found to be:

$$R_L = 80.0\,\Omega \quad \text{and} \quad C_L = 1.65 \times 10^{-5}\ \text{F}.$$

The electrical resonance rotational speed was found to be:

$$\omega_{e,res} = [1/(L_S C_L)]^{1/2} = 1130\ \text{rad/s}.$$

The mechanical resonance speed is:

$$\omega_{res} = 1799\ \text{rpm}.$$

In figure 5.25, the turbine optimum power (using $\lambda = \lambda_{opt}$) and the generator power requirement for the above mentioned values of R_L and C_L are plotted versus rotational speed. The generator power requirement was calculated using equations 5.1.6 and 5.2.2. It is P_{in} of equation 5.1.6 with P_{out} given by equation 5.2.2. At V_{IN}, ω = 322 rpm. At V_R, ω = 967 rpm. The points used for the load optimisation (ie V_R and $(V_R+V_{IN})/1.7$), are marked by crosses. The irregularities of the generator power requirement curve were caused by the irregularities in the P_{misc} curves. In the following table, the values of ω_e, $\omega_e L_S$, $1/(\omega_e C_L)$ and $(R_L + R_A)$ are shown for V_{IN} and V_R.

TABLE 7

V_∞ (m/s)	3 (V_{IN})	9 (V_R)
ω_e (rad/s)	202.3	607.5
$\omega_e L_S$ (Ω)	9.6	28.9
$\frac{1}{\omega_e C_L}$ (Ω)	303.0	99.9
$R_L + R_A$ (Ω)	108.6	112.1

For $V_\infty = V_{IN}$, $1/(\omega_e C_L) >> \omega_e L_S$ and case 1 of table 6 applies for the P_e variation with ω_e. Since $1/(\omega_e C_L)$ is comparable with $(R_L + R_A)$, the variation of P_e with ω_e is between

ω_e^4 and ω_e^2. For $V_\infty - V_R$, $\omega_e L_S$, $1/(\omega_e C_L)$ and $(R_L + R_A)$ are of the same order of magnitude and it is not possible to classify this case with respect to table 6. However, $1/(\omega_e C_L) > \omega_e L_S$ and P_e should vary with ω_e^2 to ω_e^4. It is evident from figure 5.25 that the load matching is excellent. The generator power requirement curve follows closely the turbine optimum power curve and the turbine operates at near optimum conditions throughout the partial power range. Indeed, the poorest matching occurs at $V_\infty = 5.7$ m/s, ($\omega = 595$ rpm), with λ getting its lowest value which is 6.55, about 3% less than λ_{opt}. C_p for that case is about 0.7% less than $C_{p\,max}$. It can therefore be concluded that a resonant circuit can give a very good load optimisation.

In figures 5.26, 5.27 and 5.28, $P_e(V_\infty)$, $I(V_\infty)$ and $\eta_g(V_\infty)$ are shown respectively. All three curves are divided into two parts; one in the partial power range and one in the constant power range. For the latter, a suitable control mechanism was assumed to act, in order to keep P_e, ω and I constant in that region. Consideration of such mechanisms and their suitability for the system prototype will be given in the next chapter. It can be seen from figure 5.26, that for the V_{IN} chosen (ie 3 m/s) the value of P_e is not zero. It is about 10W, which is 2.7% of P_R. However, it was not possible to extend the $P_e(V_\infty)$ curve to a lower V_{IN}, due to the limitations of the turbine performance analysis procedure. The fact that some power is produced at a windspeed which is 1/3 of the rated is encouraging, since most conventional turbines have a V_{IN}/V_R ratio of about 0.5. The low V_{IN} value can be attributed to several factors. One is that the delta wing concentrates the wind power considerably and the wind velocity in the vortex will be about 1.5 to 2.0 times as large as the undisturbed wind velocity. Therefore, the generator losses can be overcome at lower undisturbed windspeeds. Also, the turbine used here is a multi-bladed one and can provide more torque than a few-bladed counterpart at the same windspeed. Another factor is the actual amount of the generator losses. As will be

explained later, the generator was found not ideal for the prototype turbine. A generator with larger ratings would be more suitable. Such a generator would require larger torque values to operate and that would increase V_{IN}. However, V_R would also increase with the use of a larger generator, and the V_{IN}/V_R ratio is not expected to change considerably. The V_O value was chosen to be twice that of V_R, ie 18 m/s, since according to [3] and [65], a typical value for V_O/V_R is about 2.0.

It can be seen from figure 5.27, that the generator current increases within the partial power range with V_∞ increasing. At $V_\infty = V_R = 9$ m/s, I = 2.13 A, which is 6.75% larger than the generator rated current (2.0 A). As was reported before, during the generator test, it was found that for I values larger than 2.2 A, the generator was overheating. Therefore, the maximum allowable rated windspeed is 9 m/s, in order to keep I below the 2.2 A limit. Also, from figure 5.27, it can be seen that the I values within the generator resonance region (ie 700 rpm to 800 rpm, which correspond to V_∞ values of 6.6 m/s to 7.6 m/s) are relatively low (1.3 A to 1.6 A approximately). Therefore, the generator will pass through its resonance region without exibiting large vibrations. The rotational speed for V_∞ values larger than V_R is 967 rpm (see figure 5.25), well outside the resonance regime.

The generator efficiency versus windspeed is shown in figure 5.28. Fluctuations in η_g can be observed for V_∞ above 6.9 m/s. These can be explained as follows: The parameters that affect the generator efficiency are its current and rotational speed. As can be seen in figure 5.17, for each value of ω, there is a value of I that maximises η_g. With V_∞ increasing, both I and ω increase. The efficiency also increases up to a point where further increase of ω causes I to exceed its I_{opt} value. Then, increase of ω tends to increase the generator efficiency, while increase of I tends to decrease it. Those two conflicting trends produce the η_g fluctuations.

The values of η_g were found to be low. For example, $\eta_g(V_R) = 0.547$. The low values of efficiency are caused mainly by the large amount of electrical losses. The generator armature resistance is about 30 Ω. The load resistance is about 80 Ω. Hence, $R_L/R_A = 2.67$. It follows that about 1/3 of the electrical power produced by the generator is consumed on R_A. Because of that, the rated electrical power is just 364 W, while the turbine mechanical power is 665.6 W. The generator used was designed to operate at ω = 600 rpm and produce 220 W of electrical power. When used with the prototype turbine, it is taken to its limits, operating at ω = 967 rpm, with large currents flowing through it. It can be successfully used as a power absorber for the prototype experiment, since windspeeds up to 9 m/s can be sampled. For that application, the efficiency of the generator is not important. However, for the application investigated here, efficiency is important and a generator with lower R_A, capable of supplying larger currents would be more suitable as will be shown in the following. The turbine mechanical power at V_R is 665.6 W. Assuming a generator with $\eta_g = 0.8$ at V_R, P_e = 532.48 W. The electrical power from the generator (P_e) will be less than IE_A. (It is equal to IE_A if the effects of R_A and phase angle ϕ are neglected). Hence:

$$P_e \leq IE_A = IK_e\omega_e \qquad (5.2.11)$$

There are three parameters in the above equation: ω_e, K_e and I. Increase of ω_e would require a step-up gearbox which is not desirable, since the turbine operates at high enough rpm for it to be directly linked to a generator. Increase of K_e, as can be seen from equation 5.2.3, also increases I. For I to remain at the same levels, R_L will need to increase, and thus the electrical efficiency of the generator will improve. The K_e increase can be achieved by increasing the magnetic flux through the stator windings, either by using stronger rotor magnets made by rear earth materials, or by use of iron cores in the stator windings. Finally, if K_e remains the same, it follows from equation 5.2.11 that I

must be at least 1.87 A for the generator to produce 532 W of electrical power. Since equation 5.2.11 is an oversimplification of the problem, used only to give some insight to the parameters involved, I will need to be considerably larger than 1.87 A. Hence, larger diameter wires are needed for the stator coils in order to carry larger currents. Also, since a conductor's resistance is inversely proportional to its cross-section, larger diameter wires will reduce R_A and thus improve the generator electrical efficiency. It will also be possible to obtain larger values of V_R, since the maximum allowable current through the generator will increase.

b) Prototype long-term performance estimation. With the $P_a(V_\infty)$ curve known, estimation of the long-term performance followed. In these calculations, various values of k and c were tried for assessing their effects. For each set of k and c, V_{IN} and V_O were kept constant, while V_R was allowed to vary. Hence, the V_R/V_{IN} and V_O/V_R ratios changed for each V_R. Keeping V_{IN} and V_O constant implies that all prototype components are the same and only the wind regime and V_R are changing. Keeping the V_R/V_{IN} and V_O/V_R ratios constant would imply use of different components for each V_R, such as a larger turbine or generator. In figures 5.29 a, b, c and d, the plots of $P_{norm}(V_R/c)$, $P_1(V_R/c)$, $P_2(V_R/c)$ and $CF(V_R/c)$ are shown respectively, for four values of c, namely 3 m/s, 3.5 m/s, 4 m/s and 4.5 m/s, and for k = 2.0. These curves show the effect of c on P_{norm}. For the same c, and with V_R/c increasing, there is a value of V_R/c that maximises P_{norm}. However, the P_{norm} peak is not steep and a large plateau exists with near-maximum P_{norm} values. It can also be seen that with c inceasing, the value of V_R/c for which P_{norm} is maximum increases as well as the $P_{norm,max}$ value. This behaviour is due to the fact that with c increasing and for a given V_R/c value, V_R/V_{IN} increases while V_R/V_O decreases. It can be seen from figures 5.25 b and c, that with c increasing, P_{norm} in the partial power range increases following the V_R/V_{IN} increase, while in the constant

power range, P_{norm} remains at the same levels. In the following table, the values of $P_{norm,max}$ and $V_R/c(P_{norm,max})$ for various values of c are shown:

TABLE 8
Effect of c, k = 2.0

c (m/s)	$P_{norm,max}$	$\frac{V_R}{c}(P_{norm,max})$
3.0	0.896	1.94
3.5	0.969	2.01
4.0	1.021	2.12

For a change of c equal to 25% (from 3 m/s to 4 m/s):

$\Delta P_{norm,max}$ = 12.3%

$\Delta(V_R/c)$ = 8.5%

In figure 5.29.d, $CF(V_R/c)$ is shown. It can be seen that CF increases slightly for the same V_R/c with c increasing, due to the V_R/V_{IN} increase. For c constant and V_R/c increasing, CF drops rapidly. This is because P_{av} increases at a lower rate than P_R ($\sim V_R^3$).

The effect of k on P_{norm} is shown in figures 5.30 a, b, c and d, where $P_{norm}(V_R/c)$, $P_1(V_R/c)$, $P_2(V_R/c)$ and $CF(V_R/c)$ are plotted respectively, for c = 4.5 m/s and k varying from 1.5 to 3.0. For c = 4.5 m/s, according to equation 5.35, $\langle V \rangle$ = 4.02 m/s. It is evident that with k increasing, ie with the most probable windspeeds being concentrated in an increasingly narrow band, $P_{norm,max}$ as well as $V_R/c(P_{norm,max})$ is decreasing. The P_{norm} values in the constant power range differ considerably for different values of k and for V_R/c larger than 1, since as the most probable windspeeds gather in a narrower band, the constant power range contributes less to the total power. In the following table, the values of $P_{norm,max}$, $V_R/c(P_{norm,max})$ and $CF(P_{norm,max})$ are given:

TABLE 9
Effect of k, c = 4.5 m/s

k	$P_{norm,max}$	$\frac{V_R}{c}(P_{norm,max})$	CF ($P_{norm,max}$)
2.0	1.051	2.00	0.133
2.5	0.874	1.73	0.169
3.0	0.799	1.51	0.221

For a change of k equal to 33.3% (from 2 to 3):

$\Delta P_{norm,max}$ = 23.9%

$\Delta V_R/c$ = 24.7%

ΔCF = 39.8%

Comparing tables 8 and 9 it can be seen that the effect of k is larger than that of c, especially on the $V_R/c(P_{norm\ max})$ values. It can therefore be concluded that the shape of the wind velocity distribution has a larger effect on P_{norm} than the mean windspeed. The curves of figures 5.30 a and d can be compared with those of figures 5.31 a and b referring to a different turbine, taken from [65]. They seem to agree well, both qualitatively and quantitatively revealing that the normalisation of the generator power is successful.

It can also be seen from table 9, that for k = 2 and c = 4.5 m/s (which represents a typical wind regime with <V> = 4.02 m/s) P_{norm} is maximised at $V_R/c = 2.0$ (or $V_R = 9$ m/s), but CF gets a very low value, namely 0.133 and if this value of V_R/c is chosen for the prototype at that site, the turbine will operate on full capacity for about 13% of the time. This may be undesirable for some applications as explained before. The capacity factor can increase if V_R/c gets a lower value. Then the turbine will operate more time at the constant power range. Increase of CF brings about a reduction in P_{av} as shown in the following table.

TABLE 10

k = 2, c = 4.5 m/s, <V> = 4.02 m/s

CF	V_R (m/s)	V_R/c	V_R/V_{IN}	P_{av} (W)	Yearly energy production (kWh)
0.133	9.00	2.00	3.00	48.5	424.86
0.300	6.36	1.41	2.12	34.5	302.20

In this table, P_{av} was calculated using equation 5.2.8, while the yearly energy production was estimated by:

$$E = 8760\ P_{av} \quad \text{(in kWh)}$$

with 8760 the number of hours in a 365 days year. It is evident from the above table that for a CF increase of about 55.7%, a drop of 28.9% in both P_{av} and E results.

Finally, assuming that the $P_{norm}(V_R/c)$ and $CF(V_R/c)$ curves will be similar to those shown in figures 5.30 a and d when a more suitable generator is used (with η_g = 0.8 at V_R), P_{av} and E can be estimated using equation 5.2.7 with η_g = 0.8. The results are tabulated below:

TABLE 11

k = 2. c = 4.5 m/s. <V> = 4.02 m/s. $\eta_g(V_R)$ = 0.8

CF	V_R (m/s)	V_R/c	V_R/V_{IN}	P_{av} (W)	Yearly energy production (kWh)
0.133	9.00	2.00	3.00	70.9	621.1
0.300	6.36	1.41	2.12	54.1	473.9

Comparison of tables 10 and 11 reveals that with use of a more suitable generator, both P_{av} and E improve by 31.5% and 36.2% for CF values equal to 0.133 and 0.3 respectively.

5.2.4. Conclusions.

The main conclusions drawn from this study are summarised here:

1. Optimisation of the electrical load attached to the generator driven by the prototype turbine can be achieved using a series resonant circuit when the prototype is used for space heating. With that optimisation implemented, the turbine operates at near-optimum conditions throughout the partial power range.
2. The generator chosen to be used for the system prototype is adequate as a power absorber for the prototype tests, since a large range of windspeeds

can be sampled (0 to 9 m/s). However, it is not ideally suited for the prototype turbine when the system is used for space heating. Due to the large armature resistance of the generator, the electrical losses are considerable. Its efficiency can be improved if wires of larger diameter are used for the stator windings.

3. The effects of the Weibull parameters k and c on the prototype long-term performance were investigated. It was found that increasing c causes $P_{norm,max}$ and also $V_R/c(P_{norm,max})$ to increase due to the increase of V_R/V_{IN} for a given value of V_R/c. Increasing k causes $P_{norm,max}$ and $V_R/c(P_{norm,max})$ to decrease due to the fact that the most probable windspeeds concentrate at an increasingly narrow band.

4. For a wind regime with k = 2.0 and c = 4.5 m/s (ie $\langle V \rangle$ = 4.02 m/s), the maximum average power produced by the prototype when used for space heating was found to be 48.5 W (=0.133 P_R) and the yearly energy production was 424.9 kWh. With use of a more suitable generator (with $\eta_g(V_R) = 0.8$), these quantities should improve by 31.5%.

FIGURES FOR CHAPTER 5.

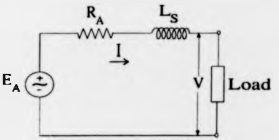

Figure 5.1. Equivalent circuit of a permanent magnet synchronous generator.

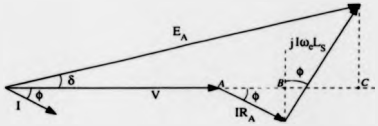

$$AB \text{ length} : AB = IR_A\cos\phi$$

$$BC \text{ length} : BC = I\omega_e L_S \sin\phi$$

Figure 5.2. Phasor diagram of a permanent magnet synchronous generator connected to a lagging load.

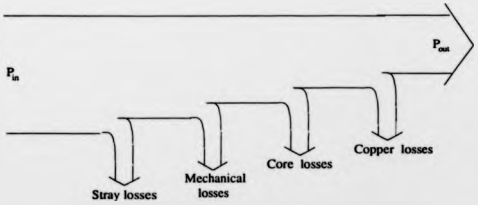

Figure 5.3. Power flow of a synchronous generator.

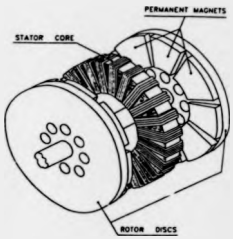

Figure 5.4. Sketch of an axial flux permanent magnet synchronous generator. (Taken from [58]).

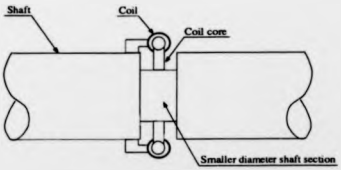

Figure 5.5. Sketch of the torque transducer measuring section.

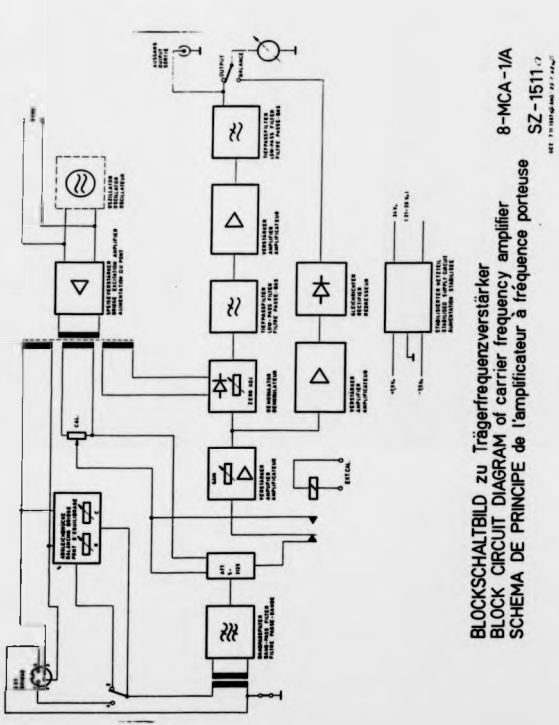

Figure 5.6. Block diagram of the 8-MCA-1/A carrier frequency amplifier.

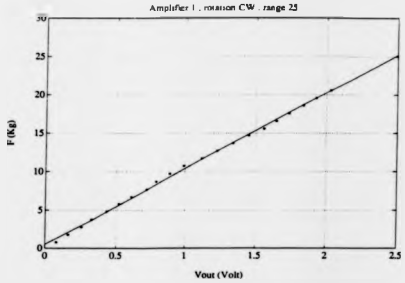

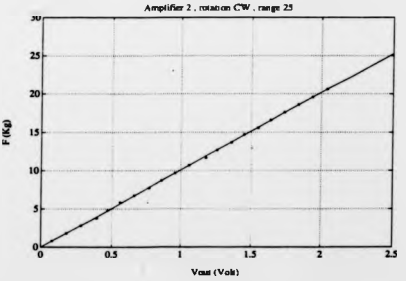

Figure 5.7. Torque transducer calibration charts.

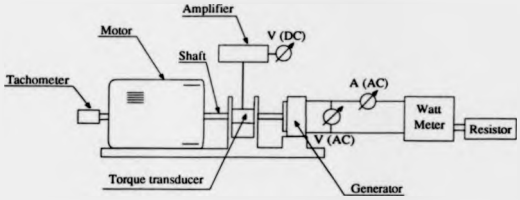

Figure 5.8. Sketch of the experimental set-up.

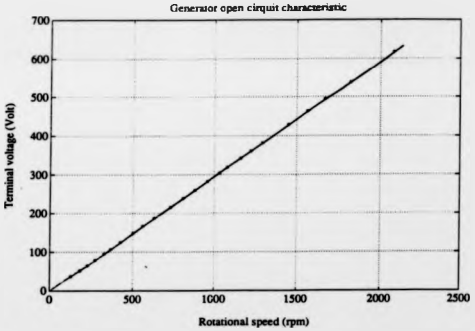

Figure 5.9. Open circuit characteristic.

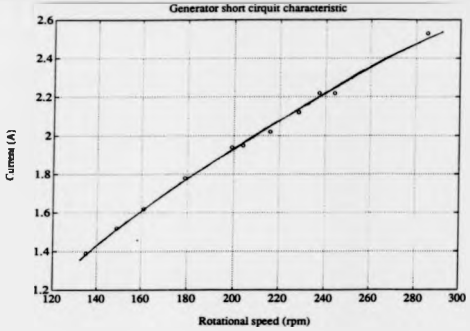

Figure 5.10. Short circuit characteristic.

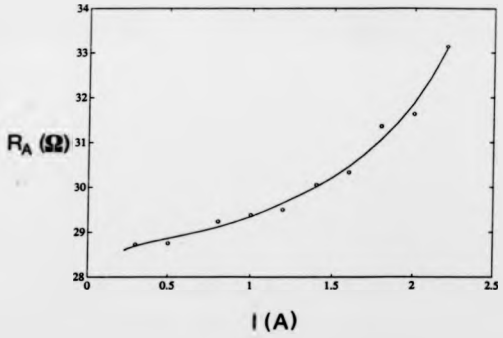

Figure 5.11. Variation of R_A with I.

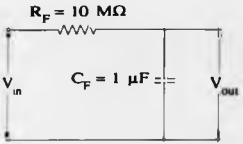

Figure 5.12. Filter circuit.

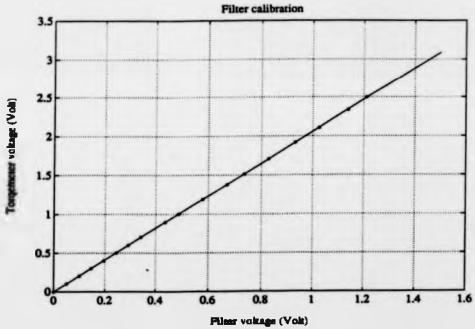

Figure 5.13. Filter calibration chart.

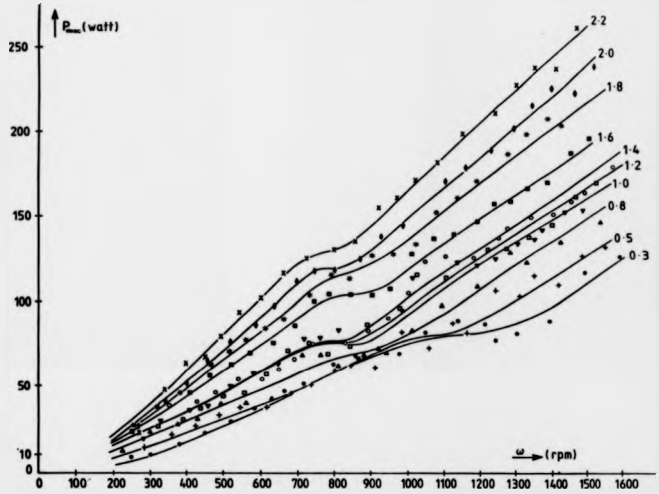

Figure 5.14. $P_{misc}(I,\omega)$ plots.

KEY:

Values of I (in A).

0.3 (•), 0.5 (+), 0.8 (Δ), 1.0 (▼)

1.2 (□), 1.4 (o), 1.6 (■), 1.8 (*)

2.0 (◊), 2.2 (x).

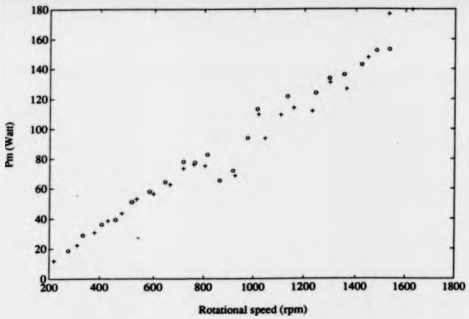

Figure 5.15. Repeatability test results for I = 1.0 A.
First run: '+'. Second run: 'o'.

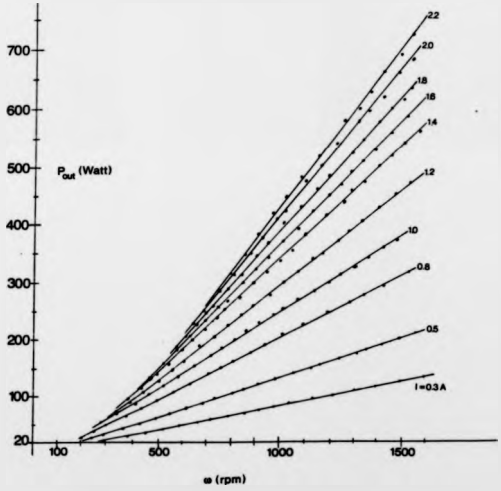

Figure 5.16. $P_{out}(I,\omega)$ plots.

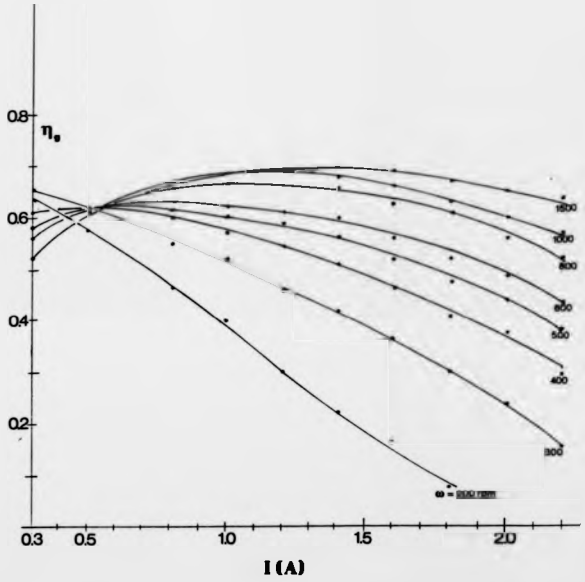

Figure 5.17. Generator efficiency plots.

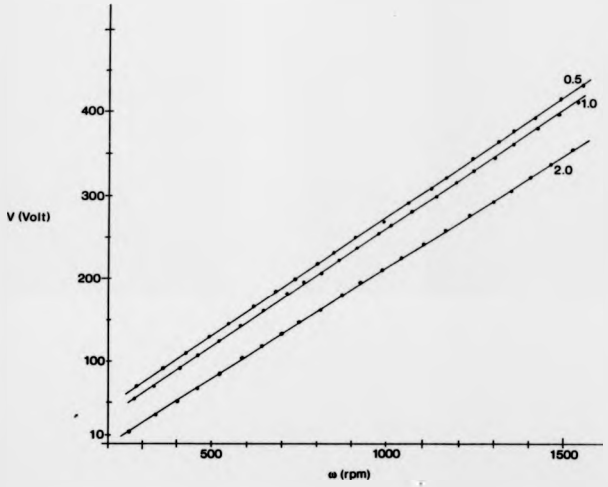

Figure 5.18. V(I,ω) plots.

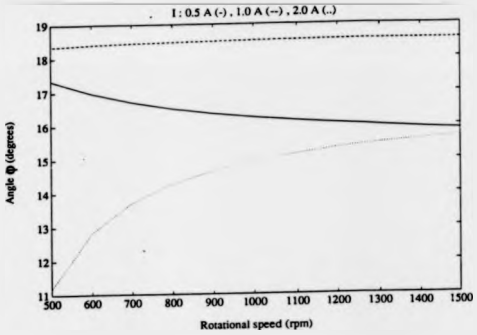

Figure 5.19. $\phi(I,\omega)$ plots

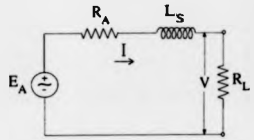

Figure 5.20. Equivalent generator circuit with a single resistor as a load.

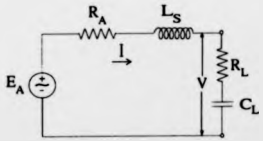

Figure 5.21. Equivalent generator circuit with resistor and capacitor in series as a load. (Resonant circuit).

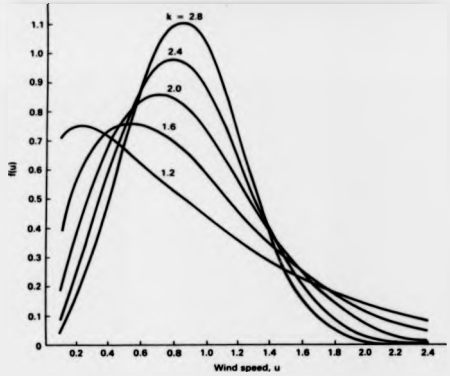

Figure 5.22. Weibull probability density distribution f(V) for c = 1 m/s and various values of k. (Taken from [3]).

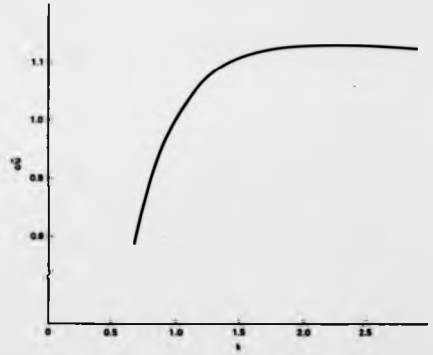

Figure 5.23. Weibull scale parameter divided by mean windspeed versus k. (Taken from [3]).

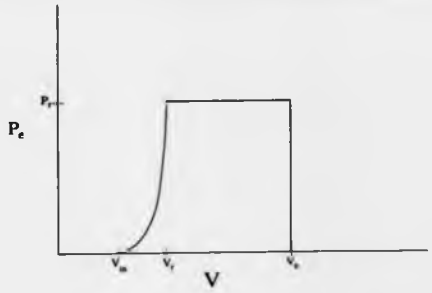

Figure 5.24. Wind turbine power versus windspeed.

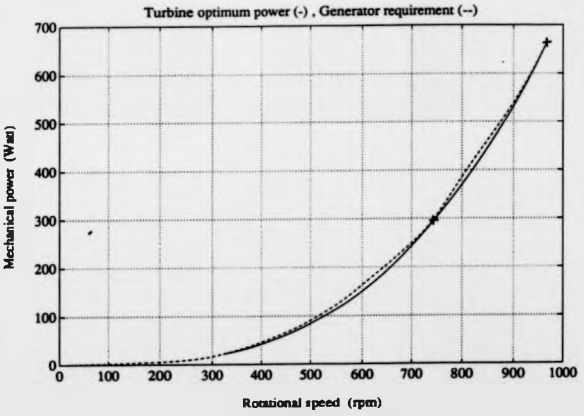

Figure 5.25. Load optimisation curves.

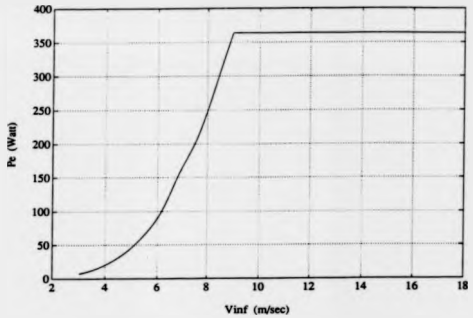

Figure 5.26. $P_e(V_\infty)$ plot. V_{IN} = 3 m/s, V_R = 9 m/s, V_O = 18 m/s.

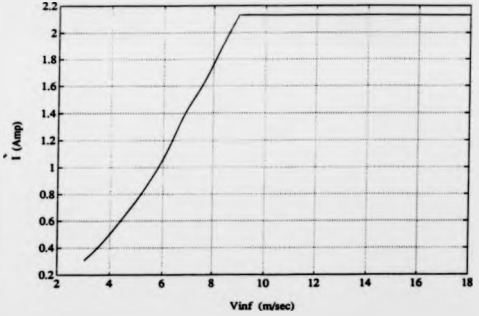

Figure 5.27. $I(V_\infty)$ plot. V_{IN} = 3 m/s, V_R = 9 m/s, V_O = 18 m/s.

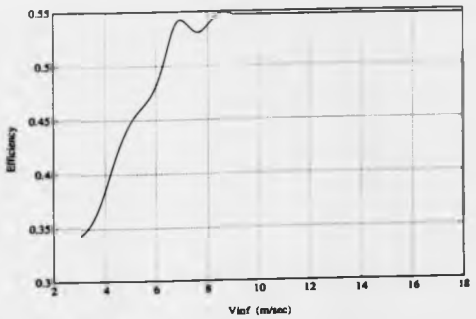

Figure 5.27. $\eta_g(V_\infty)$ plot. V_{IN} = 3 m/s, V_R = 9 m/s, V_O = 18 m/s.

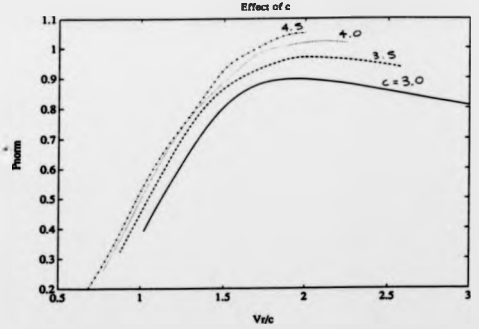

Figure 5.29.a. $P_{norm}(V_R/c)$ plots for k = 2 and various values of c (c in m/s).

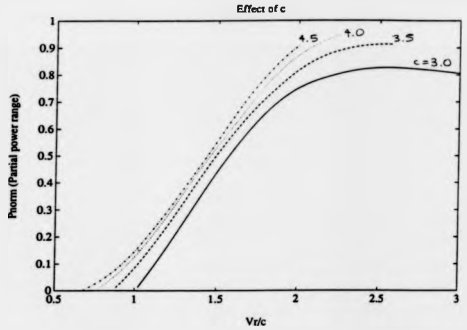

Figure 5.29.b. $P_{norm}(V_R/c)$ plots in the partial power range, for k = 2 and various values of c (c in m/s).

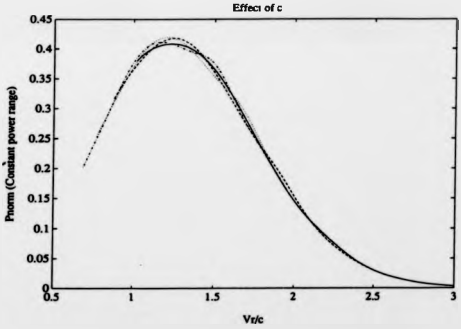

Figure 5.29.c. $P_{norm}(V_R/c)$ plots in the constant power range, for k = 2 and various values of c (c in m/s).

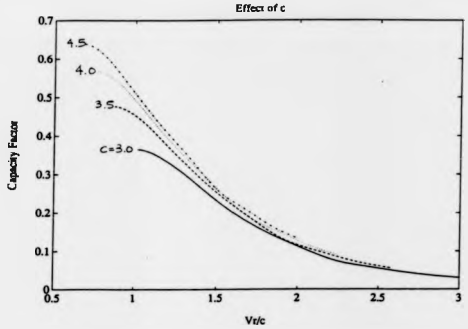

Figure 5.29.d. CF(V_R/c) plots for k = 2 and various values of c (c in m/s).

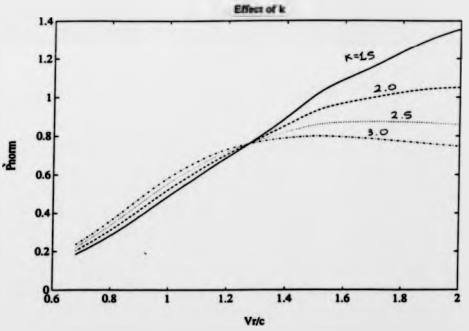

Figure 5.30.a. P_{norm}(V_R/c) plots for c = 4.5 m/s and various values of k.

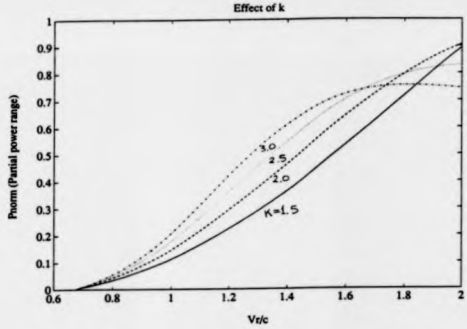

Figure 5.30.b. $P_{norm}(V_R/c)$ plots in the partial power range, for c = 4.5 m/s and various values of k.

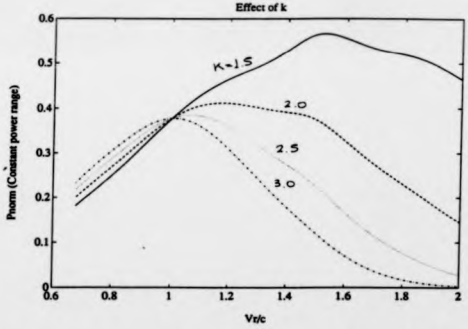

Figure 5.30.c. $P_{norm}(V_R/c)$ plots in the constant power range, for c = 4.5 m/s and various values of k.

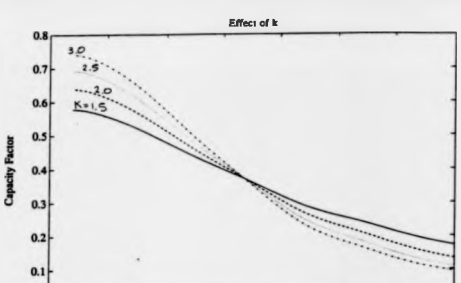

Figure 5.30.d. $CF(V_R/c)$ plots for c = 4.5 m/s and various values of k.

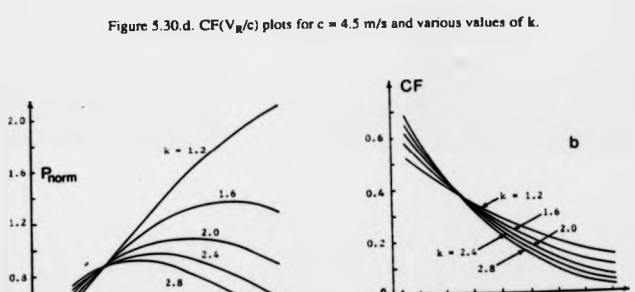

Figure 5.31. $P_{norm}(V_R/c)$ and $CF(V_R/c)$ plots (a and b respectively) for a conventional wind turbine with $V_R/V_{IN} = 2$, $V_O/V_R = 2$, $P_a \sim V^3$ in the partial power range. (Taken from [65]).

CHAPTER 6.

CONSIDERATIONS ABOUT THE SYSTEM ORIENTATION-POWER REGULATION MECHANISM.

CHAPTER 6. CONSIDERATIONS ABOUT THE SYSTEM ORIENTATION-POWER REGULATION MECHANISM.

6.0. INTRODUCTION.

In chapter 5, it was mentioned that a power regulation mechanism will be necessary for the system prototype, in order to keep the delta wing-turbine system power output constant for windspeeds in the region between V_R and V_O. In this chapter, several power regulation methods used for conventional wind turbines are presented. An alternative power regulation technique is proposed which is believed to be more suitable for the system. The results of wind tunnel tests carried out for assessing the potential of the proposed technique are also presented and discussed.

6.1. POWER REGULATION STRATEGIES USED FOR CONVENTIONAL TURBINES.

In the following, the most common power regulation techniques used for conventional turbines are presented and their potential for use with the delta wing-turbine system is considered. This information was obtained from references [1], [3], [66], [67], [68], [69] and [70].

6.1.1. Pitch control.

Each turbine blade can rotate about its longitudinal axis. Thus, the blade

pitch angle can be altered towards feathering of the blade at high wind speeds, so that the turbine aerodynamic efficiency is reduced and the power is kept constant. Often, only a small part of the blade outer region is movable, acting as an aerodynamic brake. The former method is called "total pitch control", while the latter is called "partial pitch control". There are various mechanisms for setting the turbine blades to the desirable pitch angle. For small wind turbines, masses attached to the blades, close to the hub are used. At high wind speeds, as the turbine rotational speed increases and the masses under the influence of centrifugal forces tend to turn the blades towards feathering. For large turbines, computer controlled hydraulic jacks set the blades to the appropriate angles. Pitch control can be used effectively for few bladed turbines. However, for multi-bladed turbines, such as those used for the delta wing system, the cost of installing as many pitch control mechanisms as there are blades is considered to be high. Practical difficulties may also arise from the fact that the blades are closely packed at the hub.

6.1.2. Stall regulation.

This control strategy can only be used when the turbine operates at the constant rpm mode. As the windspeed increases above V_R, the tip speed ratio of the turbine decreases (since the turbine rotational speed is kept constant) and thus the angle of attack increases, and stall occurs on the blade. It usually starts at the inboard part of the blade, and with increasing windspeed it spreads towards the blade outer part, until the blade is totally stalled. The occurance of stall reduces the turbine efficiency. The advantage of this method is that it is a passive one, and no moving parts are involved. However, stall regulation has several disadvantages, such as increased blade vibrations caused by the stalled blade part. Also, for achieving stall at the desirable windspeeds, the

blade shape has to depart from the optimum (the blade twist angles are usually reduced at the inboard part of the blade) and as an effect, the turbine aerodynamic efficiency is reduced even at optimum conditions. Finally, fine-tuning of the method in order to keep the turbine power constant is difficult, because the onset of stall cannot be accurately predicted from 2-dimensional aerofoil characteristics, due to radial flow effects as will be explained in chapter 8. This technique cannot be used for the system prototype, as it was designed to operate at the variable rpm mode.

6.1.3. Yaw control.

This strategy involves yawing the turbine out of the wind so as to reduce the effective incoming windspeed and thus keep the power output constant. For large wind turbines, this is achieved by a computer controlled yawing motor that sets the turbine to the appropriate yaw angle according to the windspeed value. For small wind turbines, a mechanical system can be used. A tail vane and the turbine are mounted eccentrically on either side of the yaw axis, so that the yawing moment of the tail vane is countered by that of the turbine. At windspeeds below the rated, the tail vane yawing moment is larger than that produced by the turbine thrust, and the turbine always faces the wind. At larger windspeeds however, the turbine thrust (and its yawing moment) increases and the system eqilibrium is at non-zero yawing angles. The difficulty of using this method for power control of the system prototype rests upon the fact that in this case, the tail vane will operate within a vortex flow (unlike the case of a conventional turbine in which a uniform flow attacks the tail vane). Operation within a vortex flow may make the tail vane behaviour difficult to predict.

6.2. PROPOSED ORIENTATION-POWER REGULATION TECHNIQUE.

Any one of the above mentioned power regulation techniques can be used in principle for the delta wing-turbine system, provided that the problems associated with its use can be overcome. However, these methods require control mechanisms to be installed on the system turbines resulting in additional components for the system, apart from the delta wing orientation mechanism. An orientation mechanism will be necessary for the system, since in a real flow situation the wind velocity direction changes continuously and the delta wing will need to be turned to face the wind.

The proposed control strategy is based on the idea of using the orientation mechanism for power regulation as well. As shown in figure 6.1, there are three stages in the operation of the orientation-power regulation mechanism: For windspeeds up to the rated (V_R), the delta wing orientation will be altered so that it is aligned to the incoming wind direction. For windspeeds above V_R, the orientation mechanism will be used to yaw the delta wing at increasingly large yaw angles, thus reducing the wind power available to the turbines. Finally, for windspeeds above the cut-out velocity (V_O), the delta wing will be turned at 90° of yaw angle, so that it presents the lowest possible frontal area to the wind in order to avoid structural damage. It is evident that this control method will be the least expensive one, since no additional components will be required.

The proposed control strategy rests on the assumption that yawing of the delta wing affects the power within its vortices. In order to investigate the yaw effects on the vortices, the following series of wind tunnel tests was carried out.

6.3. EXPERIMENTAL INVESTIGATION OF YAW EFFECTS ON THE DELTA WING VORTICES.

6.3.1. Instrumentation and experimental procedure.

The tests were carried out in the departmental wind tunnel whose working section is 1.4m by 1.1m. A 79° sweptback delta wing model was used, with sharp leading edges and a span of 300 mm, set at an angle of attack of 25°. The delta wing model configuration is the same as that chosen to be used for the delta wing-turbine system. The delta wing model was set at various yaw angles (δ), ranging from -40° to +40°. Positive values of δ represent clockwise rotation of the delta wing about its yaw axis, while negative δ values represent anticlockwise rotation, as shown in figure 6.2. The yaw axis was normal to the wind tunnel floor, and thus the yaw angle was not coupled with the wing angle of attack, as would be the case if the yaw axis was chosen to be normal to the wing surface. For each yaw angle setting, the total velocity of the vortex flow (V_{TOT}) was measured on the nodes of a 10x10 grid coinciding with the plane of one of the system turbines (see figure 6.3). The measurement grid was situated at the right hand side of the wing, as seen looking from the delta wing trailing edge towards its apex. The grid origin was placed at a chordwise distance of 0.8c downstream of the wing apex (with c being the delta wing centreline length) and 7mm above the wing surface. The instrument used for measuring V_{TOT} was a DISA 55D05 constant temperature hot wire anemometer together with the DISA 55A22 hot wire probes. Five probes were available and they were all calibrated against a known flow before they were used. Measurements of the flow direction in the vortices were not carried out as they were not considered to be necessary. During the experiment, the hot wire probe was clamped on a remotely

controlled test rig, which was situated within the wind tunnel, downstream of the model. The probe was placed at the appropriate grid positions, by use of a BBC microcomputer controlling the five stepper motors that were driving the test rig. The undisturbed wind velocity (V_∞) upstream of the delta wing was measured by a portable hot wire anemometer. The readings were then processed by an appropriate computer program, producing contours of V_{TOT}/V_∞ for each yaw angle setting. The instrumentation, experimental procedure and data analysis program are virtually the same as those used for the vortex flow investigation carried out during the author's studies for his MSc degree. More details about the anemometer operation and hot wire probe calibration as well as the test rig description and the contouring program development can be found in that MSc thesis. (Reference [43]).

6.3.2. Presentation of results.

In figures 6.4, 6.5, 6.6, 6.7 and 6.8 the experimental results are shown in the form of V_{TOT}/V_∞ contour plots. In each figure, the plots for yaw angles of equal magnitude and opposite sign are joined together. This was achieved by rotating the negative yaw angle plots from left to right about the vertical axis, so that they represent the flow on the left hand side turbine plane (at positive yaw angles), although the readings were taken at the right hand side turbine plane (at negative yaw angles). The two parts of each figure are pictures of the flow at different planes that coincide only at the vertical line where the two plots meet. Since although each figure consists of two different sets of readings joined together, the velocity contour curves almost coincide on the line where the two measurement planes meet, it can be concluded that the measurements are quite reliable. A small discrepancy occurs only at figure 6.6, (δ=20°)

due to misalignment of the two measurement planes. In figure 6.9, the zero yaw angle flow is shown for comparison.

It is evident from the above mentioned figures, that the delta wing yaw effects on the vortices are quite significant. With δ increasing, the left hand side vortex core moves spanwise towards the wing centreline. Also the distance of that vortex core from the wing surface (on the turbine plane) decreases with δ increasing. At $\delta = 5°$, an increase in V_{TOT}/V_{∞} can be observed, compared to the V_{TOT}/V_{∞} values of $\delta = 0°$. The left hand side vortex of $\delta = 5°$ has a 25% larger value of V_{TOT}/V_{∞} at the vortex core region. However, towards the vortex circumference, the V_{TOT}/V_{∞} values of the two vortices compared above are similar. This increase of the flow velocity can be attributed to the fact that the vortex is about to burst. Indeed, Hummel in [38] has observed similar phenomena in a series of delta wing vortex breakdown tests. The V_{TOT}/V_{∞} values just before vortex breakdown were found to be as large as 8.0. In our case, the left hand side vortex bursts when the yaw angle further increases and becomes equal to 10°. (See figure 6.5). With δ increasing above 10°, the burst vortex expands further. Its core also expands, with the total velocity in it becoming as low as 0.3 V_{∞} (δ = 30° to 40°). At δ = 40°, the burst vortex covers all the flow field, shifting over the other side of the wing. The flow turbulence also increases with δ increasing, as a result of the burst vortex expansion. For $\delta = 40°$, velocity readings were possible with only two significant digits inside the left hand side vortex core region, due to the large scale fluctuations of the flow there. For $\delta = 5°$ however, readings with 4 significant digits were possible throughout the flowfield.

Also, with δ increasing, the right hand side vortex moves spanwise towards the wing leading edge and the core vertical distance from the wing surface increases. At $\delta = 20°$, this vortex has almost departed out of the measurement plane. In

that case the right hand side vortex turbine will be exposed to an almost uniform axial flow. With further increase of δ, the left hand side vortex appears and it eventually takes over. For δ=30° and 40°, the right hand side turbine flowfield is dominated by the left hand side vortex. The fluid in this vortex rotates in the opposite direction to that of the turbine.

As an indication of the power available to the turbine at various yaw angles the values of $< V_{TOT}/V_\infty >^3$ were calculated for the turbine swept area. This was done as follows: The azimuthal average of V_{TOT}/V_∞ was calculated first for ten different radial distances on the turbine swept area. For each radial distance, eight azimuthally equidistant points were used for calculating the azimuthal average. Then, the radial average was calculated using the ten azimuthal means and the $< V_{TOT}/V_\infty >^3$ was estimated. The results are shown in figure 6.10. From that figure, it is evident that the maximum value of $< V_{TOT}/V_\infty >^3$ is obtained at δ = 0°. This is because at all other values of δ, the vortex core centreline and the turbine axis of rotation are not aligned and the average V_{TOT} values decrease. $< V_{TOT}/V_\infty >^3$ changes very rapidly with only a small change of the yaw angle. For example, at δ = 5°, $< V_{TOT}/V_\infty >^3$ reduces to 91.8% and 83.7% of the zero yaw value for the left and right hand side vortex respectively. Also, at δ = 40°, $< V_{TOT}/V_\infty >^3$ decreases to 20.4% and 8.2% of the zero yaw value for the left and right hand side vortex respectively. It can also be seen from figure 6.10, that the drop of $< V_{TOT}/V_\infty >^3$ is different for the right and left hand side vortex due to the different behaviour of each vortex for the same yaw angle.

6.3.3. Implications for the orientation-power regulation mechanism.

From these observations, useful conclusions can be drawn about the proposed orientation-power regulation mechanism of the system. First of all, the

significant reduction of the power available to the system turbines with increasing yaw angles calls for a fast response orientation mechanism of the delta wing for windspeeds below the rated. The orientation mechanism tolerance in yaw appears to be within ±5°, so that power losses due to turbine-vortex misalignment and vortex breakdown can be avoided. This may be feasible for the case of the system prototype, but for larger versions of the system, such as those presented in chapter 4, the large delta wing and turbine inertia will prevent large accelerations of the system to catch up with the changing wind direction. Thus, the system is likely to operate for a considerable amount of time in yaw. This can bring about an average power loss of the system, due to misalignment with the wind, as is the case for all large conventional wind turbines.

As far as the use of delta wing yaw for regulating the system's power, this study has demonstrated that it is feasible, since the power available to the turbine can be reduced to about 10% of its original value within 40° of yaw. The turbines' power output at yaw will be further reduced, due to the turbine-vortex misalignment and the subsequent loss of aerodynamic efficiency. For a system with two turbines, each turbine will produce different power at a given yaw angle, since the incoming flow that attacks each turbine will be different. However, this is not expected to be a problem, since it is the sum of the power provided by the two turbines that must be kept constant and appropriate values of δ for achieving the above at all windspeeds above V_R are likely to exist.

Possible problems that may be encountered by the use of the proposed power regulation technique are blade vibrations caused by vortex-turbine misalignment and vortex breakdown. When the turbine axis does not coincide with the vortex cetreline, the flow is no longer axisymmetric and cyclic loads are expected to be imposed on the blades, leading to vibrations. Also, the increase of turbulence in the burst vortex core

may aggravate the turbine vibrations. The severity of this problem cannot be foretold at this point, and further experimentation must be carried out during the system prototype tests (with the delta wing at yaw) for assessing its magnitude.

6.4. CONCLUSIONS.

A summary of the most important conclusions drawn from this study is given here.

1. The vortex flow produced by a 79° sweptback delta wing set at an angle of attack of 25° is greatly affected by yaw. The vortex at the left hand side of the wing looking from the wing trailing edge towards the apex behaves as follows: For positive yaw angles (ie clockwise rotation of the wing) the vortex moves towards the wing centreline with its vertical distance from the surface decreasing. At about δ = 10°, the vortex bursts. With further increase of δ, the burst vortex expands and moves towards the right hand side of the wing. At δ = 40°, it dominates the flow, covering almost all the area above the delta wing surface. Also, with δ increasing, the right hand side vortex moves towards the wing leading edge and its distance from the wing surface increases. At δ = 20°, this vortex was found to be out of the measurement area. For 20° $\leq \delta \leq$ 40°, the left hand side vortex takes the place of the right hand side one, and eventually dominates the flow.
2. As the $< V_{TOT}/V_{\infty}>^3$ values (indicative of the wind power in the vortex) decrease with increasing yaw angles, a fast-response orientation mechanism is needed for the delta wing-turbine system, in order to direct the wing towards the wind. The tolerance of this mechanism is not expected to be more than ±5° of yaw, in order to avoid power losses due to vortex core-

turbine misalignment and vortex bursting.

3. Power control of the system by yawing of the delta wing is possible since the power in the delta wing vortices decreases considerably with increasing yaw angles. On the other hand, problems may occur, due to vibrations of the turbine blades caused by vortex core-turbine misalignment (cyclic loading) and vortex bursting (increse in turbulence). The magnitude of these vibrations must be estimated during the system prototype tests.

FIGURES FOR CHAPTER 6.

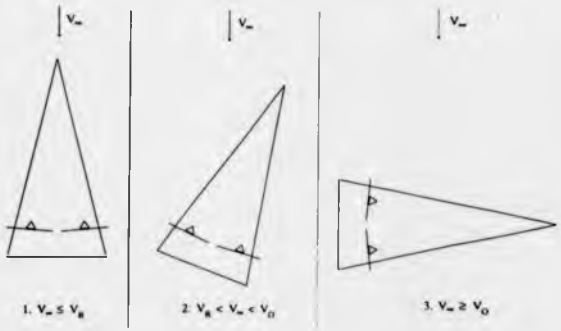

Figure 6.1. Control strategy of the proposed power regulation mechanism.

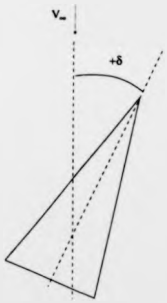

Figure 6.2. Definition of yaw angle sign. Delta wing viewed from above.

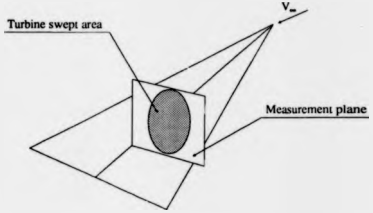

Figure 6.3. Position of measurement plane on delta wing.

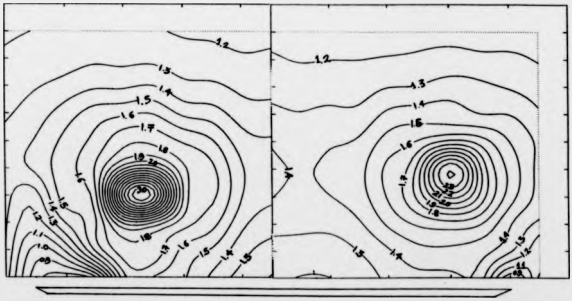

Figure 6.4. V_{TOT}/V_{∞} contours for $\delta = 5°$.

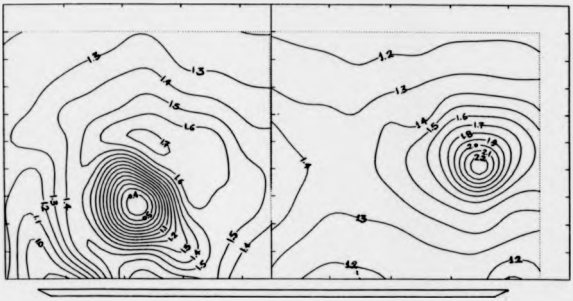

Figure 6.5. V_{TOT}/V_{∞} contours for $\delta = 10°$.

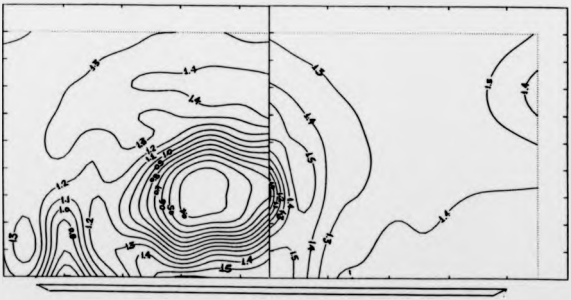

Figure 6.6. V_{TOT}/V_{∞} contours for $\delta = 20°$.

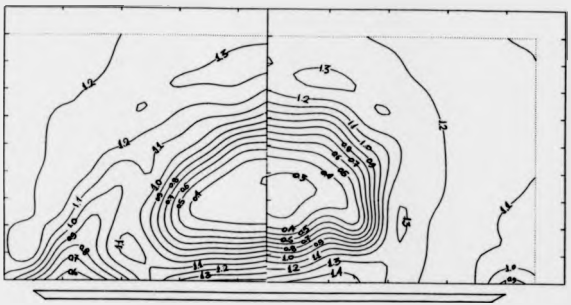

Figure 6.7. V_{TOT}/V_{∞} contours for $\delta = 30°$.

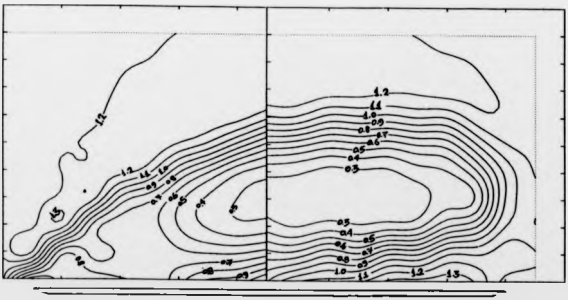

Figure 6.8. V_{TOT}/V_{∞} contours for $\delta = 40°$.

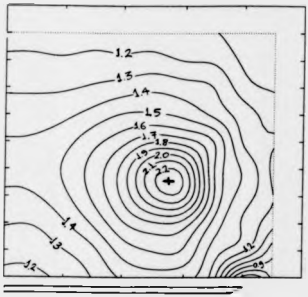

Figure 6.9. V_{TOT}/V_{∞} contours for $\delta = 0°$.

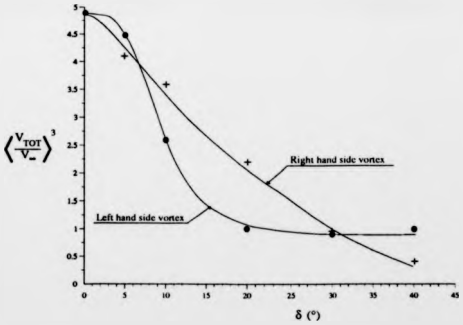

Figure 6.10. Variation of $< V_{TOT}/V_{\infty} >^3$ with yaw angle.

CHAPTER 7.

CONSTRUCTION OF THE DELTA WING-TURBINE SYSTEM PROTOTYPE.

CHAPTER 7. CONSTRUCTION OF THE DELTA WING-TURBINE SYSTEM PROTOTYPE.

7.0. INTRODUCTION.

In this chapter, the progress made in the construction of the delta wing-turbine system prototype is reviewed. The most important aspects of the prototype design are presented as well as the two different techniques tried for making the turbine blades. Finally, a brief account is given of the prototype delta wing design and the progress made in its construction.

7.1. DESCRIPTION OF THE PROTOTYPE.

The prototype design consists of a slender delta wing with sharp leading edges and a turbine mounted on it. The delta wing centerline is 7.68m long while its span is 2.98m. The turbine has 10 blades and a diameter of 1.2m. It is directly linked to the prototype generator (presented in chapter 5). The turbine blade characteristics have been described in chapter 4. A sketch of the prototype is shown in figure 7.1. The prototype dimensions were decided after considering the turbine blade construction feasibility: Initially, a model of about 1/3 the dimensions of the prototype was envisaged for testing in the departmental wind tunnel. However, the model turbine blades were found to be too small for their construction to be feasible and thus the prototype resulted. On the other hand, the prototype is too large for testing in the wind tunnel (whose working section is

1.1m by 1.4m), and hence a different testing method is necessary. As can be seen in figure 7.1, during the prototype tests, the delta wing and the turbine will be mounted on a car borrowed from the British Hang-Glider Association, used in the past for testing the longitudinal stability of hang-gliders. The car will be driven on a suitable airfield at the required speed and the resulting windspeed as well as the generator output will be measured, so that the mechanical power produced by the turbine can be estimated at various operating conditions. It is evident that the tests must be carried out on a calm day.

It was decided to attach the blades to the hub as shown in figure 7.2 having made approximate calculations of the forces, moments and stresses exerted on them. Each blade is fixed to the blade root by a pin in double shear. The blade root consists of two cylinders connected by a pin and the root is in turn fixed to the hub disc by another pin. This mechanism allows the blade to have two degrees of freedom, a flapwise one and one in lag, for reducing the stresses on the blade root.

The turbine rotor and generator are mounted on the delta wing using a tower shown in figure 7.3. The turbine tower rests on a disc shaped platform. It is connected to the platform by a car towing ball and it can be rotated and tilted in order to adjust the turbine position so that it is aligned with the vortex centreline. The tower height is also adjustable for the same reasons. An emergency brake has also been included. It consists of a flywheel attached to the turbine shaft behind the generator and a bicycle brake that operates on the flywheel. The brake can be operated by cable from inside the test vehicle.

The delta wing consists of timber boxes bolted to each other and held in place by a metal framework. The delta wing can be split into five parts so that its transportation to the test site is possible. (See figure 7.4). It is mounted on the test

vehicle by an "A" shaped rig. (See figure 7.1). The delta wing is bolted on a platform situated at the top of the rig. This platform is tilted by an angle of 25°, equal to the delta wing angle of attack. The delta wing can also be yawed by ±40°. For extra support, adjustable tension wires hold the wing on the test vehicle body. Finally, the "A" shaped rig is connected by specially made fittings on the car roof.

7.2. PROGRESS IN THE TURBINE CONSTRUCTION.

The turbine tower, generator housing, shaft and emergency brake as well as the turbine hub have all been constructed and assembled with no significant difficulty. The most difficult part of the turbine construction was the production of the blades. The following two different techniques have been tried for making the blades.

7.2.1. Sand casting of turbine blades.

A blade pattern was made first out of high grain polystyrene (styro-foam) as follows: A thin resistor wire heated-up by a DC power source was used for cutting the turbine blade shape in the polystyrene by melting it. The wire was made to slide smoothly on aerofoil shaped slots cut by a numerically controlled machine in aluminium plates. The plates were situated on either side of the polystyrene block. The hot wire was operated by two people. It was inserted in the polystyrene from the trailing edge, it was then moved around the aerofoil upper and lower surfaces, and left the polystyrene block from the trailing edge. The entire blade was divided into seven spanwise parts each of which was made separately by this method, and then the parts were glued together. Twelve blades were made.

The polystyrene blade was embedded in sand rich in resin, which was then hardened by ammonia passing through it. Thus a mould was created. Molten aluminium was then poured in the mould through an appropriate system of poureres and risers, replacing the polystyrene by melting it and thus creating the blade. Several initial trials of this method were carried out first, for deciding on the appropriate aluminium temperature. It was found that the aluminium temperature should not be less than about 740° C, which is the maximum temperature that can be used in this method. It was also found that better results were achieved when the polystyrene was removed from the mould before the metal was poured in, as the melted polystyrene gases were blocking the metal passage. After the initial trials, several moulds were produced, and the blades that resulted were not of satisfactory quality. The metal solidified before reaching the blade tip, and only the inboard 80% of the blade was produced. The metal temperature was raised above 740° C, in an attempt to produce a whole blade, but the mould cracked, resulting in an unsuccessful cast. The surface quality of the blades produced was not satisfactory, as in some parts of the mould the sand was washed away from the surface by the hot metal. Another problem was that the polystyrene being flexible, could be deflected from its original shape by the sand weight. Not being able to produce satisfactory blades, the sand casting method was abandoned and a more sophisticated one was tried.

7.2.2. Production of blade moulds using a numerically controlled cutting machine.

A numerically controlled cutting machine, available to the Microengineering Group of the Engineering department was used for producing the blade moulds. This machine is a 3-axis one, ie the cutter can be moved along its three

axes simultaneously. The machine can be programmed either directly, from its own keyboard, or indirectly, from an other computer, producing ASCII files containing the instructions. The latter method was used for this application, as the number of instructions required was found to be larger than that which the machine memory could accommodate. The programming language of the machine is the "G" codes. It is a set of instructions starting with the letter "G" (hence the name) and followed by a number, defining the cutter movement (ie linear or circular interpolation, movement along a curved path and so on), and sets of coordinates that define the start and end points of the movement.

The blade mould was made as follows: The blade was split into two parts, along the surface defined by the aerofoil chord, called "parting surface". The parting surface is not planar, due to the blade twist. Thus, the mould comprises two halves, one containing the upper blade surface (ie the suction side of the aerofoil), the other containing the lower blade surface (ie the pressure side). Each mould half was made separately, with the parting surface and the appropriate blade part machined on it. The two halves could then be joined along the parting surface and for accurately positioning them relative to each other, dowel holes were drilled using the computer controlled cutting machine on the parting surface, at exactly the same positions for each half.

A computer program was developed (written in fortran) in order to generate the instructions for the machine to cut the blade moulds. The aerofoil shape was approximated using a least squares routine. By appropriate manipulations of the aerofoil shape along the blade span (ie reduction of chord length caused by the blade taper and rotation of the aerofoil due to the blade twist), representations of the upper and lower blade surfaces (together with the parting surfaces) were generated, having the form of matrices with the coordinate values of the blade surface points at certain spanwise and

chordwise stations. These stations are effectively the start and end positions required for defining the cutter movement. Since the blade twist and taper distributions were linear (see chapter 4), it was decided to move the cutter linearly along a 3-dimensional fragmented line in the blade spanwise direction. During each passage, the cutter was programmed to move from the blade hub to the tip and back again, gradually advancing from the blade leading edge towards the blade trailing edge. The cutter used was a ball-ended one, having a diameter of 10 mm. Corrections compensating for the cutter dimensions were included in the program. Once the positions and movement of the cutter were calculated, the program created a file in G-code, with the instructions to the cutting machine. The cutter was so moved, that the blade surface was gradually sunk into the workpiece. For doing so, the program manipulated the vertical (z) axis coordinates of the blade surface. First, it calculated the lowest point of the surface and started cutting from there, aborting all other movements of larger height that would result in the tool moving above the workpiece. After that cycle was completed, the blade surface vertical axis coordinates were updated, so that the tool would cut deeper into the workpiece. This procedure was repeated, until the whole surface was sunk into the workpiece.

The command files produced from this process were about 6000 lines long. They were fed into the cutting machine sequentially by a microcomputer connected to it, since the machine's memory was not large enough. The material used for the moulds to be cut from was aluminium. The quality of the moulds produced is excellent and the aerofoil characteristics are accurately machined on the mould surface. The aluminium moulds can be used for casting plastic blades. If aluminium blades are required, steel moulds have to be made. The advantage of a metal mould over those made of sand is that it can be heated in order to minimise the thermal losses of the pouring material and thus prevent premature solidification before all parts of the mould

are filled. It is hoped that with an appropriate pouring system, casting of the turbine blades will be feasible, leading to blades of better quality than those produced by the sand casting technique.

7.3. PROGRESS IN THE DELTA WING CONSTRUCTION.

The prototype delta wing has been designed and drawings of it have been produced. The "A" shaped tower that will support the delta wing on the test vehicle has been constructed. Unfortunately, the delta wing construction was seriously delayed due to lack of adequate personnel at the departmental workshops. An effort was made for raising funds in order to assign the manufacturing work to contractors outside the university, but it failed to produce successful results. As it was not likely that the delta wing would be ready before the author's thesis submission deadline, the delta wing project was shelved, and work was transferred to the counter-rotating turbine project which is presented in part C of this thesis. More cost-effective alternative design proposals for the delta wing are now under consideration.

7.4. CONCLUSIONS.

The most important conclusions from this review are:

1. The delta wing-turbine system has been designed and most practical problems concerning its construction have been solved.
2. The sand casting technique for making the prototype turbine blades has proved to be unsuccessful. The quality of the blades produced was poor, while only the inboard 80% of the blade could be produced, due to

premature solidification of the pouring material.

3. The computer controlled cutting machine was successfully programmed for cutting moulds for the blades to be cast from. It is hoped that this technique will prove to be more successful than the sand casting one, and as the pouring material solidification problems can be overcome, good quality blades are likely to result. Furthermore, the mould geometry is more accurate than that of the hand-made polystyrene forms.

FIGURES FOR CHAPTER 7.

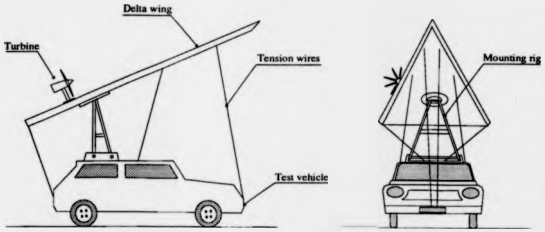

Figure 7.1. Sketch of the Prototype and test vehicle.

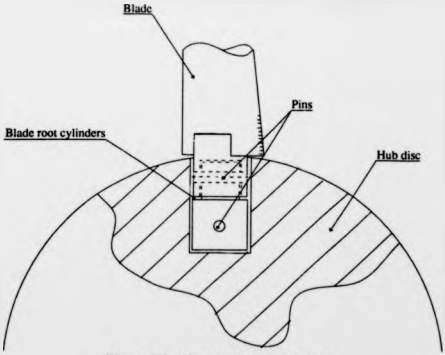

Figure 7.2. Sketch of the blade root.

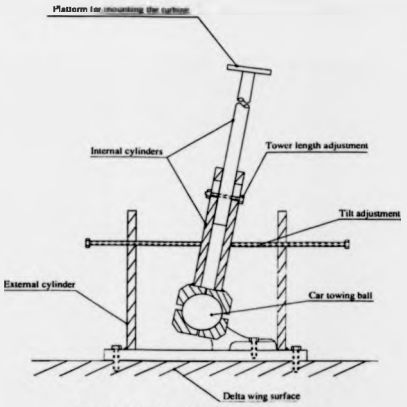

Figure 7.3. Sketch of the turbine tower.

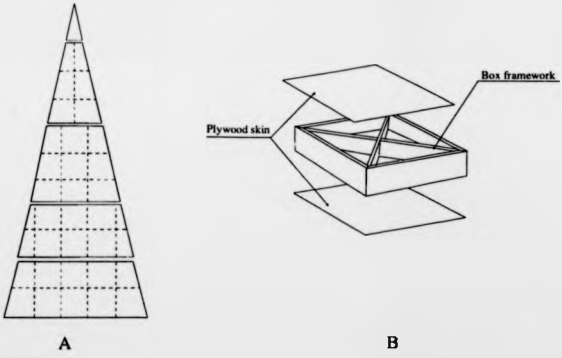

Figure 7.4. A) The five parts of the prototype delta wing. Broken lines show the timber boxes that make up each part. B) Layout of a typical box.

CHAPTER 8.

CONCLUSIONS-COMMENTS-AREAS OF FURTHER RESEARCH.

CHAPTER 8. CONCLUSIONS-COMMENTS-AREAS OF FURTHER RESEARCH.

8.0. INTRODUCTION.

In the following, the main conclusions of part B are presented, the accuracy of the system turbine modelling is commented on, and possible areas of further research are proposed.

8.1. CONCLUSIONS OF PART B.

8.1.1. Comparison with conventional turbines. Based on the results of a lifting line design model presented previously, the delta wing-turbine system was scaled-up and compared with existing horizontal axis turbines of various sizes. It was concluded that the system is suitable for small to medium size applications (up to 100 kW of rated electrical power). Beyond that however, the delta wing required becomes too big to be practical. The advantages of the system over a conventional turbine are:

•Smaller rotor area for a given rated power.

•Rotors operate in larger rotational speeds. This enables use of lighter weight and more efficient gearboxes, or if alterations in the system's design are implemented, gearboxes can be eliminated (for power outputs approximately up to 100kW).

•Rotors are closer to the ground. This reduces erection and maintenance costs.

The only disadvantage of the system is the large delta wing needed. However, for smaller power turbines, (15-100 kW), the overall sizes of equivalent machines are comparable.

8.1.2. Re effects on prototype turbine. The lifting line procedure for designing wind turbines presented in part A of this thesis was used for the design of the 1.2 m diameter turbine of the system prototype, including Reynolds number effects. It was found that as the turbine operates within the low Reynolds number regime, (below 10^5), scale effects become quite important, leading to a reduction of the original high Re turbine maximum power coefficient ($C_{p,max}$) of about 20%. The prototype turbine was redesigned in an attempt to improve its performance. It was found that use of a more suitable low Re aerofoil, (GOE 795), increase of the blade chord to twice that of the high Re turbine, reduction of the turbine blades to 10, linear blade taper and variable optimum angle of attack distribution along the blade (in order to match the variation of α_{opt} with Re) reduced the power coefficient drop to 4.7% below that of the original high Re design, whilst the prototype turbine was still operating at a high tip speed ratio (= 6.75).

8.1.3. Performance of the prototype turbine. A lifting line procedure for predicting the performance of wind turbines was developed. It was applied to the case of the system prototype turbine. It was found that increase of the blade chord towards the hub (for strength) and linearisation of the blade twist angle distribution (for ease of manufacture) did not affect the turbine performance significantly, as a reduction of 0.24% in $C_{p,max}$ resulted from these modifications. Once again, Re effects were found to affect the turbine performance considerably: An increase of the undisturbed wind velocity from 3 m/s to 13 m/s caused the turbine $C_{p,max}$ to increase by 16.6%.

8.1.4. Generator considerations. A permanent magnet, single phase, axial flux, synchronous generator which is to be used as a power absorber for the

prototype turbine was bench tested. The generator model parameters were identified as well as the power losses through it. The latter is effectively a calibration of the generator. With use of the generator test results, the turbine performance prediction data and a suitable wind distribution model, the long term performance of the prototype was estimated assuming that it is used for heating purposes. It was found that use of a series resonant circuit achieved optimisation of the electrical load to the generator, allowing the turbine to operate in near-optimum conditions throughout the partial power range. It was also found that the generator is not ideally suited to the turbine. Due to its large armature resistance (and subsequent electrical losses) only 55% of the mechanical power produced by the turbine was converted to useful electrical power, resulting in a yearly energy production of 424.9 kWh for a typical wind regime with an average windspeed of about 4 m/s. With use of a more suitable generator (with 80% efficiency) this quantity should improve by 31.5%.

8.1.5. Power regulation considerations. A wind tunnel investigation of yaw effects on the vortices produced by a delta wing model similar to that used by the system was carried out in order to facilitate decisions on the system's orientation and power regulation mechanisms. It was found that the position and shape of the vortices was significantly affected by yaw. Also, the power available to the system turbines was considerably reduced by yaw effects. Thus, a fast response orientation mechanism will be necessary for the system with a sensitivity of about ±5° of yaw. Yawing of the delta wing for regulating the system power output can be used provided that the anticipated blade vibrations due to turbine-vortex misalignment and vortex bursting are proved not to be severe.

8.1.6. Prototype construction progress. The system prototype has been designed and some parts of it have been constructed. Of the two techniques used for

producing moulds for the turbine blades to be cast from, the sand casting method proved to be unsuccessful, while good quality blade moulds were produced using a computer controlled cutting machine. Unfortunately, the prototype delta wing construction has been seriously delayed due to lack of adequate personnel at the departmental workshops. As it was not likely that the delta wing would be ready before the end of the author's period of studies, the prototype tests were postponed.

8.2. COMMENTS ON THE MODELLING OF THE SYSTEM TURBINES.

The design and performance analysis procedures used for modelling the system turbines are engineering approximations to the complicated fluid dynamics problems covered in this work. Therefore, apart from errors introduced by the numerical techniques used, (which have been mentioned at the appropriate sections of each chapter), the accuracy of these methods depends on the validity of a series of simplifying assumptions. These assumptions and the effects they may have are discussed in this section.

8.2.1. Lifting line hypothesis. For estimating the turbine interference to the flow, the blades were substituted by lifting lines neglecting the blade thickness envelope and chord. This assumption is justified from the fact that the designed blades are of high aspect ratio, equal to about 20. Lifting line theory has also been used in other similar applications such as helicopter blades and propeller analysis, with considerable success.

8.2.2. Wake expansion and vortex sheet deformation. In the wake model used for the turbine design and performance analysis (presented in chapter 2), it was assumed that the trailing vorticity consists of semi-infinite, helical vortex

sheets shed from the turbine blades that retain their shape at infinite distance downstream of the turbine. The vortex sheets however cannot sustain any load and as a result they follow the local flow. Hence, the vortex sheets' shape will only be retained if the flow within the wake remains the same downstream of the turbine. This does not happen, as the wind axial velocity within the wake decreases with increasing distance from the turbine. Therefore, the fluid mass conservation law dictates that the wake diameter increases and as a result, a radial velocity component exists within the wake that causes the vortex sheets to follow the wake expansion. Furthermore, the filaments that constitute each vortex sheet induce velocities on each other. As was explained in chapter 2, under mutual interaction, the filaments rearrange themselves around the strongest ones, causing deformation of the vortex sheet cross-section. This effect is called vortex sheet deformation. Both these effects cause the induced velocities on the turbine blades to be different from the theoretically predicted values. However, the deviations from the theory are not expected to be large as the wake expansion and the vortex sheet deformation happen gradually. The axial component of the flow velocity within the wake is large, and the vortex sheets move away from the turbine fast enough, so that substantial deviations from the assumed vortex sheet shape are expected to occur several blade span lengths downstream of the turbine. That part of the vortex sheet however (according to the Biot-Savart law) contributes little to the overall induced velocity. Also, the errors introduced from the substitution of the blades by lifting lines are expected to be much larger than those caused by the above mentioned effects.

8.2.3. Incoming flow azimuthal variations. The flow attacking the turbine was assumed to be axisymmetric. As can be seen in figure 4.3, some azimuthal variations of the vortex flow occur, especially in the axial and tangential components. The effect of these variations is to induce cyclic loads on the turbine blades and thus

cause blade vibrations. Also, some loss of power from the turbine is expected, as during one rotation, each blade will operate at non-optimum conditions for a part of the turbine swept area. As was reported in reference [43], the largest azimuthal variation of the incoming flow velocity components was that of the tangential velocity (v), at a radial distance x=0.6 from the turbine axis. Its magnitude was found to be $(\Delta v/v) = \pm 10\%$. Using equations 2.3.1, 2.3.4, 2.3.8 and 4.5.5 as well as the local flow characteristics at x=0.6 for optimum conditions, the blade driving force and thrust oscillations resulting from the tangential velocity azimuthal variations can be calculated. From equation 2.3.4, follows that the relative velocity variation (for $(\Delta v/v) = \pm 10\%$) is: $(\Delta W/W) = +3\%$. Also, from equation 2.3.8, follows that $(\Delta\beta_r/\beta_i) = \pm 3\%$ and from equation 2.3.1, $\Delta\alpha = \pm 0.5^{\circ}$. Finally, from equations 4.5.5 the driving force and thrust (per unit span) variation at x=0.6 can be obtained:

$$(\Delta F_D/F_D) = \pm 0.1\%, \qquad (\Delta T/T) = \pm 2\%.$$

The low values of the force oscillations are due to the fact that an increase of v causes W to decrease and β_i to increase (see also figure 2.8), and thus the net effect is small. The above analysis has shown that the blade vibrations due to azimuthal variations in the incoming flow are not expected to be large. Also, since the driving force (and hence torque) oscillations were found to be negligible, no significant loss of power is expected to result from the flow azimuthal variations.

8.2.4. Interaction between the system turbines. For comparing the delta wing-turbine system with conventional wind turbines (chapter 4, section 4.3), the system was taken to have two turbines. Each turbine was assumed to operate independently of the other and the aerodynamic interference caused by one turbine upon the other was neglected. This can be justified considering the findings of [71]. In that reference, a series of wind tunnel tests is reported, carried out for estimating the

interference of turbines operating side-by-side (ie with their rotors lying in the same plane), at small distances. Two similar 2-bladed turbines were used and the power produced by each turbine for different distances between them was compared to the power of each turbine when operating alone for two cases, one with the turbines rotating in opposite directions (as the system turbines do) and another with the turbines rotating in the same direction. It was found that for both cases and for values of a parameter $t < 1.4$ (defined as $t = L/D$, with L the distance between the turbine axes and D the turbine diameter), a small increase of the turbine power was observed (about 1% to 2%) compared to the power produced by each turbine when operating alone. This was attributed to the interaction of the two turbines' wakes. Indeed, flow visualisation studies have revealed that the trailing vortices shed from the blades of one turbine were considerably weakened under the presence of opposite rotation trailing vortices shed from the other turbine. For values of $t > 1.4$, no significant changes were observed in the performance of the turbines. For the case of the system turbines, $t = 1.25$, and a small increase in the turbine performance may be expected. However this does not justify the undertaking of a considerable effort for modelling the turbine wakes' interaction.

8.2.5. Radial flow effects. For estimating the forces exerted on the turbine blades, 2-dimensional aerofoil characteristics were used, assuming that the 2-dimensional aerofoil boundary layer is similar to the 3-dimensional one of the rotating blades. However, in references [72], [73] and [74] it was reported that for small tip speed ratios the turbine performance predictions (carried out using momentum theory) were found to deviate from the experimentally measured ones. The discrepancies between theory and experiment were increasing with decreasing tip speed ratio, especially when a large part of the blade was stalled. It was also found that the onset of stall (as predicted using the 2-dimensional aerofoil data) was delayed and also beyond stall, the lift

coefficient values were found to be larger than expected, while the drag coefficient values were found to be less. These effects were attributed to radial flows within the blades' boundary layer. (See references [72], [75] and [76]). These radial flows can be created by a number of causes such as centrifugal and Corriolis forces as well as spanwise pressure gradients on the turbine blades. The effect of radial flows is to thin the blade boundary layer, removing its lowest velocity regions away from the blade. Therefore, the radial flow acts as a boundary layer control mechanism (similar to that used in aeroplane wings where air is sucked away from the wing surface) inhibiting stall. At post-stall situations, thinning of the stalled boundary layer reduces form drag. As was reported in [75] and [76], use of 2-dimensional post-stall aerofoil characteristics leads to underprediction of the turbine performance. However, for pre-stall situations, the 2-dimensional aerofoil characteristics can be successfully used for modelling of wind turbines. Indeed, tuft and oil visualisations of turbine blades' boundary layer flows (see references [76] and [77]) have revealed that significant radial flows exist only at post-stall angles of attack. Therefore, for the case of the vortex turbine design, radial flow effects are expected to be negligible as the whole blade is designed to operate at the optimum angle of attack, which is well below the stall angle. Also, the prototype turbine long term operation modelling is not expected to be influenced by radial flow effects, since the turbine operates at near-optimum conditions throughout the partial power range. Radial flows may have an effect on the turbine performance predictions for low tip speed ratio values, where some part of the blade is stalled. Radial flow effects are not yet fully understood, and research in that area still goes on.

From the above, it can be concluded that the vortex turbine modelling has included most of the phenomena associated with wind turbine aerodynamics (such as tip vortex effects, Re effects, wake rotation effects and radial variations of the incoming

flow). Those not taken into account are not expected to introduce significant errors.

8.3. AREAS OF FURTHER RESEARCH.

The development of the delta wing-turbine system was taken as far as it was possible at the time. However, a great deal of research work still remains to be done. The areas of further research are highlighted here:

8.3.1. Prototype construction and testing. The prototype test aims are: Verification of the turbine model and estimation of power losses and turbine vibrations when the delta wing is at yaw. The former may also indicate possible improvements to the turbine design procedure with regard to the above mentioned limitations of its accuracy, as well as improvements of the prototype structure. The latter will determine the feasibility of the proposed power regulation technique and will provide data for modelling the system's operation under yaw. The prototype construction and testing will also provide a basis for estimating the cost of a commercially built unit, and will indicate possible ways of reducing cost, such as use of cheaper materials for the delta wing construction or reduction of some components' material if they prove to be over-designed.

8.3.2. Development of power regulation mechanism. This includes use of the prototype test data in order to model the system's operation under yaw, or, if the proposed power regulation technique proves to be unsuccessful, development of a different one.

8.3.3. Implementation of a more suitable generator. This includes repetition of the generator tests and re-modelling of the prototype long term operation, possibly using a more complicated load than the purely resistive one used,

such as battery charging.

8.3.4. Alternative delta wing configurations. This includes investigation of the flow produced by a half-delta (to be used with one turbine) in order to reduce the system size and development of a more cost-effective, lightweight delta wing for the system prototype.

8.3.5. Assessment of the system's potential for wind farms. Usually, in wind farm applications where conventional turbines are used, some turbines operate within the wake of others, depending on the wind direction. This effect reduces the power output of the wind farm, which is less than the sum of the power that would be produced if each turbine was operating alone. As can be seen in figure 8.1, it is expected that in a wind farm, there exists a critical vertical distance of the delta wing-turbine systems above the ground, that allows the vortex wake of the system situated upstream to pass beneath the delta wing of the system placed downstream. Thus, fresh fluid will attack the downstream system reducing (or even diminishing) the wake power losses. For investigating that, wind tunnel tests with delta wing models will be necessary.

FIGURES FOR CHAPTER 8.

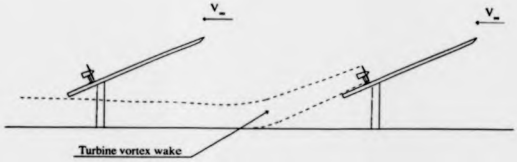

Figure 8.1. Possible advantage of the delta wing-turbine system when used in wind farm applications.

PART C.

COUNTER-ROTATING TURBINE.

CHAPTER 9.

DESCRIPTION OF THE COUNTER-ROTATING TURBINE AND PRINCIPLES OF ITS DESIGN.

CHAPTER 9. DESCRIPTION OF THE COUNTER-ROTATING TURBINE AND PRINCIPLES OF ITS DESIGN.

9.0 INTRODUCTION.

In this chapter, the characteristics of the counter-rotating turbine are presented, the two major areas of research pertaining to the turbine (ie wind turbine wakes and counter-rotating rotor aerodynamics) are reviewed and the design principles of the system rotors (deduced from the above mentioned review) are analysed.

9.1. DESCRIPTION OF THE COUNTER-ROTATING TURBINE.

The counter-rotating turbine consists of two co-axial rotors rotating in opposite directions. During operation, the front turbine rotor is situated upstream of the rear one. The two rotors do not operate independently of each-other, but are connected to the same generator which is a specially designed one. Its "stator" is not stationary as in conventional generators, but is movable and is connected to one of the turbine rotors. Hence, the "stator" and the "rotor" of the generator are connected each to one of the turbine rotors respectively. This unusual configuration was chosen in order to obtain direct conversion of the rotors' mechanical power to electricity, avoiding gearboxes necessary in conventional turbines. As the two rotors operate with rotational speeds ω_1 and ω_2, the relative rotational speed of the generator rotor "sensed" by its stator is $\omega_1 + \omega_2$. This increase in the effective generator rotational speed makes direct connection of the rotors to the generator possible.

The counter-rotating turbine rotors have some unique features: Firstly, the

two rotors being connected to the same generator must create equal and opposite torque, if the turbine is to operate at constant rotational speed. The torque reaction of the generator is the same in magnitude for both the front and the rear rotor, and therefore, if one of the rotors develops more torque then the other, it will force the lower torque rotor to accelerate, until the equal torque condition is met. Hence, when the two rotors are designed, equal torque solutions must be sought.

Another feature of the counter-rotating turbine is that its two rotors interact with each other. The rear rotor is operating within the wake of the front one and it is thus affected by the front rotor. Also, for practical reasons, the two rotors cannot be apart at an axial distance that would make the rear rotor blockage negligible and thus the rear rotor aerodynamic interference to the front one must also be taken into account during the design of the rotor blades.

Counter-rotating wind turbines have already been commercially produced. Such a turbine, called "Trimble Mill", has sold several units in the U.K. mostly used for space and water heating. (See reference [78]). Both Trimble Mill rotors have a diameter of 6 m. The front one has 3 blades while the rear one is 5-bladed. The axial distance between the front and rear rotor is about 0.2 R, where R is the radius of the rotors. Each rotor operates at 75 rpm for a windspeed of 10 m/s. This corresponds to a tip speed ratio of 2.36 for each rotor. The rotor blades have been experimentally designed using simple blade element aerodynamics as a guide. The best blade twist distribution and pitch angle settings were decided by trial and error. The Trimble Mill generator is a specially developed, permanent magnet, synchronous, single phase machine with 42 poles. An appropriate load for the generator was designed by De Paor. (See reference [61]). The Trimble Mill can deliver about 5 kW of electrical power at a windspeed of 10 m/s. The overall efficiency of the turbine is $C_p = 0.29$. Assuming a generator efficiency of 0.8, the

Trimble Mill aerodynamic efficiency becomes: $C_{p,aerodynamic} = 0.36$. All the above figures concerning the Trimble Mill are derived from manufacturer's data.

The Trimble Mill manufacturer has recently decided to improve the original turbine by redesigning the rotors as well as the generator load and the University of Warwick is involved in this effort. The work presented in this part of the thesis deals with the counter-rotating turbine aerodynamics and is an attempt to improve its performance by proper design of its rotors.

9.2. REVIEW OF RELEVANT LITERATURE.

In order to facilitate decisions on the two rotors interaction schemes to be used, a bibliography search was carried out in the two areas which seem to be the most relevant for the turbine design. These are the wind turbine wakes and their modelling, and the design of counter-rotating rotors for other applications, such as propellers and helicopters. The findings of this search and their implications to the counter-rotating turbine modelling are presented in the following section.

9.2.1. The nature and modelling of wind turbine wakes.

a). Wind turbine wakes according to momentum and lifting line theories. Modelling of wind turbine wakes is very crucial in designing and predicting the performance of wind turbines. When momentum theory is used for these purposes, the flow through a wind turbine is modelled using the flow tubes method explained in chapter 2. (See also references [8], [9], [10], and [11]). The flow tube model assumes that no mutual interaction takes place between the fluid contained in its elemental tubes.

Only the interaction of the fluid with the part of the turbine blades that is enclosed in each tube is taken into account. According to this model, far upstream of the turbine the fluid static pressure is equal to the atmospheric pressure (p_{atm}). Just upstream of the turbine the pressure rises, due to the turbine blockage. Just downstream of it the pressure drops, since power is removed from the fluid by the turbine. This pressure drop is dictated by Bernoulli's equation: Since power is removed from the fluid, the total pressure just downstream of the turbine must be less than that just upstream of the turbine. However, the dynamic pressure cannot undergo abrupt changes, since the wind velocity should not exhibit discontinuities, and hence, the static pressure is reduced. At infinite distance downstream of the turbine, the wake is assumed to have settled and the static pressure through it is again equal to p_{atm}. Thus, again, due to Bernoulli's equation, the wind velocity within the wake is decreasing with increasing distance from the turbine, as an effect of the pressure recovery that takes place. The reduction of the wind velocity within the wake brings about the wake expansion since the fluid mass must be conserved. Another feature of the wake, according to momentum theory, is the wake rotation. This is an effect of the interaction of the fluid with the turbine blades as explained in chapter 2.

For lifting line theory, the turbine wake consists of vortex sheets immersed in the flow. The velocities induced by these vortex sheets describe the turbine interaction. The axial component of the induced velocity causes the flow within the wake to decelerate. The radial induced velocity component causes the wake expansion, while the tangential induced velocity is responsible for the wake rotation.

Both momentum and lifting line theories describe some of the most important wake characteristics. However, they fail to include the equally important effects of turbulent mixing of flows within the wake as well as the interaction of the

wake with the surrounding flow, the former by assuming that the flow tubes are independent of each other, and the latter by being based on potential flow theory which doesn't cater for viscous effects or the effects of turbulence.

b) Experimental observations of wind turbine wakes and far wake models.

References [79] to [89] (among others) contain descriptions of wind turbine wakes derived from experimental measurements and observations of the wakes created by turbines during field operation or in wind tunnel tests. The most important conclusion from these studies is that a wind turbine wake can be divided into two parts, the near wake which lies from 0 to 3 rotor diameters downstream of the turbine, and the far wake extending beyond 3 diameters downstream of the turbine. This division of wind turbine wakes into near and far fields is due to the fact that their characteristics differ significantly. The near wake decay is governed by the turbulence caused by the turbine. The far wake decay on the other hand is governed by ambient turbulence. Also, the behaviour of the centreline wind velocity within the near and far wakes is different. From 0 to approximately 3 diameters downstream of the turbine, it is decreasing, due to the pressure recovery effect. Also, the azimuthal velocity differences which occur in the near wake are evened out due to turbulent mixing as the distance from the turbine increases. The near wake has a considerable component of tangential velocity, causing wake rotation, which dies out with increasing distance from the turbine. Within the far wake, the azimuthal variations of wind velocity have settled, the wake rotation is negligible, and the axial component has a universal profile which can be satisfactorily modelled by a Gaussian distribution. The wake centreline velocity increases with increasing distance from the turbine, as high momentum flow outside the far wake is mixed with the lower momentum flow within the wake, causing its boundaries to expand. The far wake finally decays within 7 to 15 diameters downstream of the turbine, depending on the ambient

turbulence levels. The larger these are, the quicker the wake decays.

Far wakes have received far more attention by researchers than near ones (references [79] to [87] deal with far wakes), as information about their characteristics and correct modelling of their decay was found to be essential in estimating wind turbine interactions in wind farms, where the distances between turbines are more than 3 diameters. Several models of the far wake decay have been developed, (see references [79], [81] and [85]), of varying complexity. In all these models, two parameters are used as input for describing far wakes. These are the turbine thrust coefficient, which gives an estimate of the fluid momentum loss, and the ambient lateral turbulence intensity affecting the wake interaction with the surrounding fluid. These models are considered to be incomplete as they do not treat the near wake. Furthermore, they fail to include other parameters that influence wake behaviour, such as wind turbine characteristics ie blade number and geometry. An attempt has been made recently, described in references [90] and [91], to develop a unified approach to wake analysis that would fill the existing gap in knowledge especially about the near wake and its dependence on turbine characteristics.

c) Near wake characteristics. The far wake is of little interest from the counter-rotating turbine design point of view, as the axial distance between its two rotors is not expected to be more than one diameter for construction feasibility reasons. Hence, the rear rotor of the turbine will operate within the front rotor's near wake. Unfortunately, very little attention has been given to the near wake. This was caused by the lack of interest from researchers, since there wasn't any particular application requiring knowledge of its characteristics. Therefore, only a few experimental studies of near wakes are available. (See references [88] and [89]). In reference [88], flow measurements in the immediate vicinity of a wind turbine (0.012 D downstream of it) are

presented. They were carried out for validating the predictions of a turbine performance analysis method, and are rather limited in scope. A far more comprehensive investigation into the flow characteristics in the near vicinity of a wind turbine is presented in [89]. In that reference, account is given of wind tunnel tests carried out for estimating the wind velocity distribution upstream and downstream of a three-bladed turbine, operating at two different tip speed ratios, namely 6 and 4. For each set of measurements, hot wire probes were placed at various radial positions starting from the turbine hub (0.15 R) and up to 1.1 times the turbine radius (1.1 R). Measurements were carried out at different axial stations, both upstream and downstream of the rotor disc. Since the flow was time-dependent, 40,000 velocity readings were taken at each measuring point for a large number of turbine revolutions. These readings were then statistically manipulated for estimating the average velocity and turbulence intensity distributions. The axial flow component was measured, as well as the radial, the tangential being neglected. The results from these tests are shown in figures 9.1 to 9.4.

In figure 9.1, the axial velocity deficit distribution (defined as $1- u(r)/V_{\infty}$) is shown, for axial positions upstream of the rotor disc and with the turbine operating at $\lambda = 6$. It can be seen from figure 9.1, that the flow upstream of the turbine decelerates due to the blockage caused by the turbine. The deceleration is more pronounced close to the turbine hub, while it diminishes at the turbine tips. Also, moving closer to the turbine, the flow velocity reduction increases slightly. (Compare plots corresponding to different distances upstream of the turbine, ie -D/4, -D/8 and -D/12).

Figure 9.2 depicts the axial velocity deficit distribution downstream of the rotor disc, with the turbine operating at $\lambda = 6$. It can be seen that for all axial distances, the velocity deficit has similar shape: It is more pronounced at mid-span, while it decreases at the tip and hub regions. Also, an increase of the velocity deficit with

increasing axial distance from the rotor disc (for any radial position) can be observed. This increase is roughly uniform with respect to radial positions. For example, the ratio of velocity deficit between axial distances D/2 and D/60 is on average 1.45 (±5%) for different radial positions. The ±5% error is within the experimental error band. The same applies for the case of $\lambda = 4$. In that case, the average ratio of velocity deficit between D/2 and D/60 is 1.44 (±1%). Therefore it can be concluded that the axial velocity decreases in a uniform way with increasing distance from the turbine, with the velocity profile retaining its initial distribution. Deduced from the plots of figure 9.2, the axial velocity at the radial position 0.5 R is plotted versus axial distance in figure 9.3. It is evident that a great drop of u(0.5R) occurs between D/20 and D/10. This was attributed by the authors of [89] to the pressure recovery taking place in the immediate vicinity of the rotor. Downstream of D/10, the velocity decreases in an almost linear way. The wake expansion can also be calculated using figure 9.2, comparing the radial distances for which the velocity deficit is nearly zero. It was found to be only 5% between D/60 and D/2.

Figure 9.4 shows the turbulence intensity radial distribution for various axial distances upstream and downstream of the rotor disc, with the turbine operating at $\lambda = 6$. (The turbulence intensity at a radial distance r is defined as: $(\langle u(r)^2 \rangle)^{1/2}$. In figure 9.4 it is made dimensionless by division with V_∞). Upstream of the rotor, the turbulence levels remain low for all radial stations, and even at axial distances very close to the rotor disc (ie -D/12). Downstream of the turbine, larger turbulence levels are observed with two peaks appearing at the tip and hub regions. A large decrease of the turbulence intensity takes place between D/60 and D/10, revealing the thorough mixing of wind velocities that occurs in that region. For axial distances above D/10, the azimuthal variations of the flow as it leaves the turbine (which must be considerable judging by the

turbulence levels at D/60) are evened-out, and a nearly-steady flow results, as can be seen from figure 9.4, since the turbulence intensity remains at low levels, similar to those upstream of the turbine. However, at the tip and hub regions, turbulence is more persistent and peaks of the turbulence intensity appear there. This is an effect of the trailing vortices that appear at the tip and hub regions. Similar trends as those observed in figures 9.1 to 9.4 were also observed for the turbine operating at $\lambda = 4$, with only trivial changes in the values of the quantities involved.

From this investigation, useful conclusions can be drawn about the flow in which the counter-rotating turbine rotors will operate, assuming that the flow described above is a typical one for a wind turbine.

1. Front rotor. From the reduction in axial velocity upstream of the turbine tested in [89], it can be concluded that the front rotor is likely to experience a reduction in the incoming flow that attacks it, due to the blockage caused by the rear rotor. Since the levels of turbulence upstream of the turbine of [89] are low (below 2.5%), the front rotor can be designed as if it is operating in a steady flow.

2. Rear rotor. The rear rotor must be placed at an axial distance of at least D/10 downstream of the front one. This is necessary in order to reduce the turbulence levels of the incoming flow according to the findings of [89]. Since the turbulence levels at such distances are low (apart from the tip and hub regions) the flow that attacks the rear rotor can be assumed to be steady. This simplifies considerably the rear rotor design. Also, the rear rotor incoming flow characteristics are as follows: The axial velocity component exhibits significant radial variations that depend on the front rotor operating conditions. It appears to decrease linearly with increasing distance from the

front rotor (for distances larger than D/10). It also appears to retain the initial shape it has just downstream of the front rotor at all axial distances, without significant deformations. Finally the wake expansion was found to be about 5% at a distance equal to D/2 downstream of the front rotor.

9.2.2. Research in counter-rotating rotor aerodynamics.

The problem of counter-rotating wind turbine rotors has not been given much attention in the past and only one reference was found dealing with it. It is reference [92] in which the interaction of two rotors, one operating within the wake of the other, was investigated theoretically. However, the modelling of this interaction is not considered to be sufficiently detailed. Momentum theory was used for the prediction of the two rotors' performances, thus neglecting the front rotor wake rotation. Also, the incoming flow to the rear rotor was taken to be equal to that just downstream of the front one. Hence, the effect of changing the axial distance between rotors was not taken into account, and the rear rotor was assumed to be just downstream of the front one. Furthermore, the rear rotor blockage to the front one was not taken into account, and the front rotor was assumed to operate as if the rear one was not present. It is therefore clear that the above mentioned model is not sufficiently detailed to be used for the design of the counter-rotating turbine rotors.

However, unlike wind turbine rotors, counter-rotating propellers and helicopter rotors have received considerable attention from researchers. Although the above two are similar, (they are devices that create thrust by accelerating air masses), there is a distinct difference between them which is reflected in their modelling. For propellers, the vorticity created by the blades is removed far away from them, following

the fast moving air masses downstream of the propeller disc. This characteristic makes the fine details of the wake not very important, and as will be seen later, propellers can be modelled adequately using potential flow theory. For helicopters in hover, the situation is different. Far upstream of the rotor, the fluid is at rest. The fluid velocity through the rotor disc is equal to the downwash created by the rotor blades. The speed of the rotor tip is much larger than that of the flow, and thus the vortex filaments shed from the rotor blades stay in the rotor vicinity for a considerable number of revolutions. Hence, the effect of the trailing vorticity on the rotor blades becomes significant. (Considering Biot-Savart law). For the case of helicopter blades, knowledge of the exact shape of the trailing vortices and their deformation with time is necessary for adequate modelling.

Below, models of counter-rotating rotors are presented. For them to be applicable to the counter-rotating turbine design, two requirements must be met: The first is that they must be reasonably accurate approximations. The second is that they must have the axial distance between the two rotors as a parameter.

a) Counter-rotating propellers. A brief account of developments in propeller theory was given in chapter 2. The foundations of this theory were laid by Betz, Prandtl, Goldstein and Theodorsen. Propeller theory was then extended to treat counter-rotating propellers (often referred to as "dual propellers"). All design and analysis methods rely on the following assumptions:

1. The interference velocities from one rotor to another, (at any blade element) may be calculated by considering the velocity fields of each rotor and adding the results.
2. The interference of one rotor is added to the undisturbed flow of the other, before the self-interference of each rotor is calculated.

3. The two rotors are close enough, so that the axial distance between them can be taken as zero when the mutual interference of the rotors is calculated. Both rotors are therefore assumed to lie in the same plane.
4. Finally, the blades of both rotors are assumed to have identical chord distributions with different twist angle distributions only, and to operate at equal and opposite rotational speeds. These assumptions facilitate the propeller optimisation. The optimisation formulas for each rotor are then reduced to one, allowing for a clear optimisation criterion to be achieved.

Lock in [93] devised a technique for designing counter-rotating propellers, based on momentum-blade element theory. The interference between rotors was estimated as follows: Each rotor was assumed to produce the same self-interference field as that of a single propeller. At each blade element of one rotor, the flow induced by the other was taken to be the average induced flow on a ring with the blade element radius. Thus, the interference velocities are dependent on radius. His model is considered to be an accurate one. However, there are problems with its application: In some cases, infinite blade chord values are produced. This is caused by the use of tip loss corrections devised for single propellers, which implies that the optimum loading of a single propeller is identical with that of a counter-rotating one. Obviously, this assumption is not correct, and this shortcoming of Lock's theory was rectified later.

Crigler, in [94], used Theodorsen's experimental data for the optimum propeller circulation and wake characteristics (derived from an electrical equivalent), for designing counter-rotating propellers. He related the velocity induced by each rotor to the wake characteristics. However, he used the average interference velocity on the entire disc (ie averaging on both radius and azimuth), and thus his interference velocities are the same for all blade elements. Due to this characteristic, his model is not considered

to be accurate.

Davidson, [95], rectified the problem of Lock's theory. He also used Theodorsen's experimental data for developing a corrected tip loss factor, applicable to counter-rotating propellers only. With that correction, design of realistic propeller blades was possible.

Playle, in [96], used Davidson's method and developed an iterative code for designing optimum counter-rotating propellers. He also developed a code for the performance prediction of counter-rotating propellers at off-design conditions. (See also Korkan, [97]). It is however questionable whether Theodorsen's experimental data, which are valid for optimum propellers, are also applicable to off-design conditions.

The models presented above are not readily applicable to the design of the counter-rotating turbine, because they ignore the axial distance between rotors, which is very important in our case as was shown by the experimental investigation of [89]. However, some of the assumptions used for desiging dual propellers are applicable. These are assumptions 1 and 2, concerning the interference velocities induced by one rotor on the other, as use of potential flow theory permits the linear superposition of velocities. Also, Lock's averaging out of the azimuthal variations of the interference velocities can be applied to the counter-rotating turbine design, as the flow within which each turbine rotor operates can be considered as steady.

b) Counter-rotating helicopter rotors. Unlike propellers, for the analysis of helicopter rotors, there doesn't exist general agreement on the method to be used. Hence, a large number of different procedures exist, with varying degree of accuracy. The most important design and analysis models for counter-rotating helicopter rotors are presented in the following.

Harrington, [98], developed a relatively simple model; the two rotors are

represented by a single one, with the same radius and solidity. Although this model is useful as a first approximation to the problem, blade loadings and torque are not realistically predicted.

Paglino, [99], developed a procedure based on momentum theory. The upper rotor (ie the rotor situated upstream) was assumed to operate like an isolated one. The induced velocity of the lower rotor however, was assumed to increase by the average downwash from the upper rotor. In this case too, blade loading is inaccurate, and torque is overpredicted.

Cheeseman followed a different approach: In [100], he assumed that the counter-rotating rotor lift is divided into two parts, translational and propeller lift. For predicting the former, a lifting line model was used, substituting each blade by a lifting line shedding straight horseshoe vortices (instead of helical shaped ones). The propeller lift was predicted using a flow tube model (ie momentum theory). This model is not very accurate either, due to unrealistic assumptions about the flow.

A more rigorous approach was suggested by Andrew in [101]. Momentum theory was used, with a tip loss correction derived from lifting line theory. The usual formula for each rotor's downwash is used, as derived from momentum theory. However, in that formula, instead of the conventional tip loss correction, a new one is introduced: The vertical ascent velocity of the helicopter, which is zero for hover, is substituted by the velocity induced on each rotor by the trailing tip vortices shed by both rotors. The trailing vorticity paths are prescribed using empirical formulae, derived from experiments in helicopter wake flow visalisation. Also, the tip vortices are considered as viscous ones, with a core of finite radius estimated using experimental data. The induced velocities outside the viscous cores are given by Biot-Savart law. The axial distance between rotors is also taken into account. Good agreement with experimental data was

obtained, but the model relays heavily on empirical knowledge of the trailing vortex system.

Davis, in [102], adopted an appropriate single rotor model to counter-rotating rotors. The upper rotor was assumed to be independent of the lower. The downwash of the upper rotor was added to the aerodynamic velocities of the lower one. The lower rotor thrust was factored by an empirical interaction coefficient derived by comparison of single and counter-rotating rotors' performances. Fairly good agreement with experimental results was obtained, although the flow was not modelled adequately.

A completely different method for the analysis of both fixed wings and helicopter blades was proposed by Azuma in [103]. This method, called "local momentum theory", is as follows: Each rotor blade is analysed as a series of wings with varying span and elliptical circulation distribution. The induced velocity created by each wing is constant (due to this particular circulation distribution). The contribution of each wing to the total lift and induced velocity can be determined by considering the instantaneous balance between the fluid momentum and the blade elemental lift at each local station on the rotor disc. The theory can therefore estimate timewise variations of airloads and velocities along the blade span. This theory was used by Saito, [104], for the analysis of counter-rotating helicopter rotors. The two rotor wakes are described by a previously developed model, using flow visualisation data for the positions of the vortices and the wake contraction. The lower rotor wake has been considered as that of a single rotor in vertical climb at the speed of the upper rotor mean induced velocity. The upper rotor is not assumed to be independent of the lower one. The interference velocity on its disc is taken to be the mean induced velocity of the lower rotor. This method can also produce reasonable results, but it relays on experimental data about the wake characteristics.

The last reference to be presented is that by Nagashima, [105]. In this paper, a method for analysing counter-rotating helicopter rotors based on generalised momentum theory is presented. Each rotor is approximated by an actuator disc. However, wake rotation and the associated losses are included. The lower rotor wake is divided into two parts. The "inner" which is essentially a continuation of the contracted upper rotor wake and the "outer", through which the lower rotor draws in fresh fluid. The general equations for thrust, power, efficiency etc, are laid out. They are solved for a special case, ie when both rotors create uniform downwash through them. The interaction between rotors is given through "influence coefficients". Each rotor's downwash is factored by an appropriate coefficient and is added to the other's incoming flow. These coefficients are functions of the axial distance between rotors and the rotor thrust (or downwash). They can be derived analytically from actuator disc theory. Comparison with experimental data reveals good agreement with the theory, justifying the proposed wake model and interaction scheme.

Of the models presented above, those of references [98], [99] and [100] are oversimplifying and do not produce accurate enough results. The models of references [101], [102] and [104] rely heavily on wake measurements which are not available for wind turbines. However, the model presented in [105] seems suitable, especially the part concerning the interaction between upper and lower rotors. It satisfies both requirements set in the beginning of this review, ie it is accurate enough, since it is supported by experimental data, and the axial distance between rotors is taken into account. An appropriate adaptation of this interaction scheme is necessary for incorporating it in the counter-rotating turbine design.

9.3. CONCLUSIONS.

The main conclusions of this investigation and their implications to the counter-rotating turbine design are summarised here:

1. According to the findings of the experimental investigation of [89], the flow around a three-bladed wind turbine is as follows: Upstream of the turbine, a reduction in the incoming flow is observed, caused by the turbine blockage. The velocity decreases with decreasing axial distance from the turbine. For the same axial distance, the velocity drop is more pronounced at the hub region, while it becomes nearly zero at the blade tips. For axial distances as low as D/12, the turbulence levels were found to be less than 2.5%. Downstream of the turbine, and within its near wake, the axial velocity component exhibits a large drop in the immediate vicinity of the turbine (ie from D/60 to D/10 downstream). For axial distances larger than D/10, the axial velocity decreases less rapidly, and in a linear fashion. This trend appears to be independent of radius, as the initial velocity profile at the immediate vicinity of the turbine seems to be retained further downstream. The turbulence levels (at midspan) are quite high just downstream of the turbine (ie at D/60). However, they drop dramatically from about 12% to 5% between D/60 and D/10, revealing the thorough mixing of the flow that takes place in that region. Further downstream, the turbulence dies out and gets values similar to those upstream of the turbine. Two peaks of turbulence were observed at the tip and hub regions, associated with the tip vortices. Finally, the wake expansion was found to be equal to about 5% between D/60 and D/2.

2. Models for the interaction of two counter-rotating rotors have been developed in the past. Of these models, the ones concerning propellers assume that the axial distance between rotors is zero, and therefore they cannot be used for the counter-rotating turbine design. Most of the models developed for the analysis of counter-rotating helicopter rotors have the axial distance between rotors as a parameter, but are strongly dependent on experimental information about the wake characteristics. Empirical knowledge of the wake decay is important, as the methods used for its prediction are based on potential flow theory and do not include viscous effects or the effects of turbulence. In all models presented (both for propellers and helicopter rotors), the interaction one rotor causes to the other is added to the latter's incoming flow.

3. The implications of the above findings to the design of the counter-rotating turbine rotors are:

   Front rotor. The front rotor is expected to experience a reduction of the incoming flow velocity caused by the rear rotor blockage. However, the flow attacking the front rotor can be regarded as steady. For predicting the rear to front rotor interference, a method similar to that presented in [105] can be used, derived from actuator disc theory.

   Rear rotor. The rear rotor must be placed at an axial distance of at least D/10 downstream of the front one, for reducing flow turbulence to acceptable levels. For modelling the incoming flow to the rear rotor, (which is the flow within the front rotor near wake), the initial velocity distribution just downstream of the rotor must be modified in order to take account of the wake decay. As in the case of helicopters, the experimental data of [89]

can be used for developing an empirical model. This will be presented in the next chapter.

FIGURES FOR CHAPTER 9.

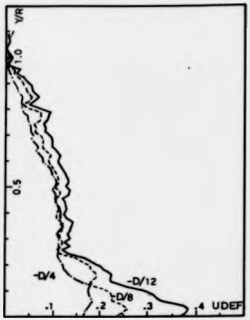

Figure 9.1. Axial velocity deficit upstream of the rotor disc, $\lambda = 6$. (taken from [89]).

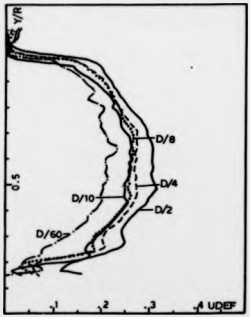

Figure 9.2. Axial velocity deficit downstream of the rotor disc, $\lambda = 6$. (Taken from [89]).

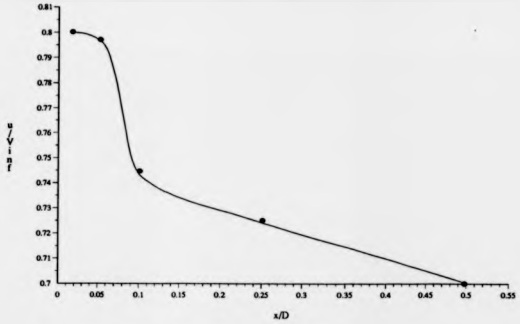

Figure 9.3. Axial velocity at 0.5 R, versus axial distance downstream of the rotor disc λ=6. (Deduced from the results of [89]).

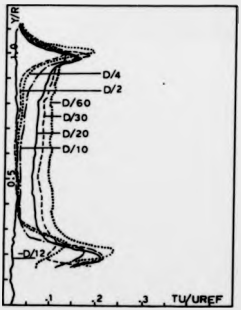

Figure 9.4. Turbulence intensity upstream (-D/12) and downstream of the rotor disc, λ=6. (Taken from [89]).

CHAPTER 10

DESIGN OF THE COUNTER-ROTATING TURBINE BLADES.

CHAPTER 10. DESIGN OF THE COUNTER-ROTATING TURBINE BLADES.

10.0. INTRODUCTION.

In this chapter, the methods for estimating the interference that the counter-rotating turbine rotors cause to each other are presented. These methods were incorporated into a procedure for designing the counter-rotating turbine blades. The design results are also presented and discussed.

10.1. INTERFERENCE ESTIMATION.

Using the findings of the literature search presented in chapter 9, it is possible to devise methods for estimating the interference caused by one rotor to the other. This interference is added to the incoming flow of the appropriate rotor before its self-interference is calculated.

10.1.1. Front to rear rotor interference.

The counter-rotating turbine rear rotor operates within the front rotor wake. For estimating the front to rear rotor interference, information about the induced velocity field of the front rotor disc is necessary. The blade design procedure presented in chapter 2 can provide that information. However, due to the mathematical formulation of that procedure, knowledge of the induced velocities is possible only on the rotor disc. This is caused by the fact that the equations for the induced velocities are derived by adapting the

velocity potential of a system of infinite vortex helices to that of a semi-infinite one. (See chapter 2). The limit of this approach is that the induced velocities can only be calculated at certain points of the rotor disc, as relations for the two vorticity systems can be obtained only at these points. A more versatile approach that permits (in principle) calculation of the induced flow at any point of the flowfield is use of Biot-Savart law for obtaining the induced velocity equations. However, even that method will not produce accurate results, as viscous effects and the effects of turbulence which are important in the wake decay are not taken into account.

Here, a semi-empirical approach was utilised: The induced velocities on the front rotor disc were calculated using the method described in chapter 2, at the two azimuthal positions where this is possible, ie on the lifting lines and on the bisectors between them. For estimating the flow on the bisectors, a method was developed described in chapter 2, section 2.2.3. As an example of the results produced by this approach, the axial and tangential induced velocities on the lifting lines and the bisectors between them are shown in figures 10.1 and 10.2 for a 3-bladed turbine, and in figures 10.3 and 10.4 for a 10-bladed one, respectively. From figures 10.1 and 10.2 it can be seen that the induced velocity distribution on the lifting lines is different from that on the bisectors. On the lifting lines, close to the tip, the values of induced velocities increase due to the effect of the strong tip vortex. However, on the bisectors the contributions of the tip vortices from neighbouring blades almost cancel each other out resulting in very low values of both the axial and tangential induced velocity. The two curves in each of the above mentioned figures are close to each other at other radial positions, apart from the hub region where differences can be observed. This picture of the flow is compatible with the findings of reference [89]. As can be seen from figure 9.4, the turbulence intensity levels close to the rotor disc (ie at D/60) exhibit two peaks at the tip and hub regions that can be associated with the large azimuthal differences in the flow. For the

case of a 10-bladed turbine, (see figures 10.3 and 10.4), the induced flow varies less between different azimuthal positions on the rotor disc. This is expected since the blades of the 10 bladed turbine are more closely packed.

The induced flow values on the lifting lines and the bisectors between them can be considered as two extremes. Given the thorough mixing of velocities that takes place downstream of the rotor (as shown in [89]), an average value of the axial and tangential induced velocities of the front rotor (u^F_i and v^F_i respectively) was calculated as shown below:

$$< u^F_i(x) > = \frac{u^F_{i,l}(x) + u^F_{i,b}(x)}{2}$$
$$< v^F_i(x) > = \frac{v^F_{i,l}(x) + v^F_{i,b}(x)}{2} \qquad (10.1.1)$$

with $u^F_{i,l}$, $v^F_{i,l}$ being the front rotor axial and tangential induced velocity values on the lifting lines (respectively), and $u^F_{i,b}$, $v^F_{i,b}$ the values of the above mentioned quantities on the bisectors. The flow velocities described by equations 10.1.1 are assumed to be the initial induced velocities, immediately downstream of the front rotor. In order further to refine the model, the wake decay (ie the increase of the velocity deficit with increasing the axial distance z from the front rotor) was also taken into account, using the results of [89] and assuming that the initial induced velocity distribution shape does not change downstream of the front rotor. Hence, the front to rear rotor interference (U_{12} and V_{12} for axial and tangential velocities respectively) is given by:

$$U_{12}(x, \zeta) = (0.25\zeta + 1.19) <u^F_i(x)>$$
$$V_{12}(x) = <v^F_i(x)> \qquad (10.1.2)$$

In the above equation, ζ is the dimensionless axial distance between the two rotors (ζ = z/R). The term (0.25 ζ + 1.19) which describes the wake decay was derived from the

results of [89] assuming a linear drop of the axial velocity with ζ increasing, as seems to be the case for ζ between 0.2 and 1.0. (See figure 9.3). The value of V_{12} was taken to be independent of the axial distance between rotors as no information about its decay was given in [89]. However, the front rotor of the counter-rotating turbine is a 3-bladed one and as will be seen later, the tangential induced velocity component in the wake is negligible compared to the axial. Finally, the incoming flow to the rear rotor becomes:

$$\begin{aligned} U_2(x,\zeta) &= u(x) - U_{21}(x,\zeta) - U_{12}(x,\zeta) \\ V_2(x) &= V_{12}(x) \end{aligned} \qquad (10.1.3)$$

where $u(x)$ is the axial component of the incoming flow to the front rotor and $U_{21}(x,\zeta)$ is the rear to front rotor interference whose derivation is decribed in the following.

10.1.2. Rear to front rotor interference.

The method chosen to be used for calculating the rear to front rotor interference is based on reference [105]. It uses actuator disc theory and Biot-Savart law. It has also been used for predicting the flow around a turbine [106], and for estimating the far wake contribution to the induced velocity field of a turbine [16]. The adaptation of this method to suit the counter-rotating turbine design is presented in this section. For assessing the rear rotor blockage effect on the front one, the rear rotor disc is assumed to be "seen" by the front as an actuator disc. The disc has infinite blades of infinitesimal chord and the axial component of the induced velocity is constant on the rotor disc. This assumption makes the induced flow around the disc steady in time which is a fair assumption for the regime upstream of a turbine (as shown in [89]). Mathematically, the flow around an actuator disc can be modelled using Biot-Savart law and substituting the trailing vorticity system shed from the disc periphery by a vortex cylinder. (See figure

10.5). This vortex cylinder consists of an infinite number of vortex rings, each of infinitesimal strength. The axial induced velocity produced by such a system at a point P in space is given by:

$$U_{21}(x,\zeta) = \frac{1}{4\pi R}\frac{d\Gamma}{d\zeta}\int_0^{2\pi}\left[\frac{\xi(\xi - x\cos\phi)}{A}\right]\left[1 - \frac{\zeta}{A}\right]d\phi \qquad (10.1.4)$$

Where: $A = \xi^2 + x^2 - 2\xi x\cos\phi$,

ξ is the dimensionless radius of the vortex cylinder (=r/R),

x is the dimemsionless radial distance of point P from the axis,

ζ is the dimensionless axial distance of point P from the disc (=z/R),

ϕ is the azimuthal angle

and Γ the circulation of the vortex cylinder.

(For a derivation of the above, see [16]).

This vorticity system also creates a radial component, (responsible for the wake expansion downstream of the rotor disc) which is not of interest from our point of view. No tangential component exists, due to the vorticity system layout. As can be seen from equ. 10.1.4 :

$$U_{21}(x = 0, \zeta = 0) = \frac{1}{4\pi R}\frac{d\Gamma}{d\zeta}\int_0^{2\pi} d\phi = \frac{1}{2R}\frac{d\Gamma}{d\zeta} \qquad (10.1.5)$$

Hence, equ. 10.1.4 can be rewritten as :

$$U_{21}(x,\zeta) = U_{21}(x = 0, \zeta = 0)\frac{I(x,\zeta)}{2\pi} \qquad (10.1.6)$$

where $I(x,\zeta)$ is the integral in equ. 10.1.4.

The values of $I(x,\zeta)$ are plotted versus x in figure 10.6 (for ξ=1, and various values of ζ). It is evident that with ζ increasing, the value of $I(x,\zeta)$ and thus $U_{21}(x,\zeta)$ is decreasing. It can also be observed that $U_{21}(x,\zeta=0)$ remains constant for x<1. (At x=1 a discontinuity

exists). The fact that the induced velocity is constant on the rotor disc characterises an actuator disc and this is why this particular vorticity system has been chosen for its description. Using the above fact, we can rewrite equation 10.1.6:

$$U_{21}(x,\zeta) = U_{21}(\zeta=0)\,\frac{I(x,\zeta)}{2\pi} \qquad (10.1.7)$$

The counter-rotating turbine rear rotor is not an actuator disc, and thus the induced velocity distribution on it will vary both in azimuth and radius. In order to use equation 10.1.7, $U_{21}(\zeta=0)$ can be approximated by $\langle u^R_i \rangle$ ie the average of the rear rotor axial induced velocity u^R_i taken on radius and azimuth. Thus the rear rotor is "seen" by the front one as an actuator disc with uniform induced velocity distribution on it, equal to $\langle u^R_i \rangle$ (the average of the r_e_a_l distribution). Therefore, the rear to front rotor interference velocity will be given by:

$$U_{21}(x,\zeta) = \langle u^R_i \rangle\,\frac{I(x,\zeta)}{2\pi} \qquad (10.1.8)$$

Also, the incoming flow to the front rotor is:

$$U_i(x,\zeta) = u(x) - U_{21}(x,\zeta)$$
$$V_i(x,\zeta) = 0 \qquad (10.1.9)$$

In the above equation, u(x) is the undisturbed (by the rotors) velocity. It was not taken to be equal to V_∞ in order to include the hub effect in the model. u(x) is given by equation 3.1.4, which was derived experimentally, as explained in chapter 3.

The predictions of equation 10.1.8 were compared with experimental results derived from reference [89]. In that reference, the flow upstream, downstream and on the rotor disc of a 3-bladed turbine was investigated. The value of $\langle u^R_i \rangle$ in equation 10.1.8 was estimated by averaging the induced velocity readings just downstream of the rotor disc (ie the curve of figure 9.1 for D/60). $I(x,\zeta)$ was calculated numerically using

Simpson's method. The results are shown in figure 10.7. In that figure, the radial distribution of U_{21}/V_∞ for two axial distances upstream of the rotor disc calculated using equation 10.1.8 is shown together with the corresponding experimental points. The agreement between the two is quite good. At the inboard part of the disc however, (ie from x=0.3 to x=0.4), the induced velocity is underpredicted in both cases. This can be attributed to the fact that the turbine centrebody causes an additional blockage which is not accounted for by equation 10.1.8. The best fit between experiment and theory was observed when the vortex cylinder radius was taken to be equal to 0.83 of the turbine radius. This is probably an effect of the vortex roll-up: After the vortex filaments are shed from the blades, they roll-up under mutual interference and tend to group around the most strong filaments, which occur close to the blade tips. The blade tip vortices are also deformed and further downstream of the rotor disc, the boundaries of the vortex system are inboard of the blade tips. Apparently, in our case, a better approximation of the physical system of trailing vorticity is obtained if the boundaries of the vortex cylinder are inboard of the turbine blade tips so that the vortex roll-up is taken into account.

Hereafter, the rear rotor will be approximated by an actuator disc with radius equal to 0.83 of the rear rotor radius for calculating its interference on the front rotor using equation 10.1.8. The induced velocity distribution on the rear rotor blades needed for their design will be calculated by the more detailed lifting line procedure.

10.2. BLADE DESIGN PROCEDURE.

The procedure used for designing the counter-rotating turbine blades is presented next.

10.2.1. Description of the procedure.

The blades of both rotors have to be designed simultaneously since each rotor's performance depends on that of the other: The front rotor depends on the rear one through the blockage the latter causes upstream of it. The rear rotor operating within the wake of the front one also depends on it. In figure 10.8, a flow chart of the algorithm is shown. The first step of the procedure is the input of the known parameters. These are: The number of blades of each rotor (B_1 and B_2), the rotors' tip speed ratios (λ_1 and λ_2), the blade chord distributions, the rotors' radii, the aerofoil data for each rotor and the axial distance between rotors. The method used for designing each rotor's blades is that presented in chapter 2, and is the same for both rotors. Only the rotor particulars (ie number of blades, tip speed ratio, etc) vary as well as the incoming flow for each rotor. For the front one, the blockage caused by the rear alters the incoming wind velocity, which becomes non-uniform but axisymmetric. It is also purely axial. The rear rotor incoming velocity is that of the front rotor wake at the axial station where the rear rotor is situated. It is axisymmetric, with two components, axial and tangential, both varying radially.

As can be seen in figure 10.8, the design procedure consists of two iterations (ie the blade design algorithms for each rotor) nested within an outer iteration. During the first step of the outer iteration, the front rotor is designed assuming that the rear rotor interference is zero. After the first rotor is designed, the front to rear rotor interference is calculated and the rear rotor design proceeds. Once that is completed, the new rear to front rotor interference is calculated (ie the induced velocity distribution upstream of the rear rotor) and is compared with the old one (which was taken to be zero for the first step). If the new and old interference values differ more than a prescribed amount the rear to front rotor interference is updated and the outer iteration is repeated

until convergence is achieved. The desired output from this design procedure is the twist angle distributions along each rotor's blades and estimates of the power and torque coefficients (C_p and C_q respectively) of the two rotors. C_p is given by equation 3.1.3, while C_q is:

$$C_q = C_p/\lambda. \qquad (10.2.1)$$

It is evident that for a design point (ie a pair of λ_1 and λ_2) to be acceptable, the torque developed by one rotor must be equal to that of the other. This condition however cannot be met before hand. Thus, a systematic search for the equal torque point must be carried out. This is done as follows: The front rotor tip speed ratio is held constant, while that of the rear one can vary. After sufficient values of the front and rear rotor torque coefficients (C_{q1} and C_{q2} respectively) are obtained using the design procedure, a root finding algorithm is used for predicting the equal torque point (ie λ_2 for which $C_{q1}=C_{q2}$). The design calculations are then repeated for that value of λ_2 and if the new C_{q1} and C_{q2} differ, the input data of the root finding routine are updated and the procedure continues until $C_{q1}=C_{q2}$. The equal torque point is thus successively approximated.

10.2.2. Numerical techniques used.

A fortran program was developed in order to perform the above mentioned calculations. Details about the numerical techniques used in that program are given below.

a) Blade design. The numerical techniques used for each rotor's blade design are similar to those used for the conventional turbine design in chapter 3 and they won't be repeated here apart from one aspect. That is the fourier expansion of the bound circulation (G). In the design of the delta wing system turbine, the fourier expansion of G

was truncated after the 31st coefficient. In our case however, 21 coefficients were used instead, as the time needed for the program to run with 31 coefficients was prohibitive of their use. With 21 coefficients, each rotor design procedure took from 5 to 10 minutes. For the outer iteration to converge 3 to 10 repetitions were necessary. Hence the minimum time for the whole program to end was 30 minutes (ie three outer iterations, taking 2x5 minutes each), while the maximum time was 3h, 20 min. The difference in Cp between 21 and 31 coefficients did not exceed 2%.

b). Front to rear rotor interference. The calculation of this type of interference requires the estimation of the induced flow on the bisectors between lifting lines. This calculation is performed after the iteration for the front rotor design has converged. The method used is similar to that for the estimation of the induced velocities on the lifting lines presented in chapter 2, ie solution of the system of equations 2.2.10 to 2.2.14. However, for the flow on the bisectors, equation 2.2.19 must be used instead of 2.2.7 for the calculation of the induction factors. Also, since the bound circulation on the lifting lines and the direction of the vortex sheets are known, the calculation of $u^F_{i,b}$ and $v^F_{i,b}$ is a straightforward one, and no iteration is necessary.

c) Rear to front rotor interference. For estimating this type of interference, equation 10.1.8 is used. In that formula, two parameters must be identified: $<u^R_i>$ and $I(x,\zeta)$. For calculating $<u^R_i>$, the induced velocity must be averaged on both azimuth and radius. For the former the same technique is used as that for the front to rear rotor interference: The axial induced velocity is calculated on two different azimuthal positions, ie on the lifting lines ($u^R_{i,l}$) and on the bisectors between them ($u^R_{i,b}$). Since these are considered to be the two extremes of u^R_i, the azimuthal average is:

$$< u^R_i(x) > = \frac{u^R_{i,l}(x) + u^R_{i,b}(x)}{2} \qquad (10.2.2)$$

Averaging on radius is not as straightforward, because the points along the blade where the induced velocity is known are not equidistant with respect to radius. Thus, for two consecutive points x_n and x_{n-1} with $u^R_i(x_n)$ and $u^R_i(x_{n-1})$ respectively, the mean induced velocity is $\{u^R_i(x_n)+u^R_i(x_{n-1})\}/2$. In order to take the average of u^R_i from n=1 to n=N, each of the above mentioned means can be weighed by the length of the interval $[x_n-x_{n-1}]$ and the overall average becomes:

$$< u^R_i > = \frac{\sum_{n=2}^{N} (x_n - x_{n-1}) \left[u^R_i(x_n) + u^R_i(x_{n-1}) \right]}{2 (x_N - x_1)} \qquad (10.2.3)$$

In the above formula, the denominator is: $x_N - x_1 = 1-x_h$. (x_h is the dimensionless hub radius). Since in equation 10.2.3 $u^R_i(x_n)=\{u^R_{i,l}(x_n)+u^R_{i,b}(x_{n-1})\}/2$, we get by substituting equation 10.2.2 in equation 10.2.3:

$$< u^R_i > = \frac{\sum_{n=2}^{N} (x_n - x_{n-1}) \left\{ u^R_{i,l}(x_n) + u^R_{i,b}(x_n) + u^R_{i,l}(x_{n-1}) + u^R_{i,b}(x_{n-1}) \right\}}{4 (1 - x_h)} \qquad (10.2.4)$$

Finally, the value of $I(x,\zeta)$ was calculated using Simpson's numerical integration with 501 intervals.

d) Outer iteration convergence. The following criterion is used for judging the outer iteration convergence $|U_{21,new} - U_{21,old}| / |U_{21,new}| < 0.0001$. U_{21} is actually a distribution of velocities along the rotor radius and thus all values of $U_{21,new}$ and $U_{21,old}$ are compared one by one.

e) Root finding algorithm. For finding the values of λ_2 for which $C_{q1} = C_{q2}$, a root finding technique is used, as mentioned above. It calculates the values of C_{q1} and C_{q2} at different λ_2 interpolating from the known values of the torque coefficients given as input. Then, using the bisection method it predicts the equal torque point. The

accuracy of that prediction depends on the input data. The closer they are to the root, the better the accuracy. Successive approximations to the solution with subsequent updating of the input data was found necessary. Usually, after two repetitions the equal torque point was estimated with sufficient accuracy (ie four significant digits).

10.3. PRESENTATION OF RESULTS.

In the following, the results obtained from the design procedure described above are presented and discussed.

10.3.1. Definition of parameters.

Several parameters are involved in the design of the counter-rotating turbine blades. Some of them were chosen to be fixed during the design procedure while others were allowed to vary, for assessing their effects. The parameters involved are:

a) Blade chord distribution. This was chosen after consultation with the counter-rotating turbine manufacturer. Linear taper (without waisting) of the blade was chosen for ease of manufacture and simplicity. The blade however is quite slender. The chord to radius ratio (c/R) of the blade is 0.0945 at the hub and 0.0182 at the tip. Hence the blade taper ratio is about 5:1. Both rotors (front and rear) have the same chord distribution. The chord distribution used in the design procedure is slightly different from the real one. As shown in figure 10.9, the blade chord becomes zero at the tip and hub. Hence, the real blade chord distribution is followed from $x \leq 0.25$ to $x \geq 0.95$. At the tip and hub region, the blade chord drops to zero. This modification to the real blade shape was necessary in order to satisfy the boundary conditions of the problem (ie zeroing of the bound circulation at the tip and hub). The blade chord transition to zero has to be

continuous, so that the bound circulation can be expanded in a fourier series. This modification is not expected to have any significant influence on the results since both tip and hub regions contribute a negligible amount to the turbine power.

b) Radii of rotors. Both rotors have the same radius which is R=2.75m. Their hub radius is R_h=0.55m. Hence R_h/R=0.2.

c) Aerofoil chosen. The aerofoil to be used was specified by the manufacturer. It is the SD7037-PT section designed for gliders. Its characteristics are given in reference [107]. The SD7037-PT optimum angle of attack is α_{opt}=5.74°, with $C_L(\alpha_{opt})$=0.786. (As both α_{opt} and $C_L(\alpha_{opt})$ were found to vary slightly with Re, the above mentioned values are the averages for a range of Reynolds numbers from 60000 to 300000). In order to incorporate Reynolds number effects into the blade design, the values of $C_D(\alpha_{opt})$ were chosen in accordance with the local Re value (at each blade element) by interpolating from a C_D(Re) database incorporated in the fortran code. The undisturbed wind velocity (V_∞) needed for the calculation of Re was taken to be equal to 10 m/sec.

d) Number of blades. The front rotor was chosen to be a 3-bladed one. The front rotor number of blades (B_1) was chosen to be a constant parameter in order to obtain the high tip speed ratios required for direct connection to a generator and because near wake decay data were available for 3-bladed turbines only. (See ref. [89]). The rear rotor number of blades varied from 4 to 7 although the 5-bladed configuration was investigated in more detail.

e) Other parameters. The tip speed ratio values of both front and rear rotors (λ_1 and λ_2 respectively) and the axial distance between rotors were used as variables and their effects were investigated.

10.3.2. Three front-five rear rotor blade configuration.

The counter-rotating turbine configuration with three blades at the front rotor and five at the rear was investigated first.

a) Behaviour of equal torque solutions. As was explained before, a systematic search was carried out in order to establish the values of λ_1 and λ_2 for which the torque coefficients of the two rotors were equal. It was found that for a given value of λ_1, two solutions for equal torque could be obtained. One (to be called solution "A") for a low value of λ_2 and another (to be called solution "B") for a higher λ_2. In figure 10.10 (a to d), plots are shown of $C_{q1}(\lambda_2)$ and $C_{q2}(\lambda_2)$ for different values of λ_1 ranging from 5.0 (10.10.a) to 5.5 (10.10.d) and for the same axial distance between rotors ζ=0.2. Note that in these plots, points lying on the same curve represent different rotor designs, with the same number of blades and chord distribution, but different twist angle distributions. It is evident from these figures that with λ_2 increasing, C_{q2} increases initially and then drops exhibiting a maximum. On the other hand, C_{q1} is decreasing gradually. This is caused by the increase of the rear to front rotor interference with λ_2 increasing. (In equation 10.1.8, $\langle u^R_i \rangle$ increases while $I(x,\zeta)$ is constant). In these plots, solution "A" appears at the point where the two curves meet, at the left of the C_{q2} crest, while solution "B" is at the right of the crest. Progression from figure 10.10 a to 10.10 d, (ie increase of λ_1), reveals that the two solutions approach until they meet (see figure 10.10 c) as with λ_1 increasing, the power in the front rotor wake decreases (as more is absorbed by that rotor) and hence the rear rotor torque (and power) decreases. Further increase of λ_1 makes it impossible for equal torque solutions to be found, as the rear rotor torque is less than that of the front one. (See figure 10.10 d). The equal torque solutions are quite sensitive to λ_1, as can be seen from fig. 10.10. This is due to the fact that C_{q2} has a rather flat crest and the intersection points of the two curves vary considerably within a small range of λ_1. Since

for each value of λ_2 two equal torque solutions can be found, the solution that produces the largest total power coefficient (ie $C_{p,tot}=C_{p1}+C_{p2}$) must be chosen. In figure 10.11, $C_{p\,tot}$ is plotted against λ_1 for both solutions and for an axial distance between the two rotors $\zeta=0.2$. It is evident that solution "B" produces more $C_{p\,tot}$. This can be explained as follows: For each rotor, $C_{p1,2}=C_{q1,2}\,\lambda_{1,2}$. C_{q1} and C_{q2} of solution "A" are larger than those of "B", while λ_2 of solution "B" is larger than that of "A". (This can be observed in fig. 10.10). Apparently, in solution "B", the increase of λ_2 is enough to overcome the drop of C_{q2} and thus the value of C_{p2} ($=C_{q2}\,\lambda_2$) is larger than that of solution "A". Also, the slight decrease of C_{p1} is not enough to cancel out the benefit of the larger C_{p2} (for solution "B"). As can be seen from figure 10.11, the maximum of $C_{p\,tot}$ occurs at $\lambda_1=5.285$, at which the two solutions collapse into one. This happens because at this case, the two rotors are very close to each other ($\zeta=0.2$) and the rear to front rotor interference gets its largest value, as will be seen later. Thus for maximizing $C_{p\,tot}$, the front rotor must operate at the largest possible tip speed ratio, while the rear one must operate at the lowest possible λ_2 (of solution "B"). This condition minimizes the rear to front rotor interference and is realised at $\lambda_1=5.285$ as can be observed from figures 10.10 a to d. However, this solution is unstable. It is quite possible that small imperfections in the blade construction may cause the rear rotor to produce less torque (or the front to produce more). If that happens, no equal torque solution will exist for the design values of λ_1 and λ_2, and the system will come to equilibrium at an off-design condition. Hence, if that axial distance is chosen for the counter-rotating turbine rotors, (ie $\zeta=0.2$), a stable design point must be chosen, at a smaller value of λ_1. This problem occurs only at $\zeta=0.2$. At larger distances between rotors, the rear to front rotor interference is not so large and the $C_{p\,tot}$ maximum occurs at values of λ_1 lower than these for which the instability occurs. This can be seen in figure 10.12 where a plot of $C_{p\,tot}(\lambda_1)$ is shown for solution "B" and for a large axial distance between rotors ($\zeta=2$). It is evident from figure 10.12 that the maximum of $C_{p\,tot}$ for $\zeta=2$ is

realised at a λ_1 value lower than 5.02, for which solutions "A" and "B" collapse into one.

From the above discussion, it was made clear that for each axial distance between rotors, a unique combination of operating conditions for the front and rear counter-rotating turbine rotors can be found (ie a pair of λ_1 and λ_2) for which both rotors produce the same torque and $C_{p,tot}$ is maximum. Hereafter, $C_{p,tot}$, λ_1 and λ_2 will denote the total power coefficient and the front and rear rotor tip speed ratios respectively for which the above mentioned situation arises.

b) Influence of axial distance between rotors. The effect of axial spacing between the counter-rotating turbine rotors will be investigated next. In figure 10.13, a plot of $C_{p,tot}$ (as defined above) versus ζ (ie dimensionless axial distance between rotors) is shown. $C_{p,tot}$ increases with ζ increasing until a maximum is achieved ($C_{p,tot,max}$) at ζ=1.4. An increase of $C_{p,tot}$ of about 7.4% can be observed between ζ=0.2 and ζ=1.4. This can be explained by a closer look at the flow characteristics of the rotor system. In figures 10.14 a and b, the front to rear rotor interference velocity components' distributions with radius are shown for various values of ζ. From figure 10.14.a it is evident that the axial component of that interference velocity (U_{12}) increases steadily with increasing ζ. U_{12} exhibits a rapid increase near the rotor tips for all values of ζ. This is caused by the strong tip vortex of the front rotor which induces large velocities at that region. At x=0.5, the variation of U_{12} between ζ=0.2 and ζ=2.0 is about 16.7%. The effect of U_{12} on the rear rotor is to reduce its incoming flow velocity. Thus, with all other parameters being constant, the further downstream the rear rotor is, the lower the power in the wind attacking it. Figure 10.14 b shows the tangential front to rear rotor interference velocity (V_{12}). Compared to U_{12}, V_{12} is negligible (less than 1/5 as much) and it doesn't vary much with ζ. This component is added to the rear rotor incoming flow. It is effectively the front rotor wake swirl. The low value of V_{12} is due to the low blade number of the front rotor. Indeed, a multi-bladed rotor would create a much stronger swirl

in its wake.

In figure 10.15, the rear to front rotor interference velocity (U_{21}) distribution for various ζ is shown. U_{21} decreases dramatically with increasing ζ and its shape changes. At low ζ, it is pronounced close to the hub and decays towards the tip, while for large ζ it tends to become uniform. It remains lower than U_{12} for all values of ζ and x. At x=0.5, the variation of U_{21} between ζ=0.2 and ζ=2 is about 84.5%. This large drop of U_{21} with ζ can explain the behaviour of $C_{p,tot}$. With increasing axial distance between rotors, U_{21} drops rapidly, so that the blockage caused on the front rotor by the rear one decreases allowing the former to perform better and as will be seen later, to operate at lower tip speed ratios. The reduction of the front rotor tip speed ratio (λ_1), leaves more power in its wake and thus the rear rotor can also operate better. The increase of the wake decay (ie the increase of U_{12}) with increasing ζ is less abrupt than that of U_{21} and does not create negative effects up to ζ=1.4. Therefore, the total power produced by the two rotors increases. Beyond ζ=1.4 however, U_{21} is very low and doesn't change considerably with ζ. Hence, in that region, the increase of U_{12} is dominant and this causes $C_{p,tot}$ to drop. The effects of U_{21} are also evident in the incoming flow velocities of the front and rear rotors as can be seen in figures 10.16 a and b respectively. In both plots the incoming velocities increase with ζ increasing. In figure 10.16 a, the increase of the incoming velocities close to the hub is caused by the suction created in that region by the turbine centrebody.

In the following table, the most important characteristics of the rotors' performance at various values of ζ are shown:

TABLE I

ζ	λ_1^*	λ_2	C_{p1}	C_{p2}	C_{p1}/C_{p2}
0.2	5.285	4.500	0.2480	0.2111	1.174
0.5	5.235	4.628	0.2528	0.2235	1.131
1.0	5.180	4.721	0.2578	0.2350	1.097
1.4	5.100	4.842	0.2544	0.2415	1.053
2.0	5.000	4.843	0.2493	0.2414	1.033

From this table can be seen that with ζ increasing, λ_1 decreases, λ_2 increases, C_{p1} increases until ζ=1.0 is reached and then drops, while C_{p2} increases up to ζ=1.4 and then, at ζ=2.0 it is slightly reduced. The combination of C_{p1} and C_{p2} gives $C_{p\,tot}$ the shape shown in figure 10.13. The power sharing ratio (C_{p1}/C_{p2}) decreases with ζ increasing and the contribution of each rotor to the total power becomes nearly equal. At ζ=1.4, for which $C_{p,tot,max}$ is achieved, the total tip speed ratio ($\lambda_{tot}=\lambda_1+\lambda_2$) gets its maximum value, namely 9.94. λ_{tot} is important, as that is the "effective" tip speed ratio the counter-rotating turbine generator will sense. It corresponds to a relative rotational speed of 345 rpm for a value of V_∞ equal to 10 m/sec. The target λ_{tot} set by the manufacturer is 10, thus that obtained by the present design is just 0.6% short.

The twist angle distributions of each rotor for various values of ζ are shown in figures 10.17 a and b. It is evident that both rotors require strongly twisted blades. The amount of hub to tip twist is about 35° to 40° for both rotors. The increase of the front rotor twist angle values (β_1) with ζ increasing is caused by the increase in the incoming velocity and the drop of λ_1 which in turn causes the axial component of the relative velocity at each blade element to increase. The rear rotor twist angles (β_2) decrease with ζ increasing, but less than β_1 increases, since λ_2 increases but its effect is opposed by the increase of the rear rotor incoming velocity.

10.3.3. Effects of changing the rear rotor blades.

The results presented so far are all pertinent to the 3 front-5 rear rotor blade configuration. In the following, another investigation is presented done for assessing the effect of varying B_2. Several different rotor configurations were tested, with B_2 ranging from 4 to 7. For each configuration, the same procedure as that described in the previous sections was followed, ie, the equal torque solutions were also identified and

the set of λ_1 and λ_2 were chosen so that $C_{p\,tot}$ would be maximum. The effects of axial distance between rotors were also investigated, but the search was limited to values of ζ around 1.4, since the experience gained from the previous work suggested that $C_{p\,tot,max}$ was more likely to be found in that region. The results are shown in the following table:

TABLE 2

B_2	ζ_{opt}	λ_1	λ_2	λ_{tot}	C_{p1}	C_{p2}	$C_{p,tot}$	C_{p1}/C_{p2}
4	1.4	4.750	5.412	10.162	0.2241	0.2553	0.4794	0.878
5	1.4	5.100	4.842	9.924	0.2544	0.2415	0.4959	1.053
6	1.3	5.420	4.325	9.745	0.2831	0.2259	0.5090	1.253
7	1.3	5.660	3.946	9.624	0.3057	0.2141	0.5198	1.428

In the above table, ζ_{opt} is the value of ζ for which $C_{p,tot}$ is maximised. It is evident from table 2, that with B_2 increasing, $C_{p,tot}$, λ_1, C_{p1} and the power sharing ratio increase, while λ_2, C_{p2} and ζ_{opt} decrease. These effects can be explained as follows: An increase of B_2 allows the rear rotor to produce more torque. Hence, in order to equal this torque, the front rotor must operate at a higher tip speed ratio and as a result, its efficiency increases. Hence, due to the increase of λ_1, less power is left for the rear rotor which produces less C_{p2}. However, the C_{p1} increase overcomes the drop of C_{p2}. Also, since λ_2 decreases, the rear to front rotor interference decreases and the two rotors can be situated closer to each other, without unduly increasing the rear rotor blockage. Thus, ζ_{opt} is reduced with B_2 increasing. The effect of using a multibladed rear rotor is to create more torque so that the front rotor can operate more efficiently. As can be seen from table 2, with B_2 increasing, the power sharing ratio rises. The $C_{p\,tot}$ gain between B_2=5 and B_2=7 is 4.6% while the λ_{tot} reduction is 3%.

The performance of the counter-rotating turbines of table 2 can be compared with that of the conventional turbines designed in chapter 3. The comparison results can only be regarded as approximate, since the counter-rotating turbines and the conventional ones have different aerofoil sections and blade chord distributions. However, from figures 3.13 and 10.9 it can be seen that the chord distribution of the

counter-rotating turbine blades resembles more closely the chord distribution with c_{max}/R =0.1 and E = 1.0 used for the conventional turbines' design. The performance results for this family of turbines are shown in table 1 of chapter 3, which appears in page 53.

From that table, and also from table 2 of the present chapter, it can be seen that the 3-bladed turbine with c_{max}/R = 0.1 and E = 1.0 produces 1.4 times the C_p of the front rotor of the counter-rotating turbine configuration with 3 front-6 rear rotor blades, and operates at a tip speed ratio 1.2 times as large. The reduced C_p of the front counter-rotating turbine rotor is due to the rear rotor interference. Also, the 6-bladed turbine with c_{max}/R = 0.1 and E = 1.0 produces 2.1 times the C_p of the rear rotor of the counter-rotating turbine configuration with 3 front-6 rear rotor blades, while it operates at a tip speed ratio 1.2 times as large. The reduced performance of the rear counter-rotating turbine can be attributed to the reduced wind power within the front rotor wake.

The equal torque condition causes both counter-rotating turbine rotors to operate at tip speed ratios lower than those for which the maximum power coefficient (for each rotor) is achieved and hence, both rotors operate at lower λ than their conventional counterparts.

Finally, comparison of the $C_{p,tot}$ and λ_{tot} of the 3 front-7 rear counter-rotating turbine configuration with the performance characteristics of the 10-bladed turbine with c_{max}/R = 0.1 and E = 1.0 reveals that the counter-rotating turbine produces a slightly higher C_p (just 0.3 more) than its conventional counterpart. However, the λ_{tot} of the counter-rotating turbine is 2.4 times as much as the λ_{opt} of the conventional turbine. This last result shows that the advantage of a counter-rotating turbine over a conventional one with the same total number of blades is the the significant increase in the tip speed ratio of the former, rather than a considerable improvement in performance.

10.3.4. Possible improvements of the counter-rotating turbine design.

The present counter-rotating turbine design (ie the Trimble mill) consists of a 3-bladed front rotor and a 5-bladed rear one. They are situated at an axial distance of 0.2R. The system's power coefficient is: $C_{p\,tot}$=0.36 and its λ_{tot} is 4.72. This study has revealed what alterations are necessary for improving the system's performance and has also quantified the possible improvements. There are three major areas where change of the present design may be beneficial:

a) Redesign of blades. By changing the blade chord and twist angle distributions to those resulting from this study, an increase in $C_{p\,tot}$ equal to 21.5% is expected. This is the most drastic change to the present design that will improve significantly the system's performance. Also, by using narrower blades than those of the original design (whose taper ratio is roughly 3:1), the value of λ_{opt} is doubled (see table 1, for $\zeta_s = 0.2$). This will make direct connection to the generator easier.

b) Increase of axial distance between rotors. By increasing the axial distance between rotors from its present value (ie 0.2R) to 1.4R, a further increase of $C_{p,tot}$ equal to 7.4% is possible. However other factors must be taken into account, such as the feasibility and cost of increasing the distance between rotors as well as structural problems that may arise.

c) Increase of rear rotor number of blades. Increase of B_2 from 5 to 7 improves $C_{p,tot}$ by another 4.6%. However, the 3% reduction in the generator's rpm may reduce the overall efficiency of the system. Also the extra cost of the additional blades must be considered. A further increase of B_2 beyond 7 is not expected to improve things, since the reduction of λ_{tot} may make direct connection of the rotors to the generator impossible.

10.4. CONCLUSIONS.

The most important conclusions drawn from this study are:

1. A semi-empirical method was used for estimating the front to rear counter-rotating turbine rotor interference: An azimuthal average of the axial and tangential induced velocities on the front rotor disc was calculated first. Then, the axial induced velocity was projected downstream of the front rotor disc (on the rear rotor disc) using the experimental results of reference [89]. The flow resulting from that model was then used for designing the rear rotor blades.
2. The rear to front counter-rotating turbine rotor interference was modelled by representing the rear rotor as an actuator disc. This model is simple and easy to use and it produces results which compare favourably with experimental data. This method was used in the design of the counter-rotating turbine rotor blades.
3. Proper design of the counter-rotating turbine blades can increase the turbine's performance by 21% above its present value. Increase of the axial distance between rotors from 0.2R to 1.4R, brings about another increase of performance equal to 7.4%, while increase of the rear rotor number of blades from 5 to 7, further improves the system's performance by 4.6%. The former alteration can be immediately implemented, as its results will be beneficial. For the other two changes however, additional factors must be taken into account, such as feasibility and cost as well as structural issues in order to make sure that they are worth implementing. For the last modification, special attention must be given to potential problems with the generator matching.

FIGURES FOR CHAPTER 10.

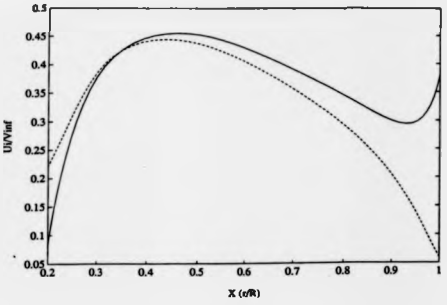

Figure 10.1. Axial induced velocity distributions along the lifting lines (—) and the bisectors between them (---), for a 3-bladed turbine operating at λ=8.75. Turbine blade chord is given by: $c(x)/R=0.0025\ \sin\phi/x^{1.5}$. $c_{max}/R=0.1$.

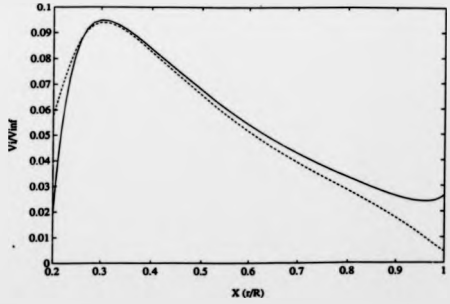

Figure 10.2. Tangential induced velocity distributions along the lifting lines (—) and the bisectors between them (---), for a 3-bladed turbine operating at λ=8.75. Turbine blade chord is given by: $c(x)/R=0.0025\ \sin\phi/x^{1.5}$. $c_{max}/R=0.1$.

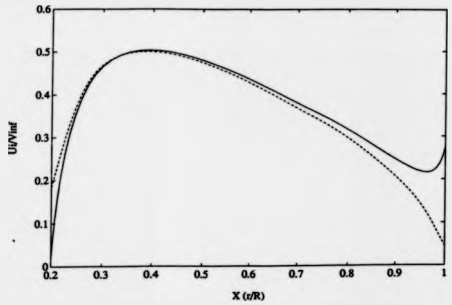

Figure 10.3. Axial induced velocity distributions along the lifting lines (—) and the bisectors between them (---), for a 10-bladed turbine operating at λ=5. Turbine blade chord is given by: $c(x)/R=0.0025 \sin\phi/x^{1.5}$. $c_{max}/R=0.1$.

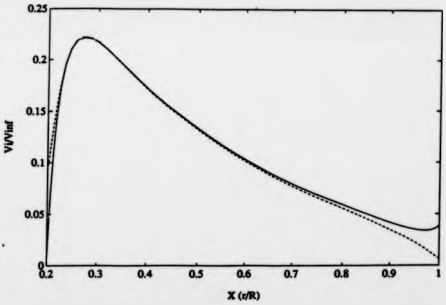

Figure 10.4. Tangential induced velocity distributions along the lifting lines (---) and the bisectors between them (---), for a 10-bladed turbine operating at λ=5. Turbine blade chord is given by: $c(x)/R=0.0025 \sin\phi/x^{1.5}$. $c_{max}/R=0.1$.

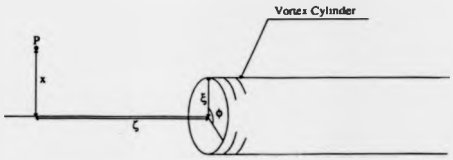

Figure 10.5. Vortex cylinder model used for estimating the rear to front rotor interference.

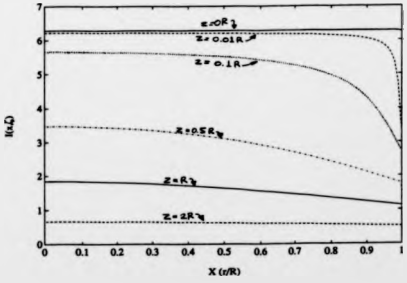

Figure. 10.6. $I(x,\zeta)$ distribution for $\xi=1.0$.

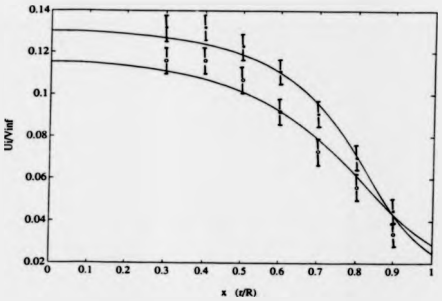

Figure 10.7. Comparison of predictions about the vortex cylinder induced flow with experimental results taken from [89]. Vortex cylinder radius: ξ=0.83R.
Symbols: "*", z=R/6. "o", z=R/4.

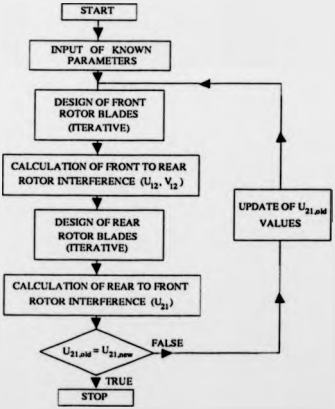

Figure 10.8. Flow chart of the procedure used for the counter rotating turbine design.

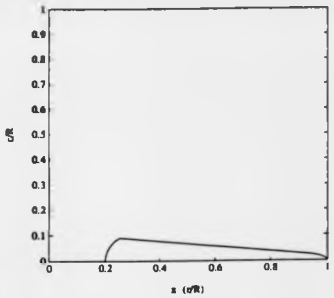

Figure 10.9. Counter rotating turbine blade chord used in the design procedure.

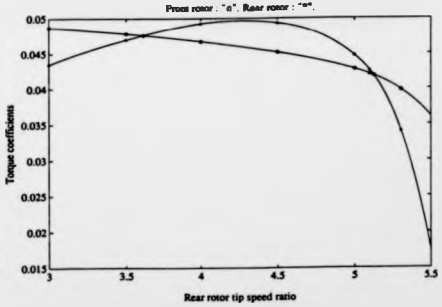

Figure 10.10.a. C_{q1} (λ_2) and C_{q2} (λ_2) plots for λ_1=5.0 and ζ=0.2

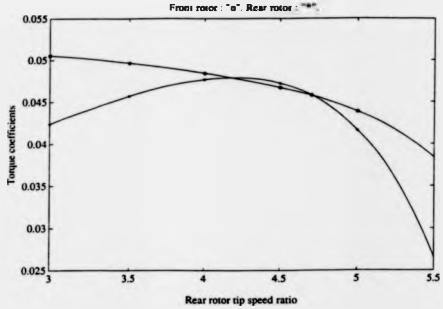

Figure 10.10.b. $C_{q1}(\lambda_2)$ and $C_{q2}(\lambda_2)$ plots for λ_1=5.25 and ζ=0.2

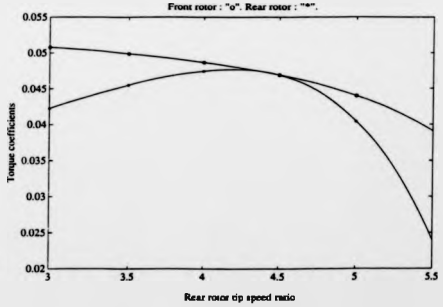

Figure 10.10.c. $C_{q1}(\lambda_2)$ and $C_{q2}(\lambda_2)$ plots for λ_1=5.285 and ζ=0.2

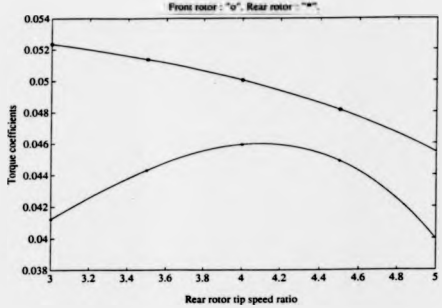

Figure 10.10.d. $C_{q1}(\lambda_2)$ and $C_{q2}(\lambda_2)$ plots for λ_1=5.5 and ζ=0.2

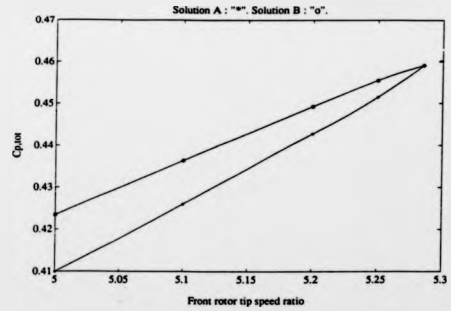

Figure 10.11. $C_{p\,tot}(\lambda_1)$ plots of solutions "A" and "B" for ζ=0.2

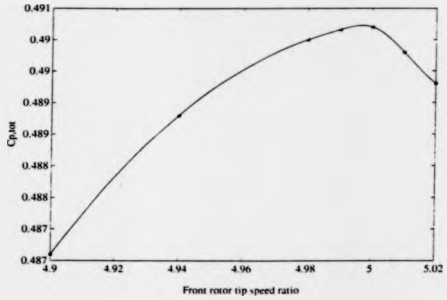

Figure 10.12. $C_{p\,tot}(\lambda_1)$ plots of solution"B" for ζ=2.0.

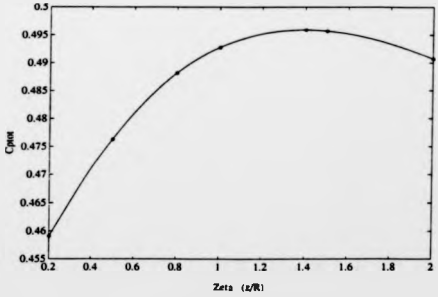

Figure 10.13.$C_{p,tot}(\zeta)$ plot.

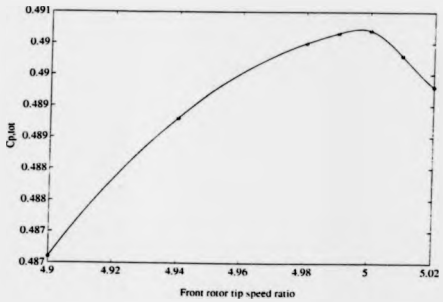

Figure 10.12. $C_{p,tot}(\lambda_1)$ plots of solution"B" for ζ_s=2.0.

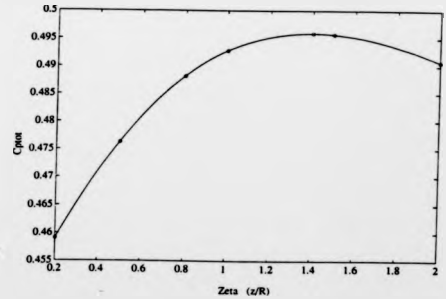

Figure 10.13.$C_{p,tot}(\zeta)$ plot.

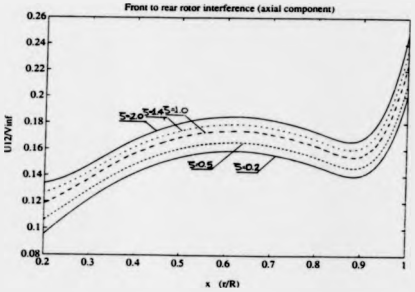

Figure 10.14.a. U_{12}/V_{∞} plots for various values of ζ.

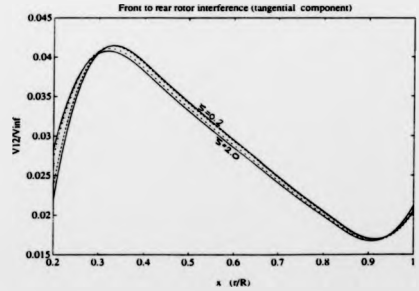

Figure 10.14.b. V_{12}/V_{∞} plots for various values of ζ.

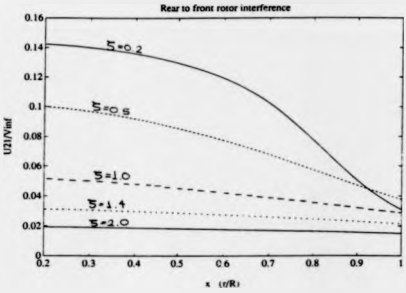

Figure 10.15. U_{21}/V_{∞} plots for various values of ζ.

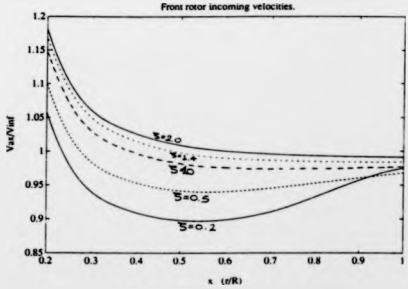

Figure 10.16.a. U_1/V_{∞} plots for various values of ζ.

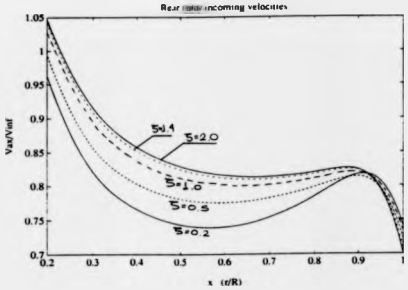

Figure 10.16.b. U_2/V_∞ plots for various values of ζ.

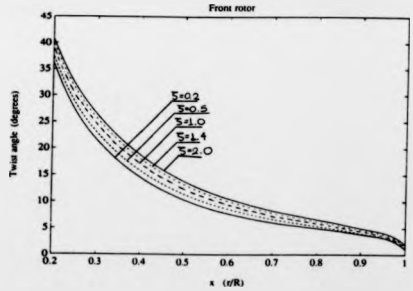

Figure 10.17.a. $\beta_1(x)$ plots for various values of ζ.

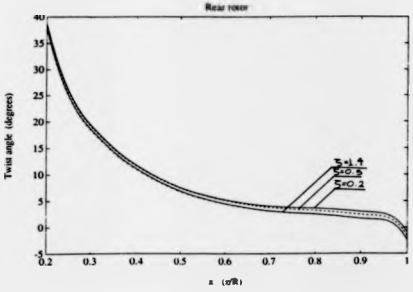

Figure 10.17.b. $\beta_2(x)$ plots for various values of ζ.

CHAPTER 11.

CONCLUSIONS-COMMENTS-AREAS OF FURTHER RESEARCH.

CHAPTER 11. CONCLUSIONS-COMMENTS-AREAS OF FURTHER RESEARCH.

11.0. INTRODUCTION.

In the following, the main conclusions of part C are presented, the accuracy of the counter-rotating turbine modelling is commented on, and possible areas of further research are proposed.

11.1. CONCLUSIONS OF PART C.

11.1.1. Wind turbine near wake structure. According to the findings of the experimental investigation of [89], the flow around a three-bladed wind turbine is as follows: Upstream of the turbine, a reduction in the incoming flow is observed, caused by the turbine blockage. The velocity decreases with decreasing axial distance from the turbine. For the same axial distance, the velocity drop is more pronounced at the hub region, while it becomes nearly zero at the blade tips. For axial distances as low as D/12, the turbulence levels were found to be less than 2.5%. Downstream of the turbine, and within its near wake, the axial velocity component exhibits a large drop in the immediate vicinity of the turbine (ie from D/60 to D/10 downstream). For axial distances larger than D/10, the axial velocity decreases less rapidly, and in a linear fashion. This trend appears to be independent of radius, as the initial velocity profile at the immediate vicinity of the turbine seems to be retained further downstream. The turbulence levels (at midspan) are quite high just downstream

of the turbine (ie at D/60). However, they drop dramatically from about 12% to 5% between D/60 and D/10, revealing the thorough mixing of the flow that takes place in that region. Further downstream, the turbulence dies-out and gets values similar to those upstream of the turbine. Two peaks of turbulence were observed at the tip and hub regions, associated with the tip vortices. Finally, the wake expansion was found to be equal to about 5% between D/60 and D/2.

11.1.2. Previous research in the field. Models for the interaction of two counter-rotating rotors have been developed in the past. Of these models, the ones concerning propellers assume that the axial distance between rotors is zero, and this parameter is important in the case of a counter-rotating turbine, they cannot be used for the turbine design. Most of the models developed for the analysis of counter-rotating helicopter rotors have the axial distance between rotors as a parameter, but are strongly dependent on experimental information about the wake characteristics. Empirical knowledge of the wake decay is important, as the methods used for its prediction are based on potential flow theory and do not include viscous effects. In all models presented (both for propellers and helicopter rotors), the interaction one rotor causes to the other is added to the latter's incoming flow.

11.1.3. Modelling of the rotors' interaction. The implications of the above findings to the design of the counter-rotating turbine rotors are:

Front rotor. The front rotor is expected to experience a reduction of the incoming flow velocity caused by the rear rotor blockage. However, the flow attacking the front rotor can be regarded as steady. For predicting the rear to front rotor interference, a method similar to that presented in [105] can be used, derived from actuator disc theory. The rear rotor was substituted by an actuator disc and the blockage it causes on the front rotor disc was thus estimated. This model is simple and easy to use

and it produces results which compare favourably with experimental data. This method was used in the design of the counter-rotating turbine rotor blades.

Rear rotor. The rear rotor must be placed at an axial distance of at least D/10 downstream of the front one, for reducing flow turbulence to acceptable levels. For modelling the incoming flow to the rear rotor, (which is the flow within the front rotor near wake), the initial velocity distribution just downstream of the rotor must be modified in order to take account of the wake decay. As in the case of helicopters, the experimental data of [89] can be used for developing a semi-empirical model: The azimuthal average of the axial and tangential induced velocities on the front rotor disc was calculated first. Then, the axial induced velocity was projected downstream of the front rotor disc (on the rear rotor disc) using the experimental results of reference [89]. The flow resulting from that model was then used for designing the rear rotor blades.

11.1.4. Turbine design results. Proper design of the counter-rotating turbine blades can increase the system's performance by 21% above its present value. Increase of the axial distance between rotors from 0.2R to 1.4R (for which a maximum of the turbine's power coefficient was observed) brings about another increase of performance equal to 7.4%. Increase of the rear rotor number of blades from 5 to 7 further improves the system's performance by 4.6%. The first alteration can be immediately implemented, as its results will be beneficial. For the other two changes however, additional factors must be taken into account, such as feasibility and cost as well as structural issues in order to make sure that they are worth implementing. For the last modification, special attention must be given to potential problems with the generator matching.

11.1.5. Comparison with other turbines. Approximate comparisons of the counter-rotating turbine performance with that of similar conventional wind

turbines (designed in chapter 3) were performed. Each counter-rotating turbine rotor was compared to a conventional turbine with similar blade chord distribution and the same number of blades. It was found that both the front and the rear counter-rotating turbine rotors produced less power coefficient than their counterparts and operated at lower values of tip speed ratio. The reduced performance of each counter-rotating turbine rotor can be attributed to the other rotor interference. Also, comparison of the $C_{p,tot}$ and λ_{tot} of the counter-rotating turbine with the performance characteristics of a conventional turbine with the same total number of blades has shown that the counter-rotating turbine produces about the same C_p as its conventional counterpart. However, the λ_{tot} of the counter-rotating turbine was found to be considerably larger than the λ_{opt} of the conventional turbine. This last result shows that the advantage of a counter-rotating turbine over a conventional one with the same total number of blades is the the significant increase in the tip speed ratio of the former, rather than a considerable improvement in performance.

11.2. COMMENTS ON THE ACCURACY OF THE COUNTER-ROTATING TURBINE DESIGN.

The accuracy of the counter-rotating turbine design depends on the validity of a series of simplifying assumptions. These assumptions and the effects they may have are described below:

11.2.1. Front to rear rotor interference. For estimating the front to rear rotor interference, the initial incoming velocity distribution on the front rotor disc was estimated and it was then projected downstream of the rotor using the experimental data of [89], in order to take into account the wake decay. The method used for estimating the initial induced velocity distribution is expected to be accurate. This is

backed by the findings of Voutsinas, [90], who used a similar method for estimating the induced velocity distribution just downstream of a turbine and compared it with the experimental results of [89], obtaining good agreement.

The assumption that the induced velocity shape does not change significantly up to two diameters downstream of the front rotor disc is expected to be a reasonable one, as it is backed by the results of [89], as well as by observations of wakes generated by other simpler bodies (such as cylinders, spheres, etc) where self-similar velocity distributions occur within the wake.

For estimating the increase of the induced velocity magnitude with increasing distance from the front rotor, the experimental results of [89] were used, assuming they are typical of a wind turbine. The accuracy of this assumption is subject to the dependence of the wake decay on the turbine characteristics. Unfortunately, a comprehensive investigation into the effects of the wind turbine characteristics on wake decay is lacking. However, in order to minimise the possibility of error, the number of blades of the front counter-rotating turbine rotor was taken to be equal to 3, ie the same as that of the turbine tested in [89].

Finally, in the model used, the wake expansion was neglected. This is justified as, for the turbine tested in [89], the wake was found to have expanded by just 5% one rotor radius downstream of the turbine.

11.2.2. Rear to front rotor interference. For estimating the rear to front rotor interference, the rear rotor was substituted by an actuator disc. This is justified by the results of [16] and [105] in which actuator disc models have been used successfully, as well as by the comparison of the predictions of this model with the experimental results of [89]. (See figure 10.7).

11.2.3. Assumptions pertinent to both rotors. The assumption

that the interference the front rotor creates to the rear (and vice versa) can be added to the incoming flow of the latter is backed by the research work done for counter-rotating propellers and helicopter rotors. The assumption that the incoming flow to each rotor is steady is also backed by the experimental results of [89]. (See figure 9.4).

Thus the existing knowledge of wind turbine wakes and counter-rotating rotor aerodynamics has been used for developing as accurate and realistic a design model for counter-rotating turbine blades as possible. This model takes into account most of the important phenomena in counter-rotating turbine aerodynamics, such as interaction between rotors, effects of axial distance between rotors and turbine wake decay.

11.3. AREAS OF FURTHER RESEARCH.

A great deal of research work still remains to be done for further developing the counter-rotating turbine concept. Some possible areas of further research are highlighted here:

11.3.1. Testing of a counter-rotating turbine prototype. This would be necessary in order to verify the theory as well as to provide guidelines for improving the present design model. Construction of a counter-rotating turbine prototype is not expected to be difficult, as some of the infrastructure already exists (such as the generator and turbine tower) and only the blades will need to be constructed.

11.3.2. Prediction of the turbine off-design performance. In this study, the counter-rotating turbine performance was estimated for optimum conditions only. In order to estimate the off-design performance of the turbine, the models used for conventional turbines (as well as that used for the vortex turbine, chapter 4, section 4.5) are not expected to be adequate. This is because for the case of the counter-rotating

turbine, the $C_p(\lambda)$ and $C_q(\lambda)$ characteristics of one rotor largely depend on the operating conditions of the other. Thus, a multitude of combinations of each rotor's operating conditions is expected to exist that would give equal torque coefficient for both rotors. (Note that the constraint of optimum angle of attack throughout the blade used in the turbine design will not apply in this case). A more appropriate method would be to examine the dynamic behaviour of the turbine. That would require modelling not only of the turbines and their interaction, but of the generator and load as well. By solving the differential equations of that system, the behaviour of the turbine in time can be obtained for certain initial conditions.

11.3.3. Development of a power regulation strategy. The counter-rotating turbine has the feature of self-orientation. For example, when the turbine is at yaw, (possibly due to a sudden change of the wind direction), the front rotor (being an upwind one) will create a yawing moment that will tend to further increase the yaw angle. On the other hand, the rear rotor, (being a downwind one) will create a restoring moment. If the rear rotor moment is larger than that of the front one, the turbine will turn to face the wind. In the same way, for windspeeds larger than the rated value, the operating conditions of each rotor can be selected (by adjusting the generator load) so that the front rotor will generate a larger yawing moment than the rear one, that will yaw the turbine to an appropriate angle. Thus the turbine will be self-regulated. For this to be achieved, an appropriate model of the turbine operation at yaw will have to be developed.

11.3.4. Effects of using different rotor radii. In the present design model, the two counter-rotating turbine rotors were assumed to have the same radius. An increase of the rear rotor radius could increase the turbine performance as the outer part of the rear rotor blades would operate outside the front rotor wake taking advantage of the the higher fluid energy in that region. However, adverse effects may also result from

this modification: A region of the rear rotor blades (inboard of the tips) will meet the front rotor trailing vortices. The interaction between the blades and the vortex may have adverse effects. Indeed, in references [17] and [108], blade-vortex interactions were observed for the case of helicopter rotors in forward flight, where the advancing blade met the trailing vortex generated by the retreating blade. It was reported that the trailing vortex caused in some instances local stall of the blade, resulting to loss of lift and increase of vibration levels.

CHAPTER 12.

RESUMÉ.

CHAPTER 12. RESUMÉ.

12.0. INTRODUCTION.

The most important achievements of this study and some concluding remarks are presented in this chapter.

12.1. ACHIEVEMENTS OF THIS STUDY.

12.1.1. Lifting line blade design procedure.

One important achievement of this work is the development and implementation of a procedure for the design of wind turbines operating in non-uniform, non-axial but axisymmetric flows. Based on lifting line theory, the blade design procedure is expected to be more accurate than those based on momentum theory. The present design method was validated by designing conventional turbines and comparing them with similar designs produced by momentum theory. It was found that both theories exhibit similar overall trends, although the lifting line procedure produces a more conservative estimate of the turbine performance.

The above mentioned design procedure is a general one and can be used in applications where momentum theory is not adequate.

12.1.2. Delta wing-turbine system.

The system dimensions were compared with those of equivalent conventional turbines. It was found that the system compares well with conventional turbines up to rated power values equal to 100 kW. Its advantages were found to be the lower turbine diameter required for a given power output and the opportunity it provides for direct connection of the turbines to generators. The cost of this advantage is the relatively large delta wing required.

A system prototype was designed for testing. The prototype turbine blades were designed taking into account Reynolds number effects which were found to be of great importance at model scales. The prototype off design performance was estimated and it was found that the simplifying modifications made to the original blade design did not affect the turbine performance significantly.

The generator to be used with the prototype turbine was bench-tested and its performance characteristics were identified. For matching the generator with the turbine, an appropriate load for the generator was found. The prototype long-term performance was also estimated.

Finally, the effects of yaw on the delta wing vortices were investigated experimentally. This was done in order to determine the feasibility of using the delta wing yaw to regulate the system power output. It was found that the above mentioned regulation technique can be used, provided that undue blade vibrations will not occur.

12.1.3. Counter-rotating turbine.

The above mentioned lifting line procedure as well as the existing

knowledge of wind turbine wakes and counter-rotating rotor aerodynamics were used for the design of the counter-rotating turbine blades and the modelling of the two rotors' interaction.

It was demonstrated that proper design of the turbine blades and appropriate axial positioning of the two rotors could considerably increase the turbine performance, compared with the performance of the Trimble Mill.

It was also found that a considerable increase of the generator effective rotational speed can be achieved by the counter-rotating turbine, compared to that of a conventional turbine with the same number of blades.

12.2. CONCLUDING REMARKS.

Neither the development of the delta wing-turbine system nor that of the counter-rotating turbine have been exhausted by this study. As was pointed out in chapters 8 and 11, many areas of both wind power systems' design and operation are still open to research. One important aspect of the work that remains to be done is the construction and testing of prototypes. This will provide a means for validating the turbine design methods used. It will also be a starting point for assessing the systems' cost-effectiveness.

It is hoped that the work presented in this thesis has helped to highlight the most important characteristics of the wind power systems examined, and that it has demonstrated their advantages and potential.

BIBLIOGRAPHY.

BIBLIOGRAPHY.

1. Le Gourieres, D. "Wind power plants". Pergamon Press, 1982.

2. Flint, B. "Windmills of East Amglia". F.W. Pawsey and Sons, 1971.

3. Johnson, L. G. "Wind energy systems". Prentice-Hall, 1985.

4. Putnam, P. C. "Power from the wind". Van Nostrand Reinhold, 1948.

5. Garrad, A. "Wind energy in Europe". The European Wind Energy Association, 1991.

6. Hensing, P. C. "Prospectives of cost reduction of large wind turbines". Proceedings of Amsterdam EWEC '91, part 1, pp 530-534.

7. Betz, A. "Wind energy and its exploitation by windmills". Gotingen: Vandenhoeck and Rupercht, 1926.

8. Glauert H. "Aerodynamic theory". Vol. 4, Div. L, pp 170-293, Editor: F.W. Durand, 1935.

9. Lysen E. H. "Introduction to wind energy". SWD, May 1983.

10. Milne L. M. and Thomson D. "Theoretical aerodynamics". Dover Publ. 1958.

11. Devries O. "On the theory of HAWT". Annual Review of Fluid Mechanics, Vol. 15, pp 77-96, 1983.

12. Prandtl L. "Theory of the lifting wing". I. Nachr. Ges. Wiss. Gotingen, Math. Phys, KI, pp 451-477, 1918.

13. Goldstein S. "On the vortex theory of screw propellers". Proceedings of the Royal Society, A, Vol. 123, pp 440-465, 1929.

14. Theodorsen T. "The theory of propellers, I, II, III, IV". Four papers: NACA Reports 775, 776, 777, 778, 1944.

15. Politis K. G. and Loukakis T. A. "On lifting line analysis of horizontal axis wind turbines". Wind Engineering, Vol. 8, No. 1, pp 23-25, 1984.

16. Afjeh A. A. "A vortex lifting line method for the analysis of HAWT". Journal of Solar Energy Engineering, Vol. 108, pp 303-309, Nov. 1986.

17. Miller R. H. "Rotor hovering performance using the method of fast free wake analysis". Journal of Aircraft, Vol. 20, No. 3, pp 257-261, March 1983.

18. Lerbs H. W. "Moderately loaded propellers with a finite number of blades

and an arbitrary distribution of circulation". SNAME Transactions, Vol. 60, pp 73-117, 1952.

19. Batcelor G. K. "An introduction to fluid dynamics". Cambridge University Press, pp 589-591, 1970.

20. Nicholson J. W. "The approximate calculation of Bessel functions of imaginary argument". Philosophical Magazine, Vol. 20, 1910.

21. Leftheriotis, G. and Carpenter, C. J. "Development of a procedure for the design of a wind turbine rotor to operate in the vortex field generated by a slender delta wing". Wind Engineering, Vol. 14, No 3, pp 153-164, 1990.

22. NAG fortran library manual. Mark 13, Vol. 5.

23. Griffiths, R. T. "Centre body effects on horizontal axis wind turbines". Applied Energy, Vol. 13, No 3, pp 183-194, 1983.

24. Binder, R. C. "Advanced fluid mechanics". Vol. II, Prentice-Hall, 1958.

25. Jackobs, E. N. and Sherman, A. "Airfoil characteristics as affected by variations in Reynolds number". NACA Report, No 586, 1939.

26. Abbot, I. H. and Von Doenhoff, A. E. "Theory of wing sections". Dover Publications Inc, New York.

27. Loftin, L. K. and Smith, H. A. "Aerodynamic characteristics of 15 NACA airfoil sections at several Reynolds numbers from $0.7x10^6$ to $9X10^6$". NACA TN 1945, Oct. 1949.

28. Althaus, D. "Stuttgarten Profilkatalog I". Insttut fur Aerodynamik und Gasdynamik der Universitat Stuttgart. 1972.

29. Anderson J. D. Jr. "Incompressible aerodynamics". Mc Graw- Hill, 1985.

30. Johnson, W. "Helicopter theory". Princeton University Press, 1980.

31. Griffiths, R. T. and Woolard, M. G. "Performance of the optimal wind turbine". Applied Energy, Vol. 4, No 4, pp 261-272, 1978.

32. Griffiths, R. T. "The effect of aerofoil characteristics om windmill performance". Aeronautical Journal, Vol. 81, Issue 799, pp 322-326, 1977.

33. Galetuse, S. "On the highest efficiency windmill design". Journal of Solar Energy Engineering, Vol. 108, pp 41-48, Feb. 1986.

34. Vanegmond, J. A. 'Evaluation of two performance prediction methods for horizontal axis wind turbines". NLR TR 85028-L, NLR, Amsterdam, 1985.

35. De Vries, O. and Den Blanken, M. H. G. "Second series of wind tunnel tests on a model of a two-bladed HAWT". NLR TR 81069-L, NLR, Amsterdam, 1981.

36. Earnshaw, P. B. and Lawford, J. A. "Low speed wind tunnel experiments on a series of sharp edged delta wings". ARC R & M, No 3424, 1966.

37. Earnshaw, P. B. "Experimental investigation of the structure of a leading edge vortex". ARC R & M, No 3281, 1961.

38. Hummel, D. "Untersuchungen uber das Aufplatzen der Wierbel an Schlanken Delta Flugeln". Zeitschrift fuer Flugwissenschaften, Vol. 13, No 5, pp 158-168, May 1965.

39. Sforza, P. M. "Flow measurements in leading edge vortices". AIAA Journal, Vol. 16, No 3, pp 218-224, 1978.

40. Sforza, P. M. "Vortex augmentation of wind energy". Wind Engineering, Vol.1, No 3, 1978.

41. Greff, E. and Holzdeppe, D. "Wind energy concentration within vortex flow fields and its utilization for the generation of energy". Proceedings of the 1st Colloquium on Wind Energy, pp 197-202, U.K., 1981.

42. Sivasegaram, S. "Power augmentation in wind rotors: A review". Wind Engineering, Vol. 10, No 3, pp 163-179, 1986.

43. Leftheriotis, G. "Investigation of the vortex field generated by a slender delta wing and development of a procedure for the design of a wind turbine to operate in this field". MSc thesis, University of Warwick, May 1989.

44. Leftheriotis, G. and Carpenter, C. J. "Investigation of the vortex field generated by a slender delta wing". Wind Engineering, Vol. 14, No 3, pp 141-152, 1990.

45. Feuchtwang, J. "Ground plan effect and wind shear effect on delta wing vortices". Third year project report, University of Warwick, Dept. of Engineering, April 1991.

46. Sisterson, D. L. "Difficulties in using power laws for wind energy assessment". Solar Energy, Vol. 31, No 4, pp 201-204, 1983.

47. Jaya Devaya, T. S. and Smith, R. T. "Generation schemes for wind power plants". IEEE transactions, Vol. AES-11, No 4, pp 543-550, 1975.

48. Johnson, C. C. "Economical design of wind generating plants". IEEE transactions, Vol. AES-12, No 3, pp 316-320, 1976.

49. Musial, W. D. and Cromack, D. E. "Influence of Re on performance modelling of HAWT". Journal of Solar Energy Engineering, Vol. 110, pp

139-144, May 1988.

50. Lissaman, P. B. S. "Low Re airfoils". Annual Review of Fluid Mechanics, Vol. 15, pp 223-239, 1983.

51. Gad-El-Hak, M. "Control of low Re airfoils. A review". Low Re aerodynamics, Proceedings of the Conference, Notre Dame, Indiana, USA, 5-7 June, 1989.

52. Carmichael, B. H. "Low Re airfoil survey". NACA CR 165803, 1981.

53. Mueller, T. J. and Batill, M. S. "experimental studies of separation on a 2-D airfoil at low Re". AIAA Journal, Vol. 20, No 4, pp 457-463, April 1982.

54. Althaus, D. "Profilpolaren fur den Modelflug". Karlsruhe: Neckar Verlag, 1980.

55. Miley, S. J. "A catalogue of low Re airfoil data for wind turbine applications". Prepared for Rockwell Inc. Corp. Energy System Group, Rocky Flats Plant, Wind Syst. Program, 1982.

56. Chapman, S. J. "Electric machinery fundamentals". Mc Graw-Hill, 1985.

57. Sen, P. C. "Principles of electric machines and power electronics". John Wiley and Sons, 1989.

58. Honorati, O. et. al. "Gear-less wind energy conversion system using an axial-flux PM synchronous machine". Proceedings of Amsterdam EWEC '91, Part 1, Oct. 1991.

59. Vibro-meter TG-.../B torque transtducer and 8-MCA-1/AO carrier frequency Amplifier manuals. 1968.

60. Selami, S. "Disc geometry synchronous machines with permanent magnets". MSc thesis, University of Warwick, Dec. 1981.

61. De Paor, A. M. et. al. "Parameter identification and passive control of a wind-driven permanent magnet alternator system for heating water". Wind Engineering, Vol. 7, No 4, pp 193-207, 1983.

62. West, M. (editor). "Alternative energy systems". Pergamon Press, 1984.

63. Justus, C. G. et. al. "Methods for estimating Wind speed frequency distributions". Journal of Applied Meteorology, Vol. 17, pp 350-353, 1978.

64. Gupta, B. K. "Weibull parameters for annual and monthly speed distributions for five locations in India". Solar Energy, Vol. 37, No 6, 1986.

65. Johnson, G. L. " Economic design of wind electric systems". IEEE

transactions, Vol. PAS-97, No 2, March/April 1978.

66. Olorunsola, O. "On free yaw behaviour of horizontal axis wind turbines". International Journal of Energy Resources, Vol. 10, Part 4, pp343-355, 1986.

67. Glasgow, J. C. et. al. "The effect of yaw on horizontal axis wind turbine loading and performance". NASA TM 82778, 1982.

68. Hohenemser, K. H. "Wind turbine speed control by automatic yawing". Journal of energy, Vol 7, No 3, pp 237-242, 1983.

69. Liebst, B. S. "Pitch control system for large scale wind turbines". Journal of Energy, Vol 7, No 2, pp 182-192, 1983.

70. Jamieson, P. et. al. "Innovative concepts for aerodynamic control of wind turbine rotors". Proceedings of EWEC '91, Part 1, pp819-823, 1991.

71. Smulders, P. T. "Aerodynamic interference between two wind rotors set next to each other in one plane". Proceedings of Hamburg EWEC '84, Paper H10, pp 529-533, Oct. 1984.

72. De Vries, O. "Wind tunnel tests of a model of a two bladed horizontal axis wind turbine". NLR TR 79071 L, NLR, Amsterdam, 1979.

73. Viterna, L. A. and Janetzke, D. C. "Theoretical and experimental power from large wind turbines". NASA report TM-82944, 1982.

74. Divone, L. "Wind energy-a glimpse at the future". 4th International Conference on Energy Options. (Organised by the IEE), London, 1984.

75. Milborrow, D. J. "Changes in aerofoil characteristics due to radial flow on rotating blades". Proceedings of 7th BWEA Conference, pp 85-93, March 1985.

76. Anderson, C. G. et. al. "Flow visualisation studies on rotating blades". Proceedings of 9th BWEA Conference , pp 169-176, March 1987.

77. Eggleston, D. M. and Starcher, K. "A comparative study of the aerodynamics of several wind turbines using flow visualisation". Journal of Solar Energy Engineering, Vol. 112, pp 301-309, Nov. 1990.

78. Warne, D. F. "Wind power equipment". E. & F. N. Spon, 1983.

79. Milborrow, D. J. "Wake and cluster research: Past, present and future". IEE Proceedings, Vol. 130, Part A, No 9, Dec. 1983.

80. Baker, R. W. and Walker, S. N. "Wake measurements behind a large horizontal axis wind turbine generator". Solar Energy, Vol. 33, No 1, pp 5-12, 1984.

81. Baker, R. W. et al. "Wake measurements around operating wind turbines". Journal of Solar Energy Engineering, Vol. 107, pp 183-185, May 1985.

82. Neustadler, E. H. and Spera, A. D. "Method for evaluating wind turbine wake effects on wind farm performance". Journal of Solar Energy Engineering, Vol. 107, pp 240-243, Aug, 1985.

83. Zambrano, T. G. and Gyatt, G. W. "Wake structure measurements at the MOD-2 cluster test facility at Godnoe Hills, Washington". IEE Proceedings, Vol. 130, Part A, No 9, Dec. 1983.

84. Taylor, G. J. "Wake and performance measurements on the Lawson-Tanchred 17m horizontal axis windmill". Journal of Wind Engineering and Industrial Aerodynamics. Vol. 31, Nos 2-3, pp 133-146,1988.

85. Ainslie, J. F. "Calculating the flowfield in the wake of wind turbines". Journal of Wind Engineering and Industrial Aerodynamics, Vol. 27, Nos 1-3, Jan. 1988.

86. Baker, R. W. and Walker, S. N. "Wake studies at the Godnoe Hills MOD-2 site". BA Report 82-11. Oregon State University, Corvallis, USA, oct. 1982.

87. Elliot, D. L. and Barnard, J. C. "Observations of wind turbine wakes and surface roughness effects on wind flow variability". Solar Energy, Vol. 45, No 5, pp 265-283, 1990.

88. Figard, R. L. and Schetz, J. A. "Flowfield near the rotor of a 10-kW horizontal axis windmill". Journal of Energy, Vol. 4, Part 2, pp 64-69, March-April 1980.

89. Papaconstantinou, A. and Bergeles, G. "Hot-wire measurements of the flowfield in the vicinity of a HAWG rotor". Journal of Wind Engineering and Industrial Aerodynamics. Vol. 31, Nos 2-3, pp 133-146, 1988.

90. Voutsinas, S. G. et al. "On the effect of the rotor geometry on the formation and the development of its wake". Proceedings of the Amsterdam EWEC '91, Part 1, pp 402-406, Oct. 1991.

91. Voutsinas, S. G. et al. "Investigation of the effect of the initial velocity profile on the wake development of a wind turbine". Proceedings of the Amsterdam EWEC '91, Part 1, pp 407-411, Oct. 1991.

92. Kotb, M. and Soliman, H. "Enhanced wind rotor performance". Modelling Simulation and Control B, Vol 10, no 2, pp 1-4, 1987.

93. Lock, C. N. H. "Interference velocity for a close pair of airscrews". R and M No. 2084, British ARC, July 1941.

94. Crigler, J. L. "Application of Theodorsen's theory to propeller design".

NACA report 776, 1944.

95. Davidson, R. E. "Optimization and performance calculation of dual- rotation propellers". NASA Technical Paper, No. 1948, 1981.

96. Playle, S. C. et. al. "Numerical method for the design and analysis of counter-rotating propellers". Journal of Propulsion and Power. Vol 2, No 1, pp 57-63, 1986.

97. Korkan, K. D. et. al. "Off-design analysis of counter-rotating propeller configurations". Journal of Propulsion and Power. Vol 3, No 1, pp 91-93, 1987.

98. Harrington, R. D. "Full scale tunnel investigation of the static thrust performance of a co-axial rotor". NACA TN 2318, 1951.

99. Paglino, V. M. "Forward flight performance of a co-axial rigid rotor". 27th Annual National Forum of the American Helicopter Society. 1971.

100. Cheeseman, I. C. "A method of calculating the effect of one rotor upon another". ARC Tech. Rep. CP No 406, 1958

101. Andrew, M. J. "Co-axial rotor aerodynamics in hover". Vertica, Vol 5, pp 163-172, 1981.

102. Davis R. A. et. al. "A practical co-axial twin rotor model". Vertica, Vol 14, pp 61-68, 1990.

103. Azuma, A. "Local momentum theory and its application to the rotary wing". Journal of Aircraft, Vol 16, No 1, pp 6-14, Jan. 1979.

104. Saito, S. et. al. "A numerical approach to co-axial rotor aerodynamics". Vertica, Vol 6, pp 253-266, 1982.

105. Nagashima, T. "Optimum performance and wake geometry of a co-axial rotor in hover". Vertica, Vol 7, No 3, pp 225-239, 1983.

106. Wilson, R. E. "Wind turbine flow field model". Journal of Solar Energy Engineering. Vol 108, pp 344-345, Nov. 1986.

107. Selig, M. et. al. "Aerofoils at low speed". Stokely, 1989.

108. Booth, E. R. Jr. and Yu J. C. "Two-dimensional blade-vortex flow visualization investigation". AIAA Journal, Vol. 24, No 9, pp 1468-1473, Sep. 1986.